Approaches to Simulation of an Underground Longwall Mine and Implications for Ventilation System Analysis

Hongbin Zhang

Thesis submitted to the faculty of the Virginia Polytechnic Institute and State University in partial fulfillment of the requirements for the degree of

Master of Science
In
Mining Engineering

Kray D. Luxbacher, Chair
Saad Ragab
Gerald Luttrell

February 12, 2015
Blacksburg, Virginia

Keywords: CFD modeling, network modeling, hybrid model, underground mine ventilation

Approaches to Simulation of an Underground Longwall Mine and Implications for
Ventilation System Analysis

Hongbin Zhang

ABSTRACT

Carefully engineered mine ventilation is critical to the safe operation of underground
longwall mines. Currently, there are several options for simulation of mine ventilation.
This research was conducted to rapidly simulate an underground longwall mine,
especially for the use of tracer gas in an emergency situation. In an emergency situation,
limited information about the state of mine ventilation system is known, and it is difficult
to make informed decisions about safety of the mine for rescue personnel. With careful
planning, tracer gases can be used to remotely ascertain changes in the ventilation
system. In the meantime, simulation of the tracer gas can be conducted to understand the
airflow behavior for improvements during normal operation.

Better informed decisions can be made with the help of both tracer gas technique and
different modeling approaches. This research was made up of two main parts. One was a
field study conducted in an underground longwall mine in the western U.S. The other one
was a simulation of the underground longwall mine with different approaches, such as
network modeling and Computational Fluid Dynamics (CFD) models. Networking
modeling is the most prevalent modeling technique in the mining industry. However, a
gob area, which is a void zone filled with broken rocks after the longwall mining, cannot
be simulated in an accurate way with networking modeling. CFD is a powerful tool for
modeling different kinds of flows under various situations. However, it requires a
significant time investment for the expert user as well as considerable computing power.
To take advantage of both network modeling and CFD, the hybrid approach, which is a
combination of network modeling and CFD was established. Since tracer gas was
released and collected in the field study, the tracer gas concentration profile was
separately simulated in network modeling, CFD model, and hybrid model in this study.
The simulated results of airflow and tracer gas flow were analyzed and compared with
the experimental results from the field study.

Two commercial network modeling software packages were analyzed in this study. One of the network modeling software also has the capability to couple with CFD. A two-dimensional (2D) CFD model without gob was built to first analyze the accuracy of CFD. More 2D CFD models with gob were generated to determine how much detail was necessary for the gob model. Several three-dimensional (3D) CFD models with gob were then created. A mesh independence study and a sensitivity study for the porosity and permeability values were created to determine the optimal mesh size, porosity and permeability values for the 3D CFD model, and steady-state simulation and transient simulations were conducted in the 3D CFD models. In the steady-state simulation, a comparison was made between the 3D CFD models with and without taking the diffusivity of SF_6 in air into account.

Finally, the different simulation techniques were compared to measured field data, and assessed to determine if the hybrid approach was considerably simpler, while also providing results superior to a simple network model.

Acknowledgements

This thesis basically consists of two manuscripts. One was published in the 2014 SME Annual Meeting and the other one will be published in the 2015 Mine Ventilation Symposium. "Modeling" is the most significant word in this thesis. Both CFD modeling and network modeling were carefully analyzed and compared in this study. I encountered more difficulties than I expected during the research process. I am lucky and I received lots of help and supports from my professors and colleagues. All the difficulties were solved finally and I want to express my appreciation to all the people who helped me in this research.

I worked hard on this research and this research was completed in one and half years. I am always optimistic although I had a bad skiing accident right before I started this research. Difficulties did not defeat me and I conquered them successfully instead.

First, I would like to thank my advisor, Dr. Kray Luxbacher. She is the nicest advisor I have ever seen. She did not only direct me to the right way on my project, but also point out things that can be improved and corrected on the project. She always encourages me and it makes me feel confident all the way. Moreover, she provided many opportunities for me to publish and present my work in public.

Secondly, I really appreciate the advice and help provided by Dr. Saad Ragab and his two Ph.D students, Hassan El-Hady Fayed and Kareem Akhtar. I could not have grasped the techniques of establishing mesh and CFD models so quickly without their instructions. More importantly, Dr. Ragab taught me the way of computational thinking and I treat CFD as "fluid knowledge center" more than just "fluid dynamics computer".

I also want to thank Dr. Harold McNair for teaching me the knowledge of gas chromatograph (GC). Even though GC was not discussed in this study, it is primary technique used to analyze tracer gas concentration in this work.

In addition, I appreciate the help and suggestions from my group members: Dr. Guang Xu and Dr. Edmund Jong. Dr. Xu introduced Ansys Icem to me and Edmund Jong taught me the injection techniques of GC.

I would like to thank Dr. Steven Schafrik for teaching me the knowledge of high performance computer and Linux systems.

Besides, I appreciate the generous help provided by Stephen Theron and Tyler Smith from PADT Inc. Both of them helped me on the hybrid model.

Additionally, I want to thank the National Institute for Occupational Safety and Health for providing me the opportunity to conduct this research.

Finally, I want to thank my family, especially, my wife, Ting Du, for her constant love, support, and trust. She did take a good care of everything at home and it allowed me to focus all of myself on my work. I owe half of my success to her. Even though my parents were in China, they are always my patrons.

Table of Contents

List of Figures

List of Tables

List of Abbreviations

API	Application Programing Interface
CFD	Computational Fluid Dynamics
EES	Engineering Equation Solver
FLAC	Fast Lagrangian Analysis of Continua
FDS	Fire Dynamics Simulator
HTR	High Temperature Reactor
IPCM	Implicit Pressure Correction Method
CFM	Cubic Feet per Minute
KCFM	Kilo-Cubic Feet per Minute
PPB	Parts Per Billion
PPM	Parts Per Million
PBMR	Pebble Bed Modular Reactor
PCU	Power Conversion Unit
RANS	Reynolds Averaged Navier-Stokes
RP	Release Point
SP	Sample Point
RKTD	Runge Kutta method with Trapezoidal Damping
SCCM	Standard Cubic Centimeters per Minute
TINTE	TIme dependant Neutronics and Temperatures
UDF	User Defined Function
UDS	User-Defined Scalar
1D	One-dimensional
2D	Two-dimensional
3D	Three-dimensional

1 Introduction

This study is important because it stands to contribute to more rapid and accurate modeling of mine systems. Computational Fluid Dynamics (CFD) modeling, network modeling, and a combination of CFD and network modeling were analyzed in this thesis. This thesis is made up of five chapters. Chapter 1 gives an overview of the thesis. Chapter 2 reviews the literature of CFD, network modeling, and tracer gas applications. Chapter 3 and 4 consist of two manuscripts. The paper in Chapter 3 was published in the SME annual meeting in 2014. The paper in Chapter 4 is planned for publication in the 2015 Mine Ventilation Symposium. Conclusions for the work are in Chapter 5.

CFD modeling has become more and more popular in mining recently. It is critical in areas where resolving flow patterns is important. Flow patterns can change considerably after an accident, like explosion that damages the ventilation infrastructure. However, by using CFD, the flow patterns and distributions in both accessible and inaccessible areas can be visualized. Additionally, CFD is useful understanding airflow behavior in low velocity areas not well represented by network modeling. However, CFD is not an easy technique you can learn in a short period. It requires understanding of both mathematics and fluid dynamics, and some familiarity with complex software. Another limitation of CFD is that it requires computing power, as well as expert knowledge, and it is time consuming for the user to build the numerical model.

Network modeling has been the most prevalent technique for simulation of mine ventilation systems applied in the mining industry for many years. Compared with CFD modeling, network modeling is much easier to learn and does not require as much computing power. There are two key software packages used in this study. One is VnetPC, developed by Mine Ventilation Services, which is based on the Square Law and the Hardy Cross process. The other one is Flownex, developed by M-Tech Industrial (Pty) Ltd., which is based on partial differential equations of mass conservation, momentum conservation, and energy conservation. VnetPC is discussed in detail in Chapter 3 and Flownex is analyzed in Chapter 4.

A combination of CFD and network modeling was established to save computing time and ensure high accuracy results at the same time. Flownex was used as the network component and Ansys Fluent was used as the CFD component in the combination. The integration capability of Flownex makes it possible to connect a one-dimensional (1D) network model with a 3D CFD component. Details about this hybrid model are shown in Chapter 4.

The field experiment in this study was conducted in an underground coal mine in the western U.S. Four students from Virginia Tech and four workers from the mine conducted the experiment. Detailed field study information can be found in Jong's dissertation (Jong 2013). The gob in the underground mine was designed for airflow to go around it instead of flowing through it. Tracer gas technique was utilized to ascertain airflow information in a two phase field study. Sulfur hexafluoride (SF_6) was selected as the tracer gas. With the help of GC and ventilation survey data, the volumetric flow rates of SF_6 at different sample points were obtained.

2 Literature Review
2.1 CFD

CFD is now widely applied in the mining industry. Due to the high level of accuracy and flexibility, CFD has been successfully applied in spontaneous combustion control, dust control, methane movement simulation, fire spread simulation, ventilation airflow simulation, and gob inertisation, just to give a few examples in mine ventilation. At the same time, many studies have been published on CFD applications in other areas of mining. However, few studies have been done on a hybrid CFD-network model. Since the purpose of this study is to figure out a hybrid CFD-networking model for the simulation of an underground longwall mine, CFD applications in longwall gob areas and other fields are briefly reviewed. An exhaustive literature of CFD applications in mining can be found in Xu's dissertation (Xu, 2013).

CFD is powerful for analyzing flow patterns and solving fluid dynamics problems, especially in the areas people cannot access, like a gob. A gob area, which is created as a longwall advances, is complex in terms of geometry and quantifying the properties of porous media, as it is subject to dynamic geomechanical conditions. Since it is made up of broken rocks falling from the roof, the gob is also not accessible. In addition, ventilation surveys and experiments around the gob are also difficult to conduct. CFD makes it possible to visualize the flow in the gob. Many CFD studies have been done on gob areas in the past. Some of the studies are reviewed here to show the advantages of using CFD in the gob areas.

CFD plays a significant role for realizing the changes of flow patterns and behavior in the gob. Yuan and others (Yuan, Smith, and Brune 2006) successfully analyzed the airflow patterns in a gob under various ventilation systems by using CFD. The gob in one panel was divided into five zones with constant permeability values in the study. This conclusion was based on Fast Lagrangian Analysis of Continua (FLAC) modeling of longwall mining used in their paper. Ren and others (Ren, Balusu, and Claassen 2011) published another paper with a CFD study and they found that the gas flow pattern in the

gob was related with the retreat direction of longwall. Karacan and others (Karacan, Ren, and Balusu 2008) summarized the techniques of numerical modeling used in the mining industry and issues faced for gas management in another study, discussing CFD and numerical reservoir modeling. They noted that CFD was better but more complicated than the network models. Besides, CFD was more effective in the areas where network models were not suitable and capable.

CFD is also helpful on figuring out the relationship between permeability and gob properties. Karacan and Esterhuizen (Esterhuizen and Karacan 2007) found that permeability in the vertical direction had a relationship with a caving and block rotation model. Both a CFD model and a FLAC3D model were used in the study, linking geomechanics with changes in the porous media. Another CFD study on the spontaneous heating in the gob was conducted (Yuan and Smith 2008a) to determine the possibility of having spontaneous heating in the gob areas. Yuan and Smith conducted another CFD study in 2008 (Yuan and Smith 2008b). The purpose of this study was to learn how the gob characteristics will change spontaneous heating in the gob. Oxidation of coal was treated as spontaneous heating in the model. They concluded that permeability and inducing time had an inverse relationship. A bleederless ventilation system and nitrogen injection in the gob was also successfully studied in a similar CFD study (Smith and Yuan 2008).

In addition, CFD models are used to develop optimum gob inertisation strategies to improve coal mine safety. Gob inertisation can help decrease the chance of potential explosion during longwall sealing operations. Ren and others demonstrated with CFD that gob inertisation can be achieved within a few hours of sealing a panel (Ren, Balusu, and Humphries 2005). Proactive inertisation strategies were also developed to suppress spontaneous heating in the gob. Results showed that the inertisation was more effective at two hundred meters behind the face than that right behind the face line. In another study, Ren and Balusu (Ren and Balusu 2005) developed gob inertisation strategies by using CFD models. The purpose of their study is to understand flow migration dynamics in the gob. One of the key techniques used in the study was linking User Defined Functions

(UDFs) to Fluent solver. With the help of the UDFs, a momentum sink was added to the momentum equations to model the airflow through the gob.

CFD can be used to improve the control of spontaneous combustion in longwall gobs (Ren and Balusu 2005). Gob permeability distributions and gas emissions are the most important part of the CFD models. With the help of pressure, flow rate, and gas distribution in a longwall gob area, initial models were calibrated and gob permeability distribution was refined. Due to CFD modeling work, innovative gob gas control strategies for spontaneous combustion have developed rapidly and efficiently. There are several major factors affecting spontaneous heating and CO production underground, such as, seam structure, condition of gateroads behind the working face, caving pattern behind the face, location of faults, and length of the back return. In addition, CFD modeling was used to study the gas flow mechanics and distribution in longwall gobs. CFD models have been useful to develop control strategies for gas and spontaneous heating, such as reducing air velocity and increasing gob drainage flow rate (Ren and Balusu 2005).

Dust control is another significant application of CFD. Dust is generated during the excavation process and it is a major concern in terms of underground miners' health and safety. CFD is a very effective tool to evaluate and improve dust suppression in continuous miner and roadheader sections as described by Heerden and Sullican in their paper (Heerden and Sullivan 1993). After the process of establishing correct geometry, defining properties of fluids and boundary conditions, velocity vectors were plotted and velocity contours were made. Respirable dust particles were assumed to follow the gas flow in the underground and flow lines were used to quantify the movement of dust particles. The model was used to investigate dust suppression with various parameters, such as the positions of a force ventilation column, a brattice, and an exhaust column, drum rotation, water sprays and air movers. In addition, methane concentration and emission rates were simulated through CFD.

CFD is a flexible modeling technique that can also evaluate methane movement in mines. During the production, methane will be released from the working face and enter the gob areas. CFD can help define the flow distribution in geometrically complex conditions. Also, CFD makes it possible to test the effects of modifications under the same ambient conditions. Hence, the control of methane emissions system can be optimized. In Kelsey's paper (Kelsey et al. 2003), CFD simulations of methane drainage were performed. The quantity of methane removed reflected the effect of drainage. In addition, methane drainage effect on flow through strata was visualized. Based on CFD and information from geotechnical modeling, numbers and spacing of methane drainage boreholes were examined and drainage was optimized.

CFD can be applied to simulate fire spread along combustibles in the underground, a serious safety issue in underground mines. Edwards and Hwang (Edwards and Hwang 2006) developed a CFD fire spread model to control fire spread and reduce CO and smoke emissions. Flame spread rate was examined for the ribs and roof of a coal mine entry, timer sets, and a conveyor belt. Char forming materials with thermal properties were also modeled in the CFD program. Fire Dynamics Simulator (FDS), which is based on CFD, was applied to simulate the fire spread in a mine entry. Navier-Stokes equations are solved numerically in the simulator. Basically, fame spread has a relationship with pyrolysis gases emission and flame front is defined by the leading edge of the fuel surface at the pyrolysis temperature. Afterwards, the flame propagation is determined by temporal movement of the pyrolysis temperature. In the paper (Edwards and Hwang 2006), the model was used to simulate the 1990 fire at Mathies Coal Mine. The coal lined tunnel flame spread rate was analyzed and it was turned out to be insensitive to the heat of pyrolysis, but significantly sensitive to the coal moisture content. Moreover, predictions made by CFD model of the dependence of flame spread along conveyor belt on air speed met the results obtained by Lazzara and Perzak (Lazzara and Perzak 1987).

Overall, CFD is a flexible, grid-based numerical technique. It has been successfully applied in various fields of mine ventilation improve underground mine safety. CFD makes it possible to conduct all kinds of simulations, even in the geometrically complex

conditions, like the gob areas. However, CFD is rarely combined with other software to produce quicker and highly accurate results, which is why this work examines a hybrid approach.

2.2 Network Modeling

Network modeling software used in this paper are VnetPC and Flownex. Since VnetPC was already reviewed in (Zhang et al. 2014), Flownex is mainly discussed in this part.

Flownex is a thermodynamic modeling software. It uses both steady state and transient simulation to compute temperature, flow rates, and other flow properties. It has been widely used in fields like fluid system design and optimization, but less widely applied to mine ventilation. An important reason for using Flownex in this study is that it is capable of integration with other software, like Ansys Fluent. VnetPC does not have this integration capability. Since Flownex is not as popular as VnetPC in the mining industry, several studies are reviewed to give a general idea about its useful features.

Flownex is able to perform both steady state simulation and transient simulation for complex geometries. Slabbert (Slabbert 2011) used Flownex to simulate a typical Pool Type Research Reactor. Both steady state and transient simulations were performed in Flownex to check the capability and accuracy of the Flownex model. Results from the Flownex model were compared with that from the Engineering Equation Solver (EES). Moreover, the results from the Flownex model matched that EES very well. Slabbert concluded that Flownex could get the results very fast and it was a good tool for both steady state and transient simulations. Flownex was used as one of the two software to model the performance of transient heat exchanger in another study (Olivier 2005). Two methods for analyzing network problems were studied. One was the Implicit Pressure Correction Method (IPCM). The network solver used in this method was Flownex. The other one was the Runge Kutta method with Trapezoidal Damping (RKTD), which was an explicit method. Xnet was applied as the network solver. Both the two solvers were used to simulate the transient heat exchange performance. Results from the Xnet were

highly accurate but Xnet required much computational time. In examining the results from these two solvers, Olivier found that the results from Flownex matched that from Xnet very well. She concluded that Flownex was an important tool to simulate the transient heat exchanger and solve complex networks.

Flownex is also powerful due to its coupling capability with external software, such as WKIND, TINTE, and CFD. Walter and others (Walter, Schulz, and Lohnert 2004) simulated a Pebble Bed Modular Reactor (PBMR) plant and its power conversion unit (PCU) with a coupled Flownex-WKIND model. WKIND is a solver for one group neutron diffusion equation and it is able to simulate one-dimensional neutronics behavior (Walter, Schulz, and Lohnert 2004). The integration capability of Flownex was enabled with a memory map file provided by the Windows application programing interface (API). Results such as, pressure drop, inlet temperature, and mass flow rate were computed in the Flownex and transferred to WKIND as the inputs. The coupled simulation stopped when both the Flownex and WKIND model reached their steady-state solutions. In addition, Marais (Marais 2007) developed a new method, which was a combination of TINTE (TIme dependant Neutronics and TEmperatures) and Flownex, to validate the point kinetic neutronic model of the PBMR. TINTE is a solver for a two-dimensional neutron diffusion equation and it is able to solve neutronic models (Gerwin, Scherer, and Teuchert 1989). The coupling feature of Flownex played an important role in the method. Results from the hybrid model showed that rough boundary conditions could be obtained thought the indirect coupling method.

According to aforementioned studies, Flownex is good at steady state and transient simulations. The integration capability of Flownex makes it possible to solve complex networks with an external software.

2.3 Hybrid Modeling

As abovementioned, Flownex has the capability to be combined with an external software. Since the hybrid approach in this study was completed based on both Flownex and CFD, the combination of Flownex and CFD is individually reviewed in this section.

Several hybrid Flownex-CFD models were successfully made with various purposes in the past.

A study on the hybrid Flownex-CFD model for simulating the flow distribution in the PBMR was investigated by Huang (Huang 2008). The hybrid model was created to save the computing time by take advantages of both Flownex and CFD. Flow paths in the reactor was simulated in the 3D CFD model. The core structure of the PBMR was simulated in the Flownex model. Flownex created a complex network structure by combining all the flow paths. Results from these two models had a good agreement on a global scale. Huang concluded that the hybrid model made it quick and accurate to get the results by taking advantages of both the Flownex and CFD models. Based on Huang's work, a similar study for PBMR was conducted by Janse Van Rensburg and Kleingeld (Janse Van Rensburg and Kleingeld 2010). Results from the Flownex model were passed to the CFD model as boundary conditions. With the help of the hybrid method, leakage flows were successfully identified and ranked in a High Temperature Reactor (HTR), which was a predictor for bypass flows and leakages in a rector. Reasons of the bypass flows and its effects on temperatures of the fuel and component were analyzed in the paper. Later on, Janse Van Rensburg and Kleingeld (Janse Van Rensburg & Kleingeld, 2011) did another study on the leakage and bypass flows in an HTR by using the same hybrid approach. They found that changes of the pressure drop in a pebble bed did not lead to same changes in the leakage flows. Janse Van Rensburg and Kleingeld have done many studies on the leakage and bypass flows in a HTR and the rest were not reviewed in this thesis due to the limited space.

Gouws (Gouws, 2007) conducted a similar Flownex-CFD study to find possible geometrical changes for the dome of a combustion chamber. The reason for making the changes was that there were crack formation on the dome. Flownex was used to simulate the combustion process while CFD was utilized to figure out the changes to the dome geometry. Pressure losses, temperature and flow distributions were obtained from the Flownex model. These data were applied as the boundary conditions in the CFD model to simulate the flow distribution inside the combustor. According to the hybrid approach, it

was concluded that high-temperature gradients on the dome could be reduced by adding an axial air swirler. The hybrid model made it possible to model the combustion chambers more accurately in less time.

Based on the studies shown above, it is clear that the hybrid Flownex-CFD approach has been successfully applied various fields. However, no study has been conducted with a hybrid Flownex-CFD model in mining industry yet. This research was created to make use of the advantages of the hybrid model.

3 The Feasibility of Hybrid Network and CFD Modeling for Mine Ventilation Applications

3.1 Abstract

This paper examines the feasibility of combining network modeling and computational fluid dynamics for modeling of underground mine ventilation systems. Both simulation methods have specific advantages and disadvantages for analysis of mine systems. Network modeling is widely utilized by many operations and allows for assessment of current systems and simulation for planning purposes. Alternatively, CFD has been utilized only marginally by operations and is typically a research tool, requiring considerable computational power, complex models, and careful analysis and calibration of results. Network modeling allows for a holistic approach to the ventilation system, giving quantity, velocity and pressure in every branch, but CFD modeling can resolve the flow regime in 2D or 3D, which is idea when examination of an area on a more detailed basis is useful, such as dust and gas control. Integration of the two can allow for more flexible systems analysis. The feasibility of integration, along with application to limited underground mine data are examined.

3.2 Introduction

Mine ventilation plays a significant role in underground mining by not allowing contaminated air to enter the working face. Generally, mining companies use network modeling to simulate the ventilation system for analysis and planning purposes. However, network modeling is not detailed enough to simulate complex airflow, nor does it resolve flow patterns in a given cross section. Computational Fluid Dynamics (CFD)

11

can be applied in this case to assist the network model. In this study, VnetPC was used as the network modeling tool and compared to a two-dimensional CFD model of an underground coal mine in the western US. The goal of this study was to analyze the feasibility of hybrid network and CFD modeling for mine ventilation applications.

3.3 Background

3.3.1 CFD Applications in Mining

Computational fluid dynamics (CFD), a grid-based numerical technique, is widely used in mine ventilation. Due to the high level of accuracy and flexibility, CFD is applied in spontaneous combustion control, dust control, gob inertisation, methane movement simulation, fire spread simulation, and ventilation airflow simulation. CFD was used to improve the control of spontaneous combustion in longwalls (Ren and Balusu, 2005). Innovative gob gas control strategies for spontaneous combustion have been developed by Ren and Balusu using CFD. In addition, Ren and Balusu used CFD modeling to study the gas flow mechanics and distribution in longwall gobs. These models were used to develop control strategies for gas and spontaneous heating, such as ensuring gas quality in gob degasification systems, reducing air velocity and increasing gob drainage flow rate, and immediate sealing of active gob.

CFD is a flexible modeling technique that can also evaluate methane movement in mines. During production, methane is released from the working face and enters gob areas. CFD can help characterize the flow distribution in geometrically complex conditions, and also makes it possible to test the effects of modifications under varying conditions, allowing for optimization of methane control systems. For example in Kelsey's work, CFD simulations of methane drainage were performed, the quantity of methane removed reflected the effects of drainage, and methane drainage effects on flow through strata were visualized (Kelsey et al., 2003). Based on CFD and information from geotechnical modeling, numbers and spacing of methane drainage boreholes were examined and drainage was optimized.

CFD is especially useful for the simulation of underground ventilation airflow. Aminossadati and Hooman built a two-dimensional CFD model to simulate the airflow behavior in underground crosscut regions (Aminossadati and Hooman, 2008). Airflow was directed into these regions by using brattice sails and a CFD model examined the effects of brattice length on airflow behavior. This CFD model made it possible to determine the optimum size of brattice sails. CFD is a useful numeric modeling tool that has been successfully applied in various fields of mine ventilation to ensure miner safety.

3.3.2 Network Modeling Applications in Mine Ventilation

VnetPC is a popular network ventilation simulation program designed to help the mine ventilation workers monitor and design underground ventilation layouts. Based on the data obtained from ventilation surveys and airway dimensions, the program is able to provide various ventilation parameters such as air quantity, air velocity, airway resistance, and pressure drops using computations based on Kirchhoff's Laws and (Mine Ventilation Services, 2013) the Hardy Cross iterative technique.

There are advantages and disadvantages to using network modeling. On one hand, it is relatively simple to build a network model, which is why it is so popular with most mining companies. Wallace and others (Wallace et al., 1990) and Banik (Banik et al., 1995) determined that network modeling was capable to simulate the longwall gob leakage. Besides, Mcpherson (McPherson, 1988) used network modeling to analyze ventilation networks in a block caving mine in Chile. Moreover, network modeling was successfully applied to evaluate the ventilation efficiency and cost by using auxiliary fans in coal mines (Wallace et al., 1990).

On the other hand, network modeling results do not characterize or visualize ventilation properties on a small scale; for example, such as velocity, pressure drop, and volume flow rate distribution in the cross-sectional area of a mine entry. This can be limiting in certain applications, including release and monitoring points for tracer gases, where

13

smaller scale behavior can affect flow and mixing. In addition, because of one-dimensional and branched nature, it is difficult for network modeling to run simulation in the inaccessible regions, like gobs (Karacan et al., 2008).

3.4 Detailed Field Study

This preliminary examination of hybrid CFD and network modeling simulation is part of a larger field study, examining characterization of a longwall ventilation system. A CFD model was developed for comparison to the network model. The purpose is to build an efficient, accurate model for detailed ventilation studies. The real world data was collected in an underground coal mine by using a multiple tracer gas technique. Sulphur hexafluoride (SF_6) and perfluoromethylcyclohexane (PMCH) were chosen as the tracer gases in this study. SF_6 and PMCH were released at release points (RP) 1 and 2 separately in the underground coal mine as shown in Figure 1. Locations of five sample points are also shown in the figure. With the help of tracer gas technique and a ventilation survey, air velocity and volume flow rate for the site are known.

3.5 Two-Dimensional CFD Model Setup

3.5.1 Geometry

The mine geometry was imported directly from the mine map into a meshing program. The original geometry for the mine was smoothed. Since characterization of the gob area is complex, the widths of four air paths around the gob were decreased to half of the original width to match the real world situation. The simplified geometry and dimensions for the geometry was shown in Figure 1. Sample points locations were also shown in Figure 1.
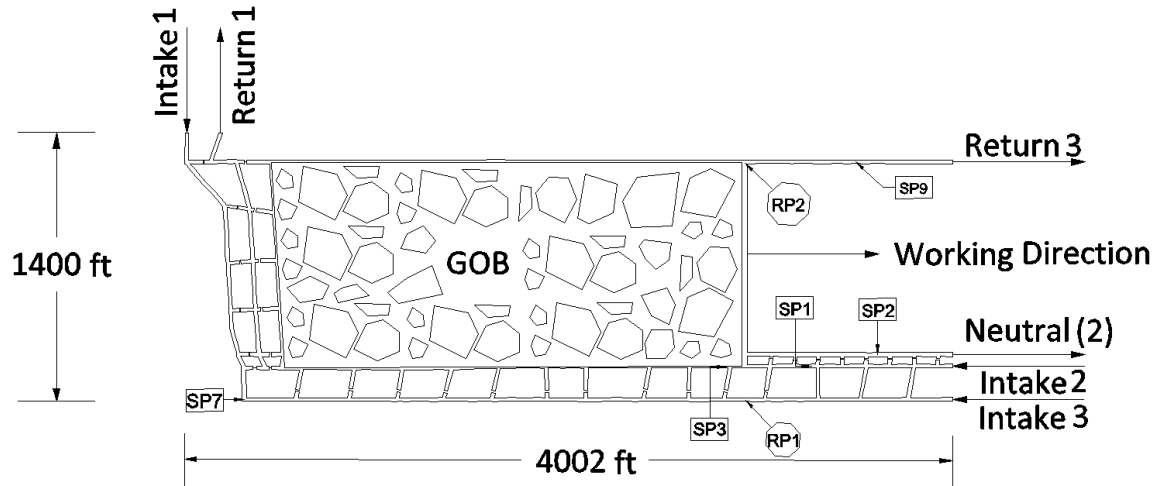
Figure 1. Plan view of the model mine. (Note: this figure has been changed for the consistency of labeling throughout the thesis.)

3.5.2 Hypothesis

Although CFD can simulate the real situation, some assumptions should be made to simplify the CFD model for grid generation and make CFD simulation feasible in terms of memory and CPU time. Several simplifications were made. There is no leakage between air passages in the model mine. Leakage can significantly influence ventilation in an underground coal mine and this model will be updated in the future. In addition, Air flow is incompressible and fully turbulent. The gravity influence on mine air is neglected. Besides, the gob area is treated as solid wall in the model. Moreover, there is no heat transfer during the procedure and the wall and air temperatures are constant.

3.5.3 Governing Equations

In general, the continuity equation, momentum equation, and energy equation are the three governing equations used in CFD. Since the fluid in the model was assumed to be incompressible and there is no heat transfer, the energy equation was not applied in this model. Reynolds Averaged Navier-Stokes (RANS) equations (Ansys, 2009), containing continuity equations and momentum equations, were used in the CFD model. The standard k-epsilon turbulence model was used to compute eddy viscosity and Reynolds stress term.

Continuity equation:

$$\nabla \cdot \vec{V} = 0 \qquad\qquad\qquad (3\text{-}1)$$

where $\vec{V}$ is the mean velocity vector.

Momentum equation:

$$\nabla(\vec{V} \otimes \vec{V}) = -\frac{\nabla P}{\rho} + \nabla \cdot (\mu_{\text{eff}}(\nabla\vec{V} + (\nabla\vec{V})^{\text{T}})) \qquad\qquad (3\text{-}2)$$

where $\mu_{eff} = \mu + \mu_t$, μ is the molecular viscosity of air, μ_t is the eddy viscosity and it is computed from k-ε model, ∇P is the pressure gradient.

3.5.4 Meshing

A two-dimensional geometry and a quadrilateral, structured mesh were created. Node density was designed to be high close to the walls and low in the middle as shown in Figure 3. The reason was that airflow velocity close to the wall changes considerably and it is necessary to have a good resolution in this region. Since the model was complex, the whole geometry was divided into two parts before meshing and combined using an interface boundary condition. The mesh for the entire model mine and for a small part of the mine was presented in Figure 2 and Figure 3, respectively.
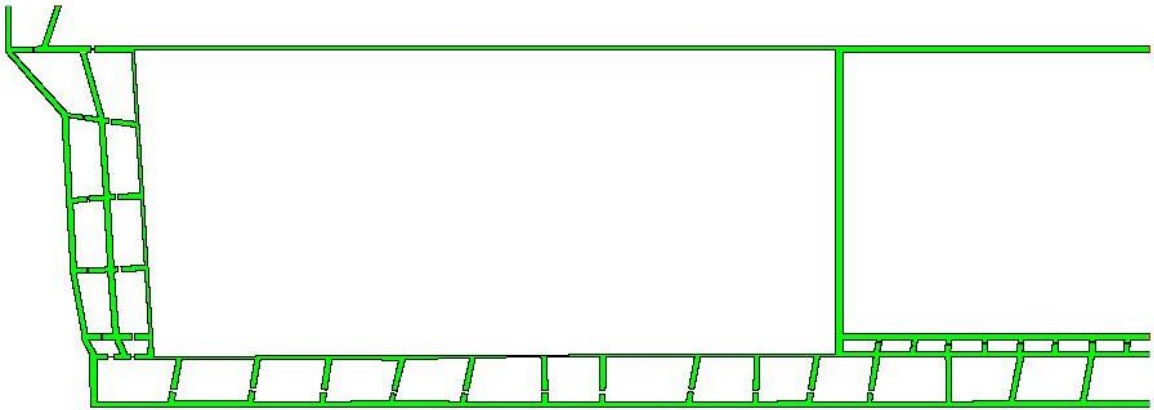
Figure 2. Meshing picture for the model mine (plan view).
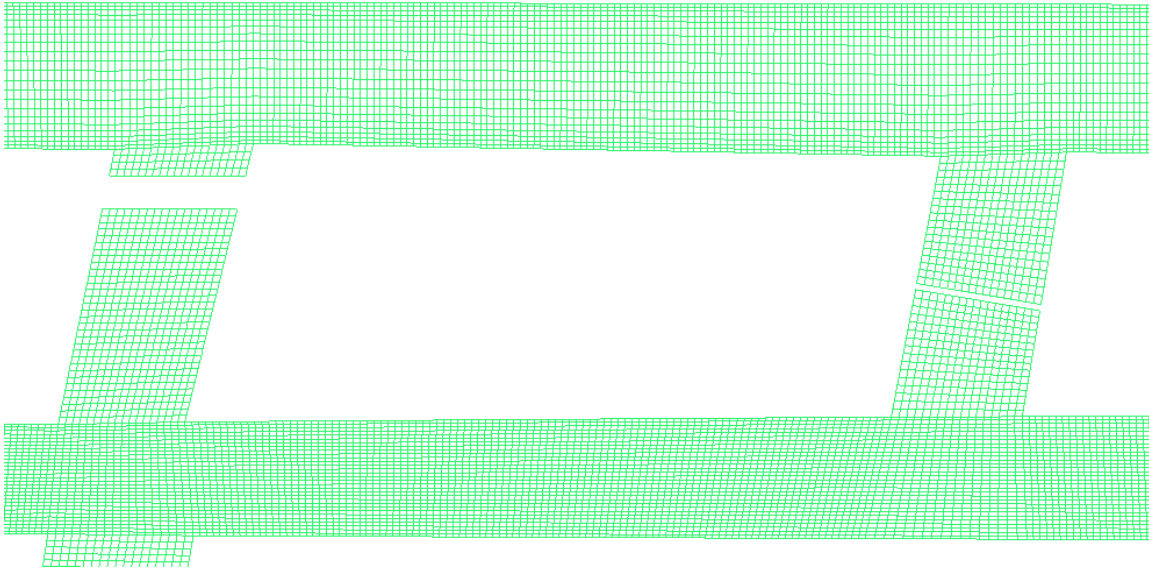
Figure 3. Mesh distribution in a small part of the model (plan view).

There were three intakes and three returns in this mine model as shown in Figure 1. All the intake air were defined as inlets in the CFD model. All the outlets represented the return air. The neutral air was treated as return 2 in the figure. Three inlets were specified as velocity inlets. Three outlets were defined as outflow. The field measured airflow quantities were applied to the outflow boundary condition. At the same time, the measured airflow velocities were applied to the velocity-inlet boundary condition. Details are found in Table 1. The remainder of the geometry was treated as no-slip, stationary walls. In this study, the gob area was also treated as wall boundary condition because of the fact that only very small amount of air would be able to flow through the whole gob area, and because this is a preliminary study. The gob area will be treated as porous media in the next study.

Table 1. Intakes, returns, and neutral boundary conditions (Note: this table has been changed for the consistency of labeling throughout the thesis.).

Airway	Velocity (ft/s)		Airway	Airflow Quantity Percentage
Intake 1	6.480		Return 1	0.192
Intake 2	2.300		Neutral 2	0.196
Intake 3	0.719		Return 3	0.630

3.5.5 Solution Setup

In this study, the numerical solutions were processed using the Ansys Fluent 14.5. The type of the solver is defined as pressure-based. Time was steady and 2D space type was

planar. Gravity was neglected in this study since it was not expect to significantly affect the airflow in the underground mine. A standard k-epsilon turbulence model was used to simulate the airflow. Fluid in the model was defined as air.

3.6 Mesh Independence Study

The mesh independence study was conducted to ensure that mesh size is not influencing results. The optimum mesh size was defined after this study. Three kinds of mesh; fine mesh, medium mesh, and coarse mesh, were analyzed. Node numbers of the three mesh size models were about 800,000, 650,000, and 500,000, respectively. The coarse mesh was generated first. Then the medium mesh fine mesh were created by increasing the nodes density on both entry direction and cross-section direction. There were two criteria to qualify the mesh. One criteria was that a determinant value should be at least 0.3 to be acceptable for a solver. The other criteria was that the minimum angle value must be greater than 18° to be acceptable for Fluent (Ansys, 2007). The mesh quality in this study matched the two criteria.

The finer the mesh, the closer the numerical solution to the exact solution (Sørensen & Nielsen, 2003). Airflow rate results of the sample points were collected from the three mesh models as shown in Figure 4. It is apparent that the solution is not changing significantly, which indicates that the solution is mesh independent. This also means that the medium mesh is sufficient for a good solution. Then only the results from medium mesh will be compared with the experimental measurements in the next section.
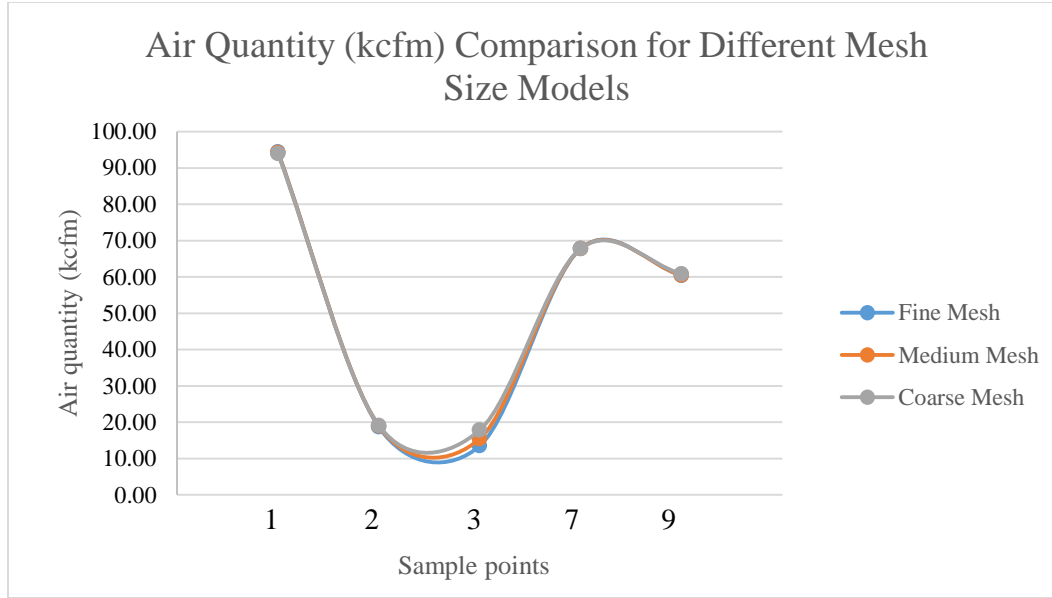
Figure 4. Air quantity profile of the three mesh size models.

3.7 Results

3.7.1 CFD Results

Air velocity and air quantity were the two main results obtained from CFD simulation. Because of the complexity of underground geometry, air velocity measured in the underground did not always match the average velocity simulated. Otherwise, air quantity, which was not affected by complex situation in the underground, was used as the indicator to make comparison between simulated results and real results. Velocity contours were generated to provide a visualization of the three mesh results. Details could be found in Figure 5. Because of the limited space, only the velocity contour of fine mesh model was shown in Figure 5.

In this study, air quantity results obtained from experimental measurements were treated as known values, although error in their measurements could have occurred, they were measured by experienced ventilation personnel. The sample point locations can be found in Figure 1. Air quantity results obtained from the medium mesh model were compared to the experimental measurements. Details are shown in
Table 2. Error from CFD simulation was calculated based on Equation (3-3):

19

$$\text{Error} = \frac{|\text{result from CFD model} - \text{result from measurement}|}{\text{result from measurement}} * 100\% \qquad (3\text{-}3)$$

Table 2. Results from CFD simulation and experimental measurements.

Sample Points	Air quantity (kcfm)		Error (%)
	Medium Mesh Model	Experimental Measurements	
SP1	94.21	81.00	16.31
SP2	19.08	19.60	2.65
SP3	15.46	17.00	9.07
SP7	67.80	67.80	0.00
SP9	60.56	63.00	3.87
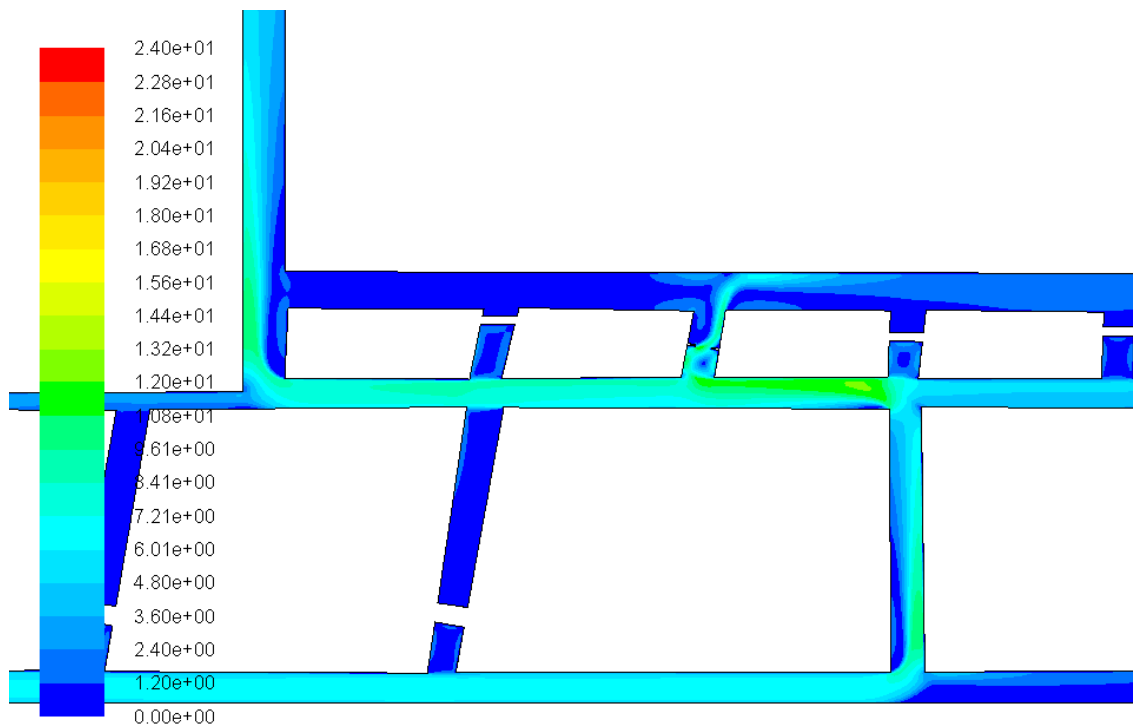
Figure 5. Plan view of velocity (ft/s) contours near the mandoor in the fine mesh model.

3.7.2 Network Modeling Results

Visualization of air quantity distribution in the network model was shown in Figure 6. Blue, red, and green lines represent the intake air, return air, and neutral air, respectively. Magenta refers to active working face. Black lines around the gob are airflow through the entries next to the gob. The small short lines are the air leakage of stoppings. Numbers in

Figure 6 indicate the airflow quantity of the branch. Air quantity results were summarized in Table 3.
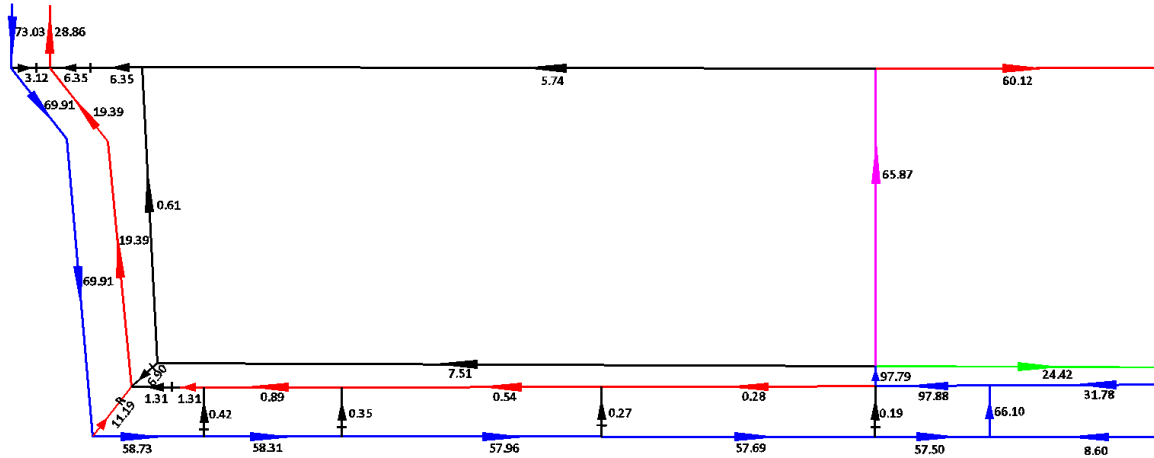
Figure 6. Air quantity (kcfm) results from the network model (plan view).

Table 3. Air quantity results from the network model.

Sample Points	Air Quantity (kcfm)		Network Model Error (%)
	Network Model	Experimental Measurements	
SP1	97.88	81.00	20.84
SP2	24.42	19.60	24.59
SP3	0.28	17.00	98.35
SP7	73.03	67.80	7.71
SP9	60.12	63.00	4.57

3.8 Conclusions and Discussion

The error from medium mesh CFD model is compared with the error from network model in Figure 7.

21
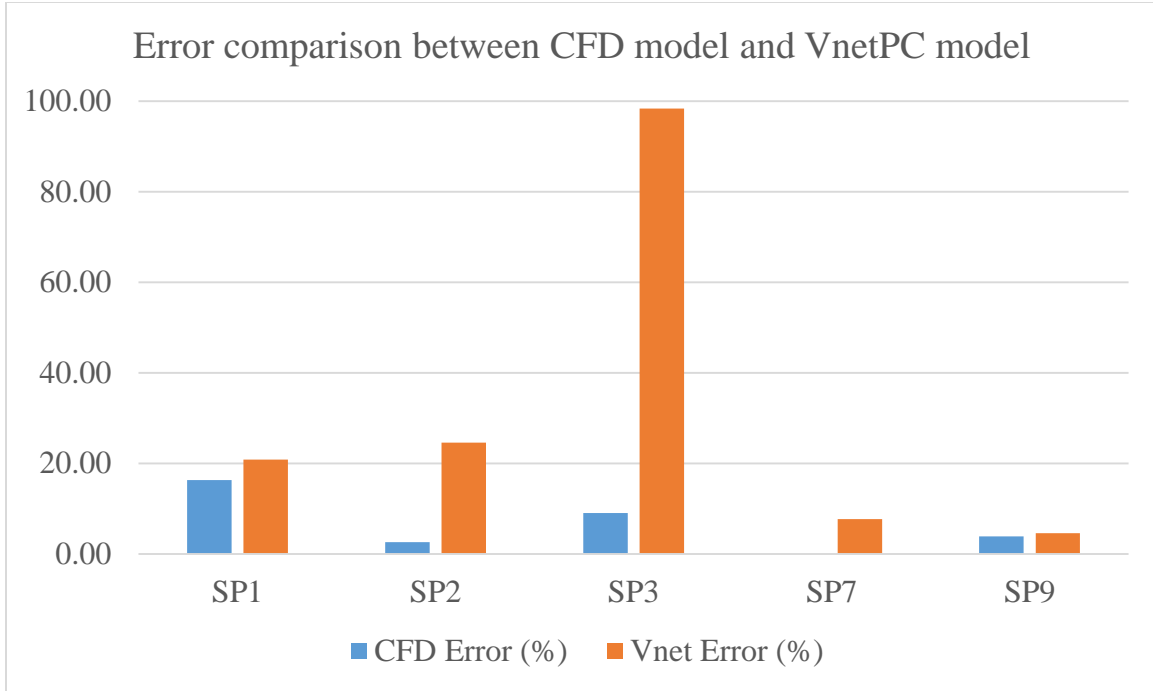
Figure 7. Error comparison between CFD model and network model.

From Figure 7, there is no doubt that the CFD model is more accurate than the network model. However, CFD model is not perfect since it still has a 16% error at sample point 1. There are several possible reasons for the error at sample point 1 in CFD model. First, the CFD model is a two-dimensional model, which is not accurate enough to represent a volume flow rate. Second, there may be error associated with the experimental measurement taken at sample point 1. Last, the gob area was treated as solid wall instead of porous media in the model. If the gob area is defined as porous media, some air will flow into the gob decreasing the air quantity at sample point 1.

From Figure 5 and Figure 6, the two-dimensional CFD model is more detailed than the network model. The airflow distribution in the cross-sectional area can be seen clearly in the CFD model. However, network modeling only uses simple lines and numbers indicating the airflow. Considerable differences for the airflow quantity can be found in the two figures. There are two kinds of places in Figure 5 where CFD is especially useful to analyze the airflow. First, CFD is necessary to resolve where the intake air comes up through the crosscut. Because when the airflow changes direction, a small part of the intake air circulates next to the wall. The airflow then becomes disordered and velocity is

no longer uniformly distributed in the cross-sectional area. Secondly, CFD is potentially needed where there is an obstacle in the airway. The open door in Figure 5 is a good example. The intake air circulates before entering the open door and is divided into several air groups with various velocity magnitudes after passing through the open door. It is obvious that a tracer released in these two kinds of places may not behave uniformly. However, with the help of CFD, the right release location of a tracer can be determined and the data collected will be more representative and accurate. Network modeling is more appropriate at a global scale, like the airways around the gob and the intake air at the bottom in Figure 6. It is also not effective to use network modeling to visualize or understand airflow at a small scale, such as, passing through an obstacle, like the open door in Figure 5.

Based on Table 3, network modeling does not represent low velocity flow well. The maximum error, 98.35%, appears at sample points 5 where the real airflow quantity is only 17 kcfm. As the airflow quantity increases, the error becomes much smaller.

In conclusion, the CFD model is accurate but requires more expertise, time to develop a model, and computational power. Network modeling, such as VnetPC, is not as complex as CFD model and it practical for assessment of ventilation systems in large mines at a global scale. It is also more appropriate to model the large value branches.

Therefore, it is time-saving to simulate the whole mine by using network modeling. After comparing results from VnetPC with experimental measurements, CFD model should be built in certain areas where there is a considerable error in a network model, and where resolution of complex flow regimes are important. A hybrid model has great potential to allow for practical modeling of large mines while still looking at detailed flow regimes as necessary. To make this hybrid network and CFD method more accurate, the gob area will be defined as porous media in the next study.

References

Aminossadati, S. M., & Hooman, K. (2008). Numerical simulation of ventilation air flow in underground mine workings. In *12th U.S./North American Mine Ventilation Symposium* (pp. 253–260). Reno, Nevada, USA.

Ansys. (2007). *ANSYS ICEM CFD 11.0*.

Ansys. (2009). *Ansys Fluent 12.0 User's Guide*.

Banik, J., Mcpherson, M. J., & Topuz, E. (1995). Ventilation control of self-heating in retreating longwall coal mines. In *7th U.S. mine ventilation symposium*. Lexington, KY, USA.

Karacan, C. Ö., Ren, T., & Balusu, R. (2008). Advances in grid-based numerical modeling techniques for improving gas management in coal mines. In *12th U.S./North American Mine Ventilation Symposium* (pp. 313–320). Pittsburgh, Pennsylvania, USA.

Kelsey, A., Lea, C. J., HSL, Lownndes, I. S., Whittles, D., & Ren, T. (2003). CFD modelling of methane movement in mines ian s lowndes david whittles (pp. 475–486). Johannesburg, South Africa.

Mcpherson, M. J. (1988). Ventilation Planning Study of the El Teniente Block Caving Mine in Chile. In *Fourth International Mine Ventilation Congress*. Brisbane, Australia.

Mine Ventilation Services. (2013). *VnetPC Pro User's Mannual*. Clovis, California.

Ren, T.., & Balusu, R. (2005). CFD Modelling of Goaf Gas Migration to Improve the Control of Spontaneous Combustion in Longwalls (pp. 26–28). Brisbane, QLD.

Sørensen, D. N., & Nielsen, P. V. (2003). Quality control of computational fluid dynamics in indoor environments. *Indoor Air*, *13*, 2–17. doi:10.1111/j.1600-0668.2003.00170.x

Wallace, K. G., McPherson, M. J., Brunner, D. J., & Kissell, F. N. (1990). *Impact of Using Auxiliary Fans on Coal Mine Ventilation Efficiency and Cost*.

4 A Comparison of Simulation Methods for Mine Ventilation Systems

4.1 Abstract

This paper introduces an approach for simulation of airflow and tracer gas distribution in an underground longwall mine located in the western U.S. The approach takes advantage of both computational fluid dynamics (CFD) and network modeling for a mine ventilation system. Network modeling is popular with mining companies because it is relatively simple and easily updated. Network modeling is usually one-dimensional (1D) while CFD can solve both two-dimensional (2D) and three-dimensional (3D) domains. A hybrid model of CFD and network modeling was developed in this paper to demonstrate the approach. Furthermore, a network model, a 2D CFD model, and a 3D CFD model were conducted separately. The gob area was simulated as porous media in both the 2D and 3D CFD models. Because there were no accurate porosity and permeability data provided for the gob, a sensitivity study on the porosity and permeability data was created in the 3D CFD model to eliminate the effects from these data. Other than the modeling work, a field study was conducted in the mine and the results from the field study were considered as right results when compared with the results from the three models. Tracer gas technique was used in the field study. One reason for releasing the tracer gas into the underground was that airflow information in complex ventilation situations could be quickly and remotely obtained, especially for an emergency, like an explosion. Besides, with the help of tracer gas technique, the CFD models could be created to simulate the areas where the airflow was complex instead of simulating the whole mine. Simulations of tracer gas were also conducted in the network model, the 3D CFD model, and the hybrid model. In the 3D CFD model, two kinds of simulations, which are steady-state simulation and transient simulation, were completed. All the

results from these models were analyzed and compared with the results from the experiment.

4.2 Introduction

The primary purpose of mine ventilation in an underground mine is to provide enough oxygen to the personnel working in the underground mine, and to dilute methane and dust concentrations. Network modeling is a popular and important method used in the mining industry to predict and analyze airflow distribution in the underground system. However, it is not a good tool for the simulation of a gob area. Furthermore, airflow distribution in a cross sectional area cannot be visualized with a network model. Computational fluid dynamics (CFD) is a good fit in these areas as demonstrated in the preliminary study (Zhang et al. 2014). The main disadvantage of CFD is that it is time-consuming and requires high computational power. Additionally, CFD is a difficult technology to acquire and individuals utilizing this time of modeling should have a background in fluid dynamics and computational methods. A hybrid model was used to demonstrate advantages of both CFD and network modeling in this paper. A preliminary 2D CFD model of this study was created (Zhang et al. 2014). However, the gob area was not simulated in the 2D CFD model. In this paper, a three-dimensional (3D) CFD model was created for an underground coal mine in the western U.S. The gob was simulated as porous media in the 3D CFD model. A network model was also created for the same underground mine and Flownex was used as the network modeling software. Moreover, a hybrid model with a 3D CFD component and a Flownex was also created. Results from all the three models were compared with the experimental data.

4.3 Detailed Field Study

The field experiment of this study was done in the underground longwall mine in the western U.S. Four students from Virginia Tech and four workers from the mining company did the experiment together. The experiment followed a release-collect process. Two trace gases were released at two release points (RP1 and RP2) and collected at five sample points (SP1, SP2, SP3, SP7, and SP9). SP1 was located at the entry inby the last open crosscut, where all the airflow from three inlets join together. SP2 was located at the

entry outby in the beltline. SP3 was located next to the gob. SP7 was located at the entry outside the airlock in the bleeders. SP9 was located at the tailgate entry. Locations for the release and sample points are shown in Figure 8.

The tracer gases were sulphur hexafluoride (SF_6) and perfluoromethylcyclohexane (PMCH). SF_6 and PMCH were released at RP1 and RP2, respectively. Since PMCH was released in the gob, only SF_6 was analyzed in this study. SF_6 was released at a constant mass flow rate of 200 standard cubic centimeters per minute (SCCM). Airflow quantity, SF_6 flow quantity, and SF_6 concentration were then obtained by using trace gas technique and conducting a ventilation survey. The results from the field experiment were treated as the exact results and they were compared with the modeling results in this study.

4.4 CFD Model

4.4.1 Geometry of the Model Mine

An overview of the model mine geometry with three monitor planes and three monitor lines is shown in Figure 8. It is obvious that the mine geometry was simplified in this paper compared to the mine geometry in the preliminary study (Zhang et al., 2014). Pathways with stoppings installed were deleted in this geometry, neglecting leakage. Comparison between these two geometries can be found in Figure 65 and Figure 66 in the Appendix. Since it is assumed that there is no leakage between air passages (in Section 4.4.3), this simplification does not have an effect on the final results. In the meantime, the simplified geometry saves the time on the grid generation for both the 2D and 3D CFD models. An enlarged view for the locations of the monitor planes and lines is shown in Figure 9.
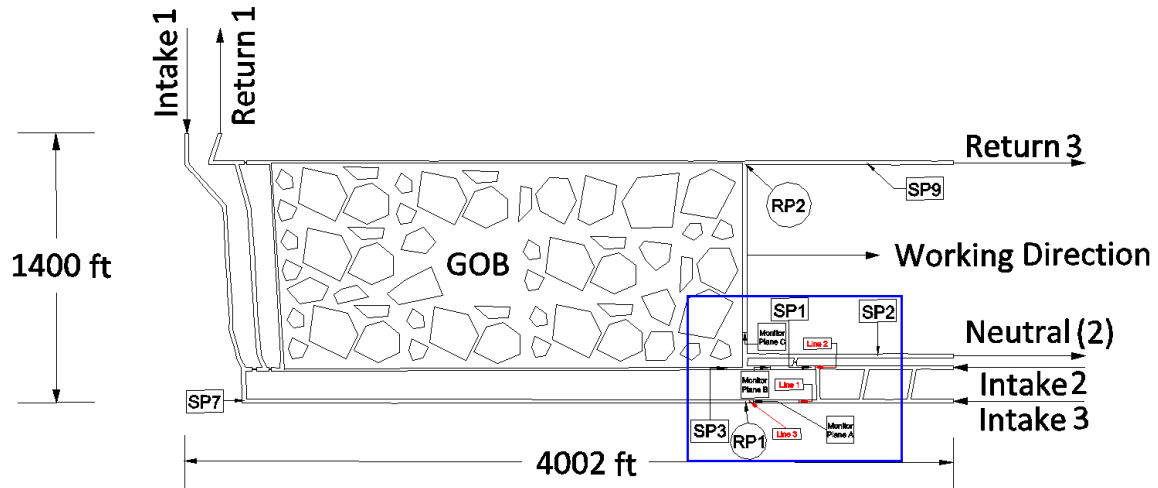
Figure 8. Plan view of the model mine geometry with monitor planes.
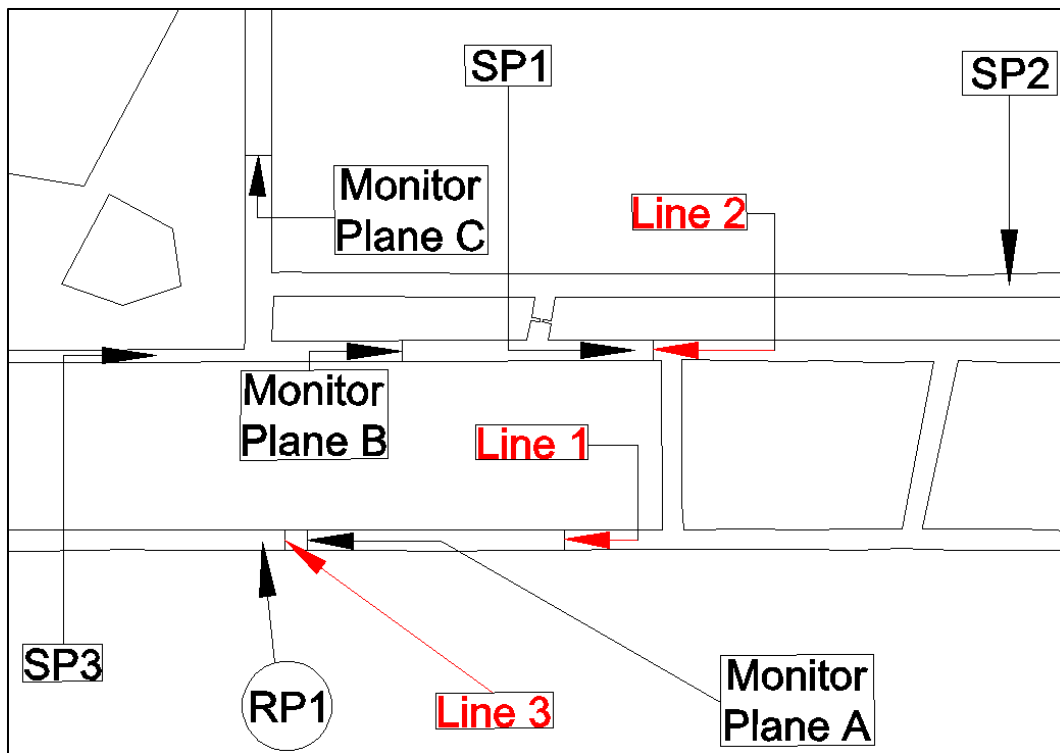
Figure 9. Locations of the monitor planes in the model mine (plan view).

4.4.2 Boundary Conditions

Boundary conditions for both the 2D CFD model and 3D CFD model were almost the same except that the 3D CFD model had a different thickness for the mine gob. Airflow in the mine gob was simulated as laminar flow (Yuan, Smith, and Brune 2006). Gob area in the CFD model was modeled as porous media. All the outside surfaces in the 2D and

3D CFD model were simulated as a stationary wall. RP1 was simulated as a small cube (shown in Figure 118) in the model. All the surfaces of the cube were assigned interface boundary conditions, which meant the upstream airflow could flow through the cube and carry on the SF_6 released from the cube. Volume inside the cube was treated as a flow domain and a source term was added to match the 200 SCCM release rate of the SF_6. All the intakes in both the models were assigned velocity-inlet boundary conditions. Two returns and a neutral in both the models were assigned outflow boundary conditions. The velocity and the airflow quantity percentage values were obtained from the field study in the underground mine. Details about the boundary conditions were shown in Table 4.

Meshes for both the 2D and 3D CFD models were divided into several parts before being solved in Ansys Fluent 14.5. Interface boundary conditions were used to combining these meshes together when they were ready to be solved. Eight meshing parts for the 3D CFD model were shown from Figure 111 to Figure 118 in Appendix.

Table 4. Intakes, returns, and neutral boundary conditions for both the 2D and 3D CFD model.

Airway	Velocity (ft/s)	Airway	Airflow Quantity Percentage
Intake 1	5.2340	Return 1	0.0586
Intake 2	2.2998	Neutral 2	0.2234
Intake 3	0.7840	Return 3	0.7180

4.4.3 Assumptions

Several assumptions are made to save the time on establishing the model without affecting the results significantly. There is no leakage between air passages. Heat transfer is not taken into account and temperature of wall and air are considered to be constant. The gravity of the air in the underground mine is neglected. Airflow in the underground is incompressible and fully turbulent. The injection of the tracer gas does not affect the airflow.

4.4.4 Governing Equations

Governing equations used in both the 2D and 3D CFD models are the continuity equation (4-1) and momentum equation (4-2). The energy equation was not used because the airflow is incompressible and there is no heat transfer in the model mine. User-Defined Scalar (UDS) transport equation (4-3) was used because SF_6 was simulated as a user defined scalar in the 3D CFD model. A user defined function (UDF) was interpreted to calculate the diffusivity in Equation (4-3). All the properties of SF_6 were obtained by solving the UDS transport equation. The standard k-epsilon model was utilized to simulate the turbulent flow. SIMPLE scheme was chosen as the solution method. All the equations shown below were obtained directly from the theory guide of Ansys Fluent (Ansys 2009a).

Continuity equation:

$$\nabla \cdot \vec{V} = 0 \tag{4-1}$$

Momentum equation:

$$\nabla(\vec{V} \otimes \vec{V}) = -\frac{\nabla P}{\rho} + \nabla \cdot (\mu_{\text{eff}}(\nabla\vec{V} + (\nabla\vec{V})^T)) \tag{4-2}$$

where $\vec{V}$ is the mean velocity vector, $\mu_{\text{eff}}= \mu + \mu_t$, μ is the molecular viscosity of air, μ_t is the eddy viscosity and it is computed from k-ε model, ∇P is the pressure gradient.

User-Defined Scalar (UDS) Transport equation:

$$\frac{\partial \rho \phi_k}{\partial t} + \frac{\partial}{\partial x_i}(\rho u_i \phi_k - \Gamma_k \frac{\partial \phi_k}{\partial x_i}) = S_{\phi_k}, \quad k=1,...,N \tag{4-3}$$

where Γ_k and S_{ϕ_k} are the diffusion coefficient and source term, ϕ_k is an arbitrary scalar, ρ is air density, u is velocity, $\frac{\partial}{\partial t}$ and $\frac{\partial}{\partial x_i}$ represent temporal and spatial derivative separately, $\frac{\partial}{\partial x_i}(\rho u_i \phi_k)$ represents the convection term in the equation, and $\frac{\partial}{\partial x_i}(\Gamma_k \frac{\partial \phi_k}{\partial x_i})$ represents the diffusion term in the equation.

A User defined function (UDF) was utilized for calculating the diffusivity of SF_6 () in air (Ansys 2009b):

$$\Gamma_{\text{eff}}\rho = \rho\Gamma_{\phi t} + \frac{\mu_t}{S_{Ct}} \tag{4-4}$$

where μ_t is turbulent viscosity, S_{Ct} is the turbulent Schmidt number, Γ_{eff} is the effective diffusion coefficient of SF_6 in air, $\Gamma_{\varphi t}$ is the diffusion coefficient of SF_6 in air in this study, $\Gamma_{\phi t}\rho$ represents the effective diffusivity, $\rho\Gamma_{\phi t}$ represents the molecular diffusivity, and $\frac{\mu_t}{S_{Ct}}$ represents the turbulent diffusivity. The Schmidt number is set to 0.7 (Ansys 2006) because all the fluids modeled in the CFD models are gases. (Ansys Fluent 12.0 Theory Guide, 2009). The diffusion coefficient is set to 5.9×10^{-6} m^2/s in this study. Ward (Ward & William, 1997) reported the range for the diffusion coefficient of SF_6 in air was from 5.9×10^{-6} m^2/s to 7.3×10^{-6} m^2/s. Besides, in Equation (4-4), the diffusion coefficient is three orders of magnitude smaller than turbulent viscosity (Xu 2013). It means the diffusion coefficient does not affect the results very much and 5.9×10^{-6} m^2/s is appropriate for this study.

4.4.5 2D CFD Model

4.4.5.1 2D CFD Model Setup

In the preliminary study (Zhang et al. 2014), the gob area was not taken into account. It was added to the 2D CFD model in this paper. Due to the complicated geometry of the model mine, the geometry was divided into seven parts in the 2D CFD model while the 3D CFD model was divided into eight parts. The reason for the difference on the number of parts was that 2D CFD model did not have a thickness and the gob had the same height as the coal seam. Since the geometry was divided into various parts in the 2D and 3D CFD models, meshes for the CFD models were created based on the parts. However, the parts of meshes for either the 2D CFD model or the 3D CFD model were combined to one mesh before being solved in the Ansys Fluent. Additionally, the original geometry was simplified by deleting the airways with no flow. The leakages of stoppings were not modeled in the 2D CFD model. In addition, tracer gas was not introduced in the 2D CFD model but it was simulated in the 3D CFD model. In order to know how the flow behaves in the gob area, two cases were generated based on the porosity and permeability values of the gob. In the first case, the gob area was treated as one zone. In the second case, the

gob area was divided into five zones (Yuan, Smith, and Brune 2006). The purpose of creating the 2D CFD model was to eliminate the concerns on the one-zone case and five-zone case. If the results from these two cases were almost the same, five-zone case would not be built up in the 3D CFD model for this study.

Icem 14.5 was used to build up both cases' meshes and Ansys Fluent 14.5 was applied to obtain the solution. Since the porosity and permeability values of the mine were unknown, assumptions of these values have been made based on a longwall study done by other people (Yuan, Smith, and Brune 2006). The porosity and permeability values for the five-zone case can be found in Table 5. Based on another longwall study (Lolon 2008), the porosity and permeability values were set to 12800 md (millidarcy) and 0.24 separately for the one-zone case.

Table 5. Assumptions for porosity and permeability values (five-zone case).

Permeability (md)	Porosity
1000000	0.25
200000	0.24
70000	0.23
10000	0.22
5000	0.21

4.4.5.2 One-zone Case

The gob area in the one-zone case was treated as one part with the same porosity and permeability values across the gob. Theoretically, the one-zone case was not true because falling rocks had a size distribution across this area and porosity and permeability values should also had a range in this area. The purpose for creating this case was to determine if a zonal, more realistic model has a considerable effect on the results. An overview of the one-zone case in the 2D CFD model is shown in Figure 10. CFD results from this case were compared with the experimental results in Table 6.

Figure 10. Plan view of one-zone case.

Table 6. Results from one-zone case.

Sample points	Air quantity (kcfm)	One-zone Case CFD Results (kcfm)	Error (%)
1	81.00	90.33	11.51
2	19.60	18.76	4.28
3	17.00	15.72	7.51
7	53.74	53.74	0.01
9	63.00	59.09	6.20

Form Table 6, it is clear that all the errors from the 2D CFD model are under 12% for all the sample points. Sample point 1 has the largest error, which is 11.51%. This is not surprising because the airflow at sample point 1 becomes very complicated after the three intake airflows come together.

4.4.5.3 Five-zone Case

In this case, the gob was divided into five parts with different porosity and permeability values. The reason for dividing the gob was because the compaction of caved rock was not constant in the gob. It was compacted more close to the center of the gob than the boundary of the gob since the loading of the overburden decreased from the center to the boundary of the gob as the working face moved forward. Therefore, the porosity and permeability values were not distributed evenly in the gob. An overview for this case was shown in Figure 11. Results from the five-zone case were compared with the experimental results in Table 7.
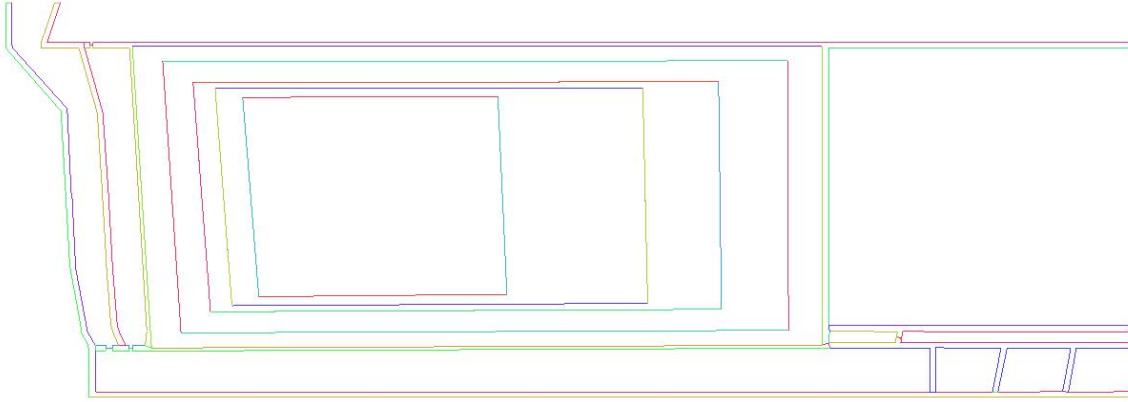
Figure 11. Plan view of five-zone case.

Table 7. Results from five-zone case.

Sample points	Air quantity (kcfm)	Five-zone Case CFD Results (kcfm)	Error (%)
1	81.00	89.82	10.89
2	19.60	18.75	4.32
3	17.00	18.27	7.49
7	53.74	53.74	0.01
9	63.00	59.10	6.20

According to Table 7, the largest error from the five-zone case is about 11% compared with the experimental results. Since the airflow at sample point 1 is complex, it was with expectation that the largest error appears at sample point 1. At the same time, the results from the CFD model verifies the accuracy of the model.

4.4.5.4 Results Comparison

Table 8. Results comparison among the 2D CFD models.

Sample points	Error (%)	
	One-zone Case	Five-zone Case
1	11.51	10.89
2	4.28	4.32
3	7.51	7.49
7	0.01	0.01
9	6.20	6.20

All the results from the one-zone case and the five-zone case summarized in Table 8. The largest error is under 12% and appears at sample point 1 for both the two cases. Results from the one-zone case and five-zone case are almost the same. In terms of the CFD

models, these results confirms that these results are accurate. It is not necessary to build up the five-zone case in the 3D CFD model for this paper. There are several reasons for the errors at the sample points. The experimental results may not be 100% accurate because of the complex mine geometry. Additionally, several assumptions were made when establishing the CFD model. The 2D CFD model is just a numerical model and it cannot simulate everything as what it is in the underground mine. However, with such complex mine geometry, the fact that errors of the results from the two 2D CFD models are under 12% is acceptable.

4.4.6 3D CFD Model with and without Turbulent Viscosity by Using UDF Approach

4.4.6.1 3D CFD Model Setup

Figure 12. Plan view of the 3D CFD model.

Based on the conclusions from the 2D CFD model, only the one-zone case was discussed in the 3D CFD model. A plan view of the 3D CFD model is shown in Figure 12. The caving height of the longwall was between 35ft to 40ft and the gob height was averaged in the 3D CFD model. As a result, the height of the gob was 37.5ft in the 3D CFD model. The height of the coal seam was 10.5ft according to the mine survey. The gob area was still simulated as porous media and airflow in the gob was modeled as laminar flow. Since the standard k-epsilon turbulence model was widely applied on turbulent flows in

35

the mining industry (Xu 2013), it was used to simulate the flow turbulence in the model mine.

4.4.6.2 Mesh Independence Study

The purpose of mesh independence study is to ensure that various kinds of meshes will not affect the results obtained from the 3D CFD models. At the same time, it shows the results does not change as the mesh goes finer. In addition, based on the results from the mesh independence study, optimal mesh size can be determined and errors from the mesh can be minimized. Three kinds of meshes were created in this study and details were shown in Table 9. Fine mesh has the most number of nodes and coarse mesh has the least number of nodes. The fine, medium, and coarse mesh were shown in Figure 13. The 3D CFD results from these three meshes were compared with the experiment data and were shown in Table 10, Table 11, and Table 12 separately. Detailed comparisons of airflow quantity and SF_6 flow quantity with experiment data for the three meshes were shown in Figure 14 and Figure 15 separately. Equation (4-5) was used to calculate the errors between the results from CFD model and experiment at certain sample point or release point.

$$\text{Error } (\%) = \frac{|\text{Result from one CFD model} - \text{Result from experiment}|}{|\text{Result from experiment}|} * 100\% \qquad (4\text{-}5)$$

Table 9. Summary of nodes numbers for three kinds of meshes.

Mesh	Nodes Number (million)
Fine	22.10
Medium	12.46
Coarse	7.19
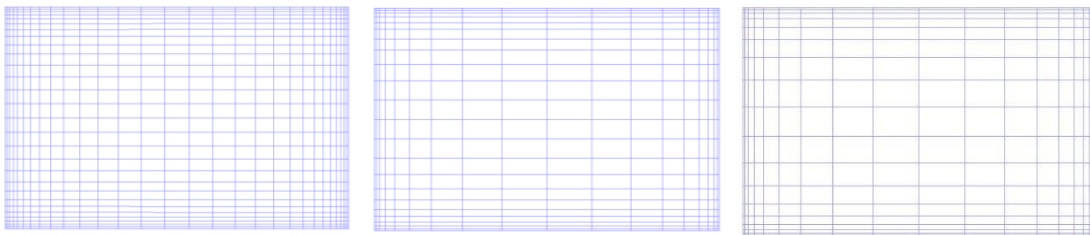
Figure 13. Plan view of the three meshes (from left: fine mesh, medium mesh, and coarse mesh) in a cross sectional area.

Table 10. Results from the fine mesh.

Sample points	Air quantity (kcfm)	SF_6 (cfm)	SF_6 (kcfm)	Fluent Results Air (kcfm)	Fluent Results SF_6 (kcfm)	Air Error (%)	SF_6 Error (%)
1	81.00	0.0129	1.29×10^{-5}	86.88	8.98×10^{-6}	7.26	30.37
2	19.60	0.0033	3.30×10^{-6}	19.60	1.99×10^{-6}	0.00	39.82
3	17.00	0.0028	2.80×10^{-6}	15.47	1.57×10^{-6}	9.02	44.02
7	53.74			53.74		0.00	
9	63.00	0.0089	8.90×10^{-6}	62.99	6.36×10^{-6}	0.01	28.56
RP1	53.60	0.0088	8.80×10^{-6}	52.87	8.82×10^{-6}	1.37	0.28

Table 11. Results from the medium mesh.

Sample points	Air quantity (kcfm)	SF_6 (cfm)	SF_6 (kcfm)	Fluent Results Air (kcfm)	Fluent Results SF_6 (kcfm)	Air Error (%)	SF_6 Error (%)
1	81.00	0.0129	1.29×10^{-5}	86.79	9.00×10^{-6}	7.14	30.26
2	19.60	0.0033	3.30×10^{-6}	19.56	1.99×10^{-6}	0.00	39.77
3	17.00	0.0028	2.80×10^{-6}	16.39	1.66×10^{-6}	3.61	40.63
7	53.74			53.74		0.00	
9	63.00	0.0089	8.90×10^{-6}	62.99	6.39×10^{-6}	0.01	28.22
RP1	53.60	0.0088	8.80×10^{-6}	52.79	8.83×10^{-6}	1.52	0.35

Table 12. Results from the coarse mesh.

Sample points	Air quantity (kcfm)	SF_6 (cfm)	SF_6 (kcfm)	Fluent Results Air (kcfm)	Fluent Results SF_6 (kcfm)	Air Error (%)	SF_6 Error (%)
1	81.00	0.0129	1.29×10^{-5}	86.70	8.98×10^{-6}	7.03	30.36
2	19.60	0.0033	3.30×10^{-6}	19.60	1.99×10^{-6}	0.04	39.74
3	17.00	0.0028	2.80×10^{-6}	5.35	5.44×10^{-7}	68.50	80.58
7	53.74			53.74		0.00	
9	63.00	0.0089	8.90×10^{-6}	62.99	6.39×10^{-6}	0.01	28.18
RP1	53.60	0.0088	8.80×10^{-6}	52.70	8.83×10^{-6}	1.67	0.30

For Table 10, Table 11, and Table 12, the first three columns (sample points, air quantity, and SF_6 quantity) were the original data obtained from the experiment in the underground. Data in the fourth column (SF_6 (kcfm)) of the three tables were obtained by converting the unit of SF_6 quantity from Cubic Feet per Minute (cfm) to Kilo-Cubic Feet per Minute (kcfm) based on the data in the third column (SF_6 (cfm)). The purpose for the conversion was to keep the consistency of units. The data in the fifth column (Fluent

results air (kcfm)) and the sixth column (Fluent results SF$_6$ (kcfm)) represented the results of airflow quantity and SF$_6$ flow quantity from the CFD models, respectively. Both the airflow quantity and SF$_6$ quantity results from the CFD models were compared with that from the experiment. Equation (4-5) was applied to calculate the errors from the CFD models. The last two columns in the three tables showed the airflow quantity and SF$_6$ flow quantity errors from the CFD models, respectively.
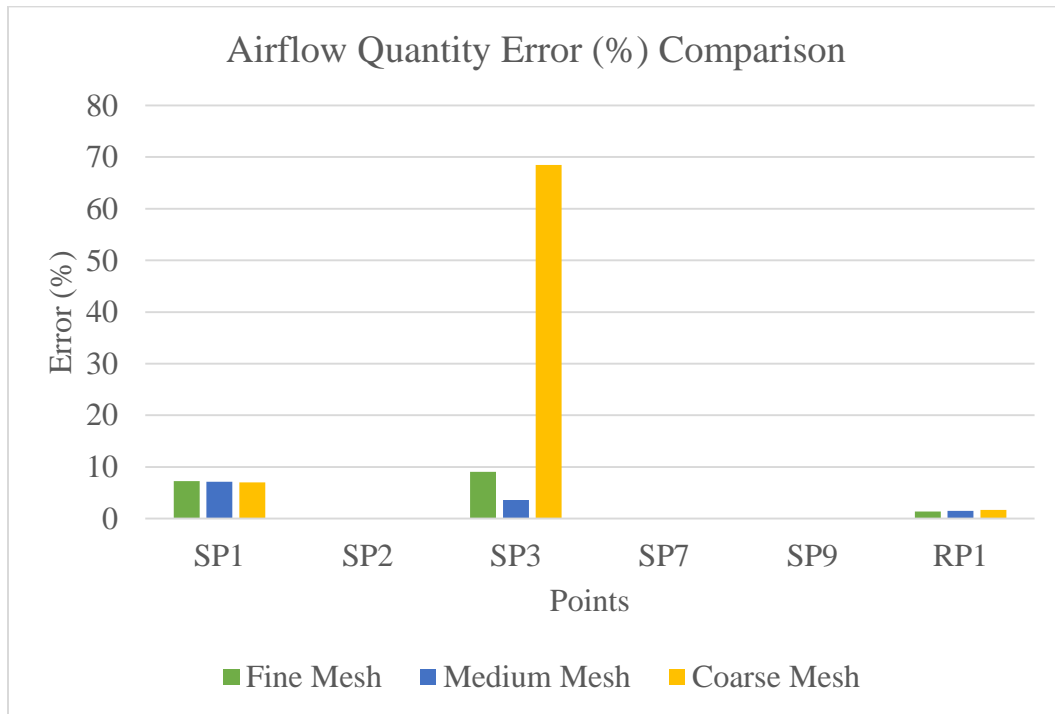
Figure 14. Airflow quantity error (%) comparison among three meshes.
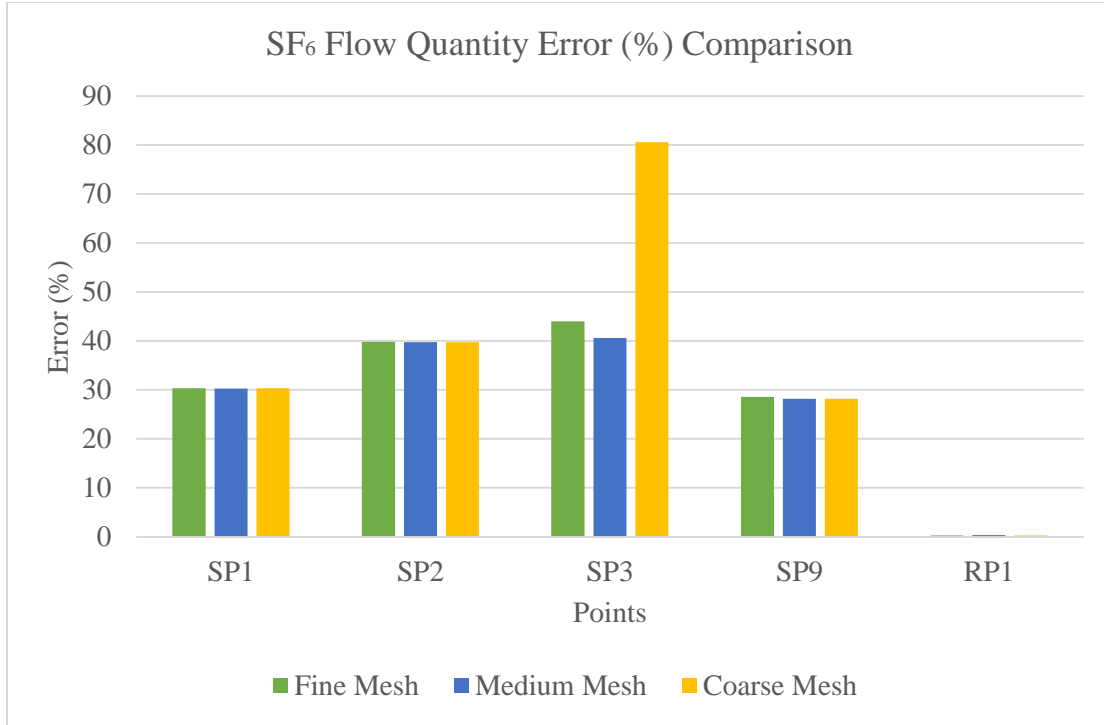
Figure 15. SF$_6$ flow quantity error (%) comparison among three meshes.

From Figure 15 and Figure 16, the CFD model with coarse mesh has a large error for both the airflow quantity and SF$_6$ flow quantity at sample point 3. For all the other sample points, the coarse mesh CFD model has almost the same results as the fine mesh and coarse mesh CFD models. It reflects that sample point 3 is considerably sensitive to the mesh size. It also proves that airflow at sample point 3 is complicated and has a relatively larger range of quantity than the other sample points.

Obviously, the coarse mesh is not a good choice to build up the 3D CFD model. Theoretically, the medium mesh should be used as the standard mesh because of its less computing time compared with the fine mesh. However, after considering the complex mine geometry, the fine mesh was selected as the final mesh for the steady-state simulation and transient simulation.

4.4.6.3 Sensitivity Study for Porosity and Permeability Values

No accurate data about porosity and permeability of the gob were provided. The reason was that there were no porosity and permeability tests done in the mine. Then a

sensitivity study for the porosity and permeability data were conducted to analyze the effects of these data on the CFD results. In a CFD model, permeability is represented by two properties, which are inertial resistance and viscous resistance.

Porosity and permeability values for a gob in anther underground mine in the western U.S. were shown in Table 13 and they were reported in Lolon's Ph.D dissertation (Lolon 2008). Since the porosity and permeability values were obtained based on experiment and field data from the underground mine (Lolon 2008), these results were reliable to be utilized in this paper. Additionally, the underground coal mine in this study is also located in the western U.S., which means the two mines have some geologic similarities. The porosity and permeability data were shown in Table 13 and were applied to the 3D CFD model in this paper.

Table 13. Porosity and permeability values used in the CFD models.

Porosity	0.24
Viscous Resistance (m^{-2})	7.91×10^7
Inertial Resistance (m^{-1})	14700

The relationship between the porosity (n) and permeability (k) were demonstrated by Kozeny-Carmen equation (Scheidegger 1957) as shown in Equation (4-6). The equations for computing viscous resistance and inertial resistance were shown in Equation (4-7) and Equation (4-8) (Lolon 2008) separately.

$$ k = \frac{d_m^2}{180} * \frac{n^3}{(1-n)^2} \qquad (4\text{-}6) $$

where d_m is the mean particle size (m), k is the theoretical specific permeability (m^2), and n is the porosity.

$$ C_1 = \frac{1}{k} \qquad (4\text{-}7) $$

$$ C_2 = \frac{3.5 * (1-n)}{d_m * n^3} \qquad (4\text{-}8) $$

where C_1 is the viscous resistance and C_2 is the inertial resistance for the gob.

Table 14 shows the porosity and permeability values used in the sensitivity study. The porosity values were set as what they were in the table. The viscous resistance and inertial resistance were then computed by using Equation (4-7) and Equation (4-8). Again, the purpose of the sensitivity study was to see the effect of the various porosity and permeability data on the results of the CFD models.

Table 14. All the porosity and permeability values used in the sensitivity study.

Porosity	$C_1\ (m^{-2})$	$C_2\ (m^{-1})$
0.15	2.25×10^8	67341.47
0.2	8.40×10^7	26738.53
0.24	4.39×10^7	14700.00
0.26	3.27×10^7	11257.69
0.3	1.91×10^7	6932.21
0.35	1.04×10^7	4053.65
0.4	5.91×10^6	2506.74

All the detailed results from the sensitivity study are shown from Table 22 through Table 28 in the Appendix. Error comparisons made for airflow quantity and SF_6 flow quantity among these cases were presented in Figure 16 and Figure 17, respectively.
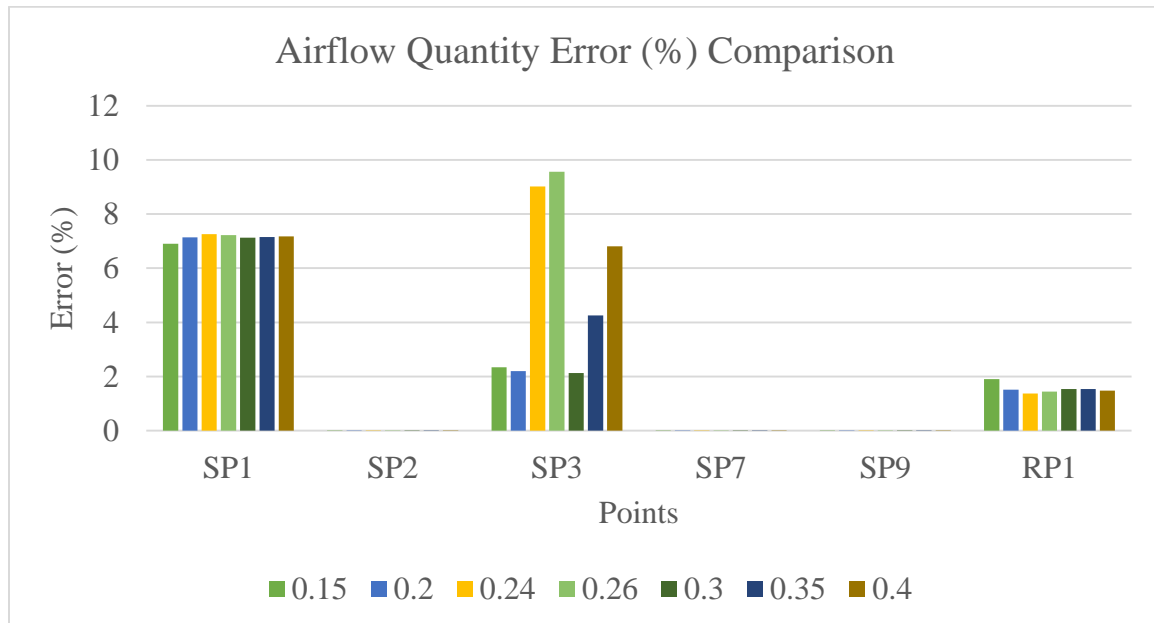
Figure 16. Airflow quantity error (%) comparison with different porosity and permeability data.
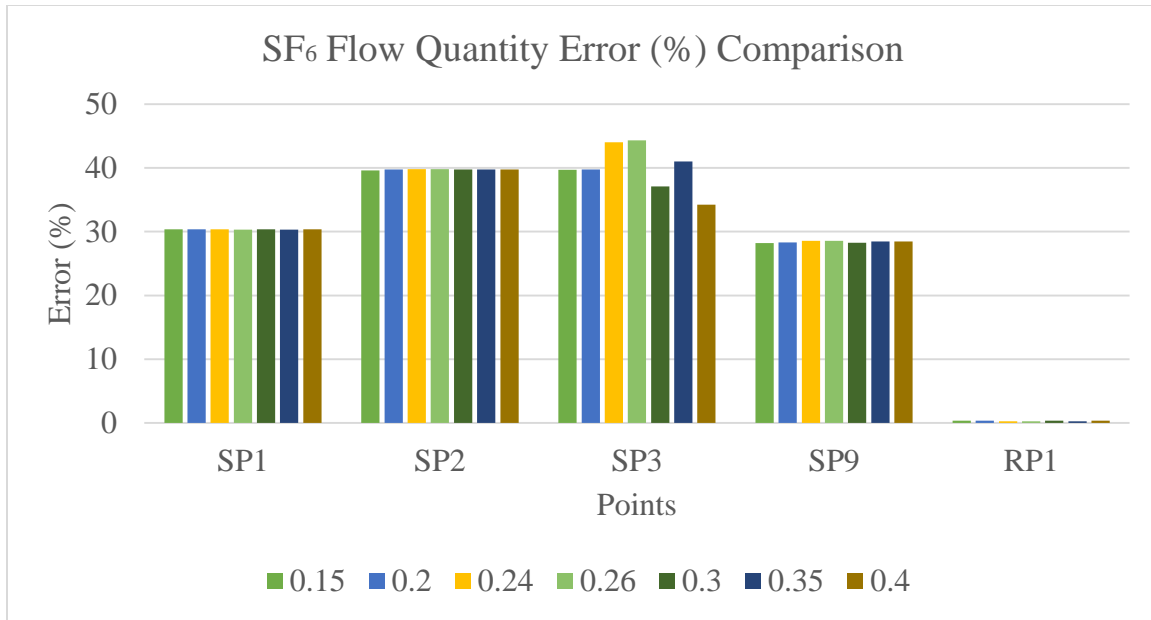
Figure 17. SF$_6$ flow quantity error (%) comparison with different porosity and permeability data.

According to Figure 16, the largest error of airflow quantity from the CFD models is 10% and it appears at sample point 3. Except sample point 3, all the other sample points have almost the same results from the CFD models. The airflow errors at sample point 3 range from 2% to 10% in the CFD model with different porosity and permeability data. It is understandable because sample point 3 is located right next to the gob and the airflow is significantly sensitive to the change of porosity and permeability in the gob.

From Figure 17, all the SF$_6$ flow quantity results from the cases with different porosity and permeability values are pretty close. It means the porosity and permeability values does not have a significant effect on the CFD results.

Based on Figure 16 and Figure 17, the porosity and permeability values does not affect the results very much. It eliminates the concerns on not having field data on the porosity and permeability for the mine gob. Therefore, the porosity and permeability values (shown in Table 13) prove fine to be utilized for this mine geometry.

4.4.6.4 Steady-State Simulation

4.4.6.4.1 Two Kinds of Simulations and Results

According to the user's guide of Ansys Fluent (Ansys 2006), the diffusivity term in the UDS equation is a constant. Due to the flow turbulence, the effective diffusivity changes as shown in Equation (4-4). The diffusivity of SF_6 in air was calculated with the turbulent Schmidt number, which meant the influence of turbulence was considered in the equation. In order to realize the effects of the turbulence on the diffusivity of SF_6 in air for this mine geometry, the steady-state simulation in the 3D CFD model was completed under two conditions. One was without taking the turbulent diffusivity (Equation (4-4)) into account. Results from this case were shown in Table 15. The other one was with the turbulent diffusivity (Equation (4-4)) taken into account., which was much closer to the actual situation in the underground. In the underground, the SF_6 flow was affected by not only the molecular diffusivity but also the turbulent diffusivity. Results were shown in Table 16. The airflow quantity and SF_6 quantity results from the two cases were compared with each other in Figure 18 and Figure 19 separately.

Table 15. Results from the 3D CFD model without turbulent diffusivity.

Sample points	Air quantity (kcfm)	SF_6 (cfm)	SF_6 (kcfm)	Fluent Results Air (kcfm)	Fluent Results SF_6 (kcfm)	Air Error (%)	SF_6 Error (%)
SP1	81.00	0.0129	1.29×10^{-5}	86.89	8.99×10^{-6}	7.27	30.32
SP2	19.60	0.0033	3.30×10^{-6}	19.60	1.99×10^{-6}	0.00	39.82
SP3	17.00	0.0028	2.80×10^{-6}	15.51	1.57×10^{-6}	8.76	43.86
SP7	53.74			53.74		0.00	
SP9	63.00	0.0089	8.90×10^{-6}	62.99	6.35×10^{-6}	0.01	28.63
RP1	53.60	0.0088	8.80×10^{-6}	52.88	8.82×10^{-6}	1.34	0.23

Table 16. Results from the 3D CFD model with turbulent diffusivity.

Sample points	Air quantity (kcfm)	SF_6 (cfm)	SF_6 (kcfm)	Fluent Results Air (kcfm)	Fluent Results SF_6 (kcfm)	Air Error (%)	SF_6 Error (%)
SP1	81.00	0.0129	1.29×10^{-5}	86.88	8.99×10^{-6}	7.26	30.33
SP2	19.60	0.0033	3.30×10^{-6}	19.60	1.99×10^{-6}	0.00	39.81
SP3	17.00	0.0028	2.80×10^{-6}	15.64	1.59×10^{-6}	7.99	43.38
SP7	53.74			53.74		0.00	
SP9	63.00	0.0089	8.90×10^{-6}	62.99	6.36×10^{-6}	0.01	28.58
RP1	53.60	0.0088	8.80×10^{-6}	52.87	8.82×10^{-6}	1.37	0.23
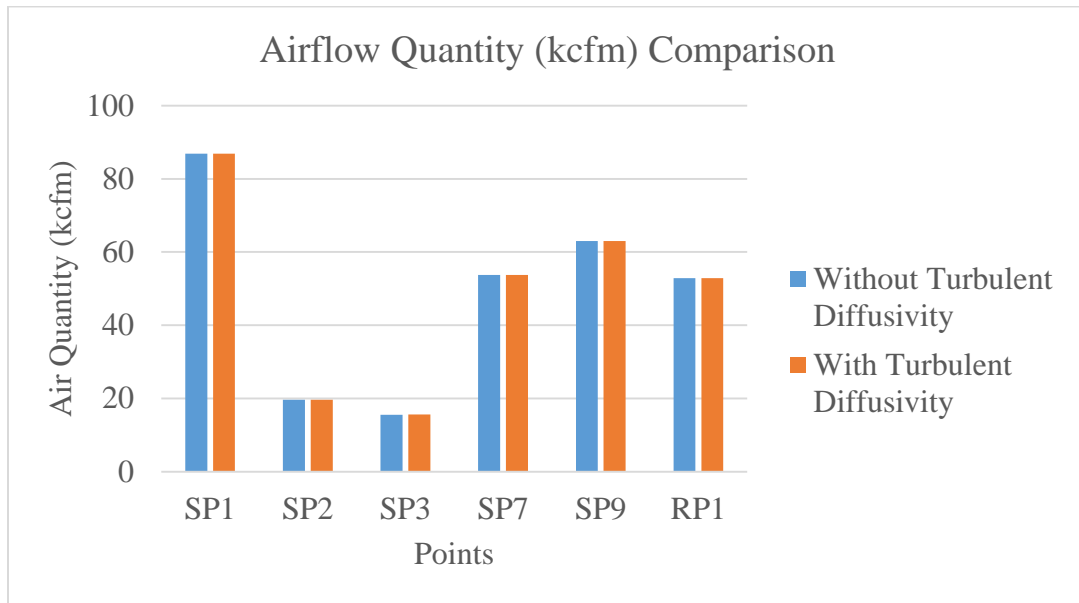
Figure 18. Air quantity comparison between two cases.
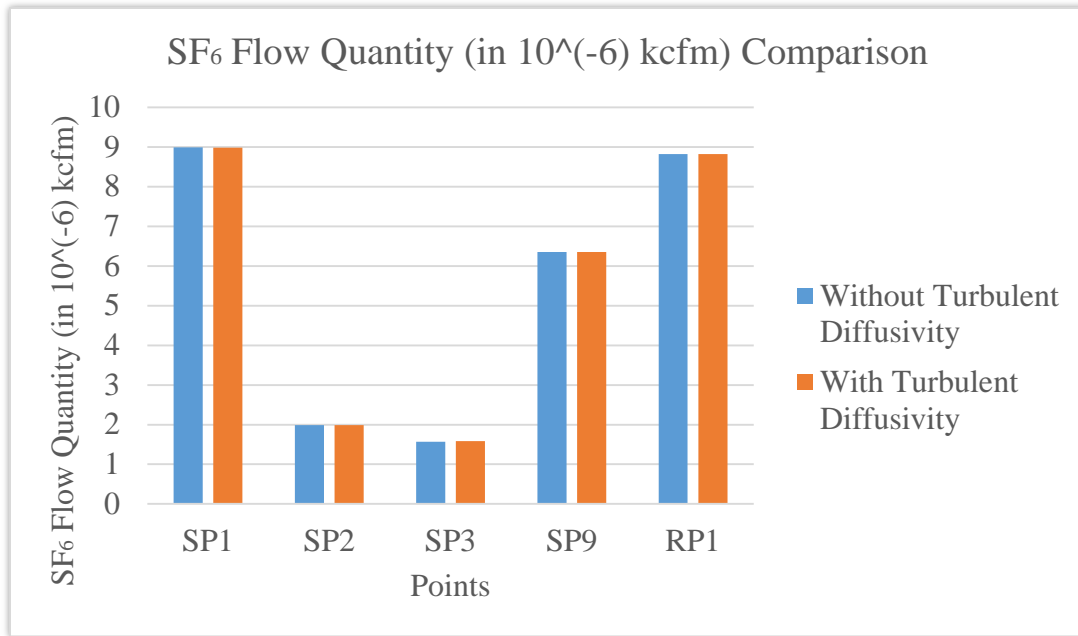
Figure 19. SF$_6$ quantity comparison between two cases.

According to Figure 18 and Figure 19, the results from these two cases does not have a big difference. Therefore, only the CFD model without turbulent diffusivity interpreted is examined. From the Table 15, on one hand, all the errors for airflow are below 9%. The largest error for air quantity appearing at sample point 3 is 8.76%. This error is acceptable due to the complexity of the geometry and the low airflow quantity at the sample point. On the other hand, the errors for the SF$_6$ flow ranges from 28% to 44% at the sample points. For SF$_6$ flow, the largest error, which is 43.86%, appears at sample points 5. It is reasonable that sample point 3 has the largest error because it is located next to the gob and this area is difficult to be accessed to do good experiments. Additionally, based on the experimental data, the quantity of SF$_6$ flow at sample point 1, which is 0.0129 cfm, is greater than that at the release point 1, which is 0.0088 cfm. The difference between these two results is about 47%. It proves the fact that error exists in the experiment data. Similarly, based on the 3D CFD model, the quantity of SF$_6$ flow at sample point 1, which is 8.99×10^{-6} kcfm, is greater than that at the RP1, which is 8.82×10^{-6} kcfm. However, the difference between these two results is less than 2%. Since all the boundary conditions were balanced in the 3D CFD model, the 2% difference

on the results between these two points comes from the numerical error (discretization error) of Ansys Fluent itself.

It is obvious that all the SF_6 concentration results from the 3D CFD models are smaller than that from the experiment. It is because the experiment is a transient simulation. But the results were compared with both the results from steady-state simulation and transient simulation in the CFD models. The researcher, who did the experiment, took an average value of the experiment results with both high and low concentration values (as shown in Figure 42). The averaged results were reported as the steady-state simulation results of the experiment by the researcher. However, it actually increased the values of the experimental results since there were higher values than lower values in the experimental results.

4.4.6.4.2   Contour Comparisons between the Two Cases (With Turbulent Diffusivity and Without Turbulent Diffusivity)

To show the complex airflow behavior in this complicated mine geometry, some figures obtained from both the two cases of 3D CFD models were shown below. Contours for both the SF_6 concentration and velocity magnitude at different locations, such as areas near the working face and the release point, were analyzed. More contours are presented in the Appendix.

The overall SF_6 concentration distribution for the two cases can be seen in Figure 20 and Figure 21. SF_6 concentration distribution near the working face for the two cases are shown in Figure 22 and Figure 23. According to the four figures, the distribution of SF_6 concentration in the 3D CFD models are the same for both the two cases.
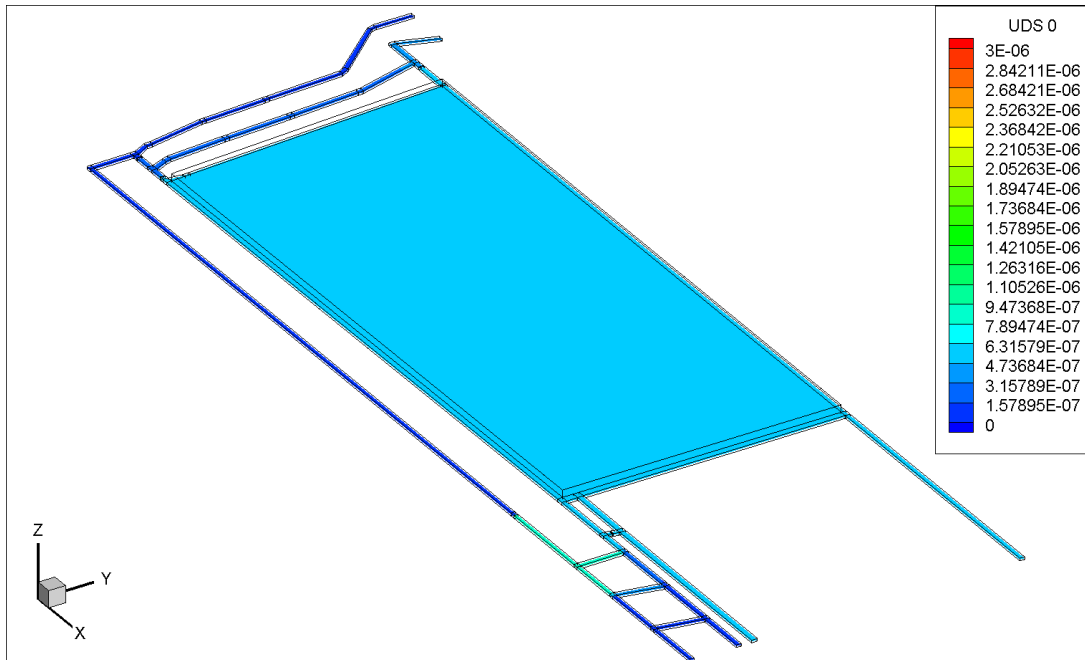
Figure 20. Visualization (in XY plane) of overall SF_6 concentration distribution in the CFD model without turbulent diffusivity.
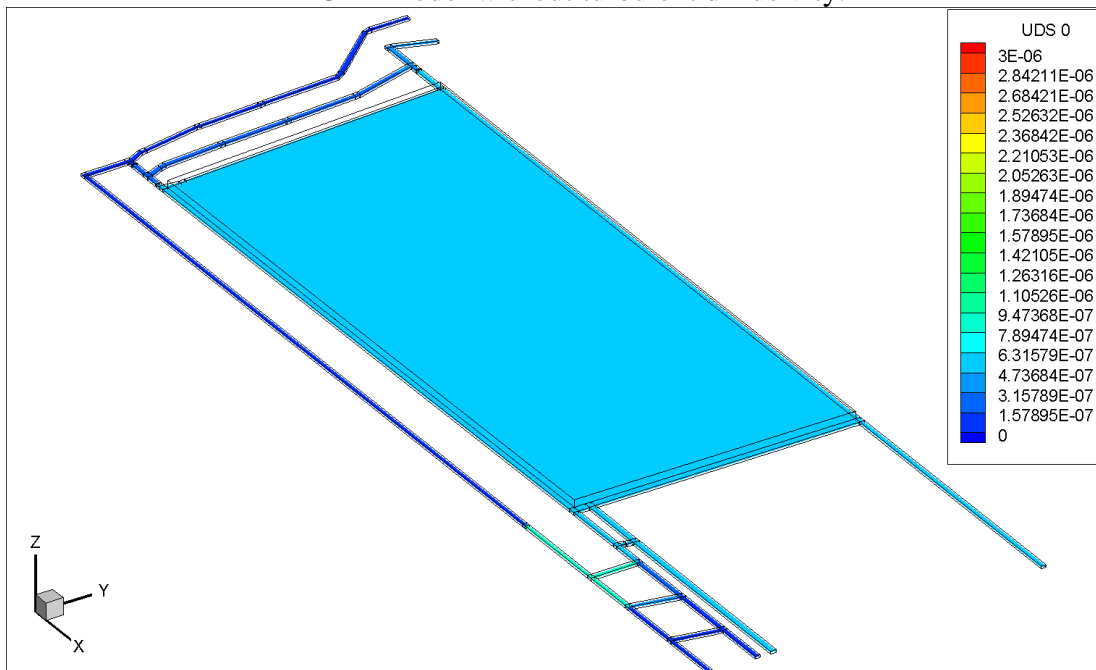
Figure 21. Visualization (in XY plane) of overall SF_6 concentration distribution in the CFD model with turbulent diffusivity.
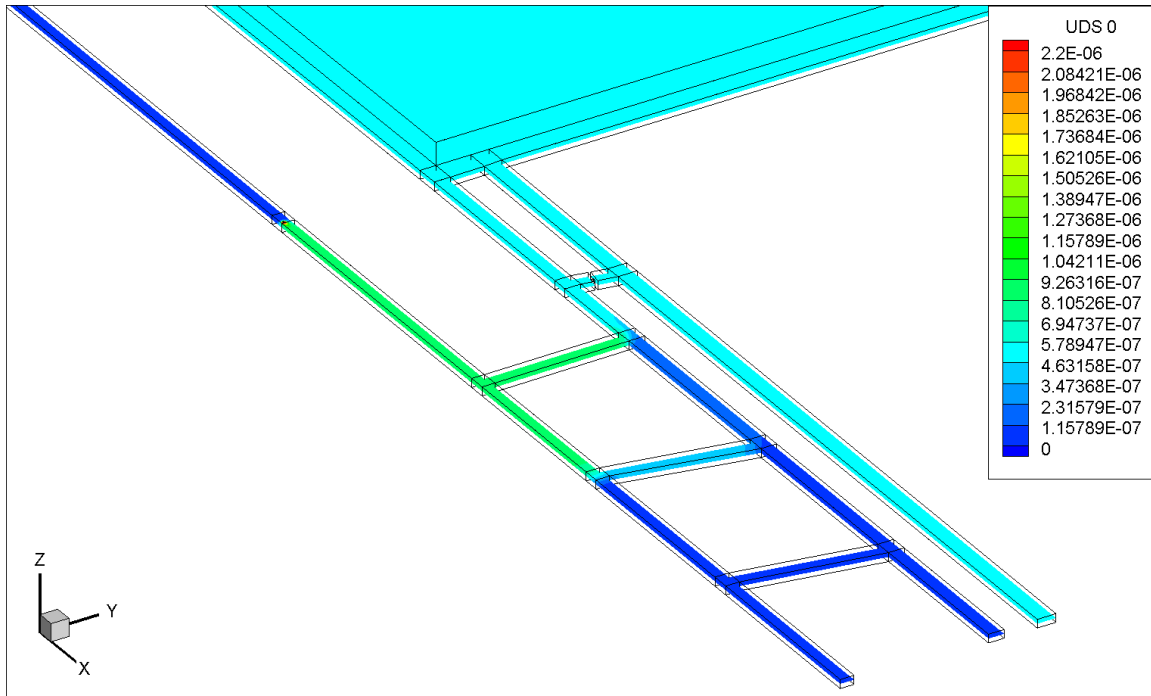
Figure 22. Visualization (in XY plane) of SF_6 concentration distribution near the working face in the CFD model without turbulent diffusivity.
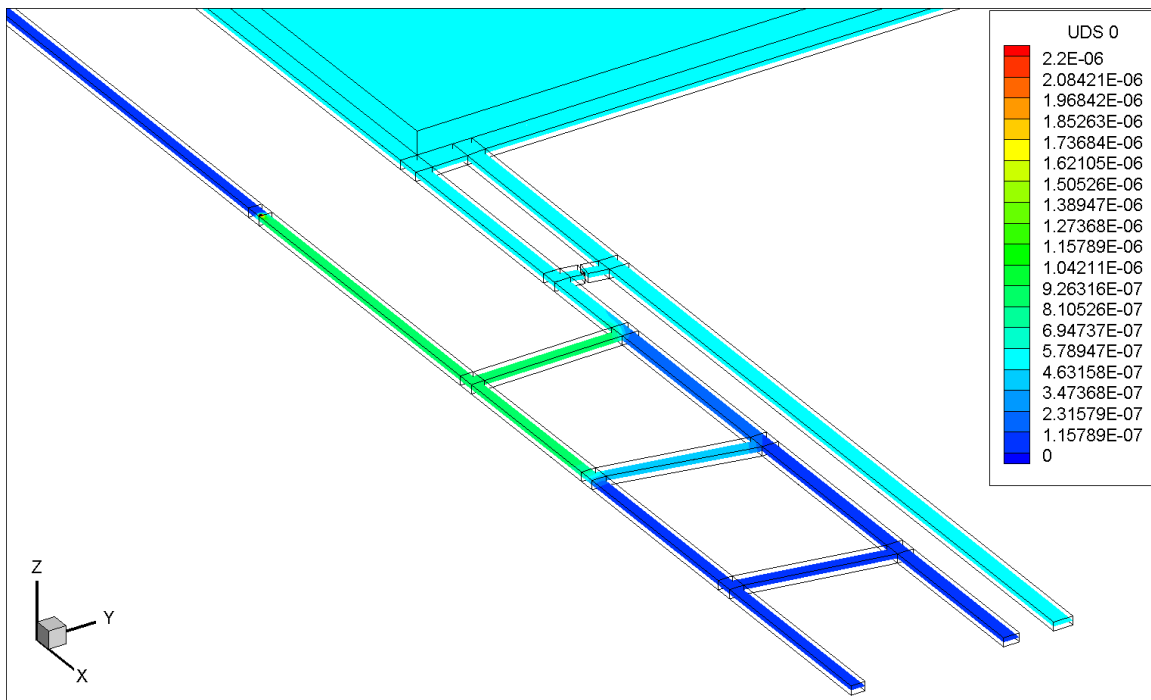
Figure 23. Visualization (in XY plane) of SF_6 concentration distribution near the working face in the CFD model with turbulent diffusivity.

48

Furthermore, the SF_6 concentration distribution at around the release point for both of the two cases can be seen clearly from Figure 24 through Figure 27. Figure 24 and Figure 25 present the contours of SF_6 concentration distribution in the XY plane. Figure 26 and Figure 27 show the contours in the YZ plane. It is obvious that SF_6 is distributed to the airway from the release point. Moreover, the SF_6 concentration is high in the center and low near the wall. The interpretation of turbulent diffusivity does not affect the SF_6 concentration distribution near the release point.
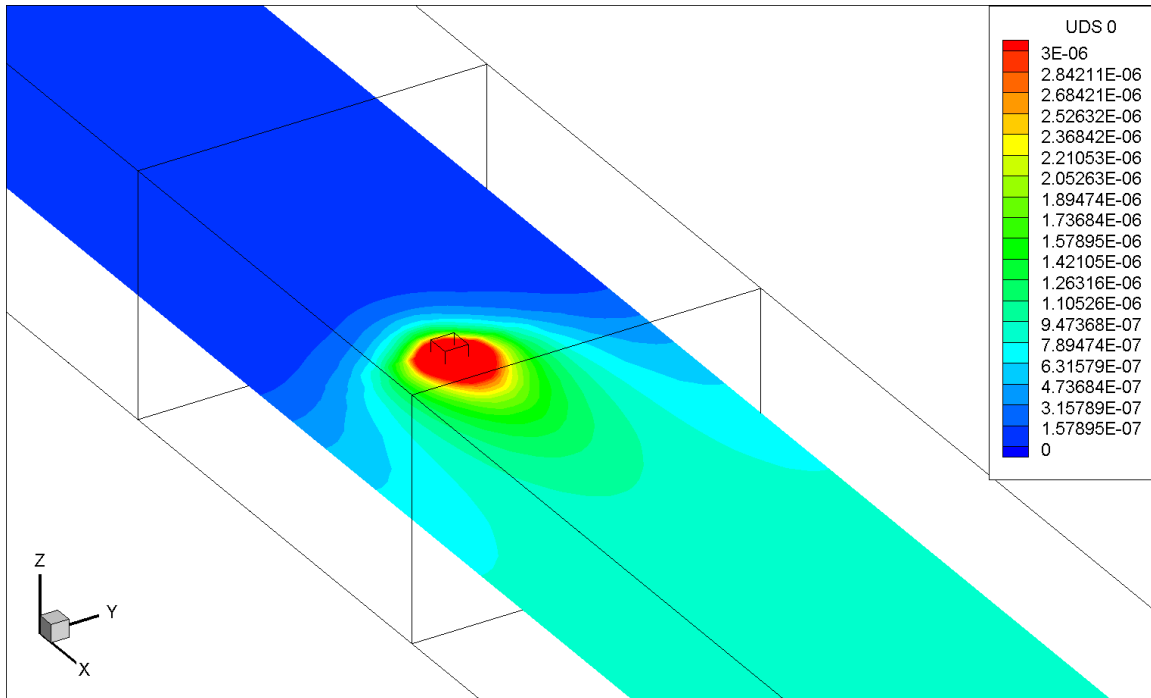
Figure 24. Visualization (in XY plane) of SF_6 concentration distribution around the release point in the CFD model without turbulent diffusivity.
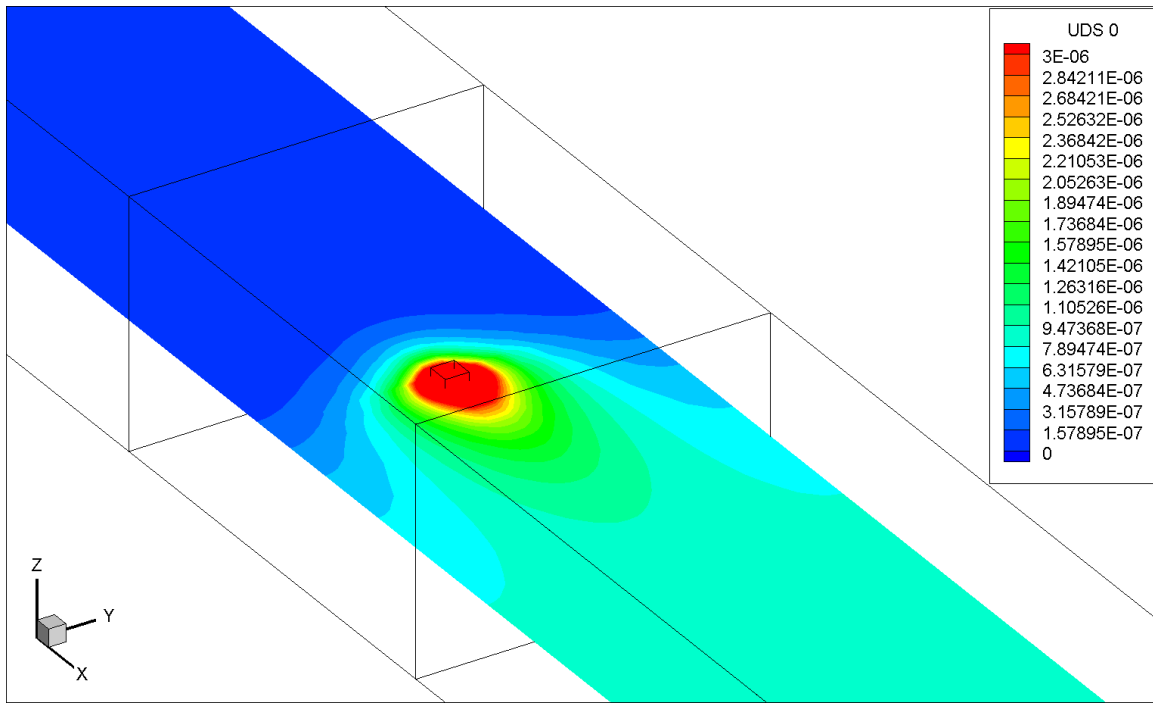
Figure 25. Visualization (in XY plane) of SF_6 concentration distribution around the
release point in the CFD model with turbulent diffusivity.
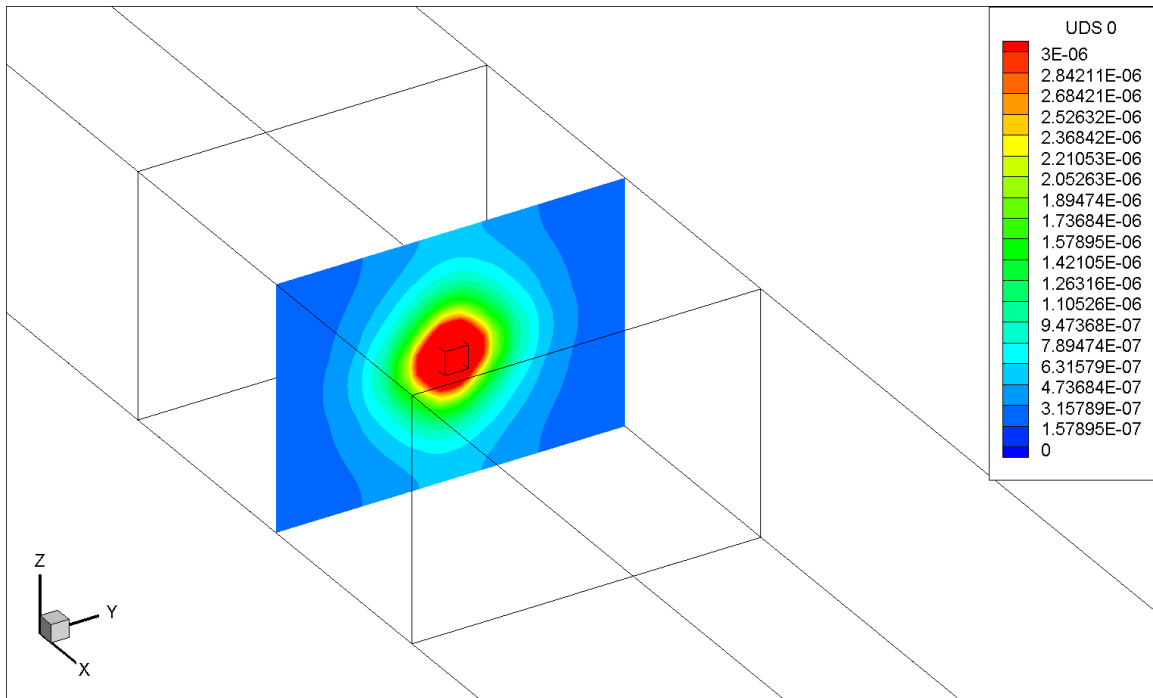
Figure 26. Visualization (in YZ plane) of SF_6 concentration distribution around the
release point in the CFD model without turbulent diffusivity.
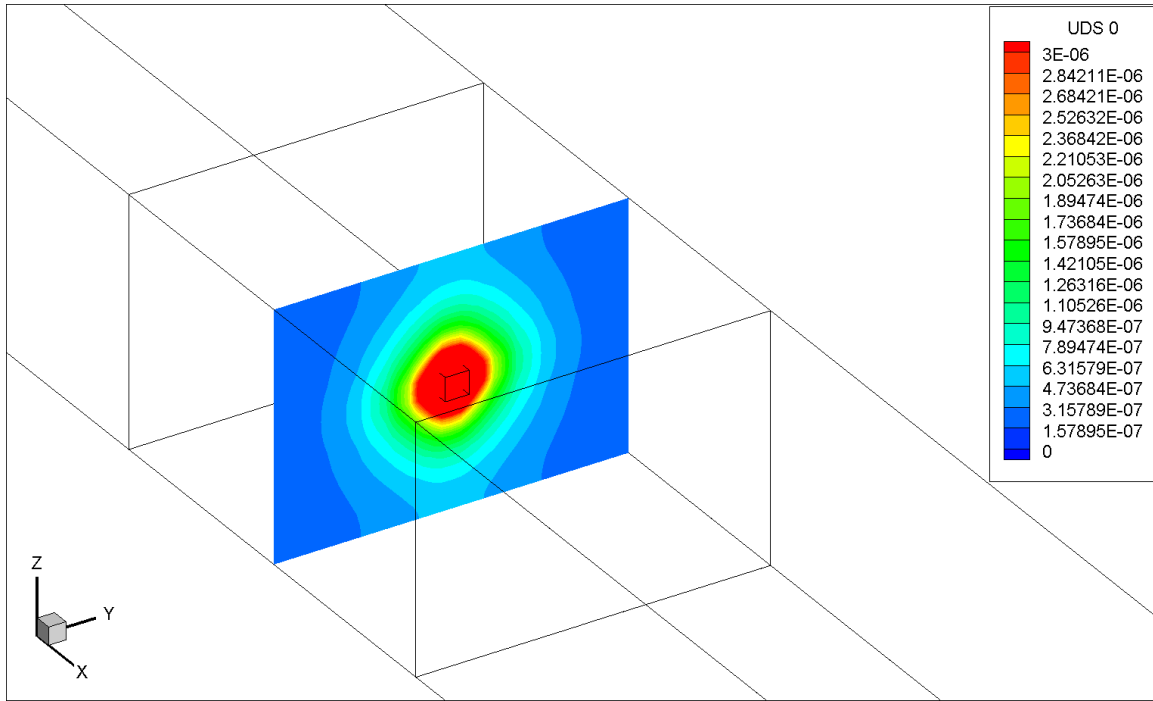
Figure 27. Visualization (in YZ plane) of SF_6 concentration distribution around the release point in the CFD model with turbulent diffusivity.

The overall velocity contours for the model mine are shown in Figure 28 and Figure 29. Figure 30 and Figure 31 show the velocity contours near the working face in the CFD model for the two cases. Based on the four figures, the airflow distribution for the two 3D CFD models are the same.
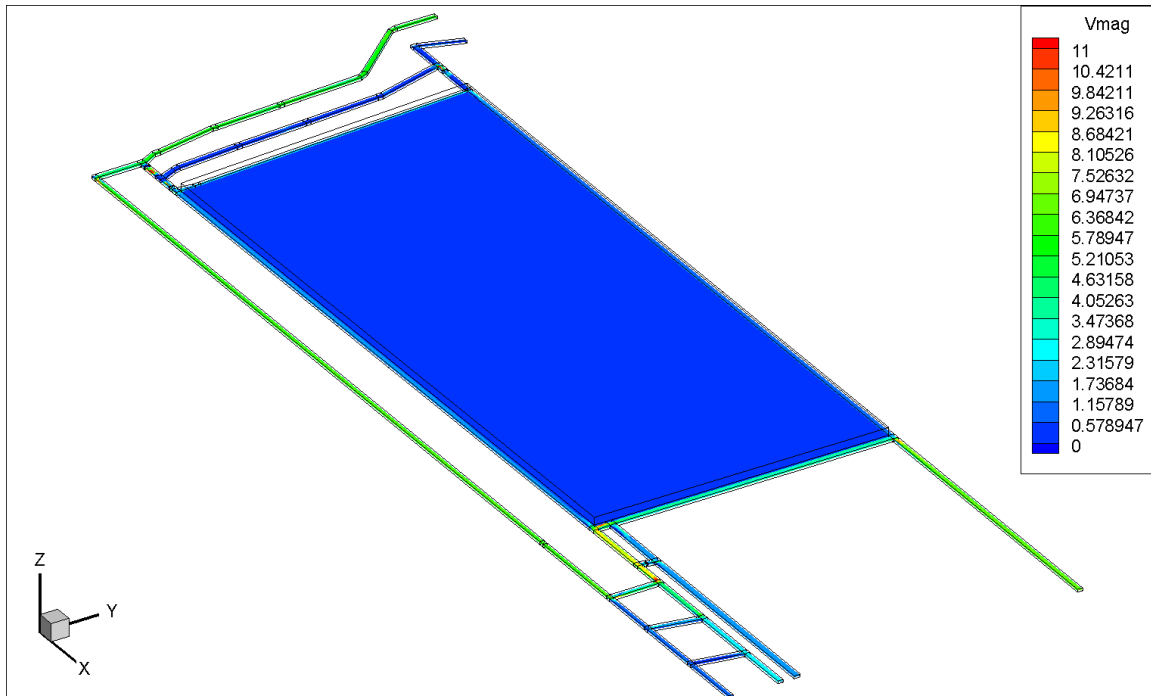
Figure 28. Contour (XY plane) of velocity magnitude (ft/s) for the entire mine in the CFD model without turbulent diffusivity.
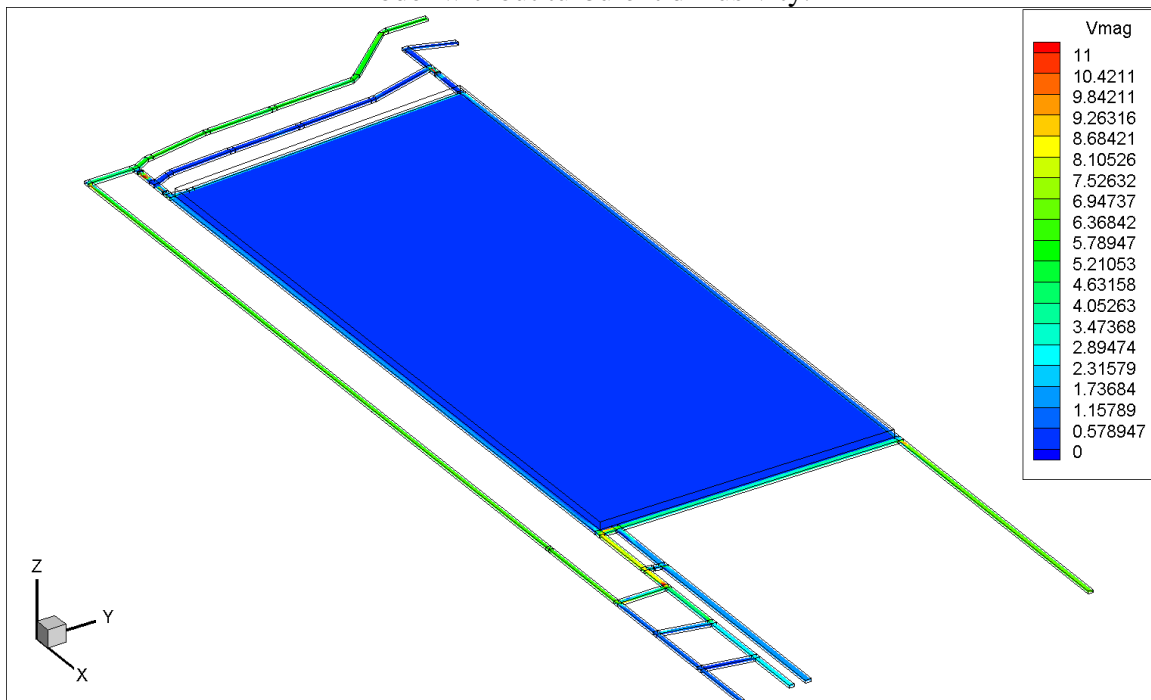
Figure 29. Contour (XY plane) of velocity magnitude (ft/s) for the entire mine in the CFD model with turbulent diffusivity.
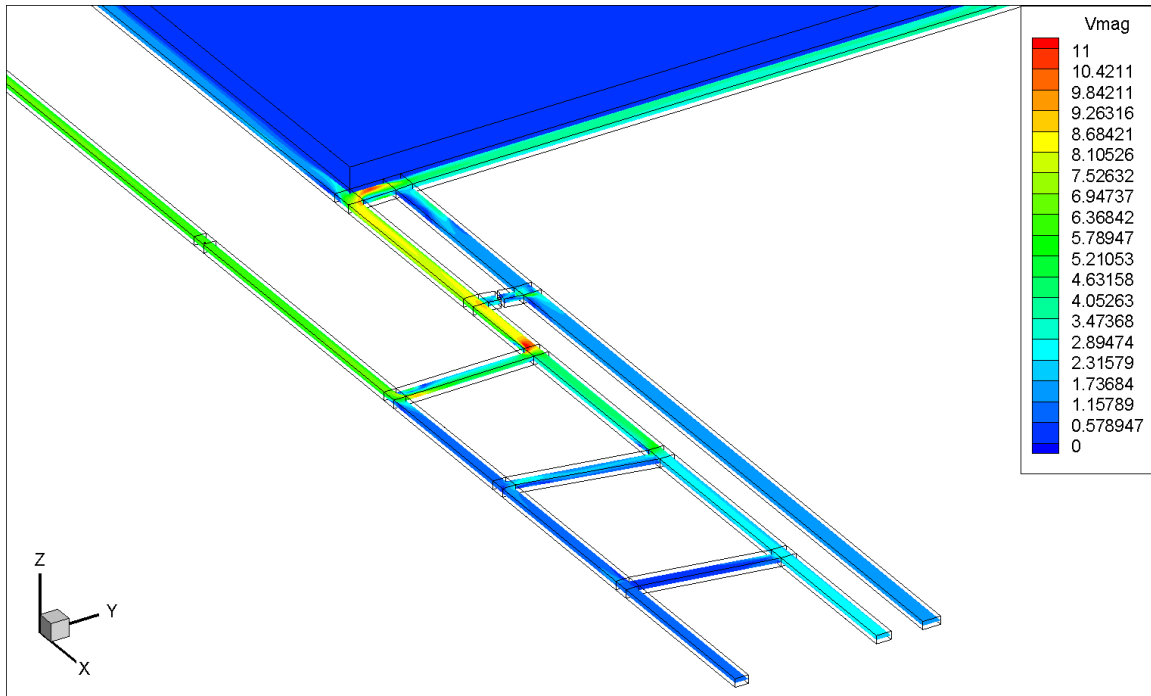
Figure 30. Contour (XY plane) of velocity magnitude (ft/s) near the working face in the CFD model without turbulent diffusivity.
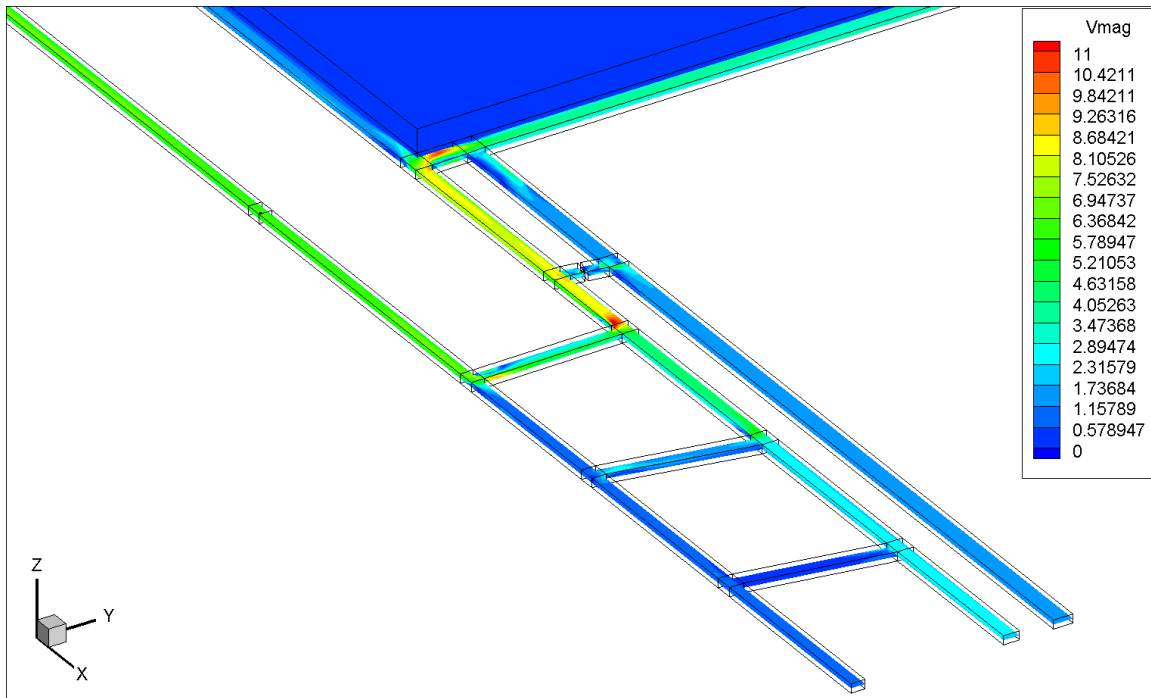
Figure 31. Contour (XY plane) of velocity magnitude (ft/s) near the working face in the CFD model with turbulent diffusivity.

The distribution of airflow velocity magnitude at around the release point for both of the two cases are presented in Figure 32 and Figure 33. Contours of the velocity magnitude

are the same for the two cases. In addition, there is high velocity in the center and low velocity near the wall for both the two cases. It also verifies that the injection of SF_6 does not affect the airflow behavior.
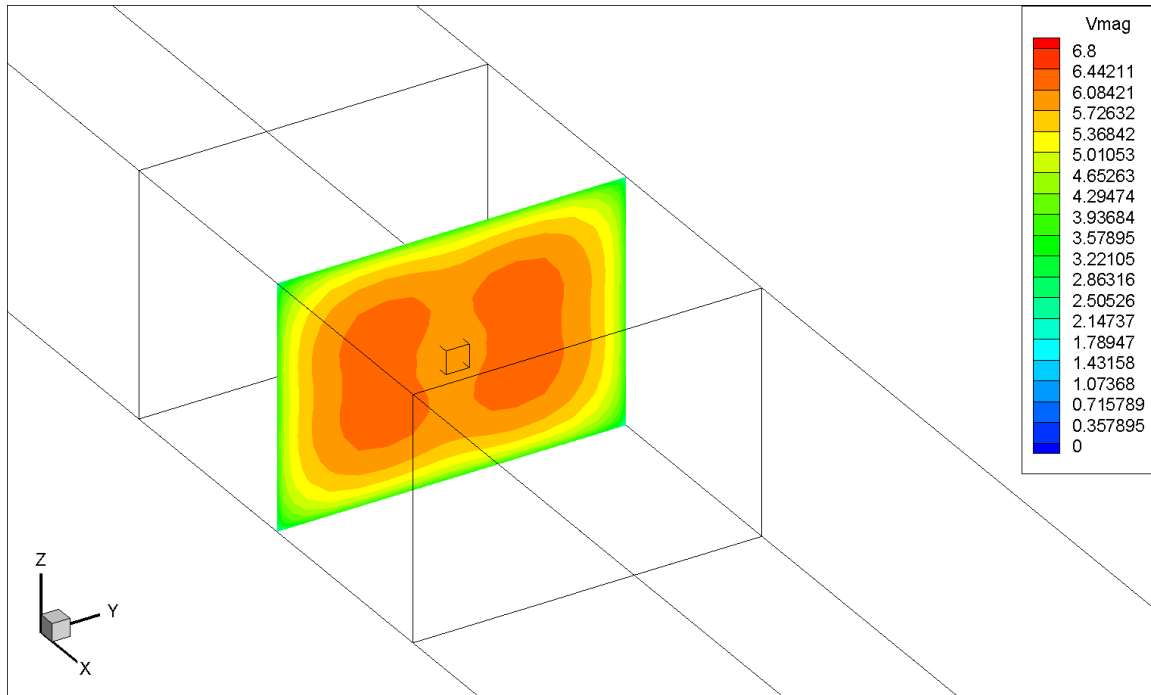
Figure 32. Contour (YZ plane) of velocity magnitude (ft/s) around the release point in the CFD model without turbulent diffusivity.
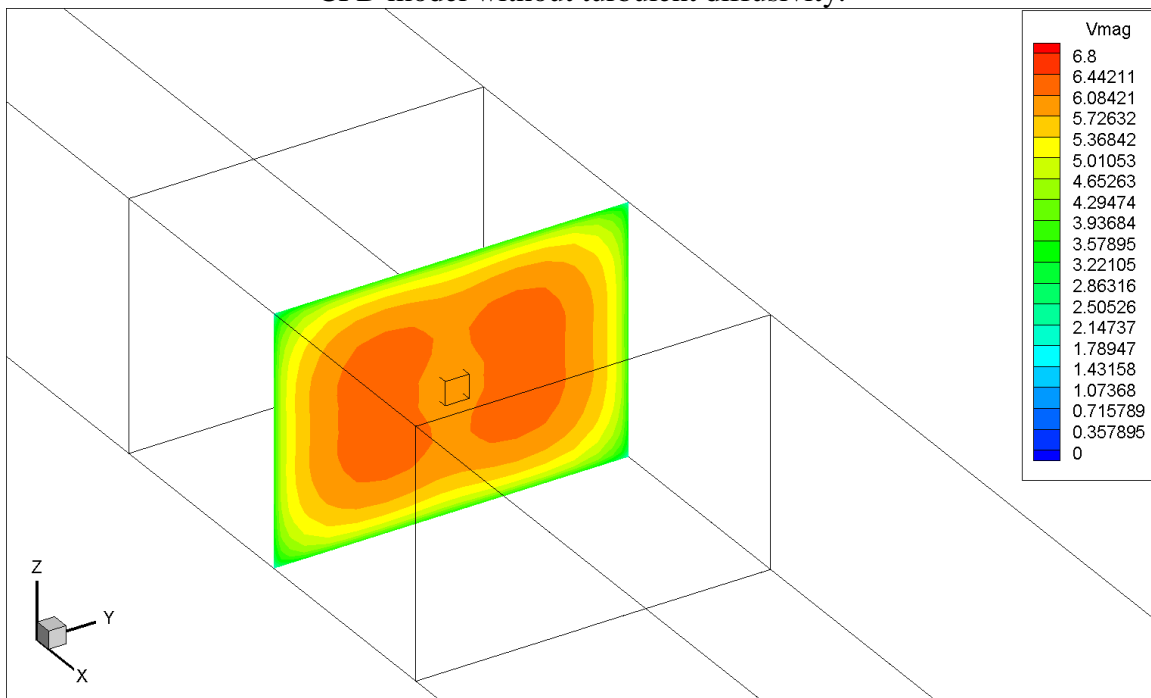
Figure 33. Contour (YZ plane) of velocity magnitude (ft/s) around the release point in the CFD model with turbulent diffusivity.

Figure 34 and Figure 35 show the SF_6 concentration distribution in the cross sectional area right after sample point 1 for both the two cases. These contours were made to show the SF_6 concentration distribution in a complex flow field. The contours are the same as seen in the two figures. The SF_6 concentration decreases from the left side to the right side in the cross-sectional area for both the two cases.
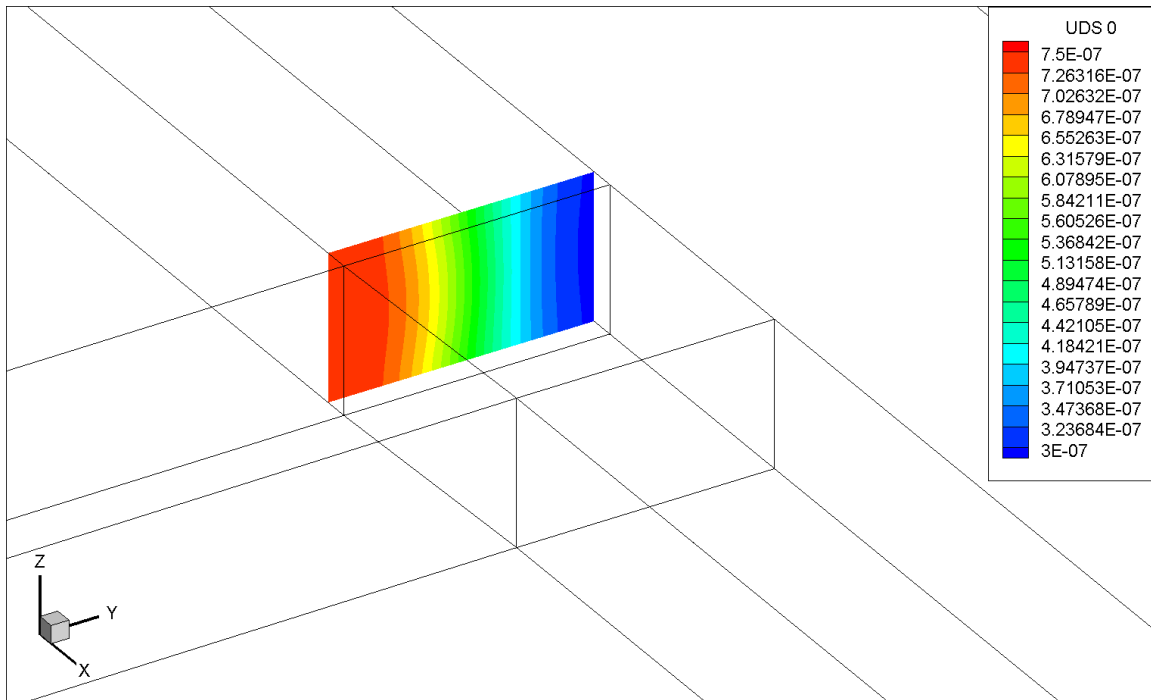
Figure 34. Contour (YZ plane) of SF_6 mass concentration right after sample point 1 in the CFD model without turbulent diffusivity.
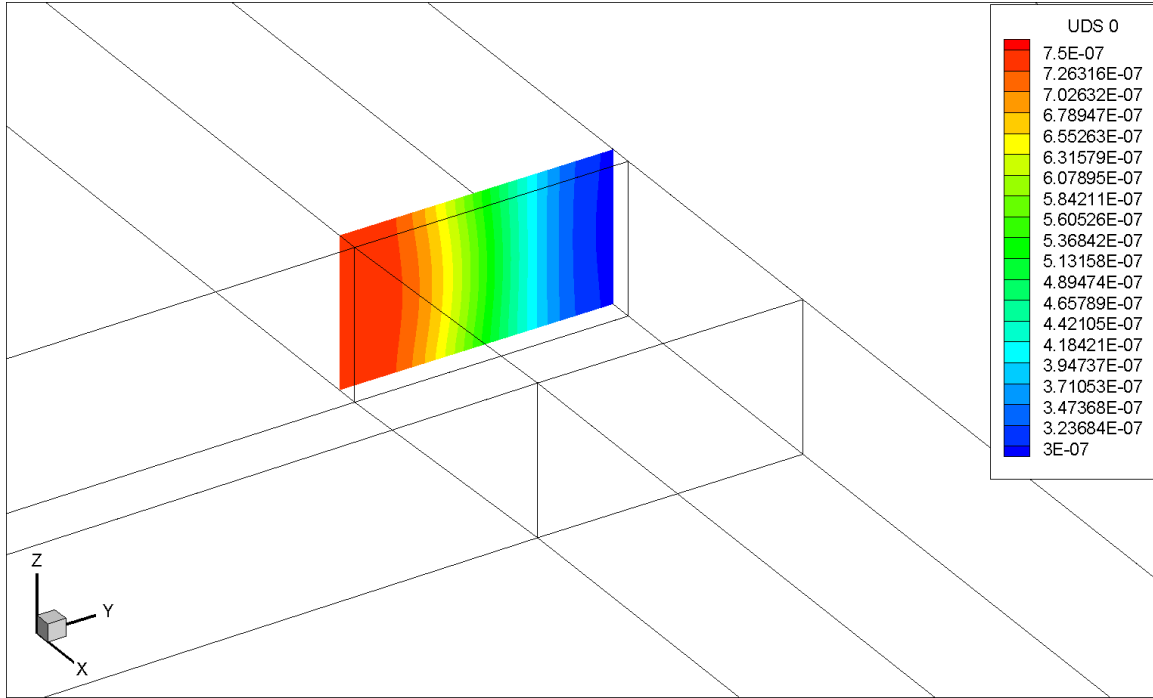
Figure 35. Contour (YZ plane) of SF_6 mass concentration right after sample point 1 in the CFD model with turbulent diffusivity.

According to the contours from Figure 20 to Figure 35, it is clear that contours for both SF_6 concentration and airflow velocity magnitude at different locations are the same in the 3D CFD models with turbulent diffusivity or without turbulent diffusivity. It means that turbulent diffusivity does not affect the results very much for this specific mine geometry.

4.4.6.4.3   Monitor Lines for the Two Cases (With and Without Turbulent Diffusivity)

To better understand these two cases, three monitor lines were created for both of the two CFD models. Locations of the monitor lines can be found in Figure 9. All the monitor lines were created in the center of the cross sectional areas and an example is shown in Figure 36. Since the injection of SF_6 does not affect the airflow distribution, only the distribution of SF_6 concentration across the monitor lines were examined. SF_6 concentration comparisons between the two cases at the three monitor lines are presented from Figure 37 to Figure 39.
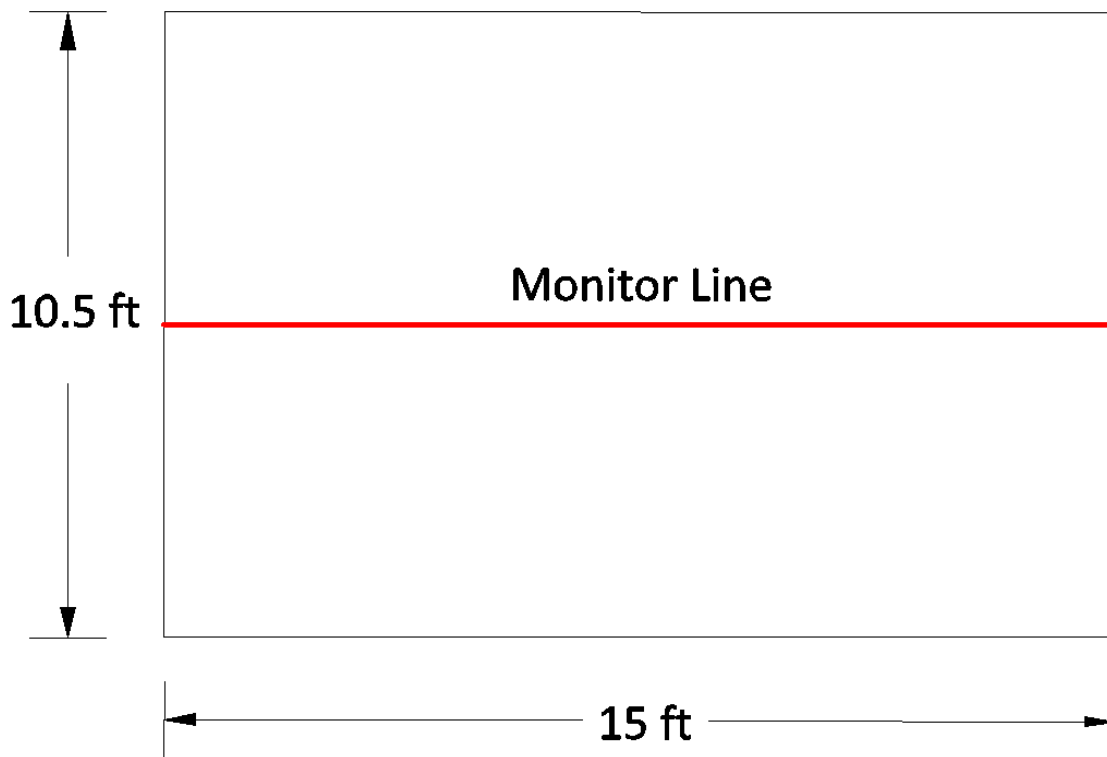
Figure 36. An example of a monitor line in a cross sectional area.
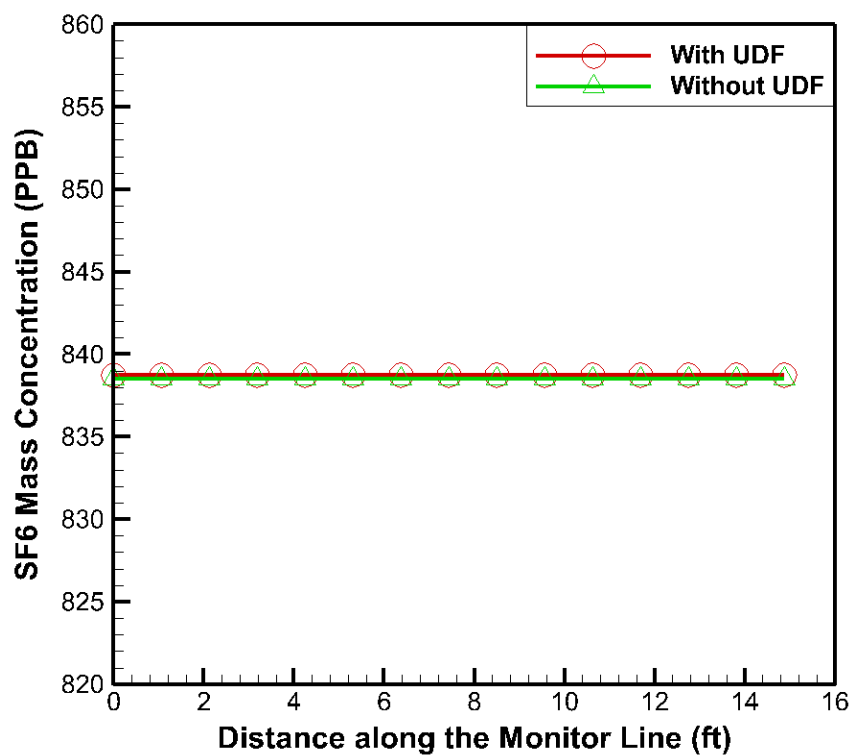
Figure 37. SF$_6$ mass concentration profile at line monitor 1.
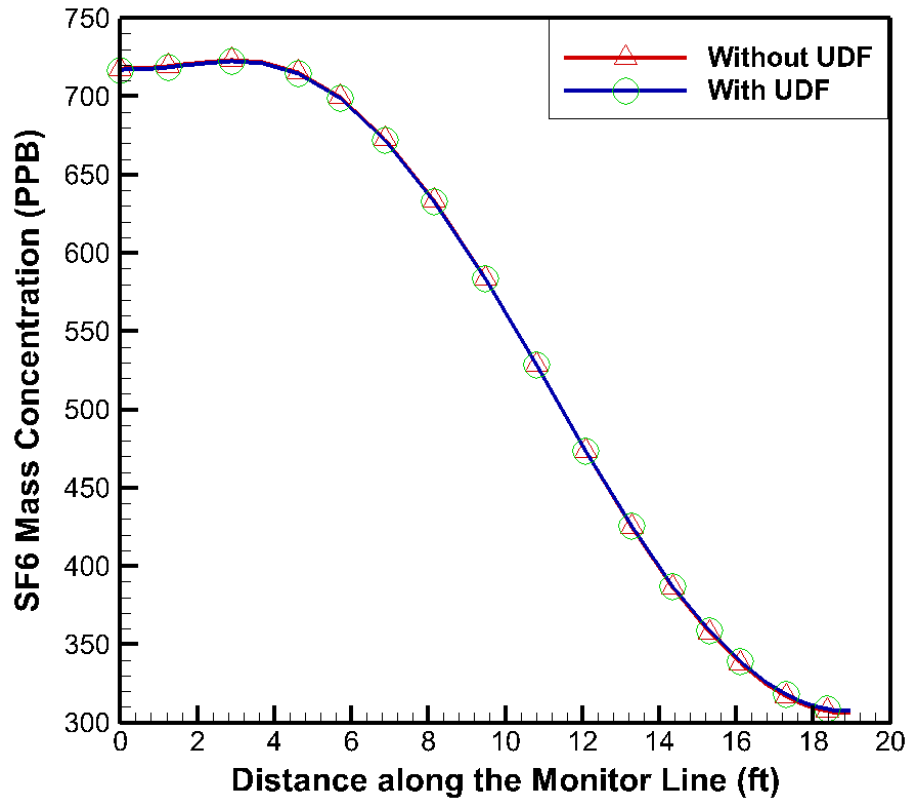
Figure 38. SF$_6$ mass concentration profile at line monitor 2.
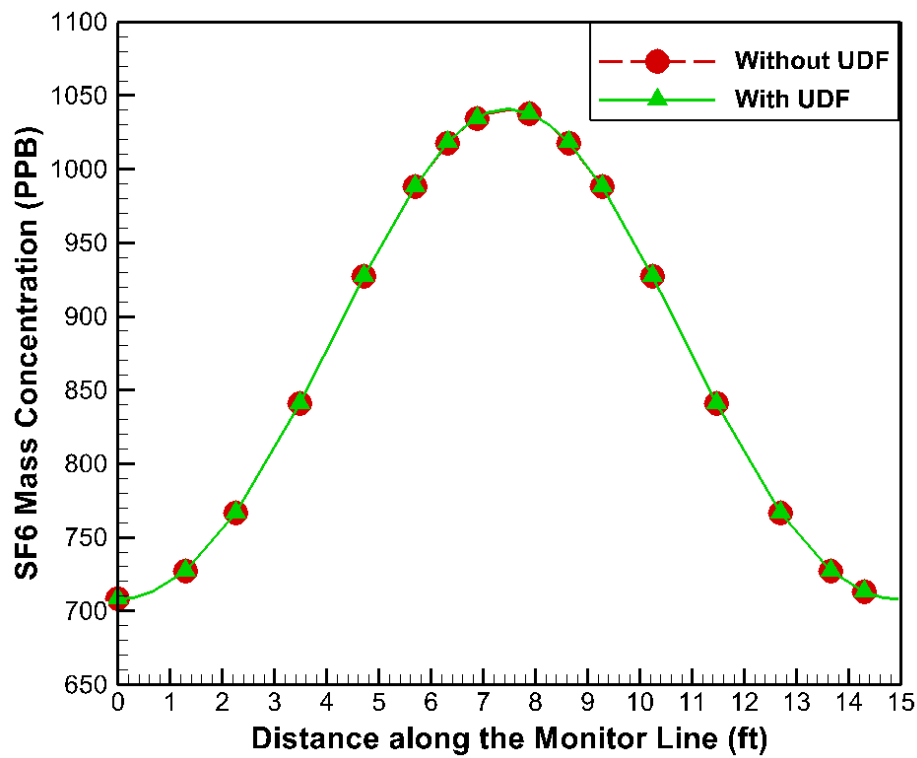
Figure 39. SF$_6$ mass concentration profile at line monitor 3.

Based on Figure 37, the SF_6 mass concentration stays the same across the monitor line 1 for both of the two cases. The reason is that the monitor line 1 is located a little bit far from the release point and no other flows can disturb the airflow at monitor line 1. Moreover, it shows the SF_6 is evenly distributed at monitor line 1 for the two cases.

From Figure 38, the SF_6 mass concentration differs across the monitor line 2 for both of the two cases. At the same time, the trend of SF_6 concentration in the two cases are the same. The SF_6 concentration is high at the beginning of the monitor line 2 and then it drops to about 305 PPB (part per billion) at the end of the monitor line. The SF_6 concentration trend at monitor line 2 can also be verified in Figure 34 and Figure 35. It is because monitor line 2 is located right after the location where all the airflows from three intakes join.

The distribution of the SF_6 mass concentration at monitor line 3 is like a normal distribution chart as shown in Figure 39. It is within expectation since the monitor line 3 is located right after the release point of SF_6. The location of monitor line 3 also explains the high SF_6 mass concentration value (about 1.05 PPM (parts per million)) in the figure. The results from Figure 39 matches the contours of SF_6 mass concentration very well from Figure 24 to Figure 27.

As a result, the turbulent diffusivity does not contribute a lot to the 3D CFD model. It may be caused by this mine geometry and other uncertainties.

4.4.6.5 Transient Simulation

The field study in this paper was completed after a six-hour experiment (Jong 2013) in the underground mine. Since research group was curious about the difference between the results from the 3D CFD model and the results from the experiment. The 3D CFD model with transient simulation was then built up to make a comparison to the experiment. Since the turbulent diffusivity does not affect the results in the steady state simulation, the 3D CFD model with transient simulation was simulated without interpreting the turbulent diffusivity.

4.4.6.5.1 Results from the 3D CFD Model

In order to better understand the SF_6 flow behavior after the airflow reached steady state in the underground, two SF_6 concentration profiles are created (by using the 3D CFD model) as shown in Figure 40 and Figure 41. The SF_6 concentration was monitored at the three outlets, four sample points, and three monitor planes over time. Locations for the outlets, sample points, and monitor planes can be found in Figure 8. The monitor plane A was a plane created right next to the release point 1. The monitor plane B was a plane created in the entry where the airflow was about to enter the working face. The monitor plane C was a plane created in the working face.
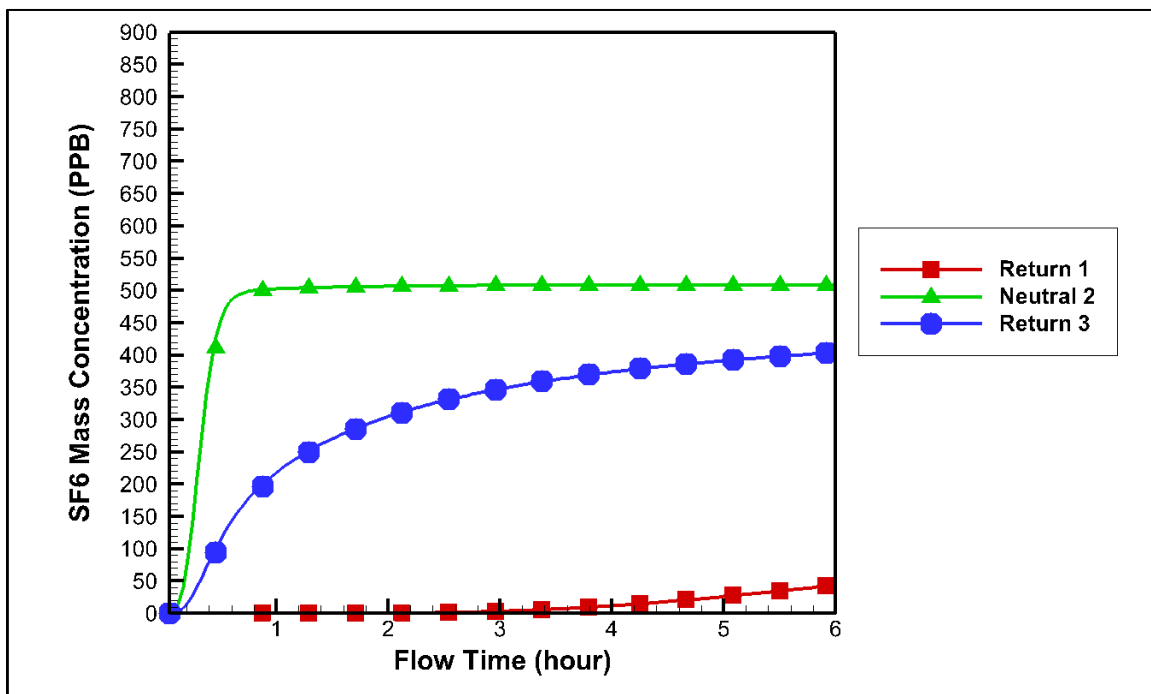
Figure 40. SF_6 mass concentration over time at the two returns and a neutral.
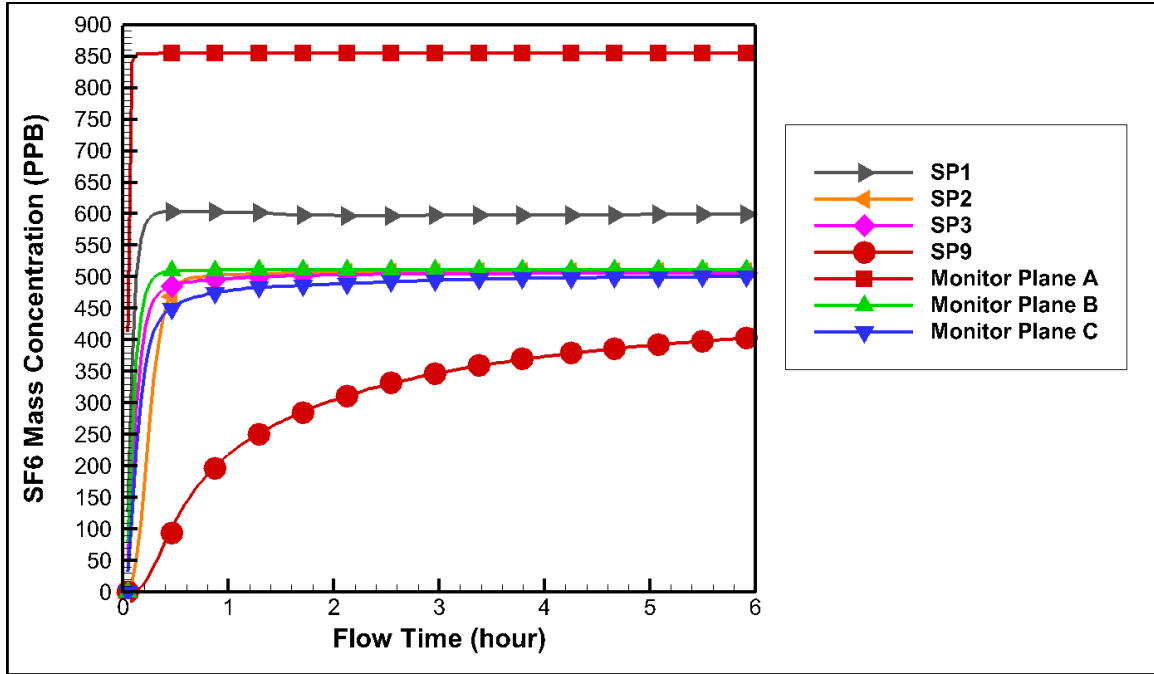
Figure 41. SF$_6$ mass concentration over time at sample points and monitor planes.

Since the model mine has a very large scale (about 4000ft in length and 1400ft in width) with a relatively small velocity magnitude (about 5.2ft/s at intake1), it takes a long time for the SF$_6$ to reach the three outlets (as shown in Figure 40), especially return 1. Since monitor plane A is very close to the release point 1, SF$_6$ flow reaches this plane very fast and a peak shows up after about five minutes (shown in Figure 41). Additionally, mass concentration of SF$_6$ in monitor plane A is about 850 PPB, which is much larger than that in other monitor planes and sample points. For the rest monitor planes and sample points, there is an increasing trend shown in each of their profiles (shown in Figure 41). SF$_6$ flow reaches steady state in about six hours. That SF$_6$ are detected proves the airflow actually follows the path from the release point 1 to the sample points.

4.4.6.5.2 Results Compared with Experimental Results

Results from the 3D CFD model were compared with the experimental results at four sample points. Locations for the sample points could be found in Figure 8 and Figure 9. An overall comparison for the results at the four sample points between the 3D CFD model and the experiment was shown in Figure 42. Results comparison at a single sample point (sample point 1, 2, 3, and 9) were shown from Figure 43 to Figure 46, respectively.
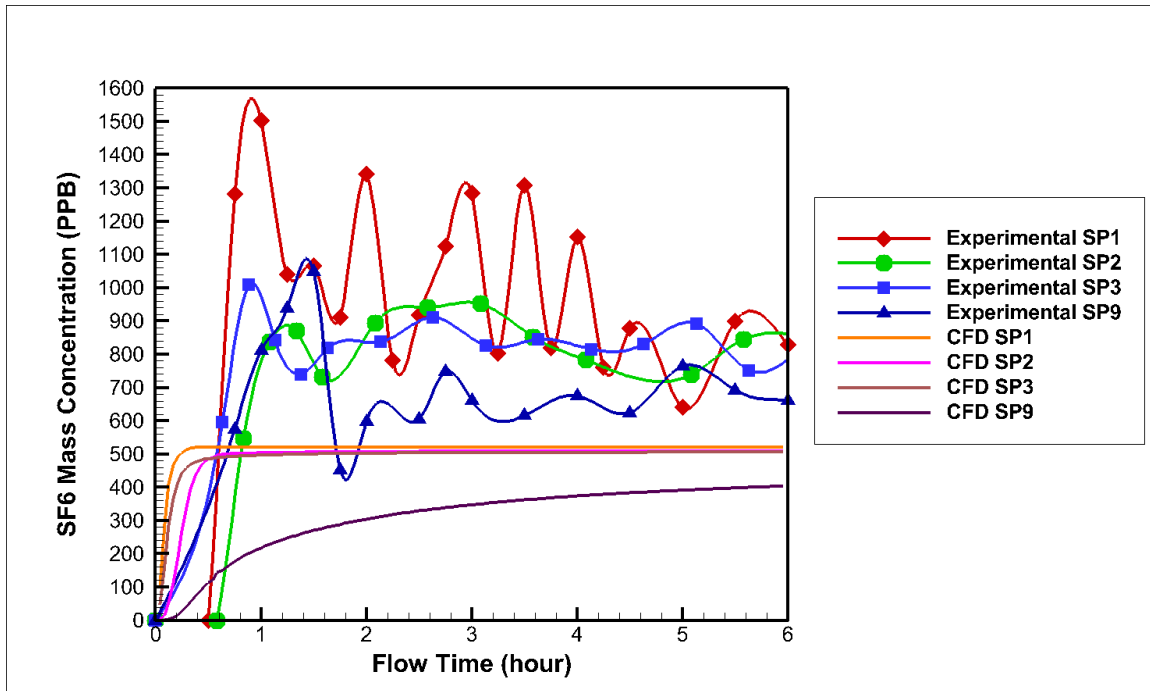
Figure 42. Comparison between CFD results and experimental results from transient simulation at four sample points.
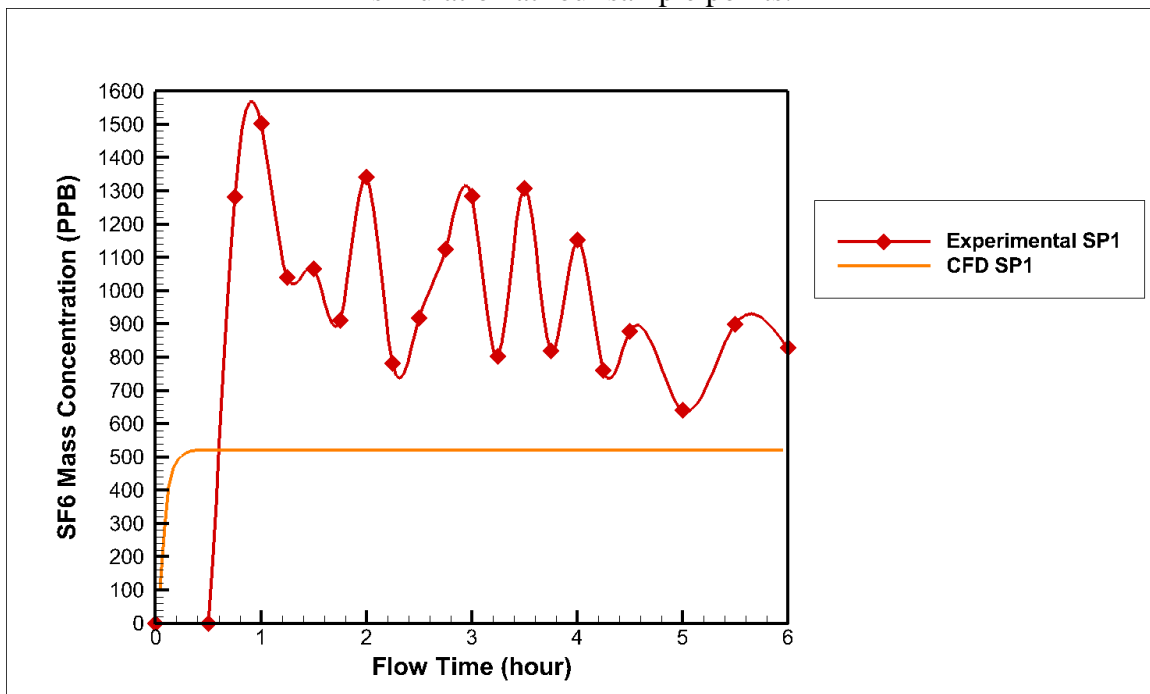
Figure 43. Comparison for transient simulation results at SP1.
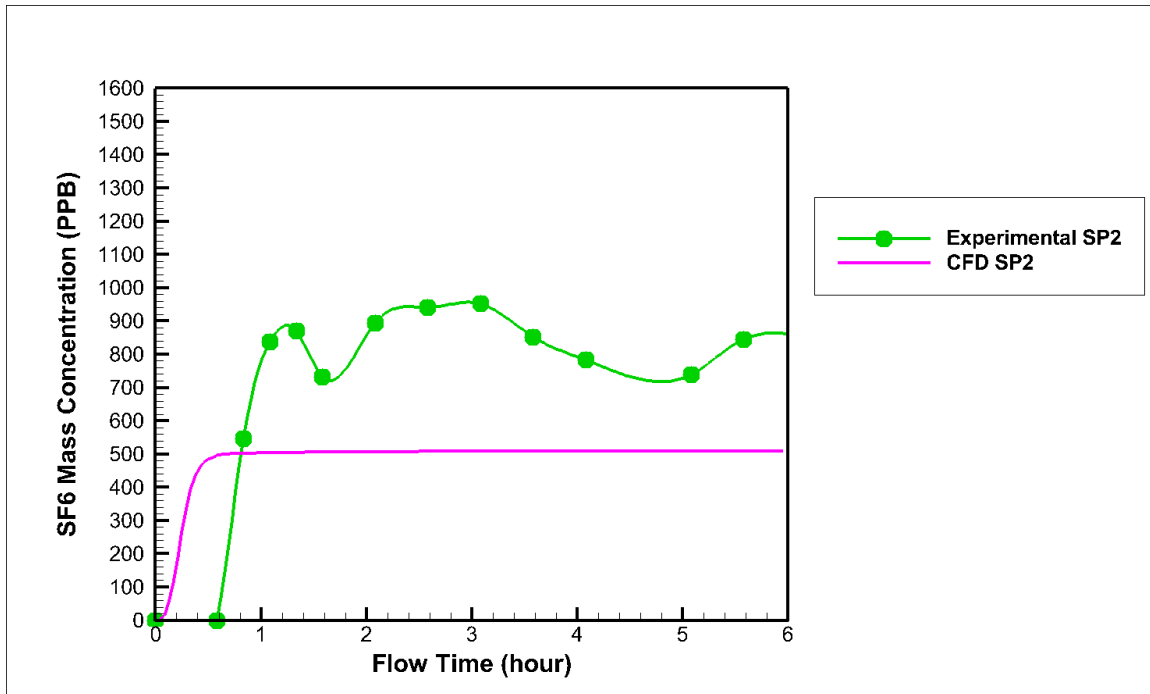
Figure 44. Comparison for transient simulation results at SP2.
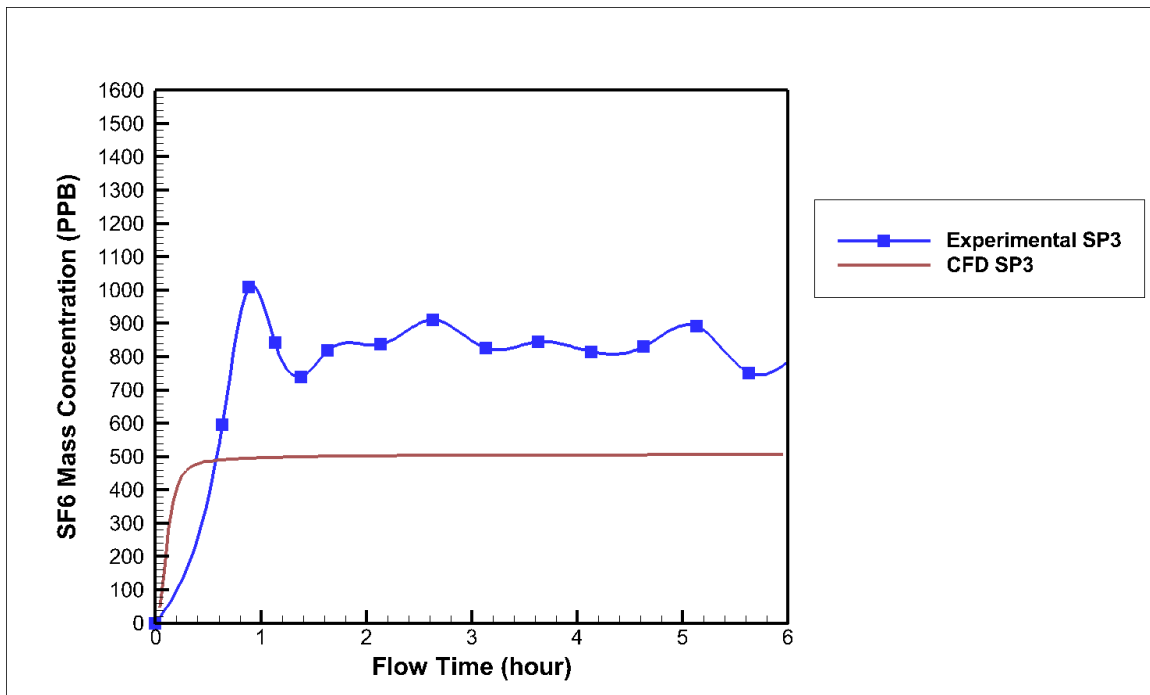
Figure 45. Comparison for transient simulation results at SP3.
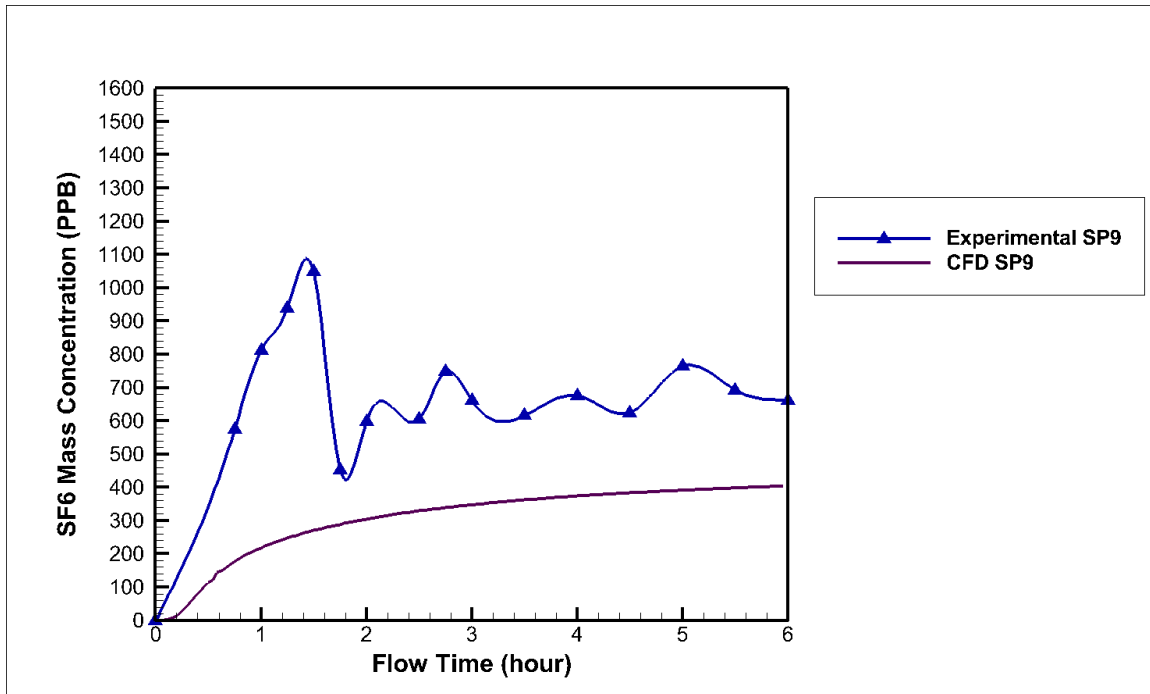
Figure 46. Comparison for transient simulation results at SP9.

According to Figure 42, it is clear that experimental results fluctuate a lot while the CFD results are more stable. In examining Figure 43, Figure 44, Figure 45, and Figure 46, results from the experiment have a higher SF_6 concentration than that from the 3D CFD model on average. SF_6 mass concentration increases at first and then it has a decreasing trend for all the four sample points in the experiment. Oppositely, it takes at most half an hour for SP1, SP2, and SP3 to reach a steady state in the CFD model. SP9 reaches its steady state at around six hours because it is farthest away from the SF_6 release point.

There are several reasons for the higher SF_6 mass concentration results in the experiment. The k-epsilon turbulence model is not perfect and does not represent turbulent flow in the model very well due to the complex mine geometry. Additionally, there were people and mining equipment (a huge chuck) moving when the experiment was conducted. However, these factors were not simulated in the model. Besides, the injection of tracer gas was not modeled exactly as what it was in the underground. In the 3D CFD mode, tracer gas acts more like a "marker" flowing with the airflow. In the injection point for the tracer gas, air passes the injection point and carries the tracer gas with it in the CFD model. But in reality, the tracer gas was released from a container held by an individual.

64

Moreover, the airflow and SF_6 flow might not be well-mixed when the sample points were taken in the experiment. Oppositely, the conditions set in the 3D CFD model are perfect and flows of air and SF_6 are mixed very well in the model.

4.5 3D CFD Model with Species Transport Model

As aforementioned, the turbulent diffusivity in the previous 3D CFD models was taken into account by interpreting the UDF into the model. However, the results from the steady-state simulations showed that there was no difference between the cases with and without turbulent diffusivity. Additionally, according to Figure 24 and Figure 25, back diffusion appeared before the release point for both the two cases with and without turbulent diffusivity. Moreover, SF_6 diffused quickly after it was released for both two cases. However, in theory, SF_6 should concentrate in the center of the duct and gradually diffuse according to Equation (4-3). In addition, results from the CFD model with turbulent diffusivity taken into account should be different from that from the model without turbulent diffusivity. The reason is that in Equation (4-4), the molecular diffusivity is three orders of magnitude smaller than turbulent diffusivity, which means the effective diffusivity of SF_6 in air depends on the turbulent diffusivity. Furthermore, the back diffusion before the release point is not understandable.

To conclude, the 3D CFD models built with and without UDF did not show the right behavior of the tracer gas in the underground. As a result, the new CFD model with species transport model was created to correctly simulate the tracer gas behavior in the underground.

4.5.1 Geometry of the Model Mine

The geometry for the 3D species transport model is shown in Figure 47. There are four intakes, two returns, one neutral, four sample points, two release points, and three monitor planes presented in the figure. An enlarged view, which is shown in Figure 48, is made to see the locations of the sample points and monitor planes more clearly.
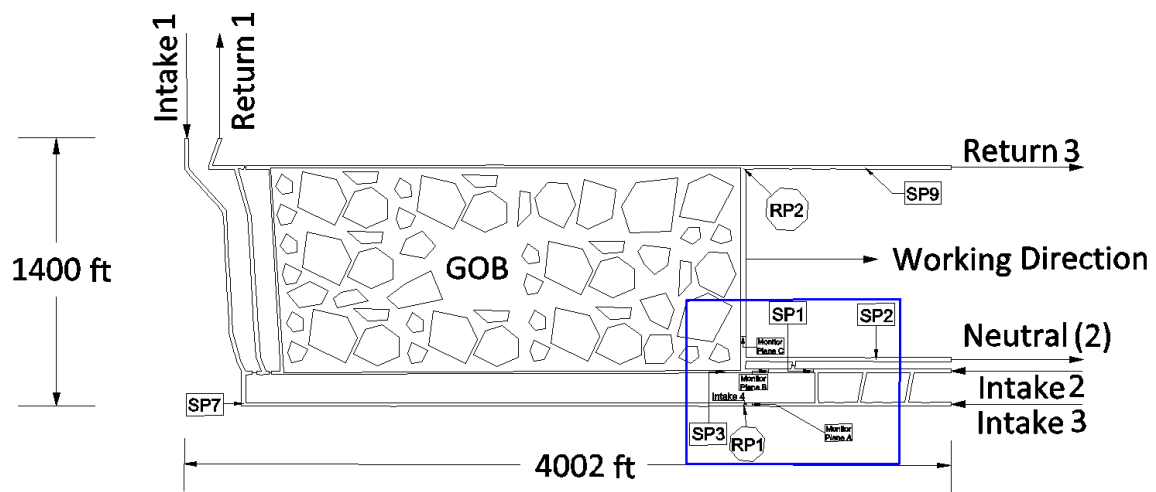
Figure 47. Plan view of the mine geometry in the species transport model.
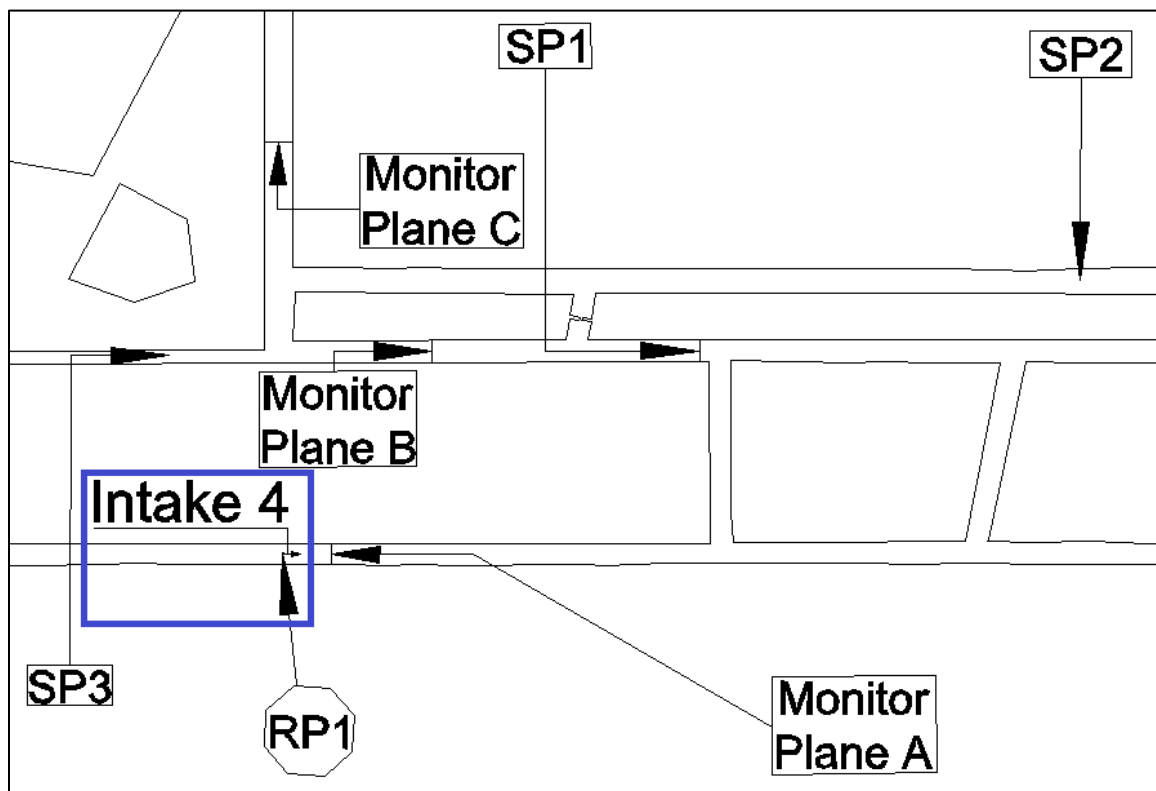
Figure 48. Locations of the monitor lines and planes in the model mine (plan view).

Figure 48 shows the locations of SP1, SP2, SP3, RP1, monitor planes, and intake 4. Since intake 4 is too small in this figure. An enlarged view is made in Figure 49 to have an idea about the location of intake 4.
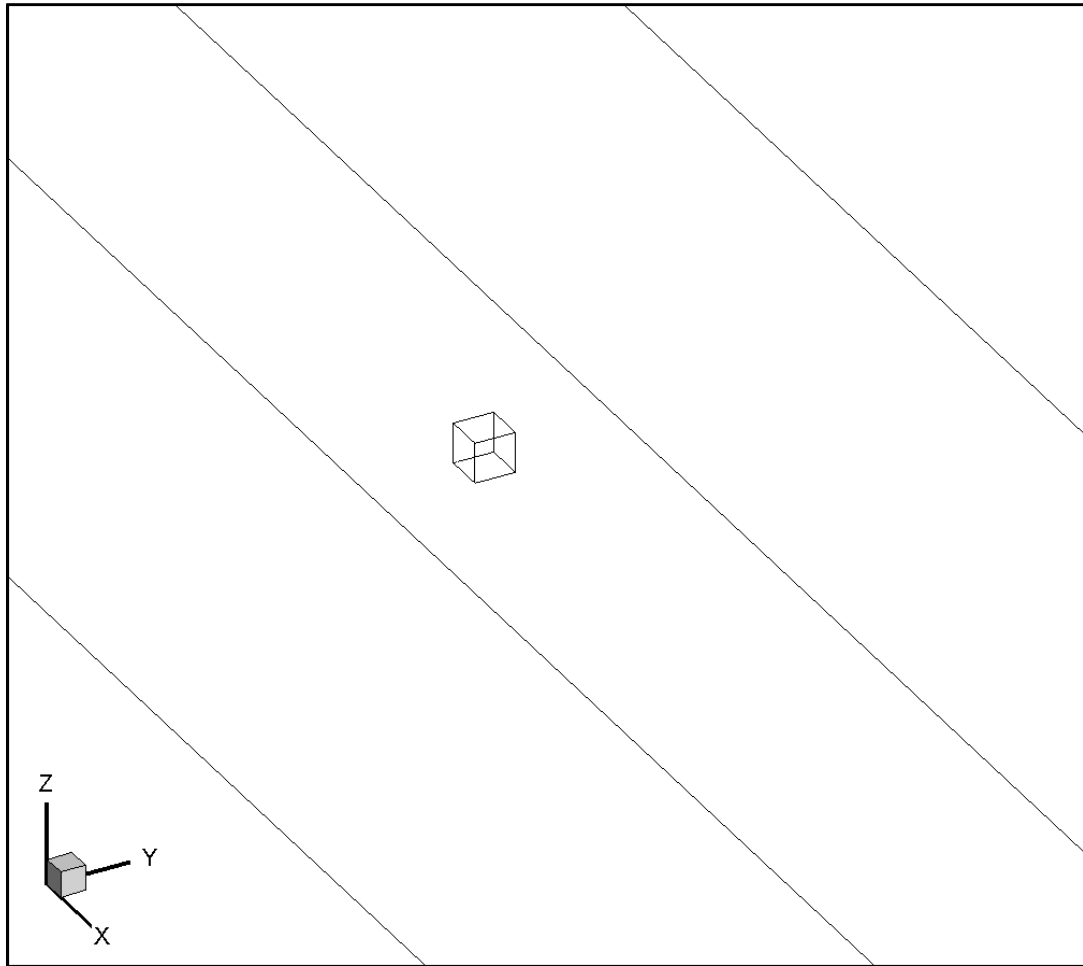
Figure 49. Enlarged view (XY plane) of the SF$_6$ release point.

4.5.2 Boundary Conditions

For 3D species transport model, airflow in the mine gob was still simulated as laminar flow (Yuan, Smith, and Brune 2006) and gob area in the model was modeled as porous media. All the outside surfaces in the model were simulated as a stationary wall.

As aforementioned, a small cube was created as the release point for the SF$_6$. Compared to the 3D CFD models (with and without interpreting UDF), boundary conditions for the six surfaces of the cube were changed in the species transport model. Location of the release point and an enlarged view (XY plane) were shown from Figure 48 to Figure 49. The surface, which is facing to the positive direction of x axis in Figure 49, was treated as

intake 4 and a mixture of air and SF_6 was released from it. In reality, only SF_6 was release from the RP1, the reason why the mixture instead of only SF_6 was released was discussed later on. The rest five surfaces of the cube were treated as stationary wall. The volume inside the cube was not treated as a flow domain so there was no flow inside the cube.

All the intakes in the model were assigned velocity-inlet boundary conditions. Two returns and a neutral in both the models were assigned outflow boundary conditions. The velocity and the airflow quantity percentage values were obtained from the field study in the underground mine. Details about the boundary conditions were shown in Table 17 and Table 18.

The mesh, which was used in the species transport model, was divided into several parts before being solved in Ansys Fluent 14.5. Interface boundary conditions were used to combining these meshes together when they were ready to be solved.

Table 17 Intake boundary conditions in the species transport model.

Airway	Mixture Velocity (ft/s)	SF_6 Mass Fraction
Intake 1	5.234	0
Intake 2	2.2998	0
Intake 3	0.784	0
Intake 4	5.5	0.0001078

Table 18 Boundary conditions for the two returns and one neutral in the species transport model.

Airway	Flow Rate Weighting
Return 1	0.0586
Neutral 2	0.2234
Return 3	0.718

As presented in Table 17, the boundary conditions for intake 1, 2, 3, return 1, 3, and neutral 2 in the species transport model were the same as that in the 3D CFD models (with and without UDF). SF_6 mass fraction in the intake 1, 2, 3 were all set to zero, which meant that no SF_6 was released from these three intakes.

The mixture velocity at intake 4 was set to 5.5 ft/s and the SF_6 mass fraction was computed as 0.0001078 according to Equation (4-9). In the experiment, only SF_6 was released from intake 4 but both air and SF_6 were released in this model. If only SF_6 was released in the model, it would take a long time for SF_6 to be carried by the airflow coming from the upstream. However, if air was released together with SF_6 from intake 4, SF_6 would get a higher velocity at the beginning due to the high mixture velocity. At the same time, SF_6 mass fraction was changed from 1 to 0.0001078 to match the experimental release rate. Then SF_6 would be able to join the main flow stream quickly. The reason why the mixture velocity was set to 5.5 ft/s was that the amount of SF_6 released from intake 4 was very small (200 SCCM, which is 4.53×10^{-5} lb/s in the experiment) and therefore, the velocity was also small compared to the average velocity across a cross-sectional area in the upstream before the release point measured as 5.6 ft/s in the model. The mixture velocity was smaller than 5.6 ft/s so the downstream flow would not be affected by the injection of the mixture. Simple calculation was claimed below to prove the injection of mixture did not change the flow behavior in the downstream very much. The volumetric flow rate measured in the upstream before the release point was 883.874 ft^3/s and the volumetric flow rate at the intake 4 was 5.5 ft^3/s. So the ratio between these two flow rates was computed as 0.00618, which meant the mixture released from the cube was negligible.

$$\varphi_{mass} = \frac{\dot{m}_{SF6_{exp}}}{\rho_{air} * V_{intake4} * A_{intake4}} \qquad (4\text{-}9)$$

where φ_{mass} represents the SF_6 mass fraction in the mixture, $\dot{m}_{SF6}$ is the mass flow rate (lb/s) of SF_6 measured in the experiment, ρ_{air} is the air density, $V_{intake4}$ is the velocity for the mixture at the release plane, $A_{intake4}$ is the area of the release plane. Since the cube volume is 1 ft^3(1ft×1ft×1ft), $A_{intake4}$ is 1 ft^2.

4.5.3 Assumptions

Several assumptions are made to save the time on establishing the model without affecting the results significantly. There is no leakage between air passages. The gravity of the air in the underground mine is neglected. Airflow in the underground is incompressible and fully turbulent.

4.5.4 Governing Equations

All the equations shown below were obtained directly from the theory guide of Ansys
Fluent (Ansys 2009a).

Species transport equations:

$$\frac{\partial}{\partial t}(\rho Y_i) + \nabla \cdot (\rho \vec{v} Y_i) = -\nabla \cdot \vec{J_i} + R_i + S_i \qquad (4\text{-}10)$$

where ρ is the mixture density, Y_i is the local mass fraction of each species (in this model,
there are two species, which are SF6 and air), $\vec{v}$ is the mixture velocity, $\vec{J_i}$ is the diffusion
flux of species i, R_i is the net rate of production of species i by chemical reaction, S_i is
the rate of creation by addition from the dispersed phase plus any user-defined sources. In
this case, both R_i and S_i equal to zero since there is no chemical reaction and user-
defined sources in the model mine.

In turbulent flows, mass diffusion is computed by using the following equation in
ANSYS Fluent:

$$\vec{J_i} = -\left(\rho D_{i,m} + \frac{\mu_t}{S_{C_t}}\right)\nabla Y_i - D_{T,i}\frac{\nabla T}{T} \qquad (4\text{-}11)$$

where ρ is the mixture density, S_{C_t} is the turbulent Schmidt number ($\frac{\mu_t}{\rho D_t}$ where μ_t is the
turbulent viscosity and D_t is the turbulent diffusivity). The default S_{C_t} is 0.7. $D_{i,m}$ is the
mass diffusion coefficient for species i in the mixture, $D_{T,i}$ is the thermal (Soret) diffusion
coefficient.

Momentum equations:

$$\frac{\partial}{\partial t}(\rho \vec{v}) + \nabla \cdot (\rho \vec{v} \vec{v}) = -\nabla p + \nabla \cdot (\bar{\bar{\tau}}) + \rho \vec{g} + \vec{F} \qquad (4\text{-}12)$$

where p is the static pressure, $\vec{v}$ is the mixture velocity, $\bar{\bar{\tau}}$ is the stress tensor, and $\rho \vec{g}$ and
$\vec{F}$ are the gravitational body force and external body forces, respectively. $\vec{F}$ also contains
other model-dependent source terms such as porous-media and user-defined sources.

The tensor stress $\bar{\bar{\tau}}$ is given by

$$\bar{\bar{\tau}} = \mu \left[(\nabla \vec{v} + \nabla \vec{v}^T) - \frac{2}{3} \nabla \cdot \vec{v} I \right] \tag{4-13}$$

where μ is the molecular viscosity, I is the unit tensor, and the second term on the right-hand side is the effect of volume dilation

Energy equation:

$$\frac{\partial}{\partial t}(\rho E) + \nabla \cdot (\vec{v}(\rho E + p)) = \nabla \cdot \left(k_{eff} \nabla T - \sum_j h_j \vec{J_j} + (\bar{\bar{\tau}}_{eff} \cdot \vec{v}) \right) + S_h \tag{4-14}$$

where k_{eff} is the effective conductivity ($k + k_t$, where k_t is the turbulent thermal conductivity, defined according to the turbulence model being used), and $\vec{J_j}$ is the diffusion flux of species j. the first three terms on the right-hand side of the equation represent energy transfer due to conduction, species diffusion, and viscous dissipation, respectively. S_h includes the heat of chemical reaction, and any other volumetric heat sources you have defined.

In Equation (4-14),

$$E = h - \frac{p}{\rho} + \frac{v^2}{2} \tag{4-15}$$

where sensible enthalpy h is the defined for ideal gases as

$$h = \sum_j Y_j h_j \tag{4-16}$$

and for incompressible flows as

$$h = \sum_j Y_j h_j + \frac{p}{\rho} \tag{4-17}$$

in equation (4-16) and (4-17), Y_j is the mass fraction of species j and

$$h_j = \int_{T_{ref}}^{T} C_{p,j} dT \tag{4-18}$$

where T_{ref} is 298.15 K.

4.5.5 Model Setup

As aforementioned, species transport model was applied to simulate both the airflow and the SF_6 flow in the underground. Obviously, the mixture species were air and SF_6. The standard k-epsilon model was also used to take care of the turbulence. For near-wall treatment, the standard wall functions were applied.

4.5.6 Mesh Independence Study

Mesh independence study was conducted to make sure the results from the species transport model were mesh independent. It also meant that the modeling results were constant with various mesh sizes. Three meshes, which were fine mesh, medium mesh, and coarse mesh, were created for this study. A comparison of nodes number for the three meshes were shown in Table 9. Plan view of the three meshes were provided in Figure 13.

4.5.6.1 Comparisons at the Monitor Points

Based on the three meshes, three species transport models were created. Transient solver was chosen to complete the simulation in six hours for all the three models. For comparison purposes, SF_6 mass concentration were monitored at SP1, SP2, SP3, and SP9, respectively, in the three models. Monitor points were created in the center of the planes where the sample points are located. An example of the monitor point location was shown in Figure 50. Results for the sample points were shown from Figure 51 to Figure 54.
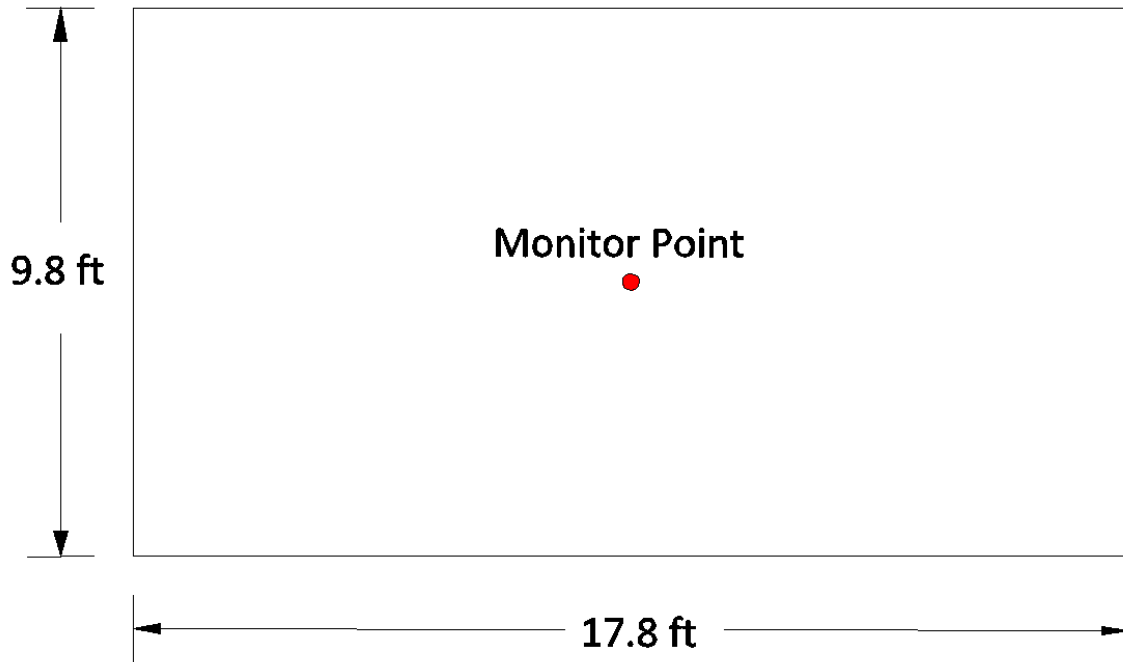
Figure 50. Location of the monitor point in return 3 in the model mine.
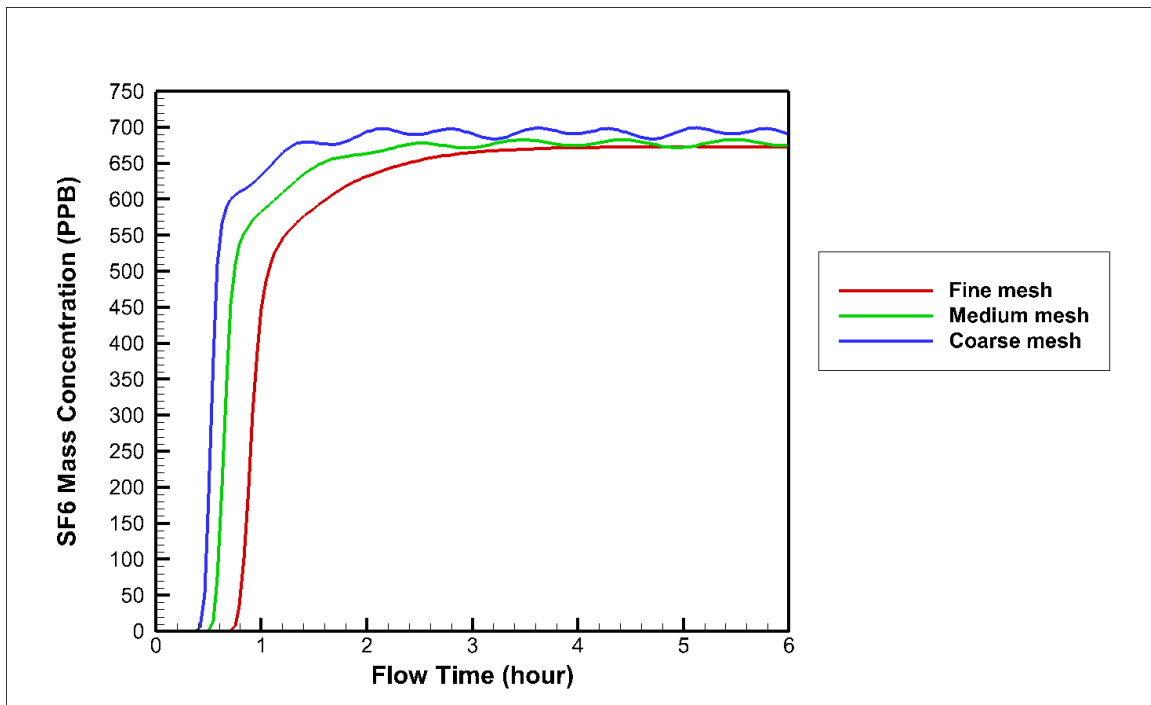
Figure 51. SF$_6$ mass concentration over time at SP1 for the three meshes.

From Figure 51, it is obvious that the red curve, which represents the results from the fine mesh, is the most stable one among the three curves. SF$_6$ mass concentration fluctuates

with time for the medium mesh and coarse mesh models. However, the final SF_6 mass concentration after the six-hour simulation is nearly the same for the three models. The range of the final SF_6 mass concentration is from 650 PPB to 700 PPB, which is not a big difference in terms of the small unit (PPB).
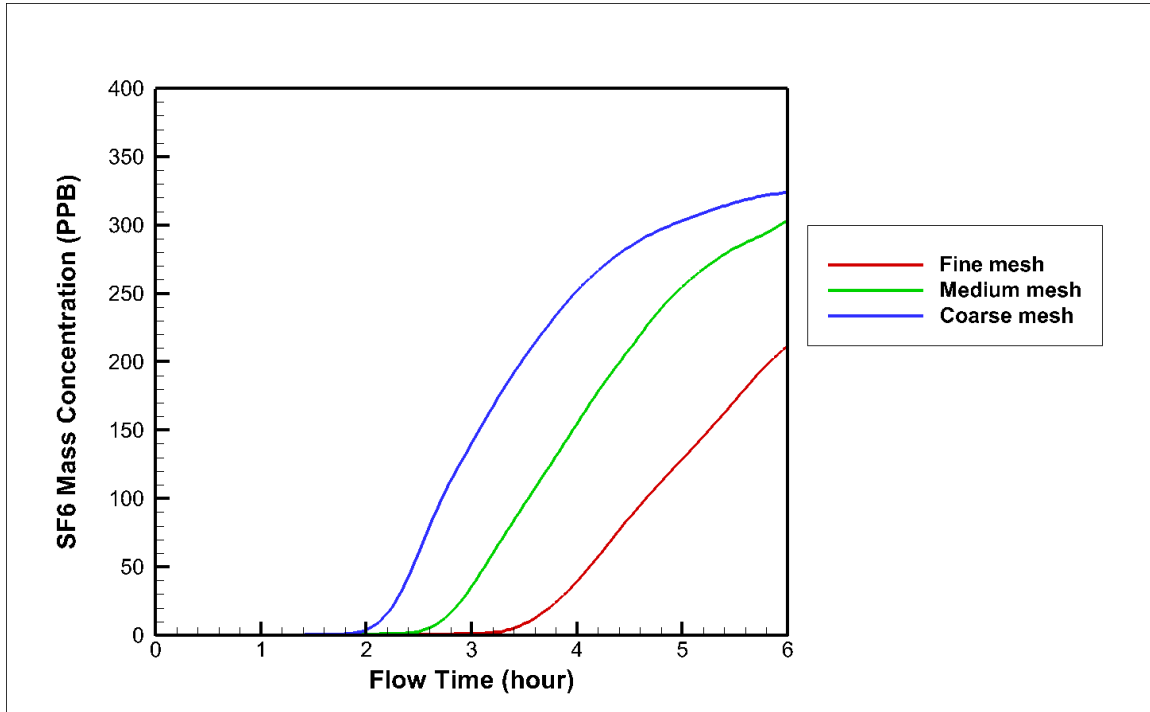
Figure 52. SF_6 mass concentration over time at SP2 for the three meshes.

In Figure 52, the three curves represent the results from the three meshes, respectively. SF_6 mass concentration at SP2 almost reach a stable level (about 320 PPB) after six hours in the medium and coarse mesh models. The SF_6 concentration still has an increasing trend after six-hour simulation in the fine mesh model. However, the final SF_6 mass concentration in the fine mesh model was also 320 PPB in the ten-hour simulation as shown in Figure 93. The reason why the three curves have not reached a stable level is that SP2 is further away from the release point compared to SP1 and it takes longer for SF_6 to reach SP2.
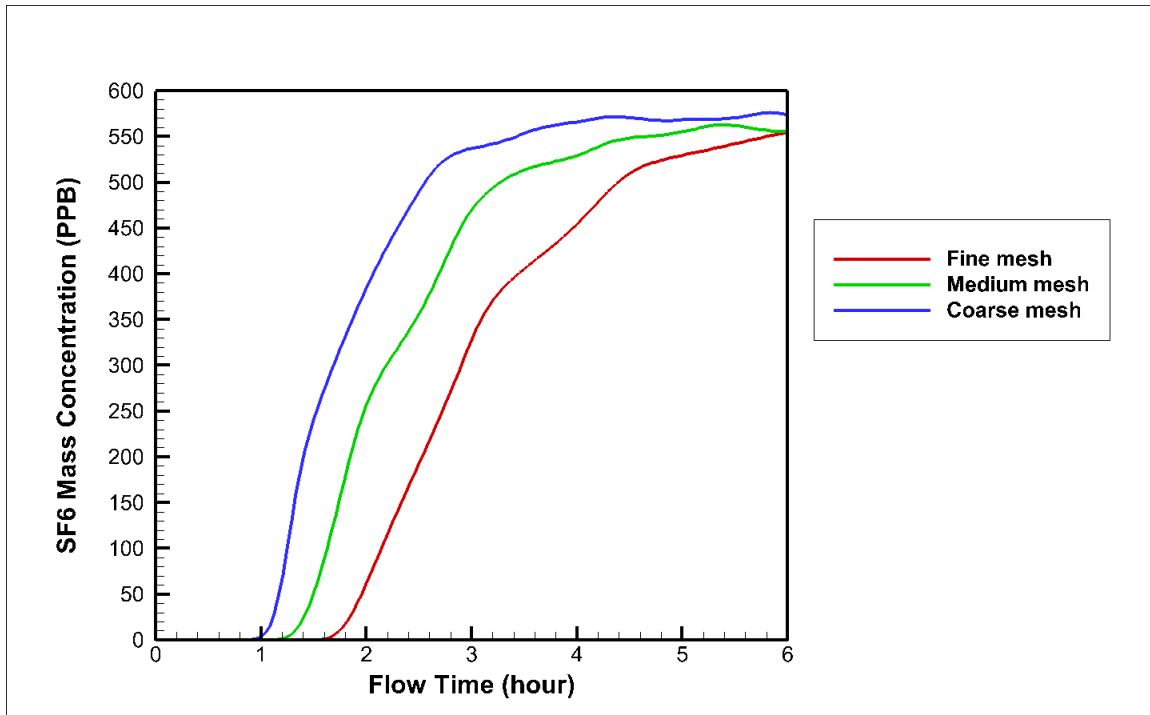
Figure 53. SF$_6$ mass concentration over time at SP3 for the three meshes.

It is clear that SF$_6$ mass concentration at SP3 reaches a relatively stable level after the six-hour simulation in the three models. The final SF$_6$ mass concentration is around 550 PPB for the three models.
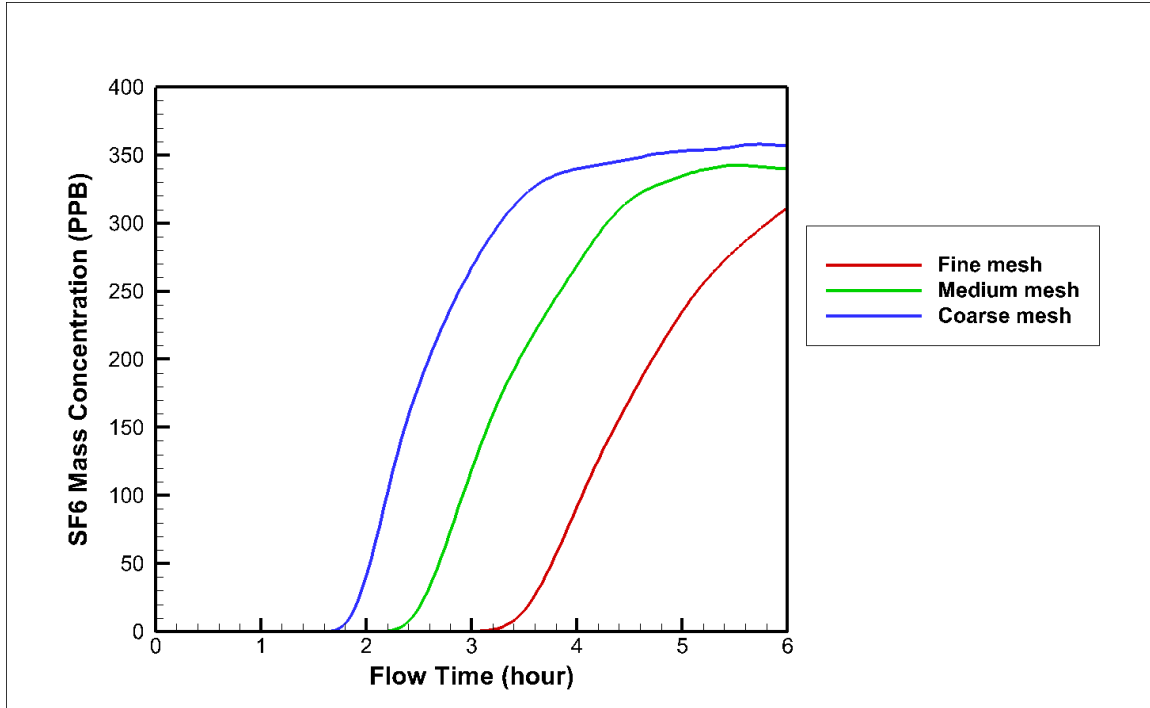
Figure 54. SF$_6$ mass concentration over time at SP9 for the three meshes.

As shown in Figure 54, SF$_6$ mass concentration reaches a stable level (around 350 PPB) in the medium and coarse mesh models after the six-hour simulation. It has an increasing trend in the fine mesh model after the six-hour simulation. However, the final mass concentration was also 350 PPB for the fine mesh model as shown in the ten-hour simulation in Figure 99.

4.5.6.2 Comparisons at the Monitor Lines

Monitor lines were also created in the planes where the four sample points are located. An example of the monitor line location was shown in Figure 55. Comparisons between the three models were shown from Figure 56 to Figure 57. Data used in the figures were obtained at the end of the six-hour transient simulation.
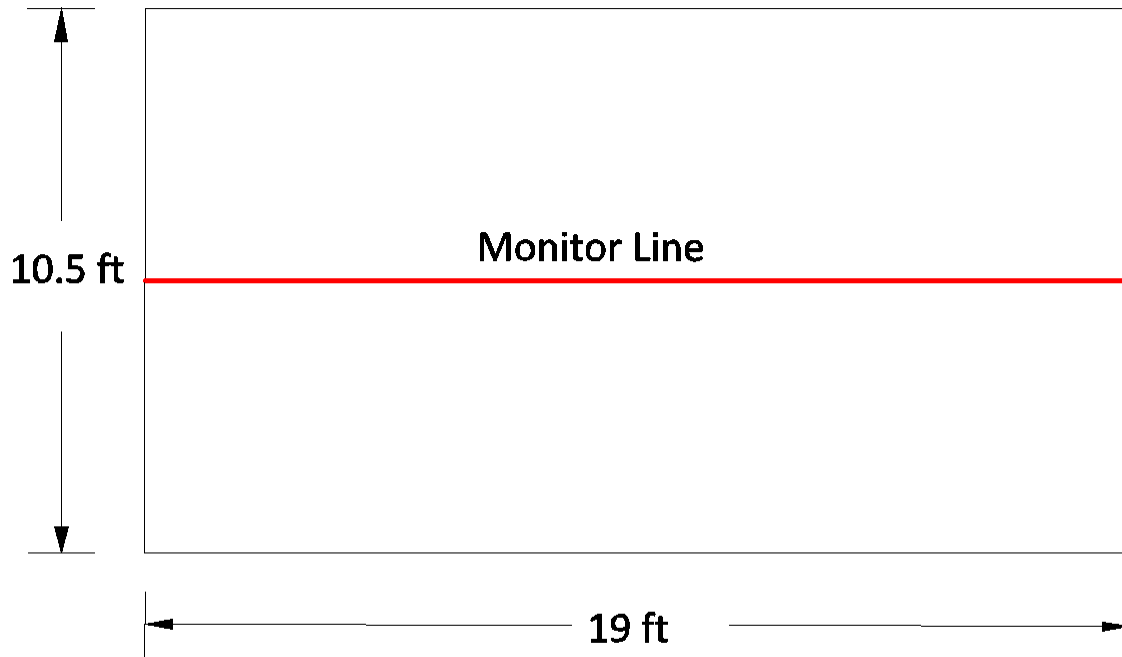
Figure 55. Location of the monitor line in the plane where SP1 is located in the model mine.

Both SF$_6$ mass concentration and velocity magnitude data were collected at the monitor lines in the three models.
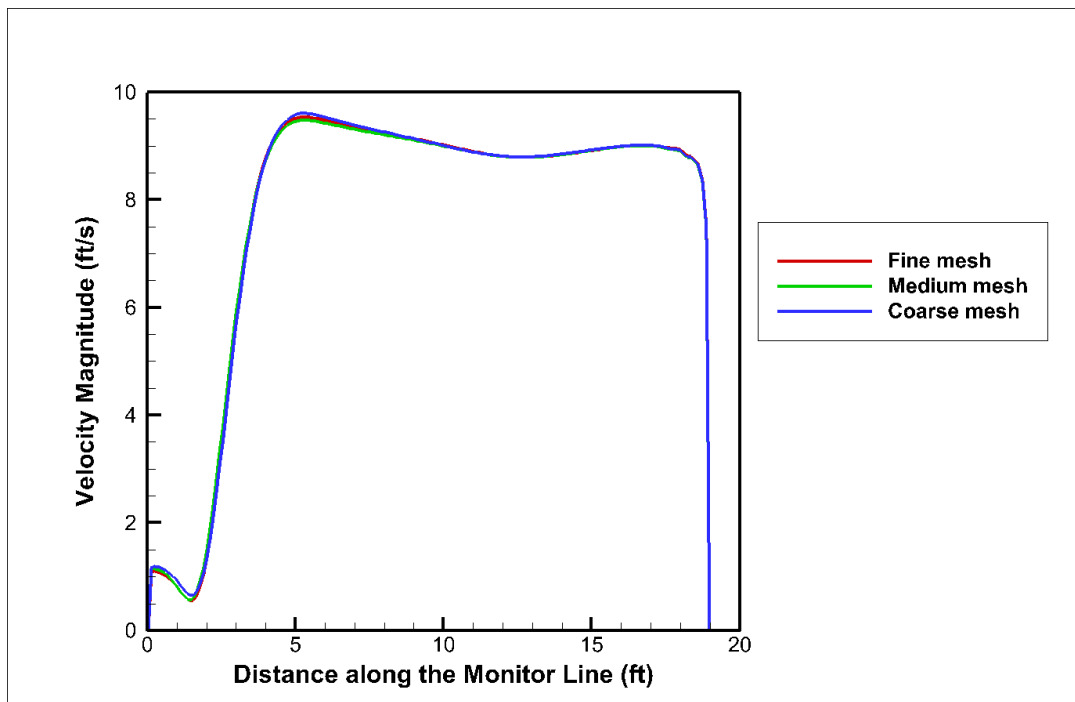
Figure 56. Velocity profile at the monitor line where SP1 is located.

From Figure 56, the three lines in the figure almost coincide with each other, which means the velocity magnitude from the three models are the same across the monitor line in the plane where SP1 is located.

According to Figure 57, not only are the velocity magnitude profiles the same for the three models, but also SF$_6$ mass concentration are the same across the monitor line in the plane where SP1 is located.
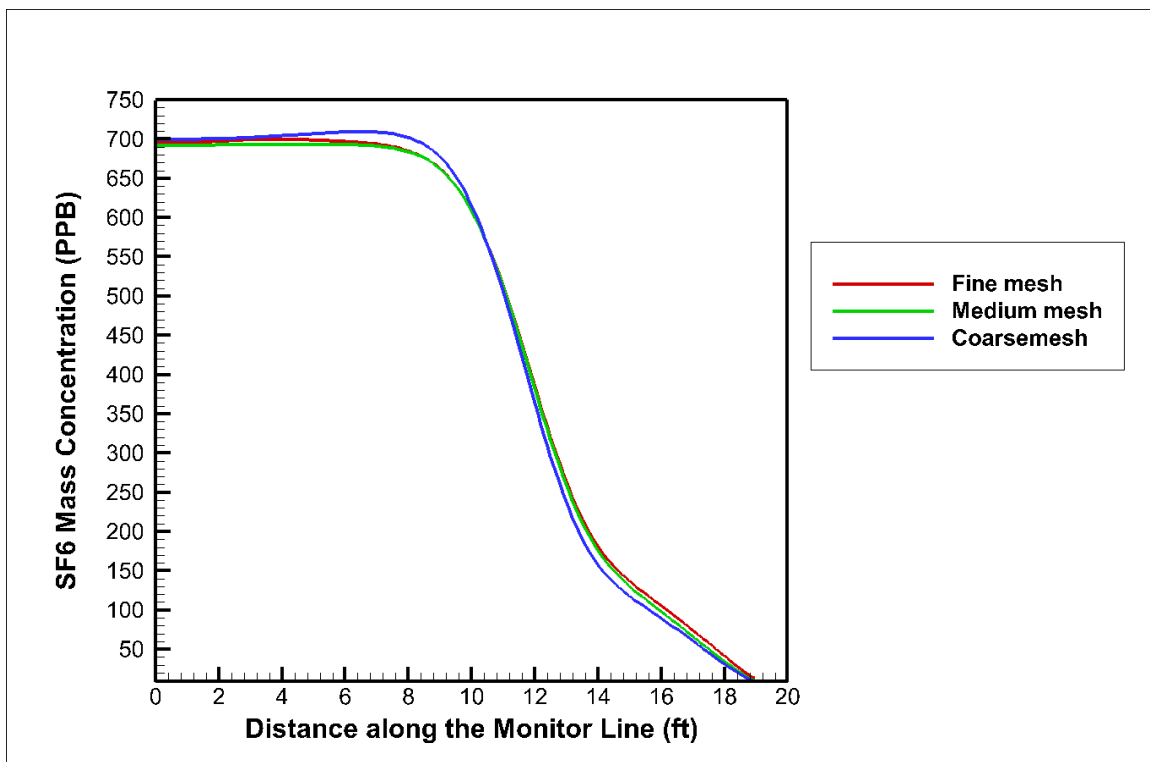
Figure 57. SF$_6$ mass concentration profile at SP1.

More comparisons of the results at monitor lines can be found in the Appendix.

As a result, the results from the model is independent from the mesh sizes. Since it is not that computational expense with the fine mesh in the species transport models, results from the fine mesh model were chosen to be compared with that from the experiment.

Additionally, the following simulations, which were steady-state simulation and transient simulation, were performed in the fine mesh model.

4.5.7 Steady-State Simulation

The purpose for the steady-state simulation is to have an overall idea about the final SF_6 flow and airflow status in the steady state flow domain. There were two steps to finish the steady-state simulation. The first step was to let the species transport model run on a steady solver to let the airflow reach its steady state. Boundary condition for intake 4 was assigned as wall and no mixture was released in the steady state simulation. The second step was to continue running the model on the steady solver and begin to release the mixture from the intake 4. Boundary condition for intake 4 was changed to velocity inlet in the second step. Convergence criteria was set to 10^{-3} in both the steps. It took 6900 iterations for the airflow in the first step of the steady-state simulation to get converged. Results at the monitor points and planes were recorded right after the first step. After 16000 iterations of calculation in the model, SF_6 mass concentration at the monitor points and planes reached their stable levels except return 1. Then the CFD model was kept running to 36560 iterations when the SF_6 mass concentration reached a stable level. Contours shown below were created at 16000 iterations. Contours and figures created at 36560 iterations would be specifically mentioned if they were shown below. A monitor point was created for each sample point in the center of the plane where the sample point was located. An example for the location of a monitor point was shown in Figure 50. Results from the steady state simulation were shown in Table 19.

4.5.7.1 Results Comparisons

Table 19. Results from the steady state simulation in the species transport model.

Sample points	Air quantity (kcfm)	SF$_6$ (cfm)	SF$_6$ (kcfm)	CFD Results Air (kcfm)	CFD Results SF$_6$ (kcfm)	Air Error (%)	SF$_6$ Error (%)
1	81.00	0.0129	1.29×10^{-5}	87.04	1.15×10^{-5}	7.45	10.49
2	19.60	0.0033	3.30×10^{-6}	19.68	1.31×10^{-6}	0.40	60.33
3	17.00	0.0028	2.80×10^{-6}	11.50	1.28×10^{-6}	32.35	54.42
7	53.74			53.04		1.31	
9	63.00	0.0089	8.90×10^{-6}	64.05	5.31×10^{-6}	1.67	40.28
RP1	53.60	0.0088	8.80×10^{-6}	53.04	7.05×10^{-6}	1.05	19.93

In Table 19, the first four columns are the data obtained from the experiment. Column five and six represent the CFD results of airflow quantity and SF$_6$ flow quantity, respectively. The SF$_6$ flow quantity was computed based on the SF$_6$ mass concentration in the center of the cross-sectional area instead of the area-weighted concentration across the area. The last two columns show the CFD errors of airflow quantity and SF$_6$ flow quantity, respectively. The errors are calculated based on Equation (3-3). Figure 58 and Figure 63 were made according to Table 19 to show the comparisons more straightforwardly.

In Figure 16, there was no SF$_6$ data at SP7 for both experiment and CFD. The reason was that SP7 was located far away from RP1 in the upstream and there was no SF$_6$ detected in the field study. Obviously, there was also no SF$_6$ found at SP7 in the CFD model.

Both air and SF$_6$ data were monitored at RP1 to make sure what was released in the CFD model matched that in the experiment. Results at RP1 in the model actually came from the results at monitor plane A. The reason why the results at intake 4 were not used as the results at RP1 was that the airflow quantity at intake 4 could not represent the airflow quantity across the entry in the model mine. In addition, the airflow quantity at RP1, which was shown in the second column in Table 19, was measured across the entry in the experiment.
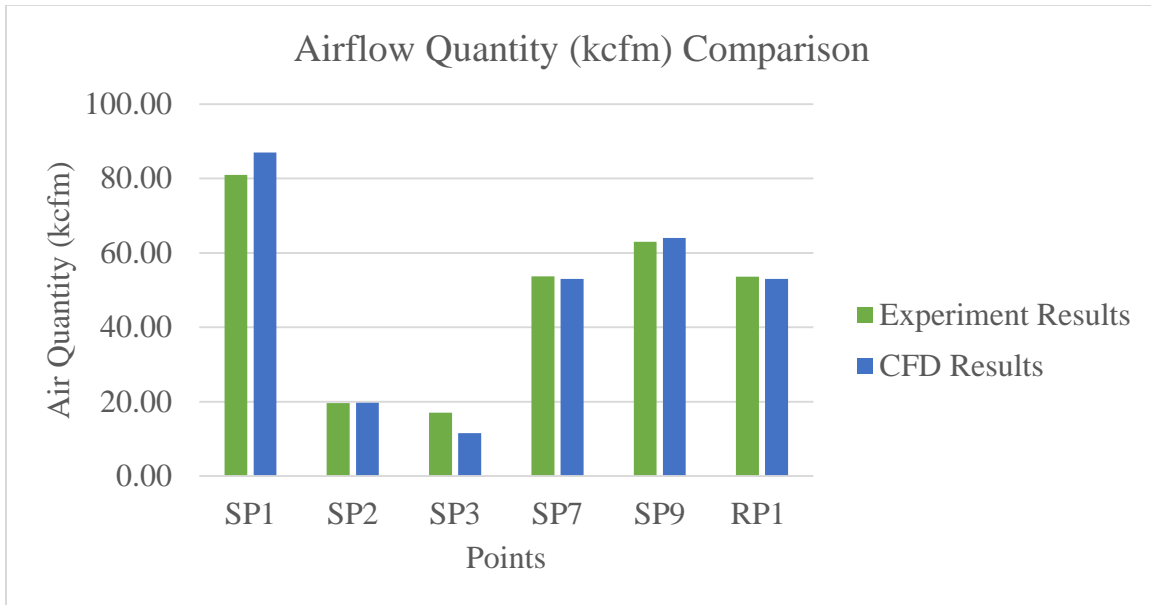
Figure 58. Airflow quantity (kcfm) comparison.

As aforementioned, in the species transport model, a mixture of air and SF_6 were released from intake 4. However, since the SF_6 mass fraction is only 0.0001078 in the mixture, the following mixture velocity magnitude contours were treated as airflow velocity magnitude contours to make the comparisons between the experiment and CFD model more clearly.

It is clear that the airflow quantity at SP3 has the largest error, which is 32.35%, among all the sample points. There are several reasons for this error. Firstly, SP3 is located right next to the gob. It is very hard for the personnel to get access to and get the experimental data. Secondly, the CFD model does not simulate everything in the underground. For instance, there are people and machine moving around SP3 but CFD model does not simulate it. Thirdly, the experiment itself is not accurate at SP3. There are falling rocks at SP3 and it creates problems for the personnel to collect data. Finally, airflow at SP3 is complex and the velocity contours at SP3 can be found in Figure 59 and Figure 60.
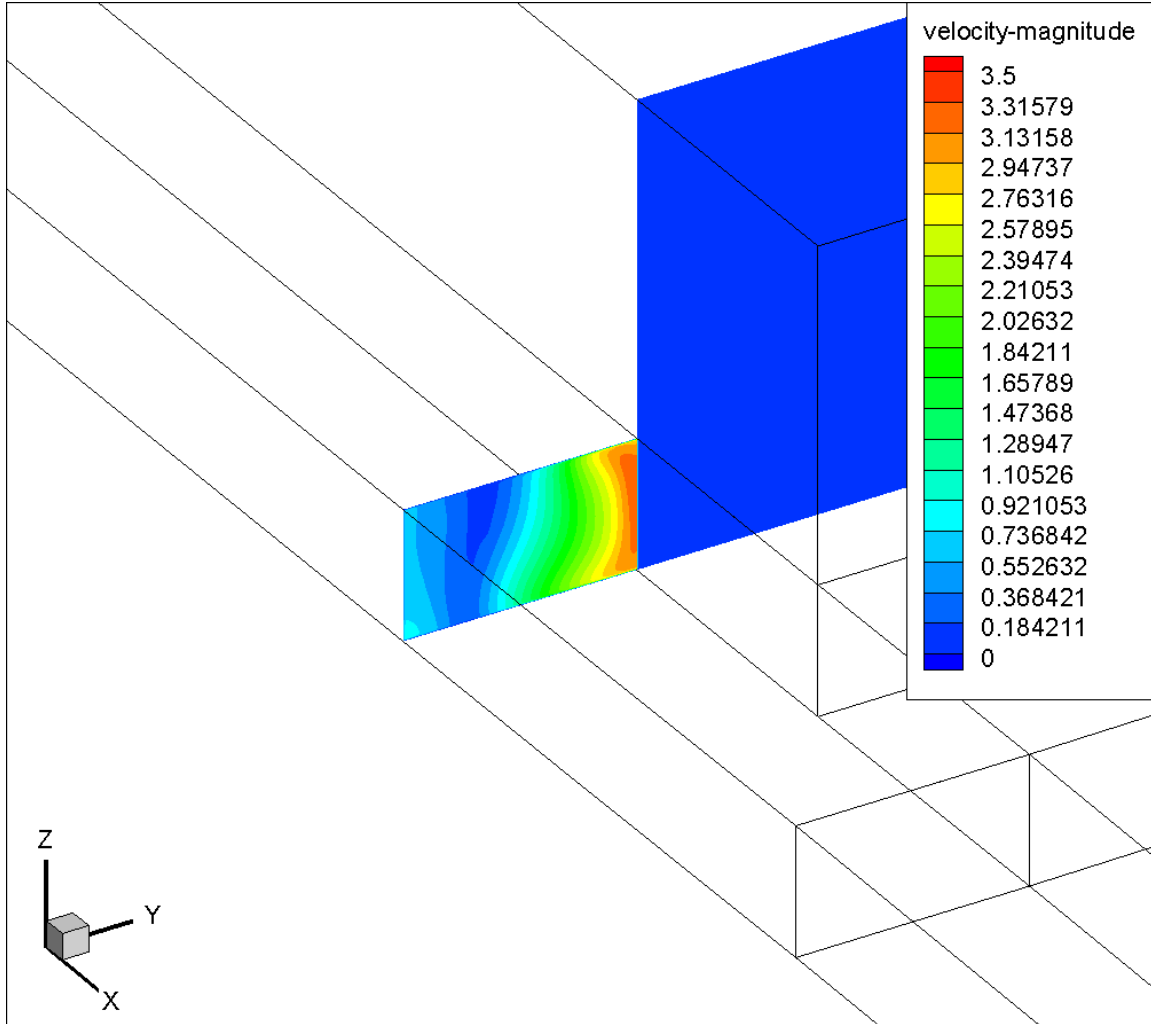
Figure 59. Contour (YZ plane) of velocity magnitude (ft/s) at SP3 in the CFD model.

Figure 59 shows the velocity contour in YZ plane at SP3. It is obvious that the airflow velocity is not evenly distributed in the cross-sectional area. The velocity magnitude ranges from 0 to 3.36 ft/s. Since the area of the plane where SP3 is located was measured as 198.4 ft^2 in the field study, the velocity magnitude at SP3 in the experiment, which is computed by dividing the volumetric flow rate (17 kcfm) by area, then becomes 1.43 ft/s. The experimental result, which is 1.43 ft/s, is actually within the range obtained from the CFD model. Another velocity contour (in XY plane) is shown in Figure 60 to have a better idea about the complexity of the airflow behavior at around the SP3.
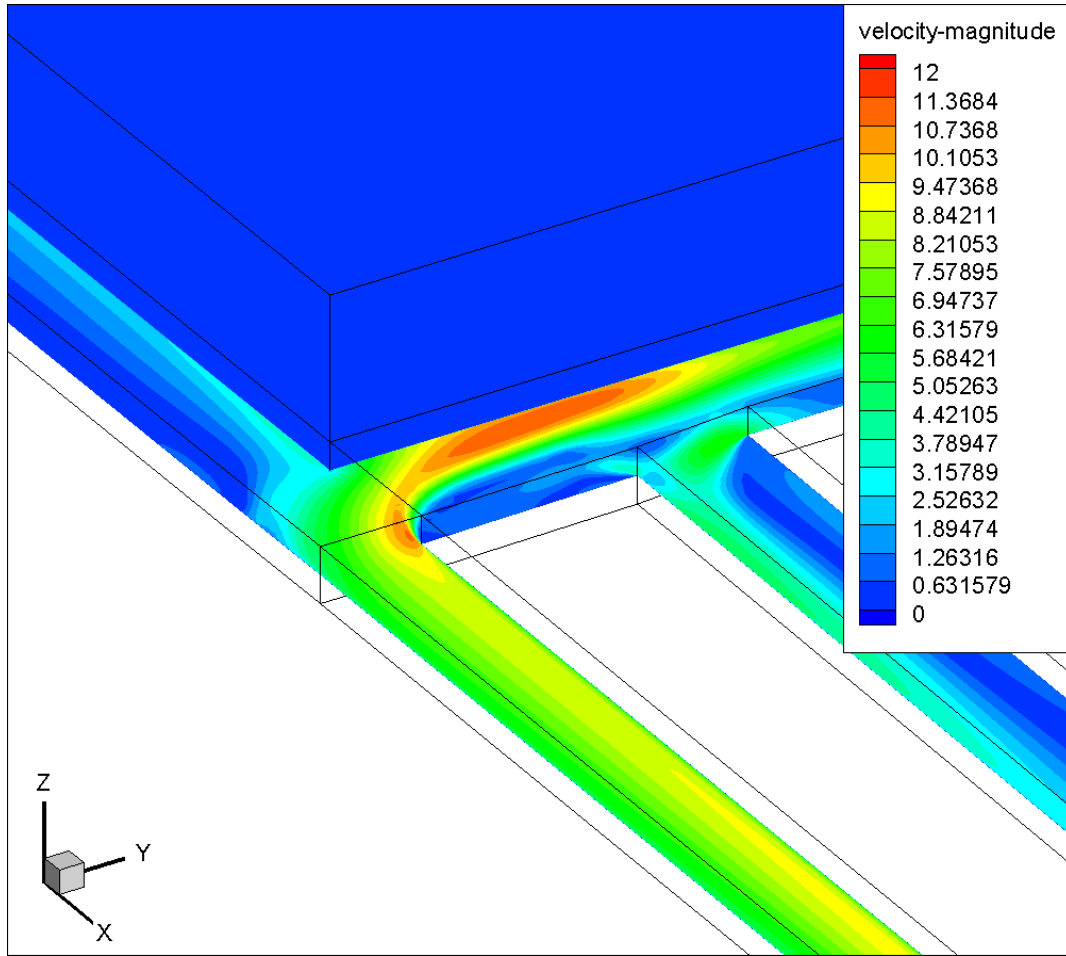
Figure 60. Contour (XY plane) of velocity magnitude (ft/s) at SP3 in the CFD model.

From Figure 58, airflow quantity at SP1 simulated in the CFD is a little bit higher than that measured in the experiment. The airflow magnitude contour in the cross-sectional area where SP1 was located is shown Figure 61 and Figure 62. It is clear that velocity is also not evenly distributed in the cross-sectional area as shown in Figure 61. The range of velocity magnitude is from 0 to about 10 ft/s. Since the area of the plane where SP1 is located was measured as 187.7 ft^2 in the field study, the velocity magnitude at SP1 in the experiment, which is computed by dividing the volumetric flow rate (81 kcfm) by area, then becomes 7.19 ft/s. The experimental result, which is 7.19 ft/s, is actually within the range obtained from the CFD model. Another velocity contour (in XY plane) is shown in Figure 62 to have a better idea about the complexity of the airflow behavior at around the SP1.

Figure 61. Contour (YZ plane) of velocity magnitude (ft/s) at SP1 in the CFD model.
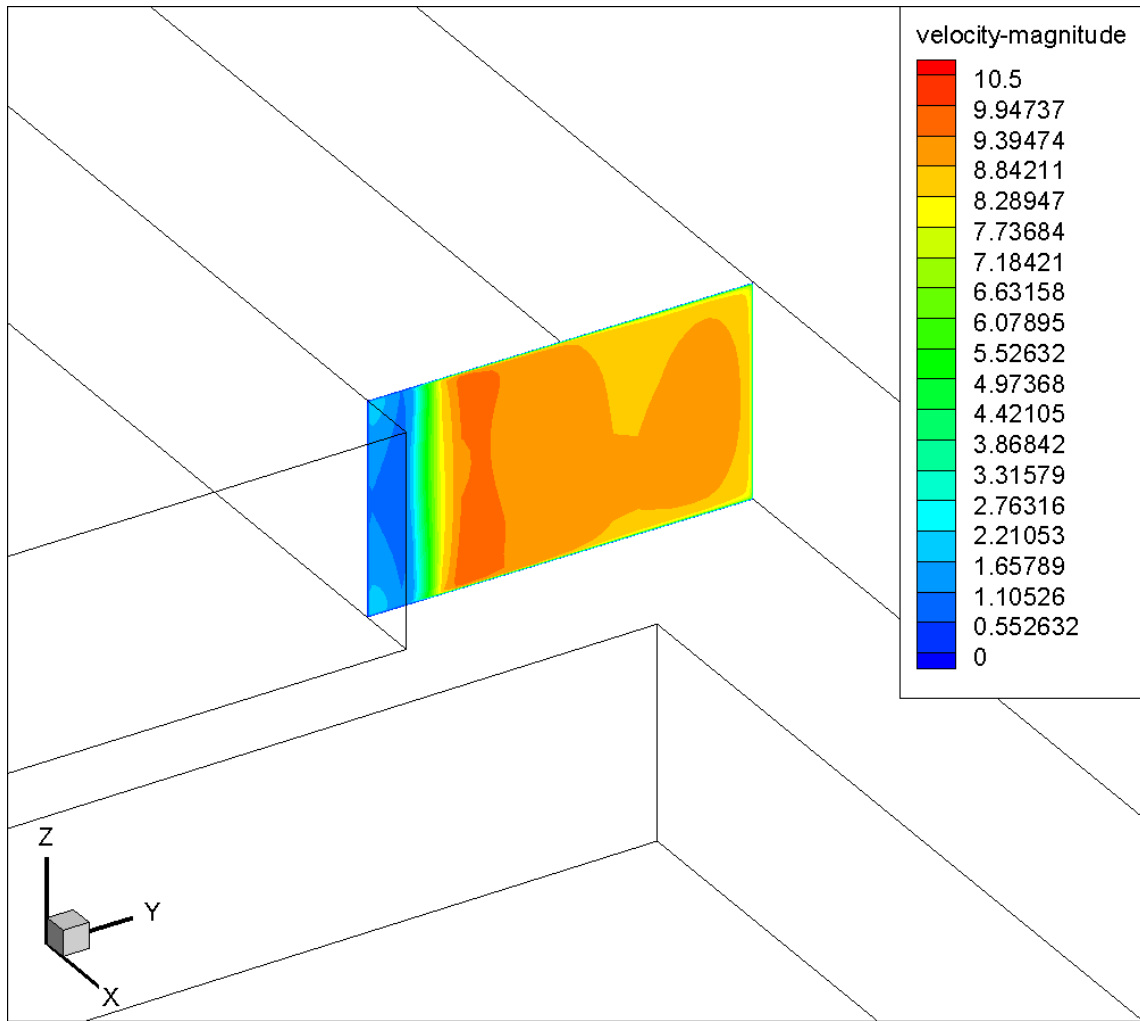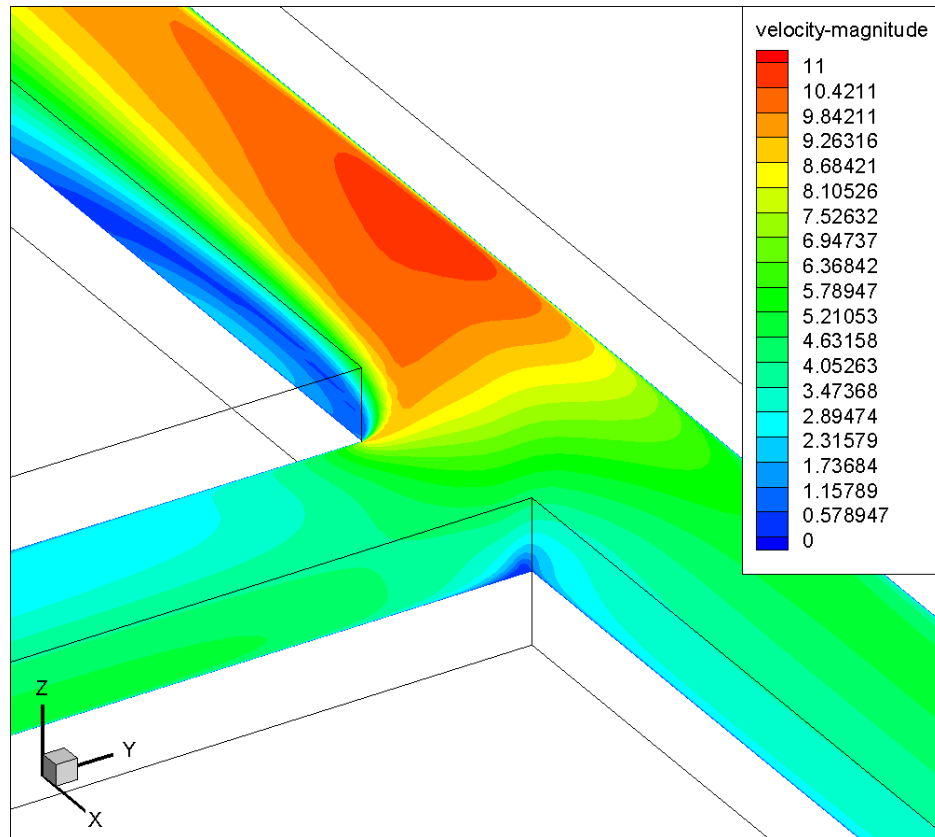
Figure 62. Contour (XY plane) of velocity magnitude (ft/s) at SP1 in the CFD model.

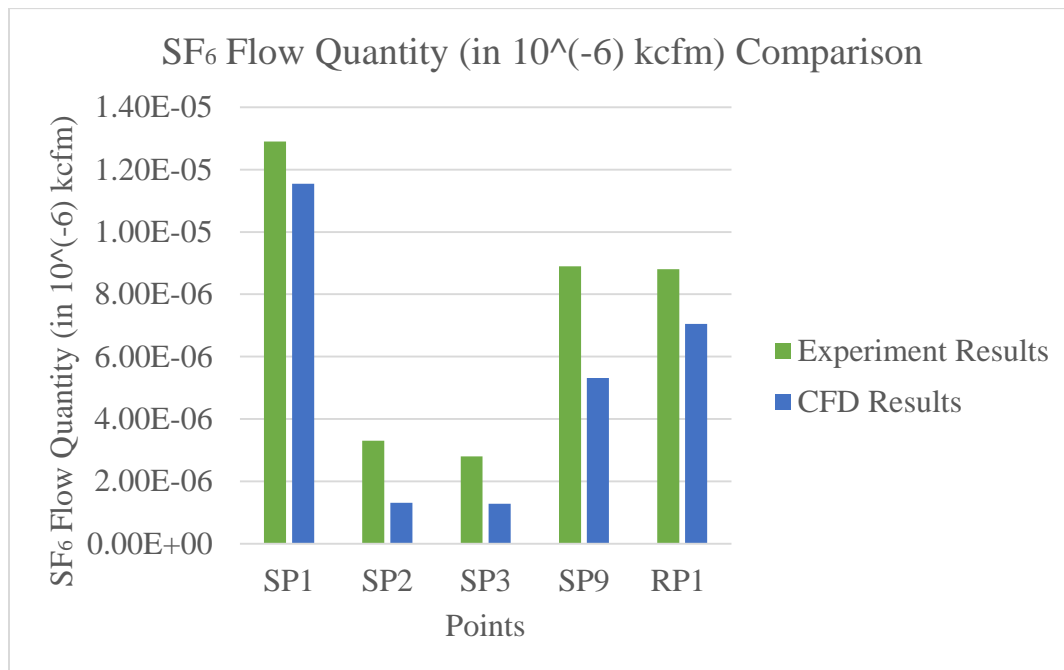Analysis on Figure 58 is completed at this point and Figure 63 is the next focus.

Figure 63. SF_6 flow quantity (kcfm) comparison.

In Figure 63, the SF$_6$ flow quantity at the sample points obtained from the experiment and the CFD model are compared with each other. It is obvious that all the results from the experiment are higher than that from the CFD model. It looks like there are big differences between the results. However, the largest SF$_6$ flow quantity is still smaller than 1.4×10^{-6} kcfm in Figure 63. In other words, the differences between the experimental and CFD results are not that big in terms of units of the SF$_6$ flow quantity.

There are several reasons for the higher SF$_6$ mass concentration results in the experiment. The k-epsilon turbulence model is not perfect and does not represent turbulent flow in the model very well due to the complex mine geometry. Additionally, there were people and mining equipment (a huge chuck) moving when the experiment was conducted. However, these factors were not simulated in the model. Besides, the injection of tracer gas was not modeled exactly as what it was in the underground. In the species transport model, SF$_6$ was released from a cube but in reality, the tracer gas was released from a container held by an individual. Moreover, the airflow and SF$_6$ flow might not be well-mixed when the sample points were taken in the experiment. Oppositely, the conditions set in the 3D CFD model are perfect and flows of air and SF$_6$ are mixed very well in the model.

The reason why the SF$_6$ mass concentration measured in the experiment is higher than that in the CFD mode is that the results at RP1 actually come from the results at monitor plane A as aforementioned. Due to the diffusion of SF$_6$ across the monitor plane A, the SF$_6$ mass concentration measured in the CFD model is lower than what is released from intake 4. However, the SF6 mass concentration at intake 4 is measured The contour of SF$_6$ mass concentration distribution near the RP1 can be found later in Figure 72.

Contours of the SF$_6$ mass concentration at SP1 and SP3 are shown below to illustrate the SF$_6$ mass concentration distribution in the cross-sectional area, where the sample points are located. Contours of the SF$_6$ mass concentration at SP2 and SP9 can be found in the Appendix.
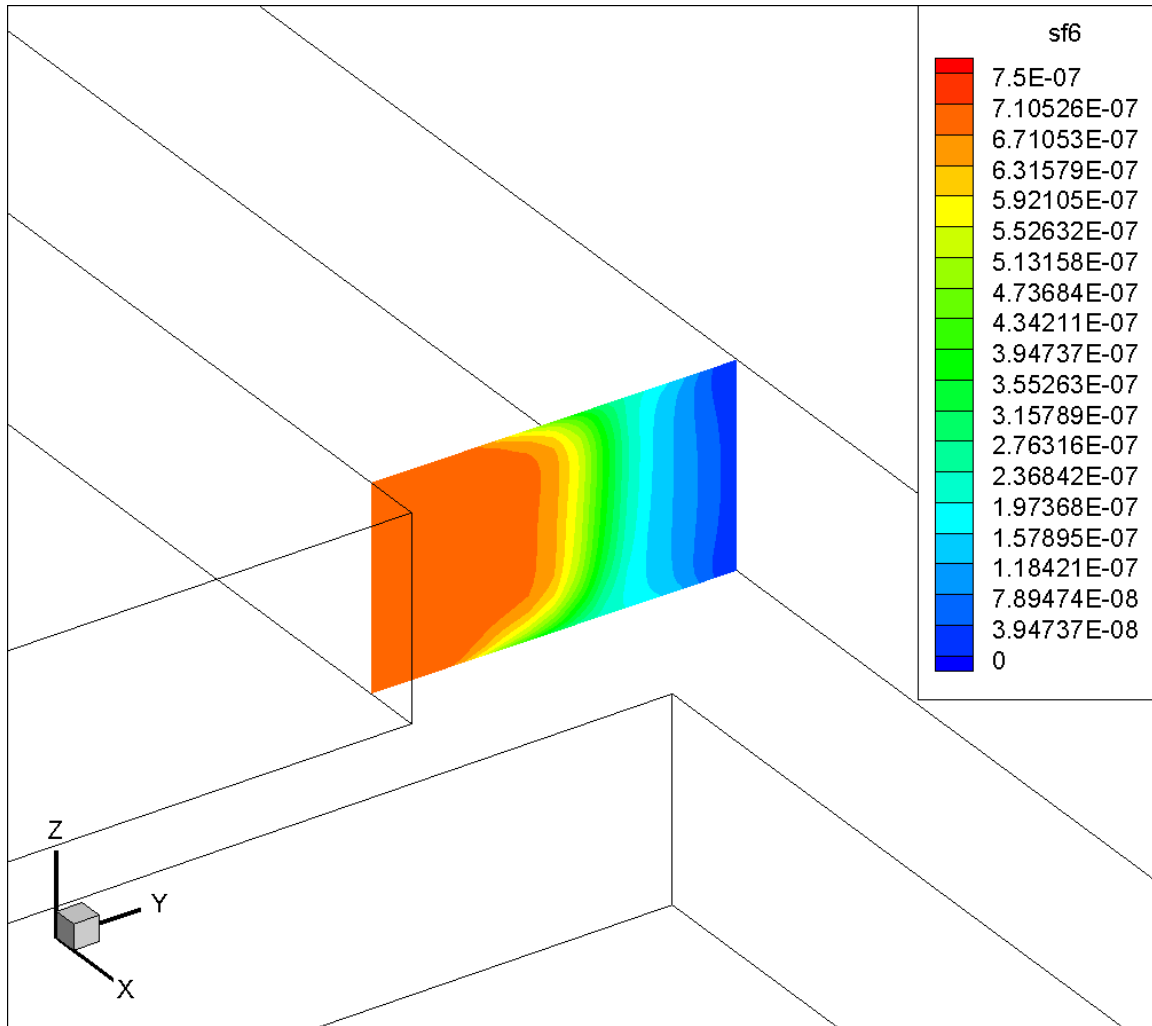
Figure 64. Contour (YZ plane) of SF$_6$ mass concentration at SP1 in the CFD model.

According to Figure 64, the SF$_6$ mass concentration in the cross-sectional area is not evenly distributed. It is higher close to the left side and lower in the right side of the figure. The contour in XY plane is shown in Figure 65 to provide an overview of the SF$_6$ mass concentration distribution in the area around SP1. It is clear that the SF$_6$ mass concentration distribution is complex at SP1. In addition, from Figure 61, the velocity magnitude uniform in the cross-sectional area. Moreover, the SF$_6$ flow quantities in the Table 19 were computed based on both the airflow velocity magnitude and SF$_6$ mass concentration in the center of the cross-sectional area, where the sample points were located. So the 10.49% error from the CFD model is acceptable.
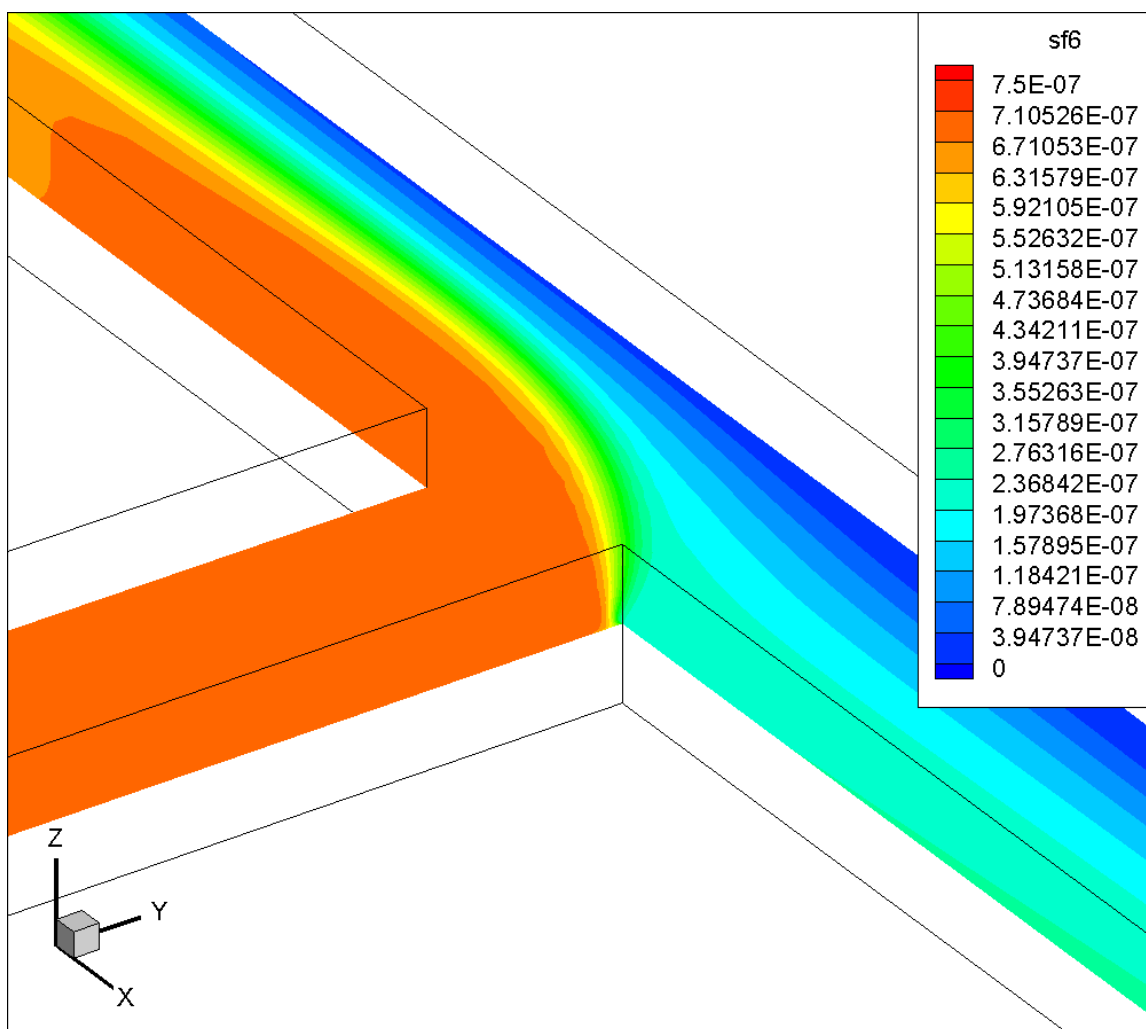
Figure 65. Contour (XY plane) of SF$_6$ mass concentration at SP1 in the CFD model.
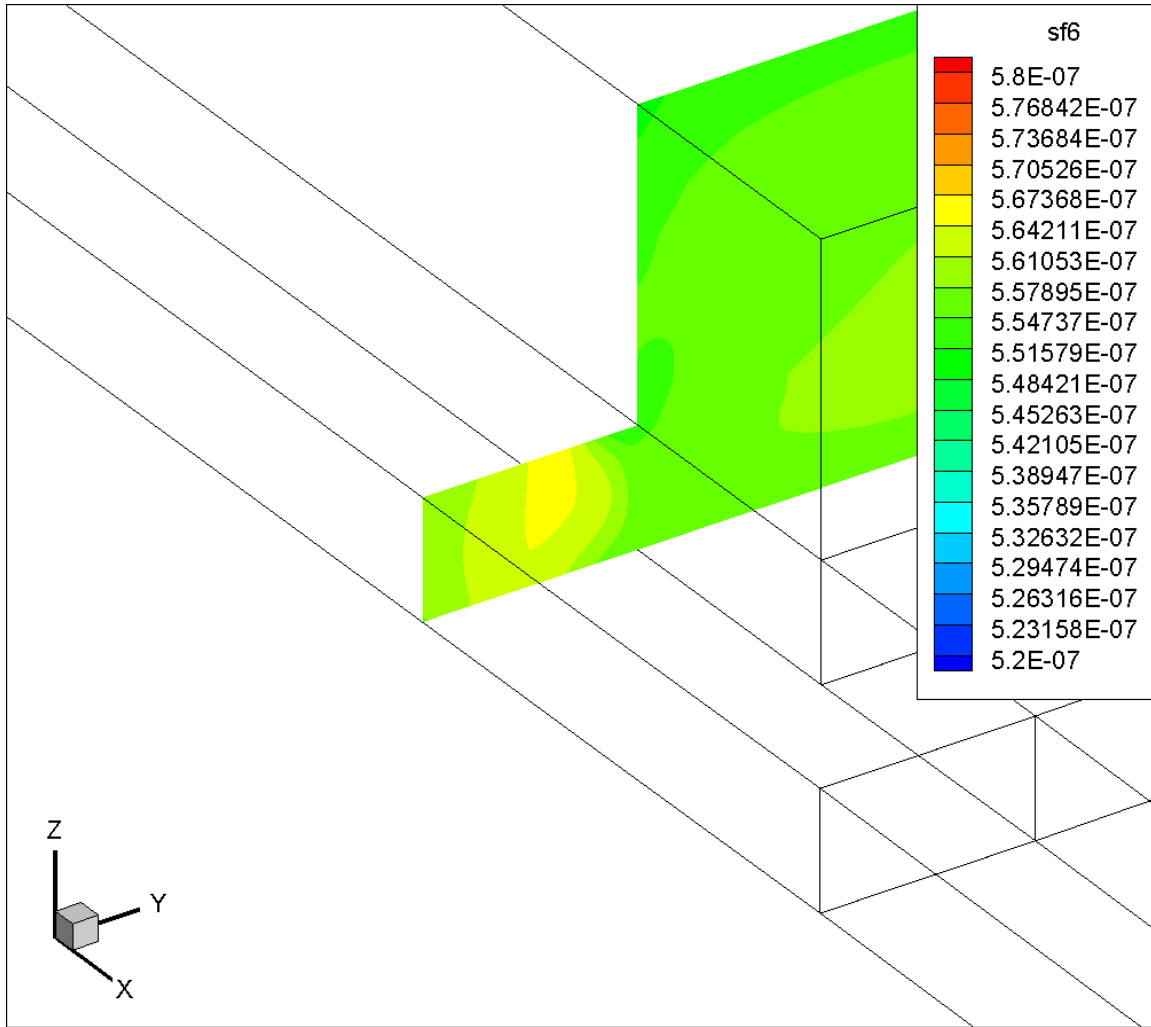
Figure 66. Contour (YZ plane) of SF$_6$ mass concentration at SP3 in the CFD model.

Based on Figure 66 and Figure 67, the SF$_6$ mass concentration at SP3 is around 5.67×10^{-7} and it does not have a big range in the cross-sectional area. However, as shown in Figure 59, the airflow velocity magnitude has a big range across the area. Even though the error at SP3 in the CFD model was computed as 54.42%, it is not surprising after taking all the erratic factors into account.
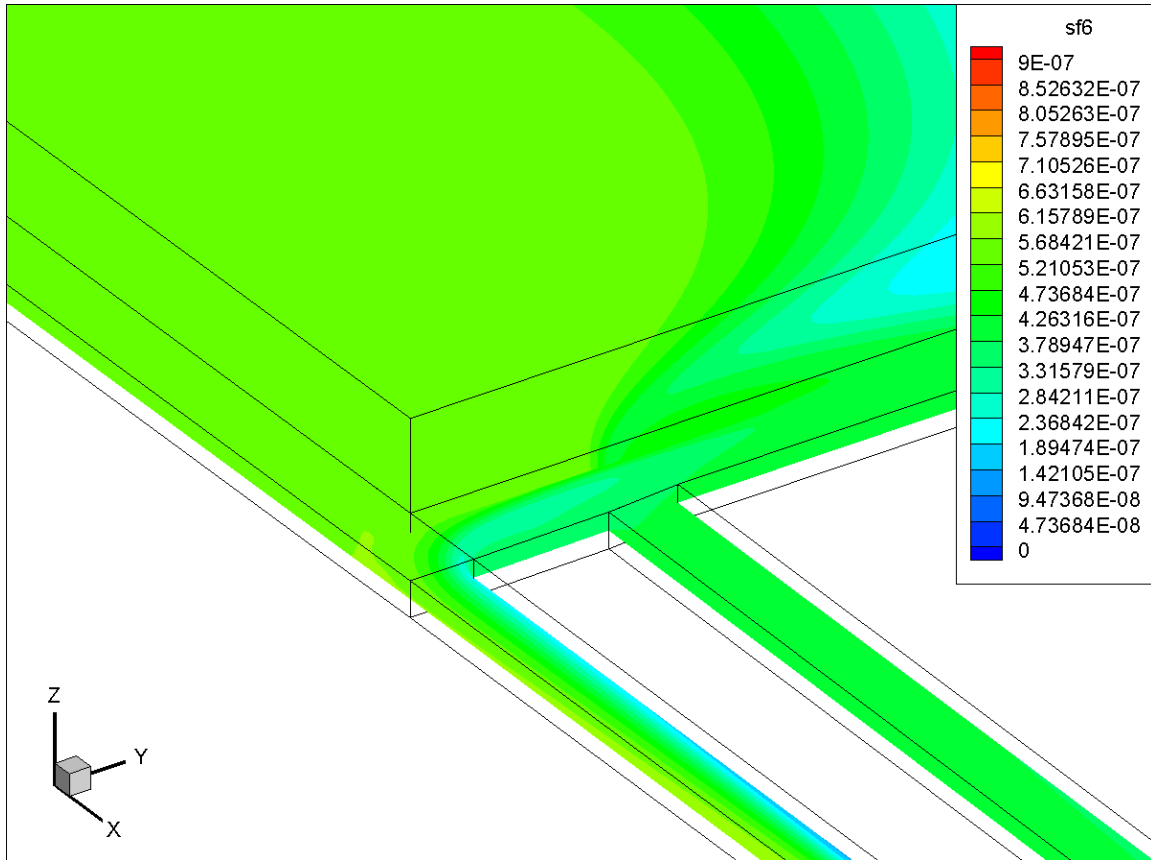
Figure 67. Contour (XY plane) of SF$_6$ mass concentration at SP3 in the CFD model.

4.5.7.2 Contour Comparisons

The results from the CFD model was analyzed above. To have a better idea about how the air and SF$_6$ behave in the underground, contours of airflow velocity magnitude and SF$_6$ mass concentration at various locations in the model were created below. All the contours were created when the steady-state simulation reached 16000 iterations. Another overall contour (created when the simulation reached 36560 iterations) of the SF$_6$ mass concentration distribution in the model mine was shown in the Appendix. The contour was created to have an idea about the diffusion process.
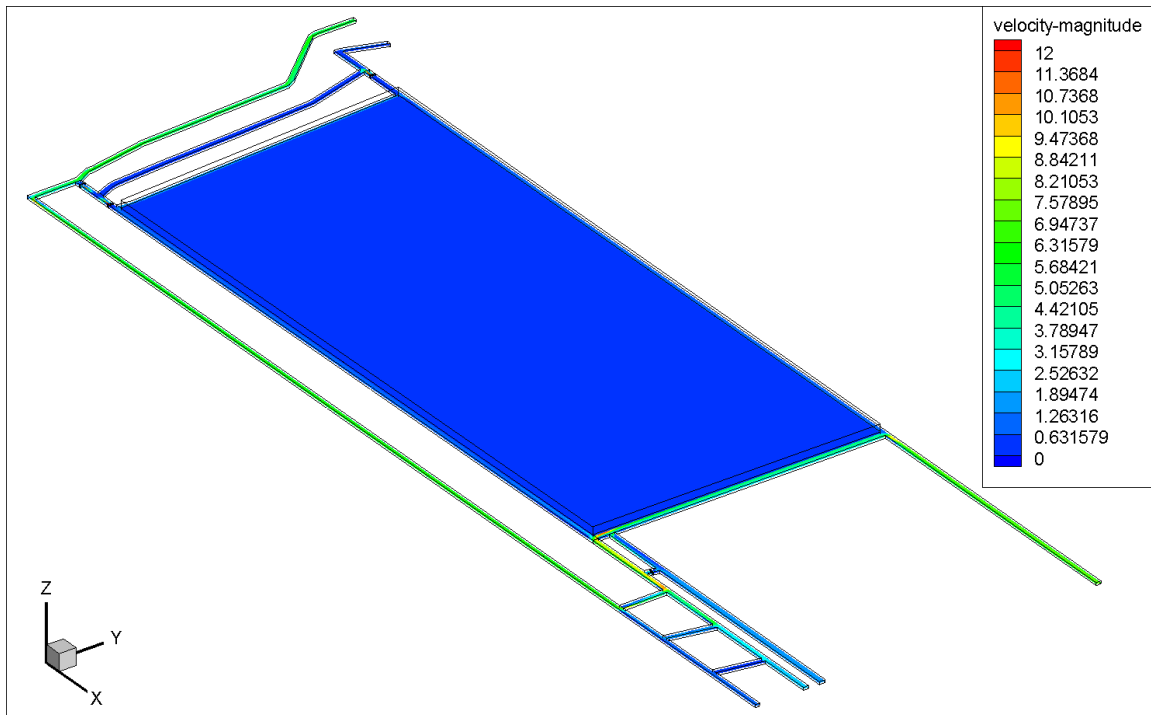
Figure 68. Contour (XY plane) of velocity magnitude (ft/s) for the entire mine in the CFD model.
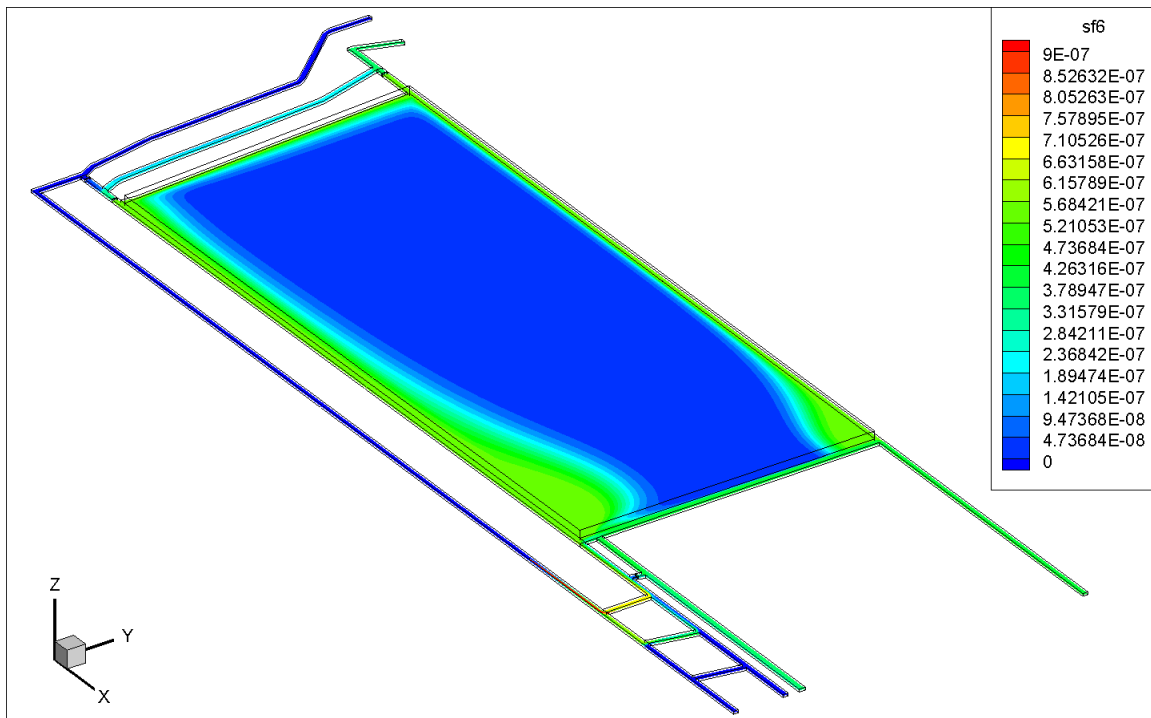
Figure 69. Visualization (in XY plane) of overall SF_6 concentration distribution in the CFD model.

91

From Figure 68, there is no airflow in the gob area in the model mine. However, in Figure 69, SF_6 diffuses to the gob and the SF_6 mass concentration is lower in the center of the gob and higher close to the walls. Additionally, Figure 69 shows that the diffusion of SF_6 is affected by the velocity magnitude, which agrees with Equation (4-10). According to Equation (4-10), as long as the mass fraction of the species (SF_6 in this case) is constant, the sum of convection and diffusion of SF_6 should also be constant. When the velocity magnitude is high, the convection term in the equation dominant the SF_6 flow behavior. If the velocity magnitude is low, the effects from convection will be reduced and diffusion will dominant the behavior of SF_6. For instance, SF_6 diffuses less in the high velocity magnitude areas like the working face. The contour of velocity magnitude and SF_6 mass concentration near the working face were shown in Figure 70 and Figure 71, respectively.
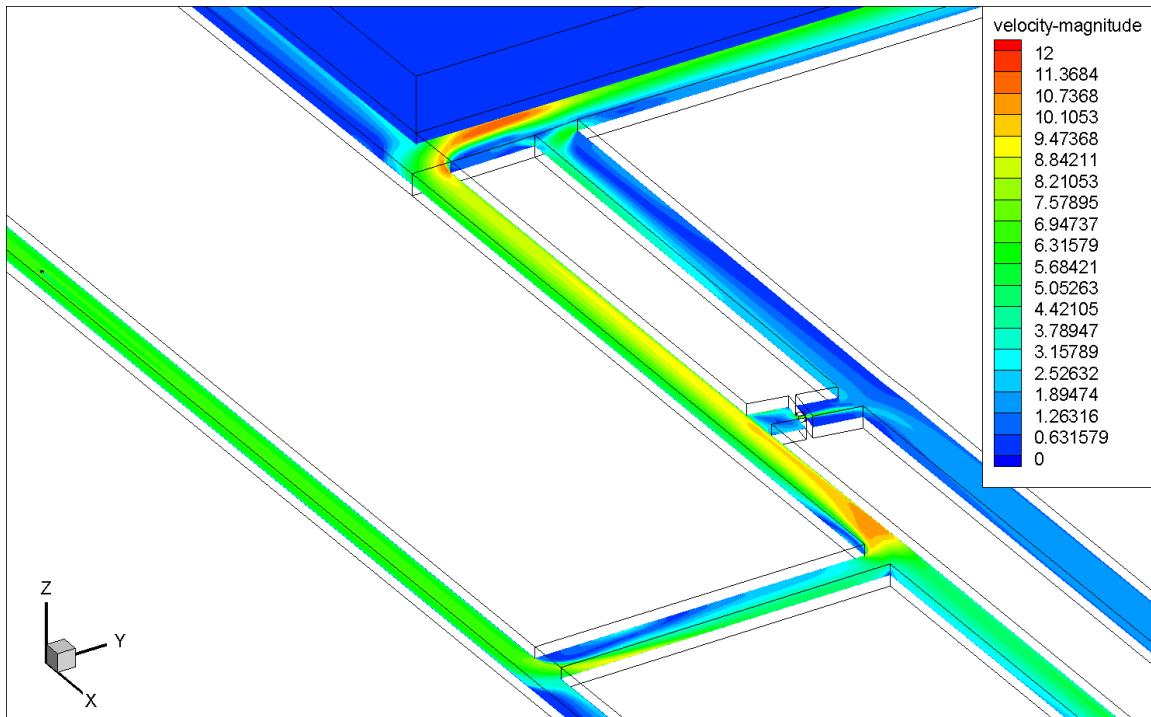
Figure 70. Visualization (in XY plane) of velocity magnitude (ft/s) near the working face in the CFD model.

According to Figure 70, it is obvious that most of the airflow goes to the working face and the rest of the airflow goes to the gob and the entry next to the gob. However, SF_6 diffuses more to the entry next to the gob than to the working face.
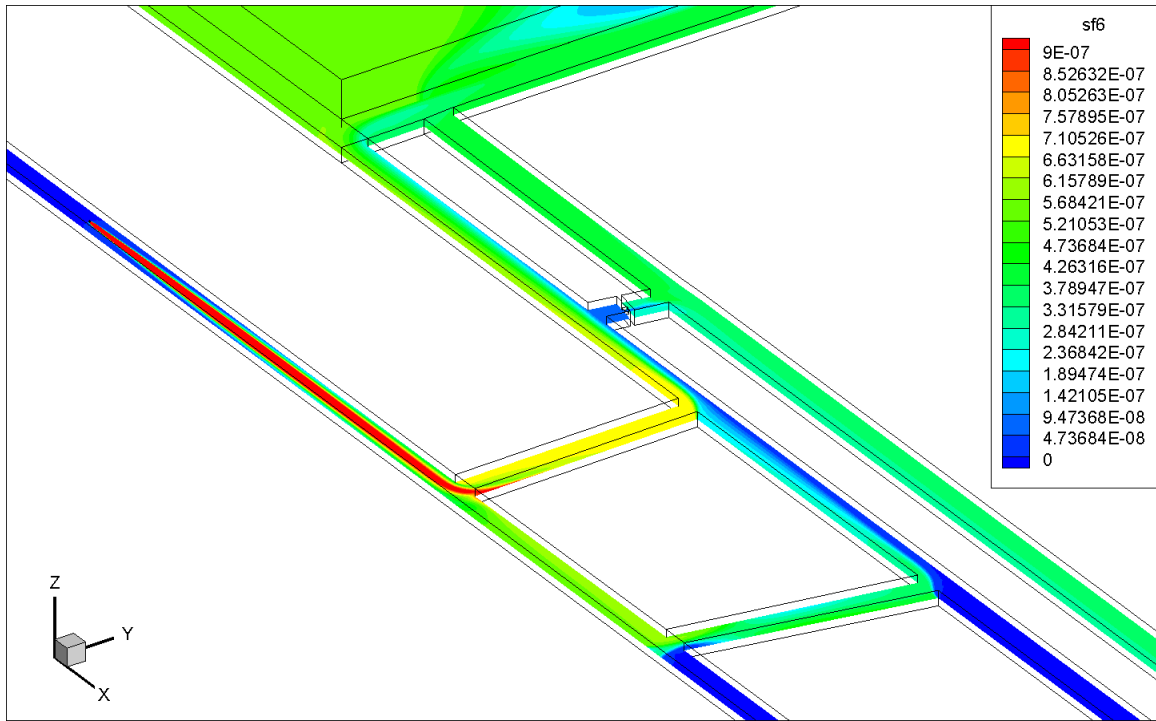
Figure 71. Visualization (in XY plane) of SF$_6$ concentration distribution near the working face in the CFD model.

Since the SF$_6$ mass concentration near the release point 1 is not clearly shown in Figure 71, Figure 72 and Figure 73 were created to get an idea of the SF$_6$ flow behavior near the release point 1.
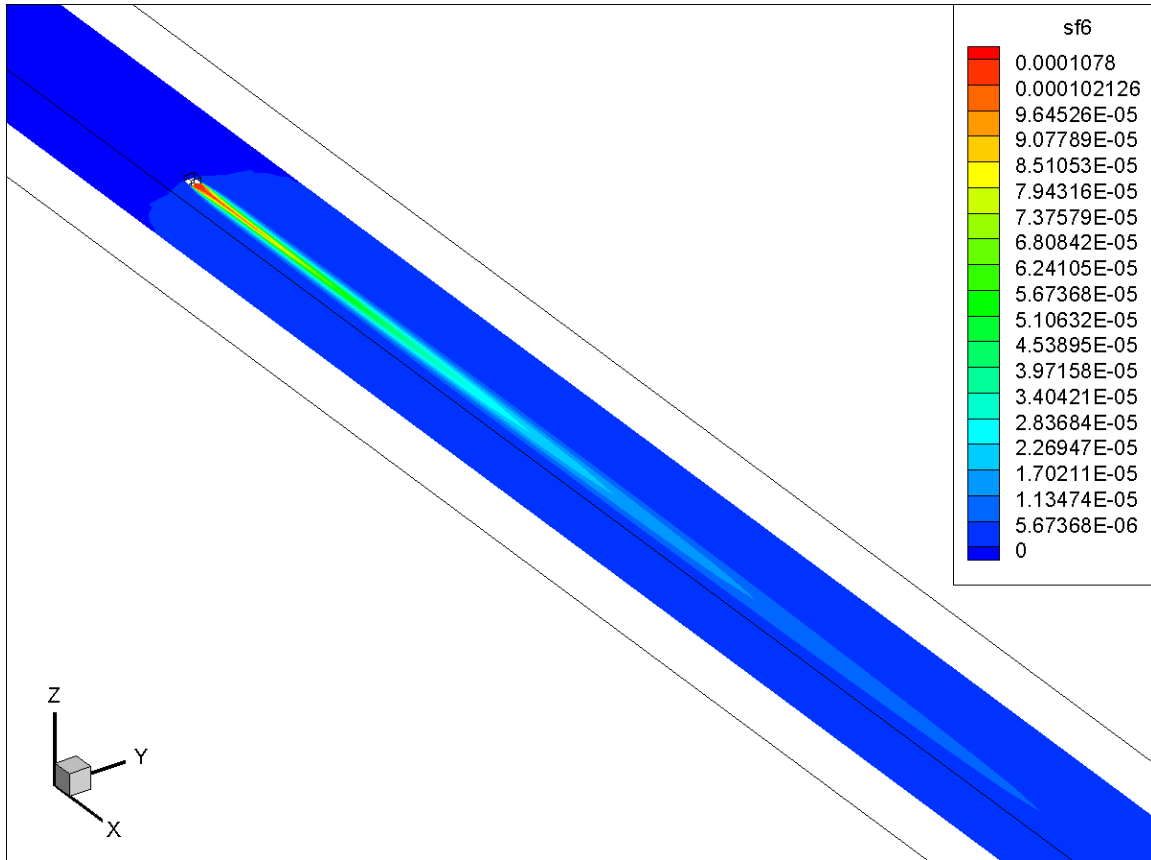
Figure 72. Visualization (in XY plane) of SF$_6$ concentration distribution near the RP1 in the CFD model.

From Figure 72 and Figure 73, SF$_6$ released from the intake 4 is concentrated in the centerline of the entry for a while and then slowly diffuses across the cross-sectional area. The contour is more meaningful than that shown in Figure 24 and Figure 25, which are obtained from the CFD models with and without turbulent viscosity. The reason is that SF$_6$ should not fully diffuse to the cross-sectional area right after the RP1 due to the effects from airflow convection. In addition, SF$_6$ does not back diffusion in the upstream before RP1 in Figure 72. However, there is SF$_6$ back diffusion in Figure 24 and Figure 25, which does not make sense according to the governing equations.

The distance from RP1 to the place where SF$_6$ is evenly distributed is 37 ft (measured in the CFD model). This 37 ft can be used as a reference for determining the locations of sample points in future field study. If the sample points are located at the places where SF$_6$ mass concentration are evenly distributed, the error from experiment can be

minimized very much. However, if the sample points are taken in the places where the SF$_6$ mass concentration has fluctuations across the cross-sectional area, the unexpected error will appear at these locations.
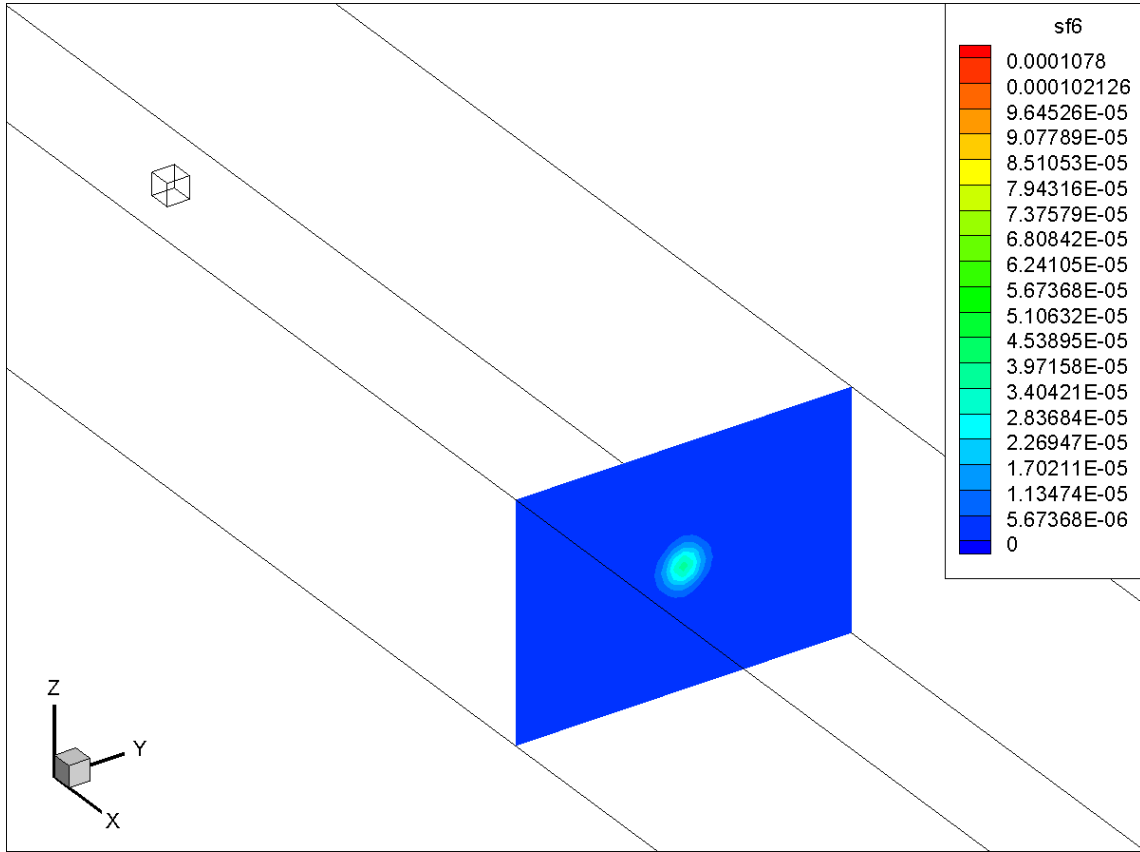
Figure 73. Visualization (in YZ plane) of SF$_6$ concentration distribution in a plane near the monitor plane A in the CFD model.

More contours of velocity magnitude and SF$_6$ diffusion at different locations can be found in the Appendix.

Not only contours were made to understand the flow behavior, but also monitor points and planes were created to simulate the change of SF$_6$ mass concentration over iteration in the species transport model. The simulated results were presented from Figure 74 to Figure 78. The reason why the iterations in the x axis in the following figures start from 6900 iterations is that the results at the monitor points and planes were not recorded in the first step of the steady-state simulation as aforementioned.

95
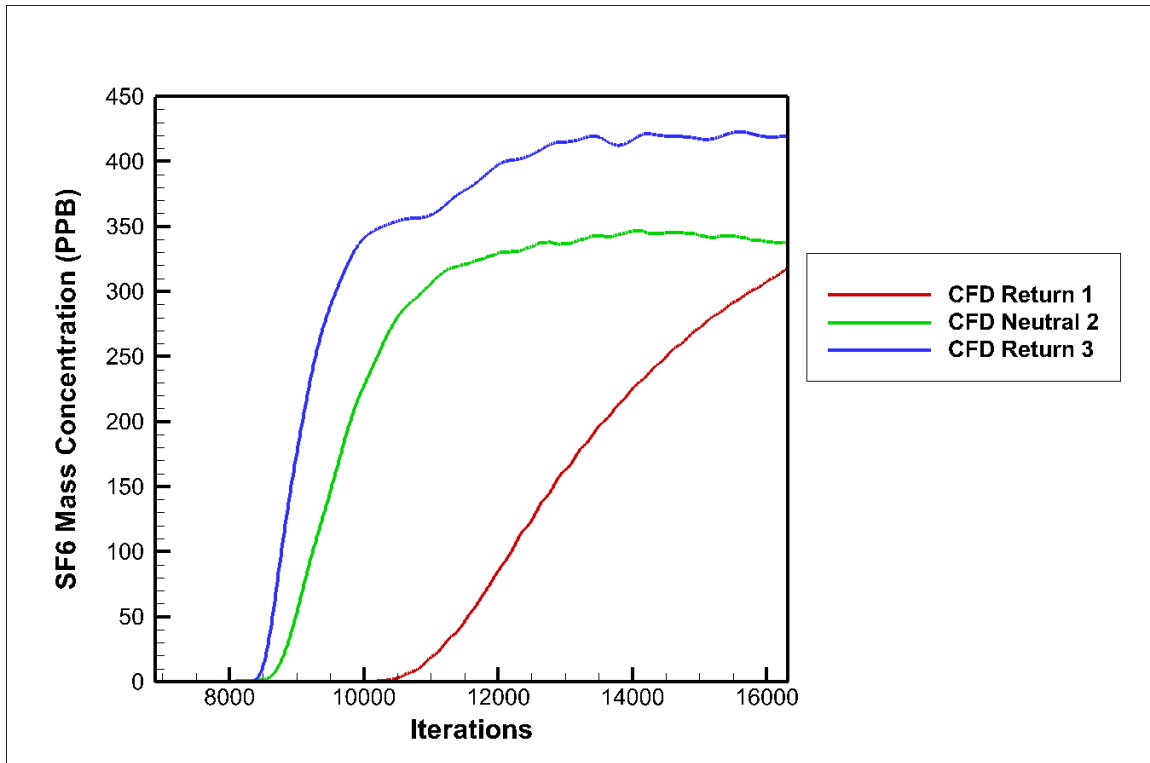
Figure 74. SF$_6$ mass concentration over iterations at the two returns and a neutral.

Monitor points were created in the center of the two returns and one neutral. Locations of the monitor points were same as what was shown in Figure 50. Results, which are SF$_6$ mass concentrations in this case, are recorded with number of iterations for the returns and neutral, respectively, as shown in Figure 74. It is clear that after 16000 iterations, the SF$_6$ mass concentration at neutral 2 and return 3 reach their stable levels. The final SF$_6$ mass concentration at return 3 and neutral 2 are about 430 PPB and 350 PPB, respectively. The SF$_6$ mass concentration at return 1 still increases because it is located the farthest from the RP1. To know the final SF$_6$ mass concentration at return 1, the simulation was kept running to 36560 iterations and the results were shown in Figure 75.
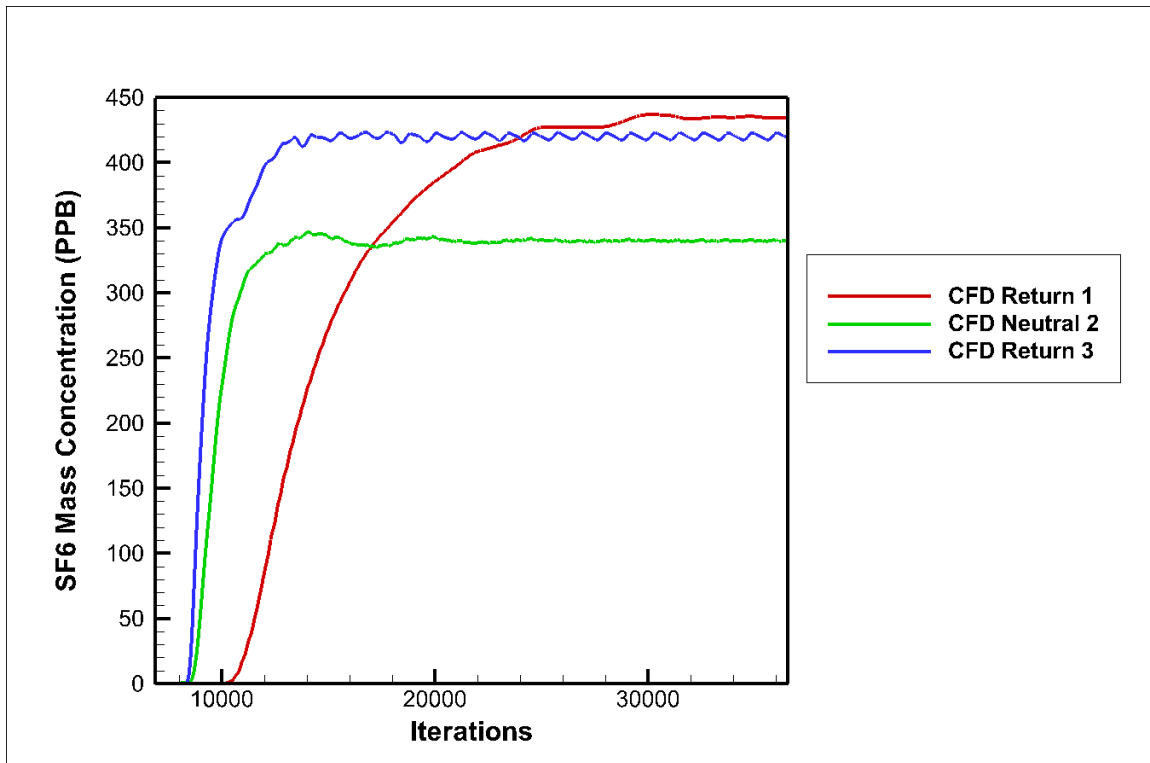
Figure 75. SF$_6$ mass concentration over 36560 iterations at the two returns and a neutral.

As shown in Figure 75, the SF$_6$ mass concentration reach a stable level at return 1 after about 30000 iterations in the model. The final mass concentration is 440 PPB, which is a little bit higher than that at neutral 2 and return 3. It is reasonable since SF$_6$ diffuses to the low airflow areas according to Figure 69.

CFD makes it possible to see the final SF$_6$ mass concentration level at return 1 in the steady-state simulation. However, it may take a very long time to wait for the SF$_6$ mass concentration to reach a stable level in the filed study. The transient simulation performed later on (Figure 79 and Figure 86) also proves how time-consuming it is for SF$_6$ to just show up at return 1.
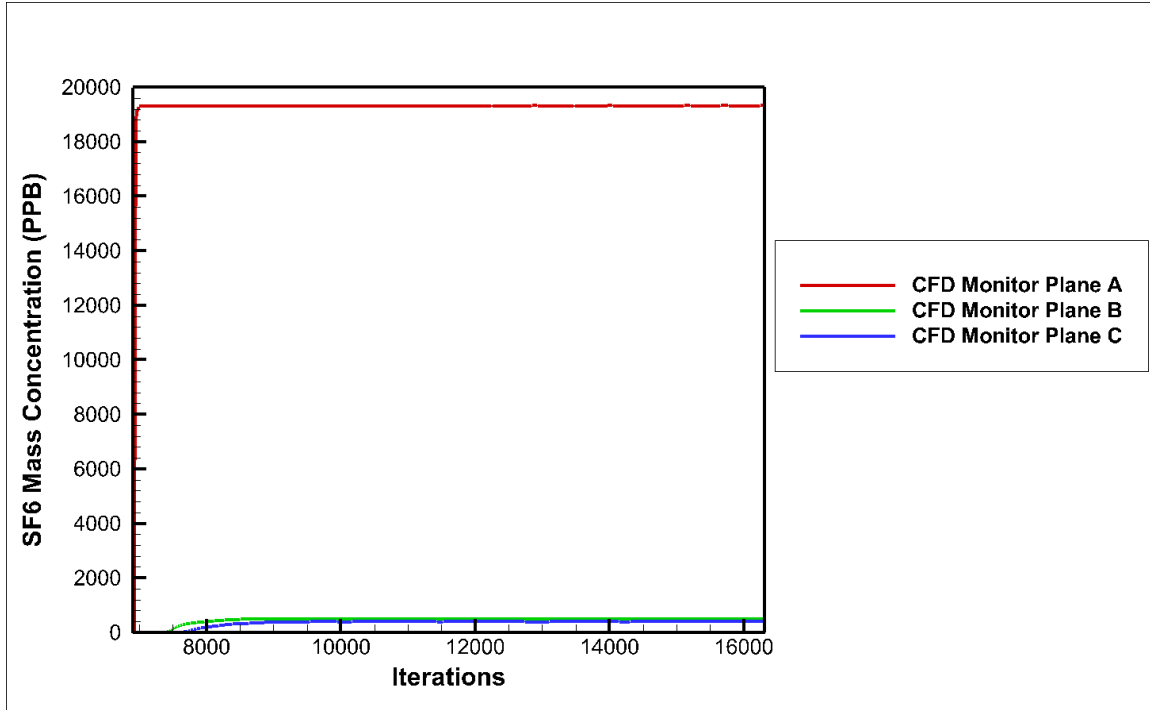
Figure 76. SF$_6$ mass concentration over iterations at the monitor planes.

Locations of the monitor planes are shown in Figure 48. Although they are called monitor planes in Figure 77, a monitor point was created in the center of each monitor plane and was used to record the changing of SF$_6$ mass concentration with iterations. According to Figure 76, it is obvious that the SF$_6$ mass concentration at the monitor plane A is the largest among the three monitor planes. The final SF$_6$ mass concentration is about 19000 PPB at the monitor plane A, while it is lower than 1000 PPB at monitor plane B and C. It seems 19000 PPB ($1.9{\times}10^{-5}$) at monitor plane A is unreasonable. However, it is still smaller than the SF$_6$ mass fraction at intake 4, which is $1.078{\times}10^{-4}$. The reason why the SF$_6$ mass concentration at monitor plane A is different from that at intake 4 is due to the SF$_6$ diffusion across the monitor plane A. The differences of SF$_6$ mass concentration at the monitor planes are due to their locations in the model mine. For example, the SF$_6$ mass concentration at monitor plane A is higher than that at monitor plane B because the SF$_6$ flow is separated before arriving at monitor plane B but it is not separated at monitor plane A. To better visualize the SF$_6$ mass concentration at plane B and C, Figure 77 is created below. It is obvious that the final SF$_6$ mass concentration at monitor plane B and C are about 500 PPB and 400 PPB, respectively.
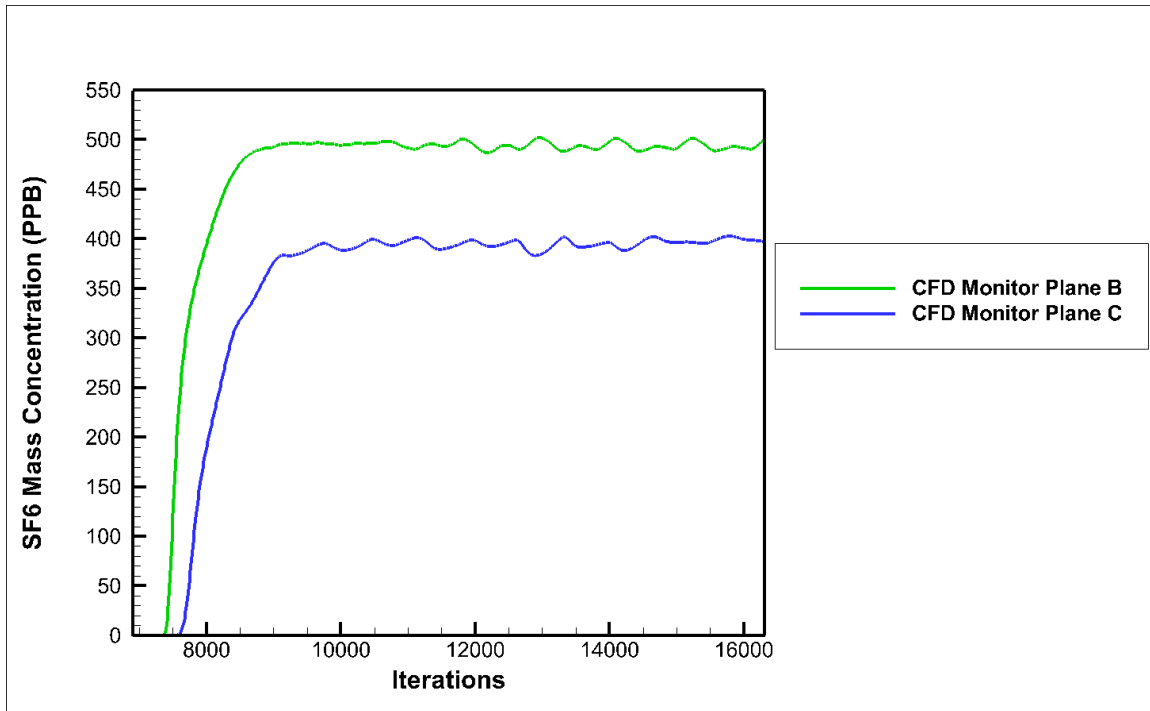
Figure 77. SF$_6$ mass concentration over iterations at the monitor plane B and C.

Monitor points were also created at the sample points to understand the SF$_6$ flow behavior. The monitor points are located in the center of the cross-sectional area where the sample points are located. The SF$_6$ mass concentration with iterations at the sample points in the model is shown in Figure 78.
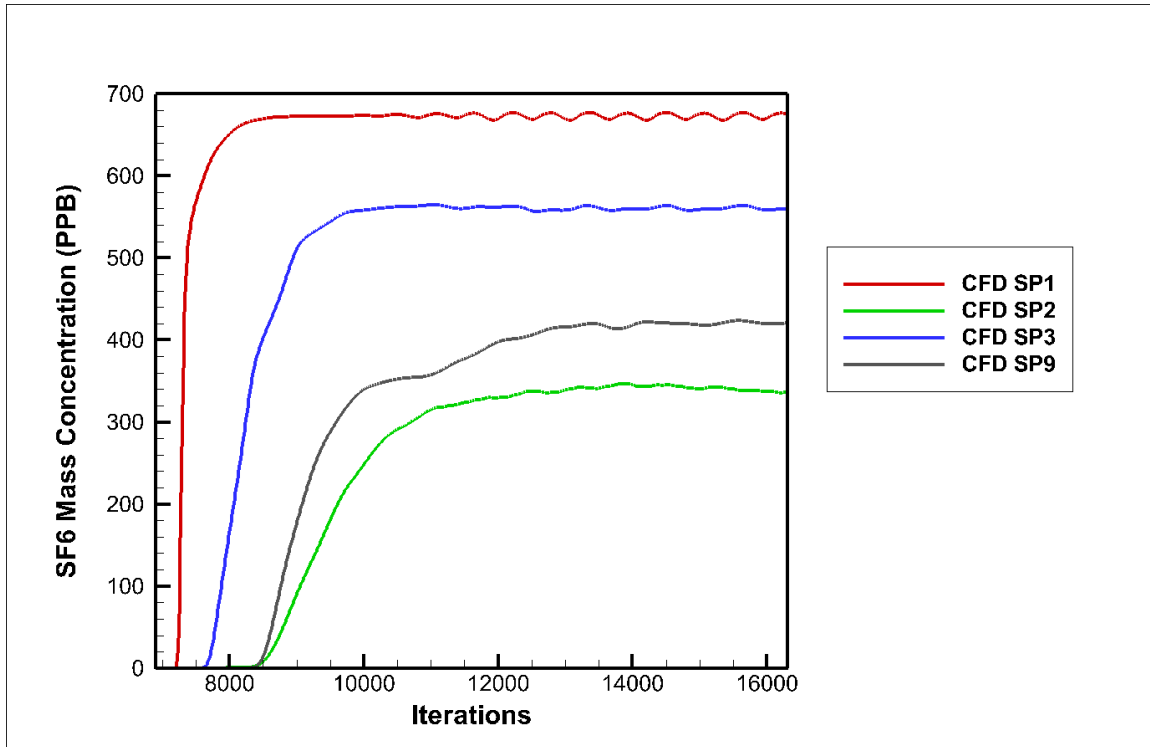
Figure 78. SF$_6$ mass concentration over iterations at the sample points.

According to Figure 78, the SF$_6$ mass concentration at the four sample points reach a stable level after about 14000 iterations in the model. The final SF$_6$ mass concentration at SP1 is the largest among the four sample points while it is the smallest at SP2. The reason is that SP1 is located right next to RP1 and SP2 is located in the entry close to neutral 2 as shown in Figure 48. The SF$_6$ flow, which is originally released form RP1, is separated several times before reaching SP2. However, it reaches SP1 without any separations or obstacles.

4.5.8 Transient Simulation

Transient simulation was also processed in two steps. At first, the species transport model was ran on a steady solver to let the airflow reach its steady state. Boundary condition for intake 4 was changed to wall and no mixture was released in the steady state simulation. Then the model continued to be ran on a transient solver and the mixture was released from intake 4. Boundary condition for intake 4 was changed to velocity inlet. Convergence criteria for both the steady state simulation and transient simulation were

set to 10^{-3}. The transient simulation, which was the second step, has been run for ten hours. Compared to the six-hour experiment, it was longer. The reason was that the SF₆ concentration has not reached a steady level in six hours for some returns and sample points far from the release point in the CFD model. The ten-hour simulation made it possible to visualize the final SF₆ mass concentration at different locations.

4.5.8.1 Results from the Species Transport Model

The results from the transient simulation were made up of two parts. One was from the six-hour simulation and the other was from the ten-hour simulation. Both the results were compared to the results from the six-hour experiment. SF₆ mass concentration was monitored at various locations in the model mine.

4.5.8.1.1 Six-hour Simulation

The six-hour transient simulation was performed to make a comparison with the six-hour experiment. SF₆ mass concentration was monitored at two returns, one neutral, and three monitor planes. A monitor point was created for the returns and neutral, respectively. The monitor point was located at the center of the returns, neutral, and monitor planes because the sample points were located in the center of entries in the experiment. An example for the location of the monitor point in return 3 was shown in Figure 50.
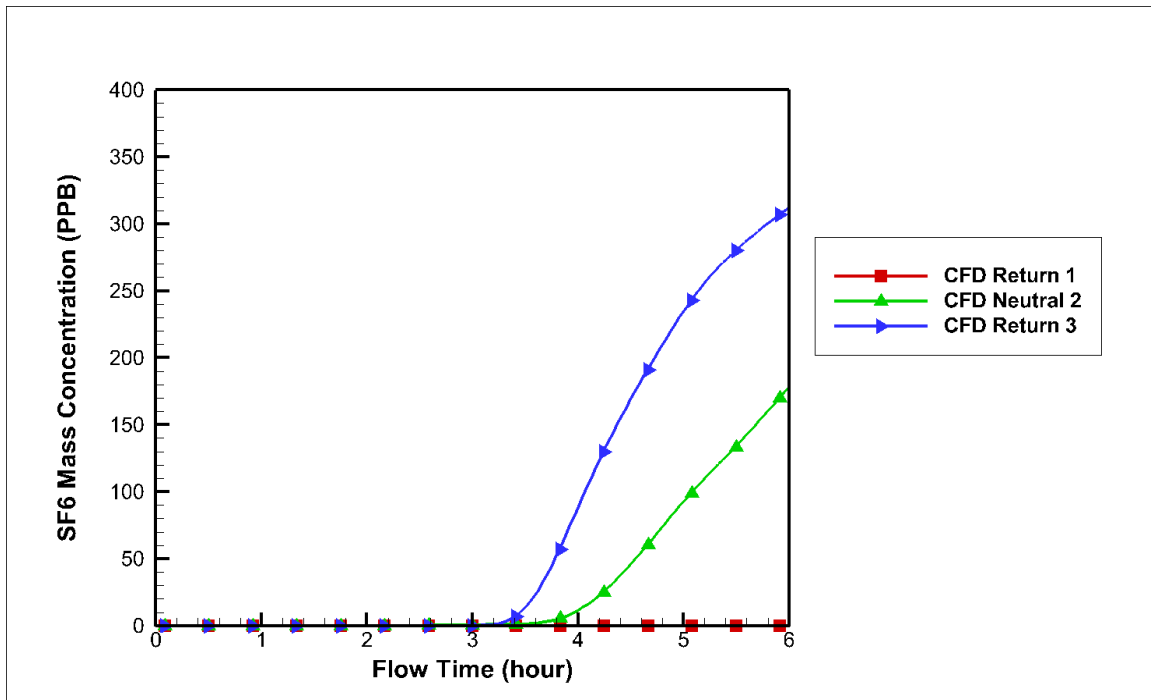
Figure 79. SF$_6$ mass concentration over time at the two returns and a neutral.

In Figure 79, the SF$_6$ mass concentration does not reach a stable level at the two returns and one neutral after the six-hour simulation. The SF$_6$ mass concentration stays around 0 PPB at return 1 because return 1 is located the farthest from the release point compared to neutral 2 and return 3. For neutral 2 and return 3, there is an increasing trend of the SF$_6$ mass concentration after the simulation. A better explanation of the SF$_6$ mass concentration over time at the two returns and one neutral can be found in the ten-hour simulation in Figure 86.
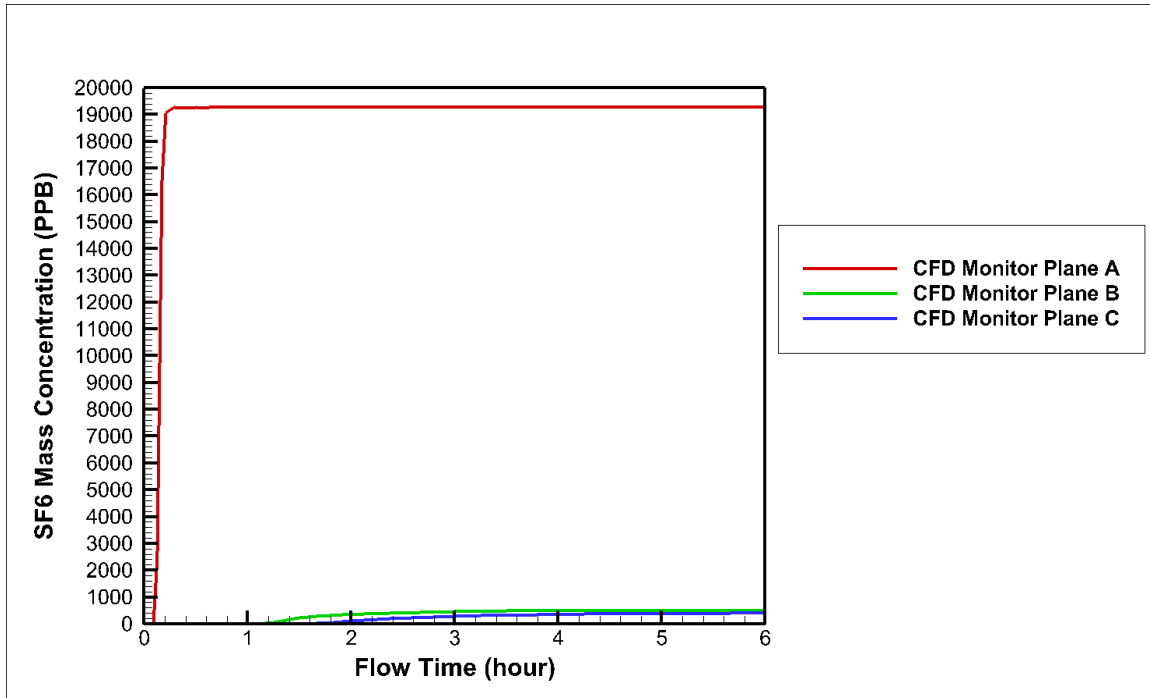
Figure 80. SF$_6$ mass concentration over time at all the monitor planes.

The three monitor planes were created in the species transport model. Locations of the monitor planes were shown in Figure 48. Monitor plane A was located right after the release point 1. Monitor plane B was a plane created in the entry where the airflow was about to enter the working face. The monitor plane C was a plane created in the working face. Contours of velocity magnitude and SF$_6$ mass concentration were created at the three monitor planes to have an idea about the distribution of the velocity magnitude and SF$_6$ mass concentration. Monitor points were also created at the three planes, respectively. All the monitor points were located in the center of the monitor planes like the location of the monitor point in return 3 in Figure 50. SF$_6$ mass concentration over time was monitored at the monitor points in the three monitor planes and was presented in Figure 80.

Figure 80 shows the SF$_6$ mass concentration over time at the monitor points located in the three monitor planes. It is clear that the SF$_6$ mass concentration reach a stable level in a short period of time at monitor plane A because it is located right after the release point 1. The final SF$_6$ concentration at monitor plane A is about 19000 PPB (19 PPM), which is much higher than that in the monitor plane B and C. There are two main reasons for the

higher SF₆ mass concentration in monitor plane A. One is SF_6 flow has not been separated because of turns or obstacles in the entry. The other one is no new airflow joins the original mixture at monitor plane A. So the amount of SF_6 originally released from the intake 4 is not reduced A while the airflow rate keeps the same at monitor plane. SF_6 mass concentrations are much lower at monitor plane B and C due to the aforementioned reasons. Figure 81 was created because the SF_6 mass concentration values at monitor plane B and C are hard to be read in Figure 80.
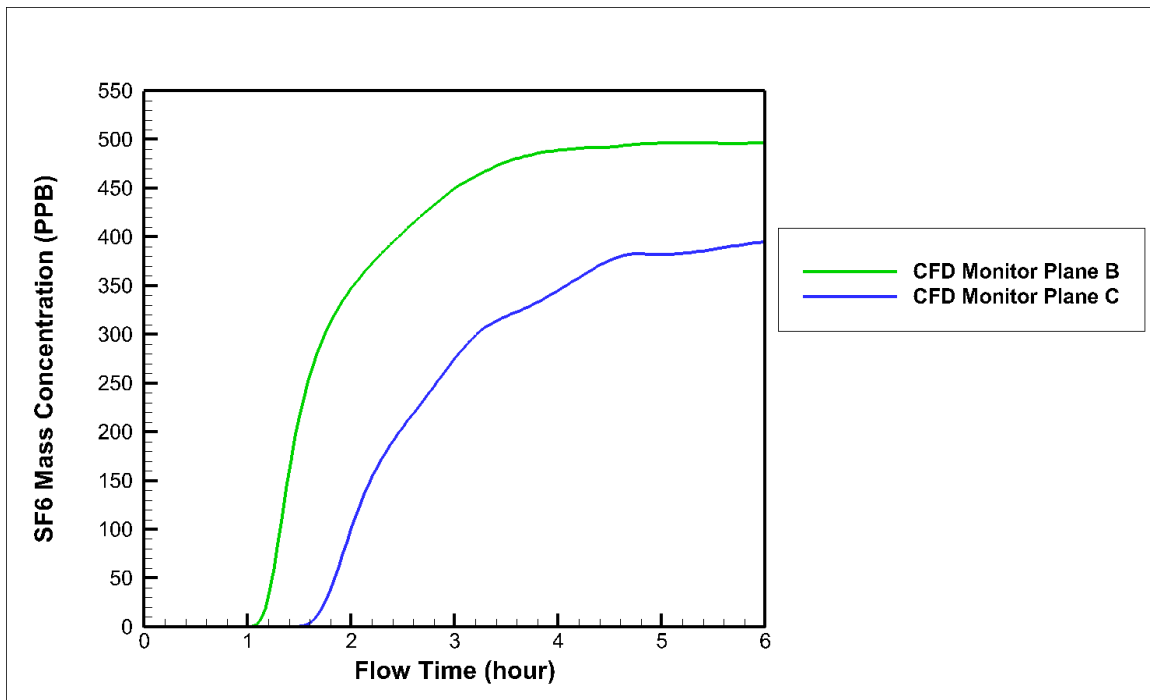
Figure 81. SF_6 mass concentration over time at monitor plane B and C

From Figure 81, the SF_6 mass concentration reaches a stable level after the six-hour simulation for monitor plane B and C. The final SF_6 mass concentration are 500 PPB and 400 PPB for the monitor plane B and C, respectively. The difference in the SF_6 mass concentration between the two monitor planes is caused by the distribution of the amount of SF_6 at monitor plane B before arriving monitor plane C. In addition, the SF_6 mass concentration at monitor plane B shows up about half an hour earlier than that at monitor plane C. It is because the monitor plane B is located closer to the release point 1 compared to the monitor plane C.

Similar to the steady-state simulation, contours at some locations where the SF$_6$ behavior is not clear are created below to help understand what happens in the underground.
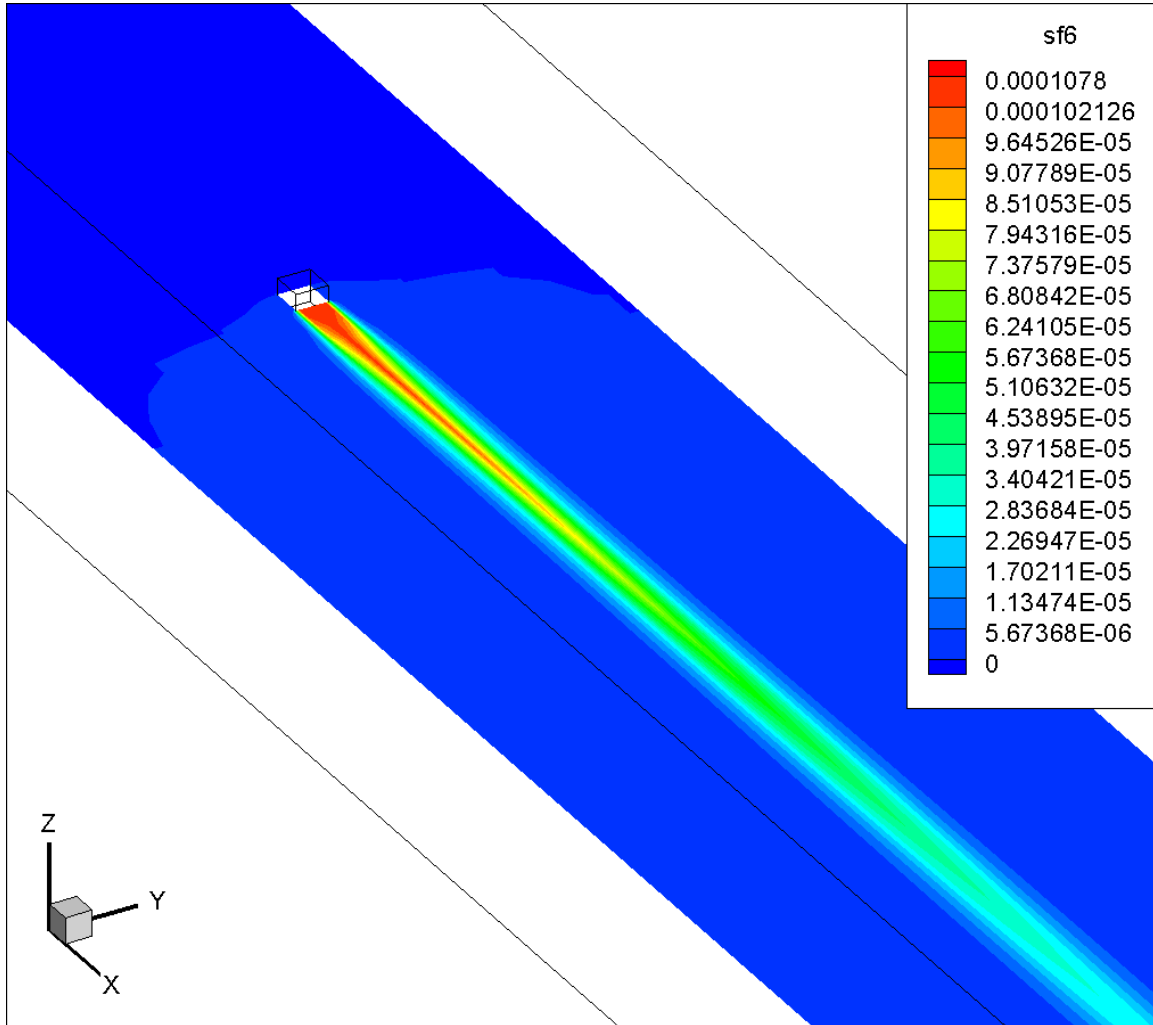
Figure 82. Visualization (in XY plane) of SF$_6$ mass concentration distribution at around RP1 in the species transport model.

The contour shown in the Figure 82 is the same as that in Figure 72. It makes sense because there is no turns or obstacles in the downstream in Figure 82. In addition, the area in the figure is close to RP1 and SF$_6$ flow has already reached a steady-state level, which has also been verified in Figure 80.

Contour of SF$_6$ mass concentration at monitor plane A, B, and C are shown from Figure 83 to Figure 85, respectively.

Figure 83. Visualization (in YZ plane) of SF$_6$ mass concentration distribution at monitor plane A in the species transport model.

Figure 83 shows the SF$_6$ mass concentration distribution in the monitor plane A and it also proves that the SF$_6$ concentrates in the center.

The SF$_6$ mass concentration distribution in the monitor plane B is shown in Figure 84.

Figure 84. Visualization (in YZ plane) of SF$_6$ mass concentration distribution at monitor plane B in the species transport model.

Based on Figure 84, the SF$_6$ mass concentration varies across the monitor plane B. The range for the mass concentration is from 1×10^{-7} to 6×10^{-7}. The location of monitor plane B actually results in the variation across the plane. Part of the incoming flow is separated and flow to neutral 2 via the mandoor. Additionally, the incoming flow itself is not evenly distributed according to Figure 65.
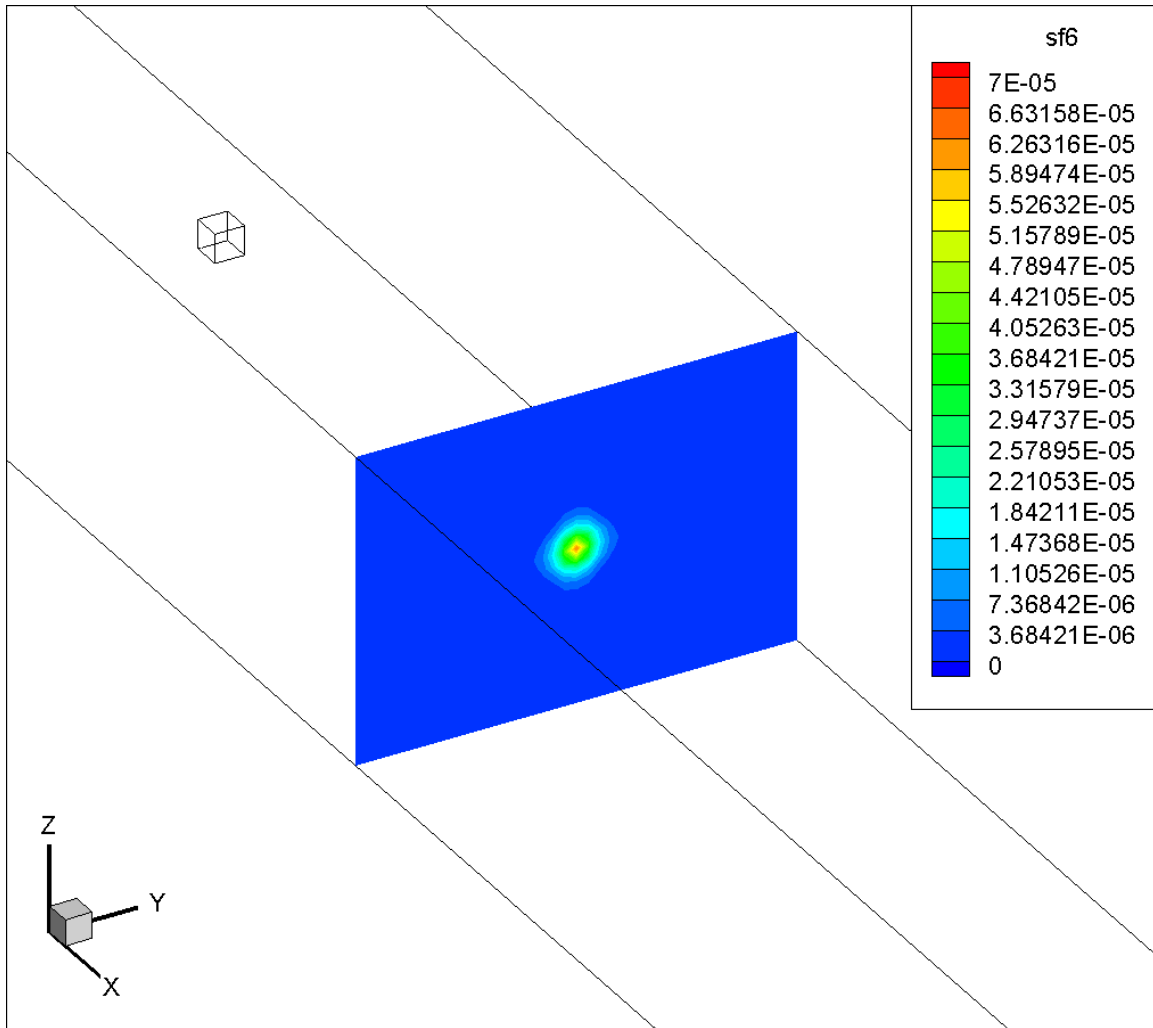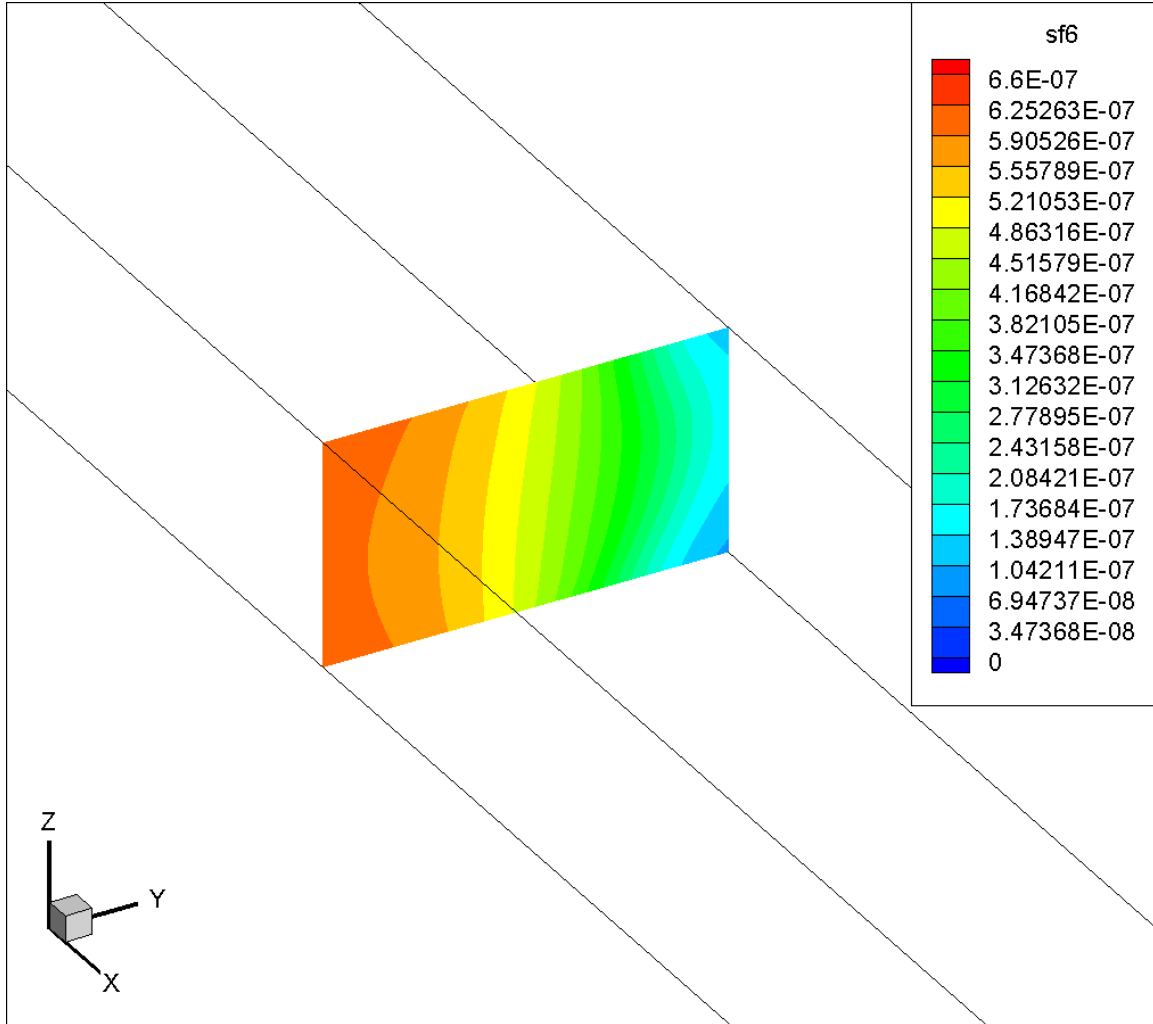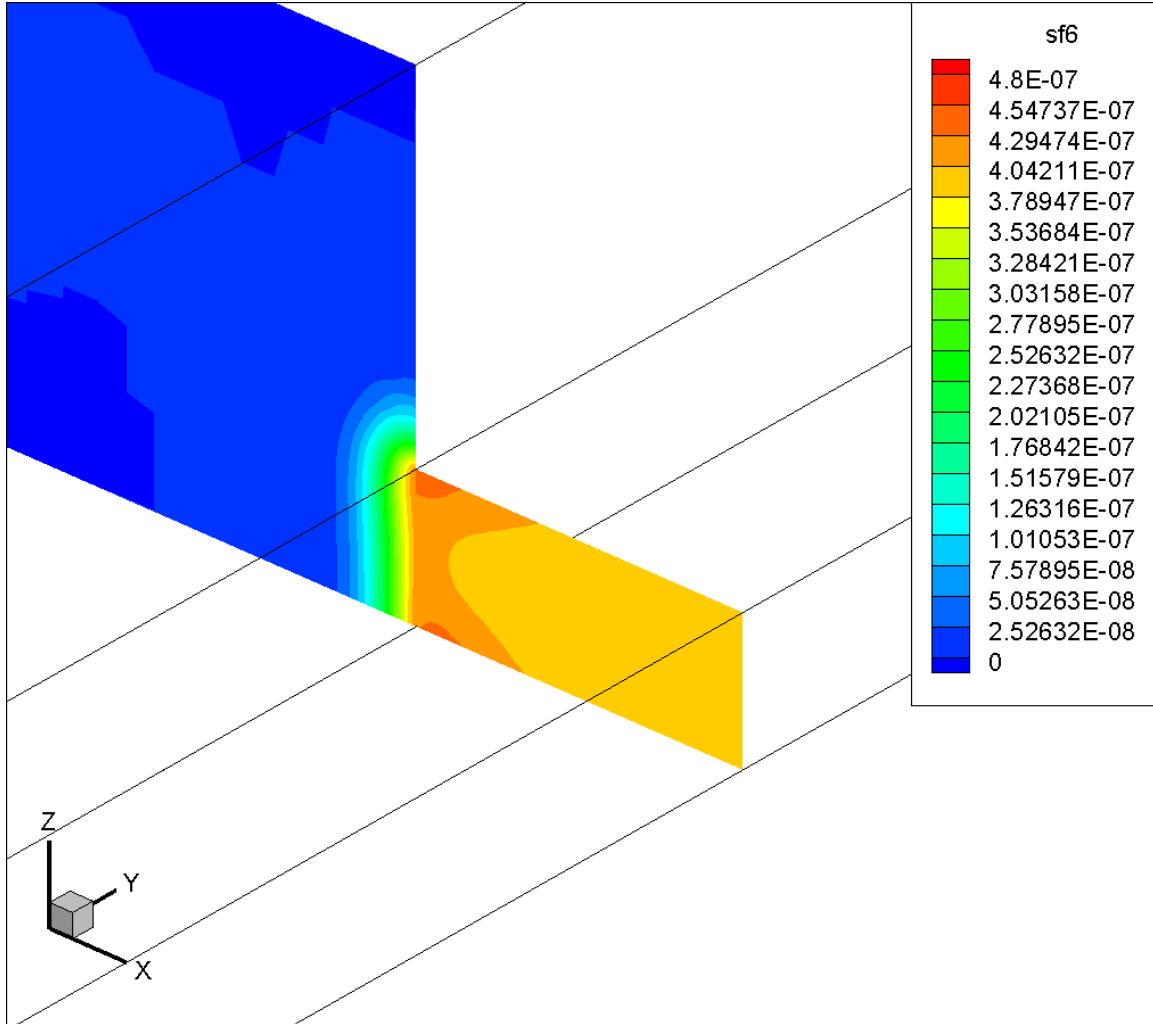
107

Figure 85. Visualization (in YZ plane) of SF$_6$ mass concentration distribution at monitor plane C in the species transport model.

From Figure 85, it is clear that SF$_6$ already starts to diffuse to the gob. Although six hours passed, the diffusion to the gob is not that much due to the high velocity magnitude in the working face, which has also been discussed in Figure 69.

4.5.8.1.2 Ten-hour Simulation
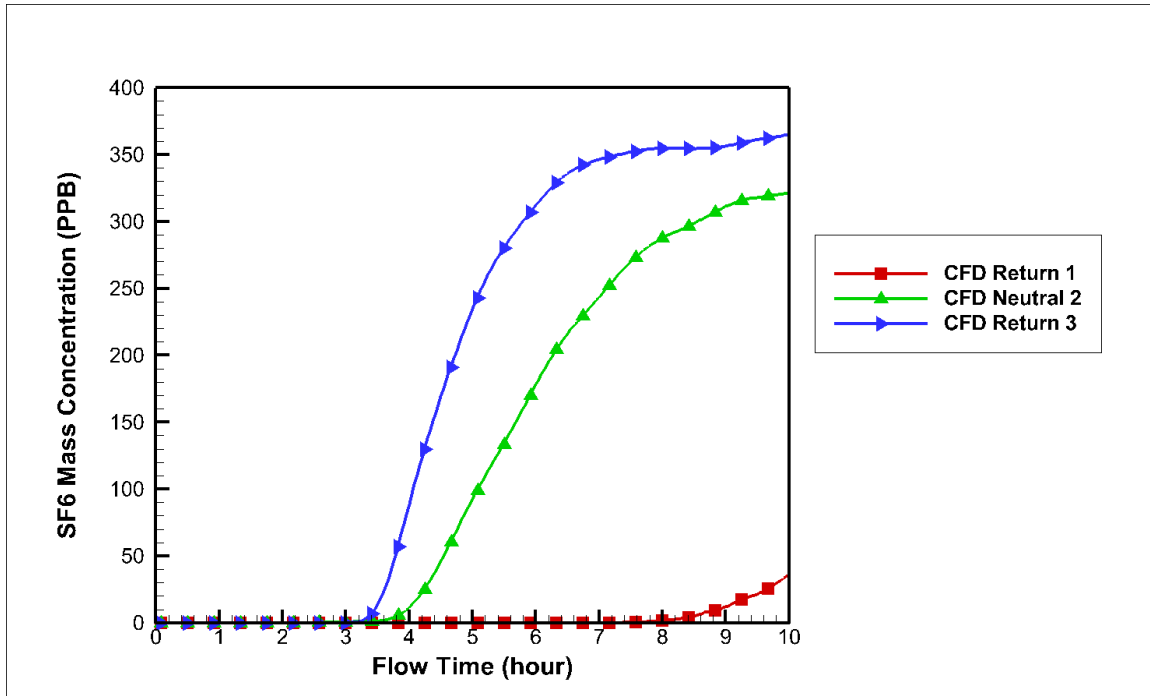
Figure 86. SF₆ mass concentration over time (ten hours) at the two returns and a neutral.

4.5.8.2 Results Compared with the Experimental Results

The results from the six-hour transient simulation and the ten-hour transient simulation at the sample points were compared with that from the experiment, respectively. Monitor points were created in the CFD model to simulate the SF₆ mass concentration at the sample points. The monitor points were located in the center of entries like Figure 50.

4.5.8.2.1 Overall Comparisons for All the Sample Points

Figure 87 shows an overview of the comparisons between the results from the species transport model and the experiment at the sample points in the six-hour simulation. The comparisons in the ten-hour simulation are shown in Figure 88. Individual comparisons at each sample point are made and shown from Figure 89 to Figure 98.

Figure 87. Comparison between CFD results and experimental results from the six-hour transient simulation at four sample points.

From Figure 87, it is obvious that the experimental results fluctuate very much while the CFD results are stable for the four sample points. The SF_6 mass concentration at SP3 and SP9 does not reach a stable level in the six-hour simulation. However, the SF_6 mass concentration at all the sample points reach the stable levels in the ten-hour simulation as shown in Figure 88.
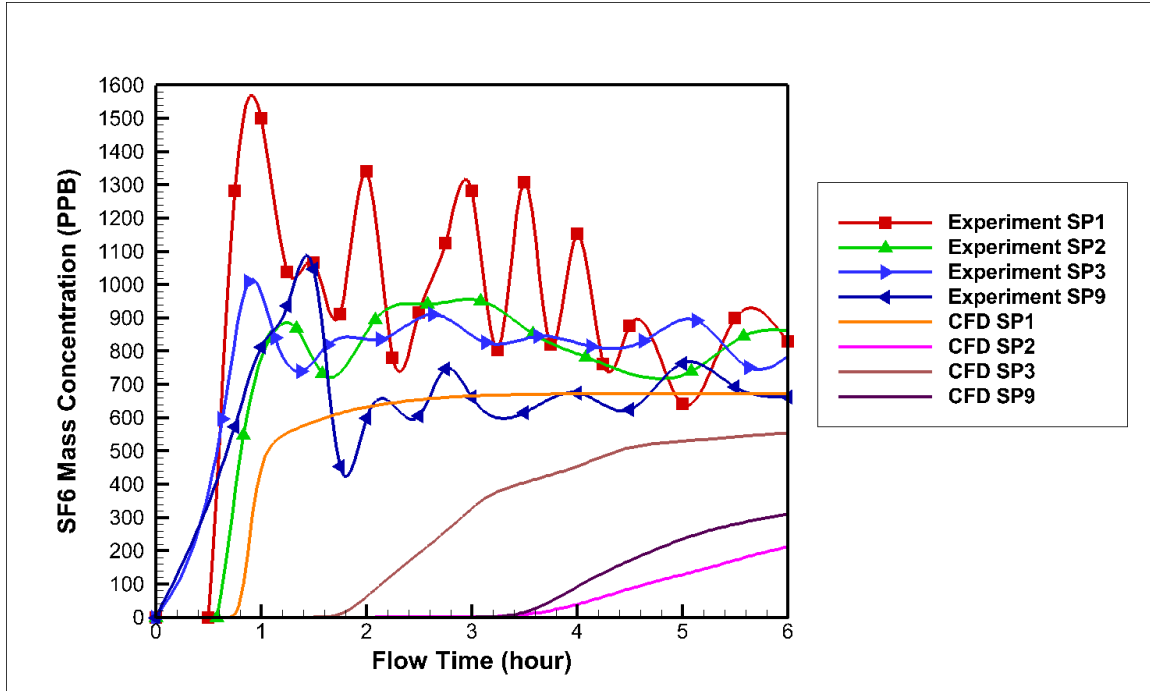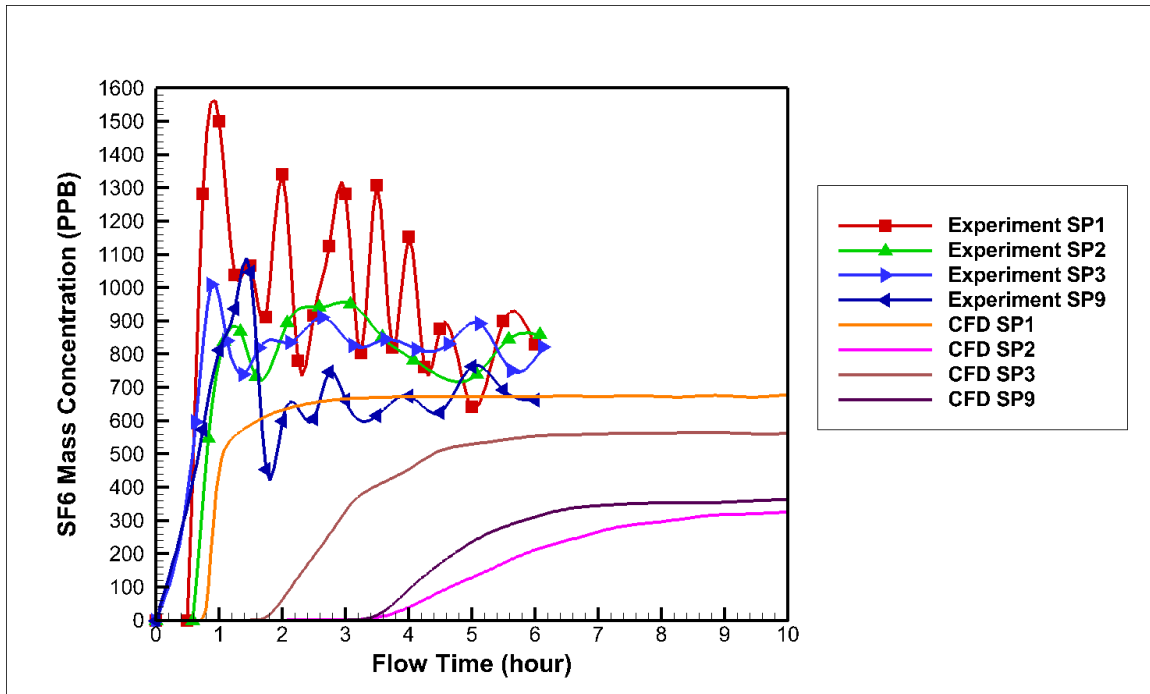
Figure 88. Comparison between CFD results and experimental results from the ten-hour transient simulation at four sample points.

4.5.8.2.2 Comparisons on SF₆ Mass Concentration at SP1
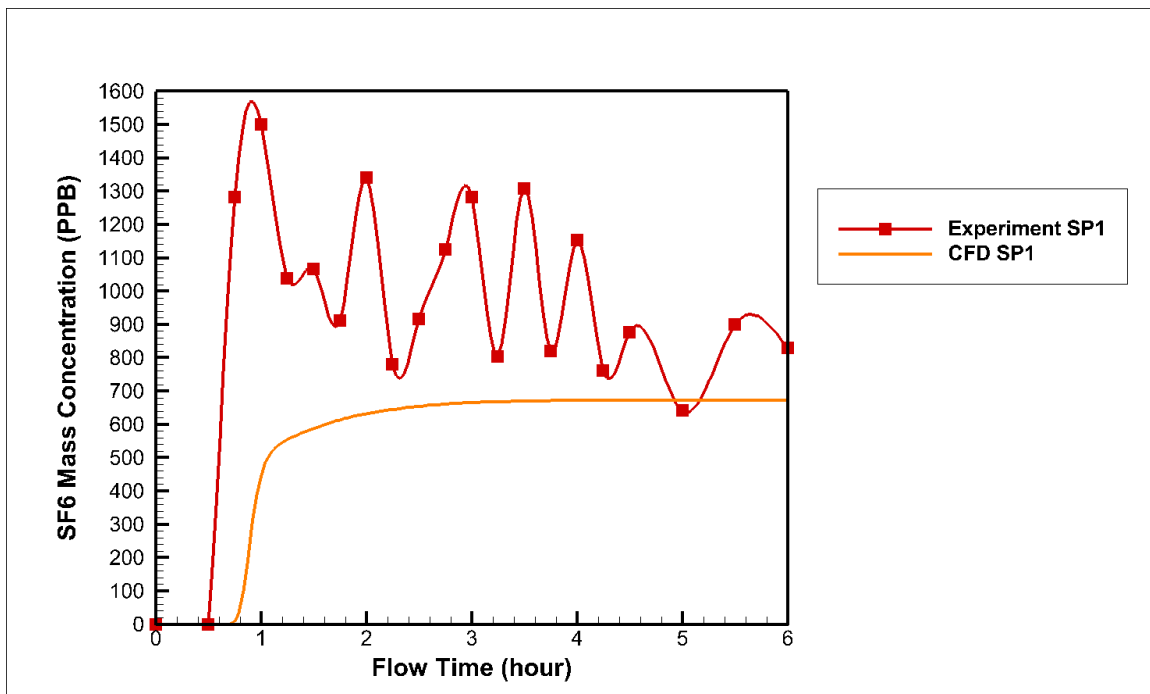
Figure 89. Comparison for the six-hour transient simulation results at SP1.

In Figure 89, the experimental results have a decreasing trend towards the stabilized CFD results during the six-hour period. Although the averaged SF₆ mass concentration in the experiment is higher than that in the CFD model, the final SF₆ mass concentration from both the experiment and CFD model are close to 700 PPB.

Figure 90. Comparison for the ten-hour transient simulation results at SP1.

A SF₆ mass concentration contour at the plane, where SP1 was located, was created and shown in Figure 91 to visualize the concentration distribution in the plane after the six-hour simulation. According to Figure 91, the range of the SF₆ mass concentration is from 0 to 7.11×10^{-7} (711 PPB). The approximate SF₆ mass concentration in the center of the contour is 700 PPB, which matches the CFD results shown in Figure 91.
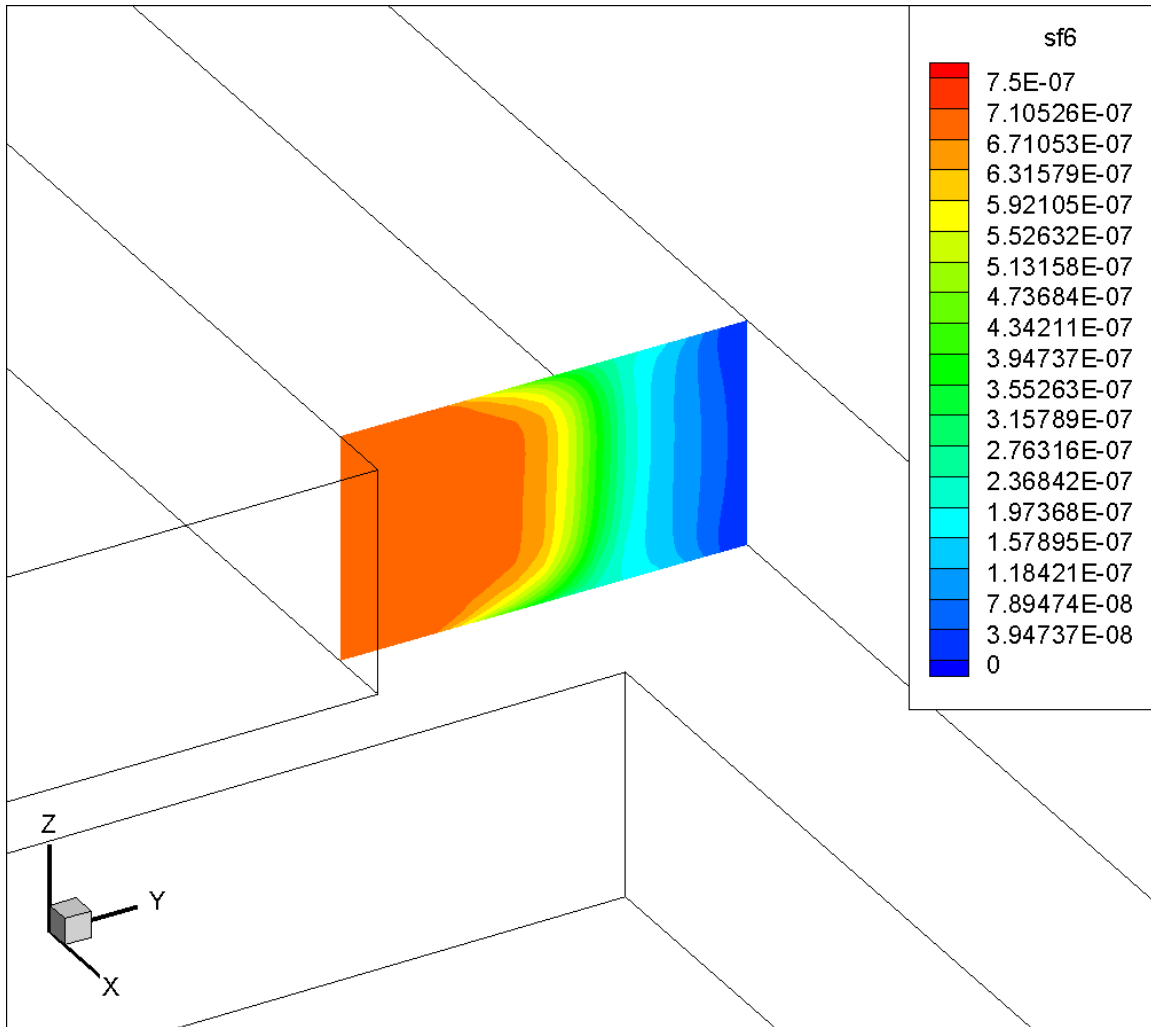
Figure 91. Visualization (in YZ plane) of SF$_6$ mass concentration distribution at SP1 in the six-hour simulation in the species transport model.

4.5.8.2.3   Comparisons on SF₆ Mass Concentration at SP2

Figure 92. Comparison for the six-hour transient simulation results at SP2.

According to Figure 92, it is clear that the SF₆ mass concentration at SP2 simulated in the CFD model is much lower than that measured in the experiment. The range for the SF₆ mass concentration in the CFD model is from 700 PPB to 1000 PPB after it reaches a relatively stable level. It still increases in the CFD model after the six-hour simulation. However, it reaches a stable level in the ten-hour simulation and the final SF₆ mass concentration is about 350 PPB as shown in Figure 93.
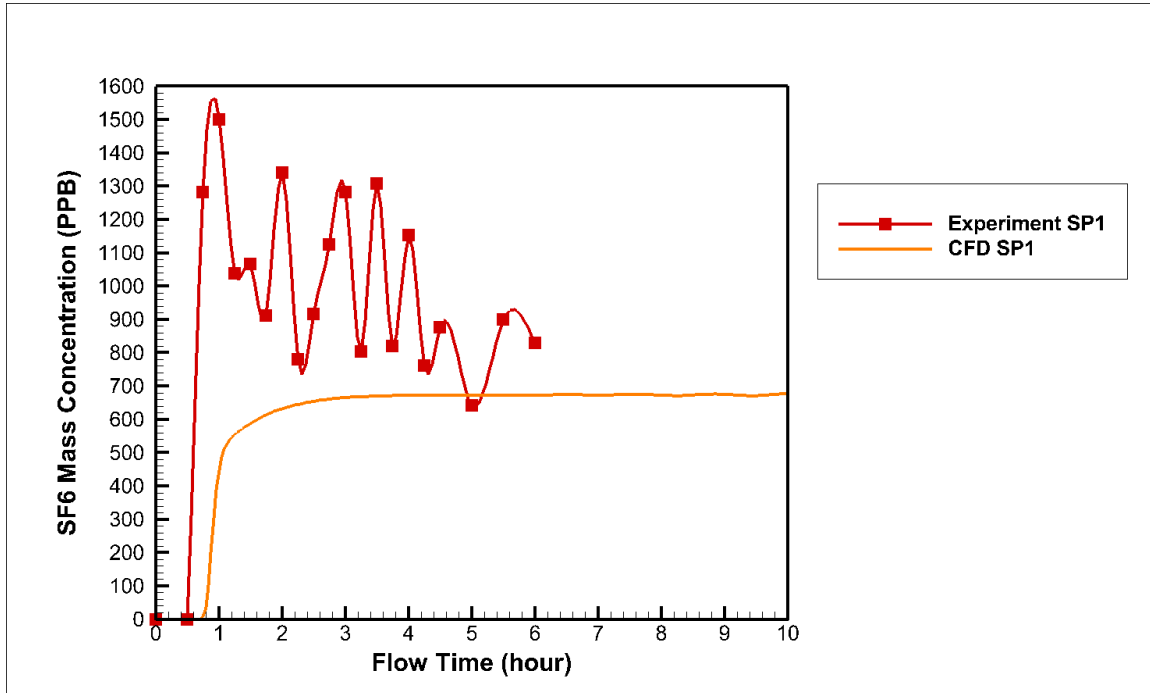
Figure 93. Comparison for the ten-hour transient simulation results at SP2.

A SF$_6$ mass concentration contour at the plane, where SP2 was located, was created and shown in Figure 94 to visualize the concentration distribution in the plane after the six-hour simulation. According to Figure 94, the range of the SF$_6$ mass concentration is from 1.98×10^{-7} (198 PPB) to 2.23×10^{-7} (223 PPB). The approximate SF$_6$ mass concentration in the center of the contour is 200 PPB, which matches the CFD results shown in Figure 92. It is a little smaller than the final SF$_6$ mass concentration in the ten-hour simulation because it still increases at the six-hour simulation.

Figure 94. Visualization (in YZ plane) of SF$_6$ mass concentration distribution at SP2 in the six-hour simulation in the species transport model.

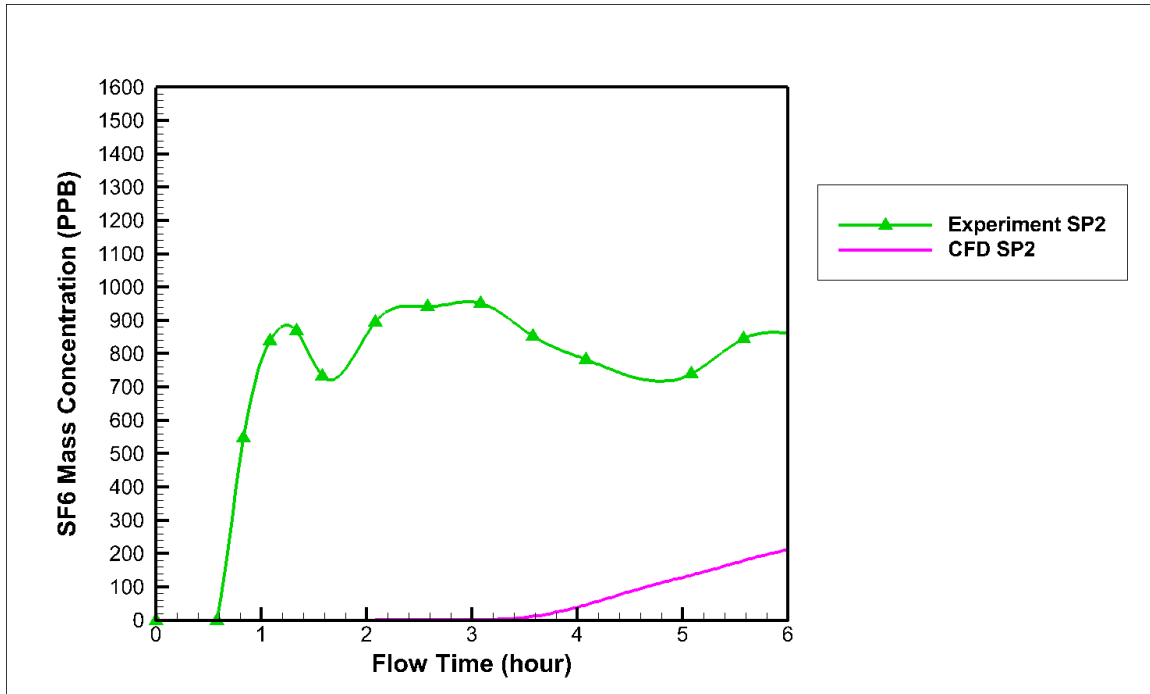**4.5.8.2.4   Comparisons on SF$_6$ Mass Concentration at SP3**

Figure 95. Comparison for the six-hour transient simulation results at SP3.

According to Figure 95, it is clear that the SF$_6$ mass concentration at SP3 simulated in the CFD model is lower than that measured in the experiment. The range for the SF$_6$ mass concentration in the CFD model is from 700 PPB to 1000 PPB after it reaches a relatively stable level. It still increases in the CFD model after the six-hour simulation. However, it reaches a stable level in the ten-hour simulation and the final SF$_6$ mass concentration is about 550 PPB as shown in Figure 96.
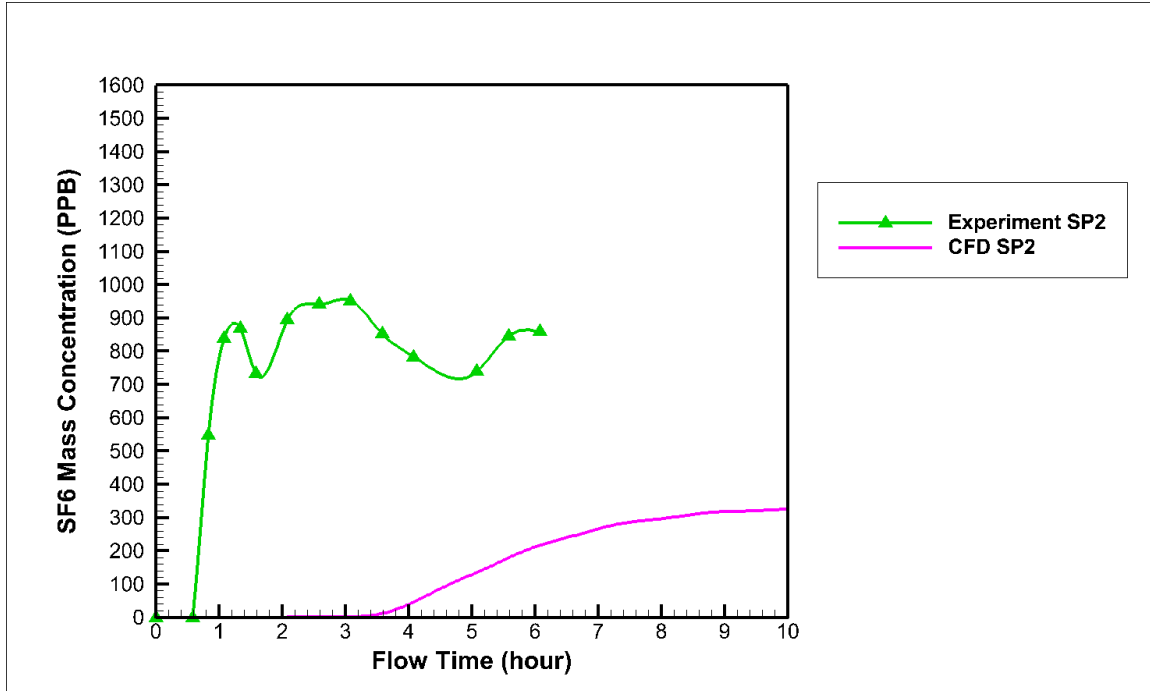
Figure 96. Comparison for the ten-hour transient simulation results at SP3.

A SF_6 mass concentration contour at the plane, where SP3 was located, was created and shown in Figure 97 to visualize the concentration distribution in the plane after the six-hour simulation. According to Figure 97, the approximate SF_6 mass concentration in the center of the contour is 550 PPB, which matches the CFD results shown in Figure 95.
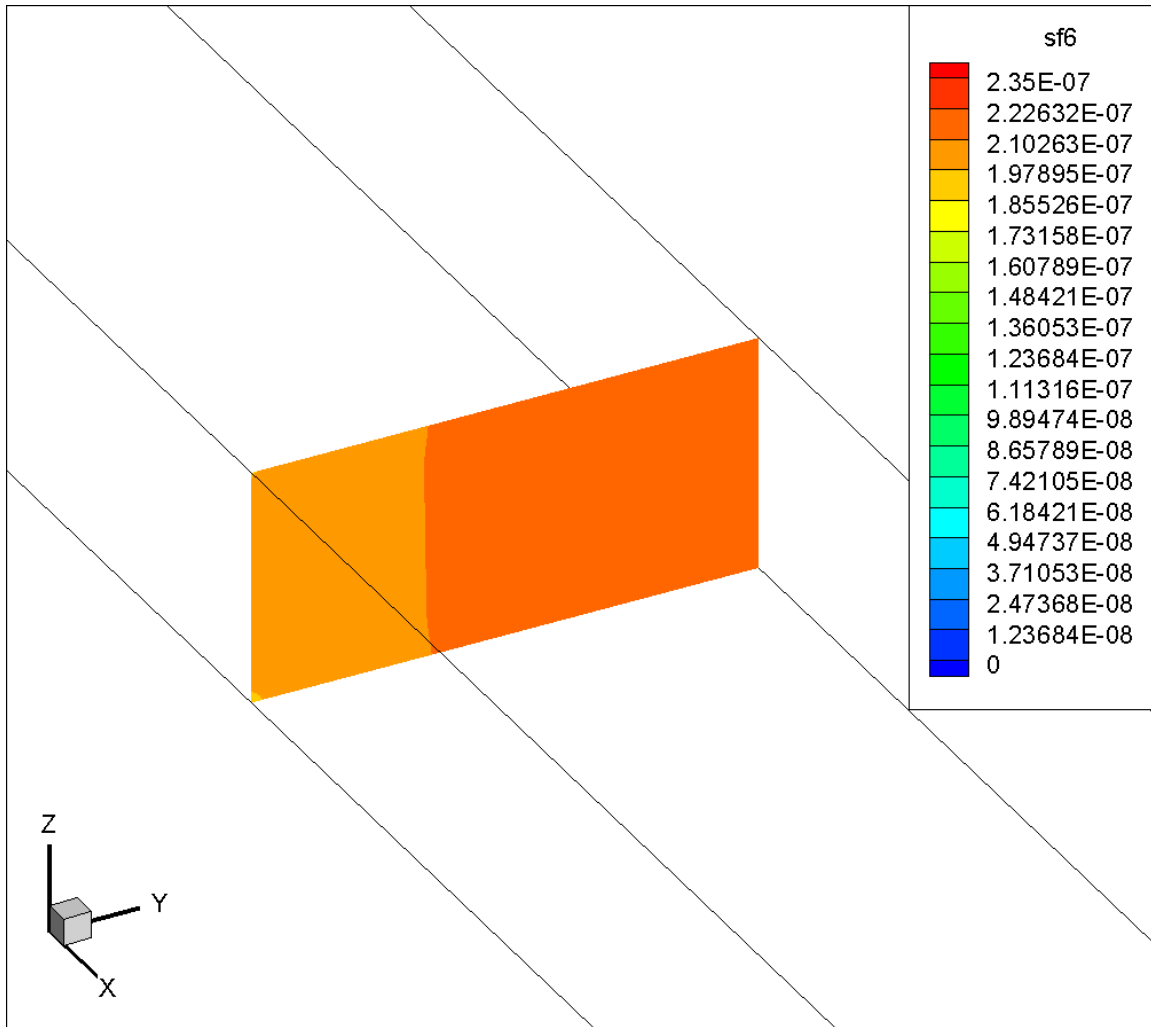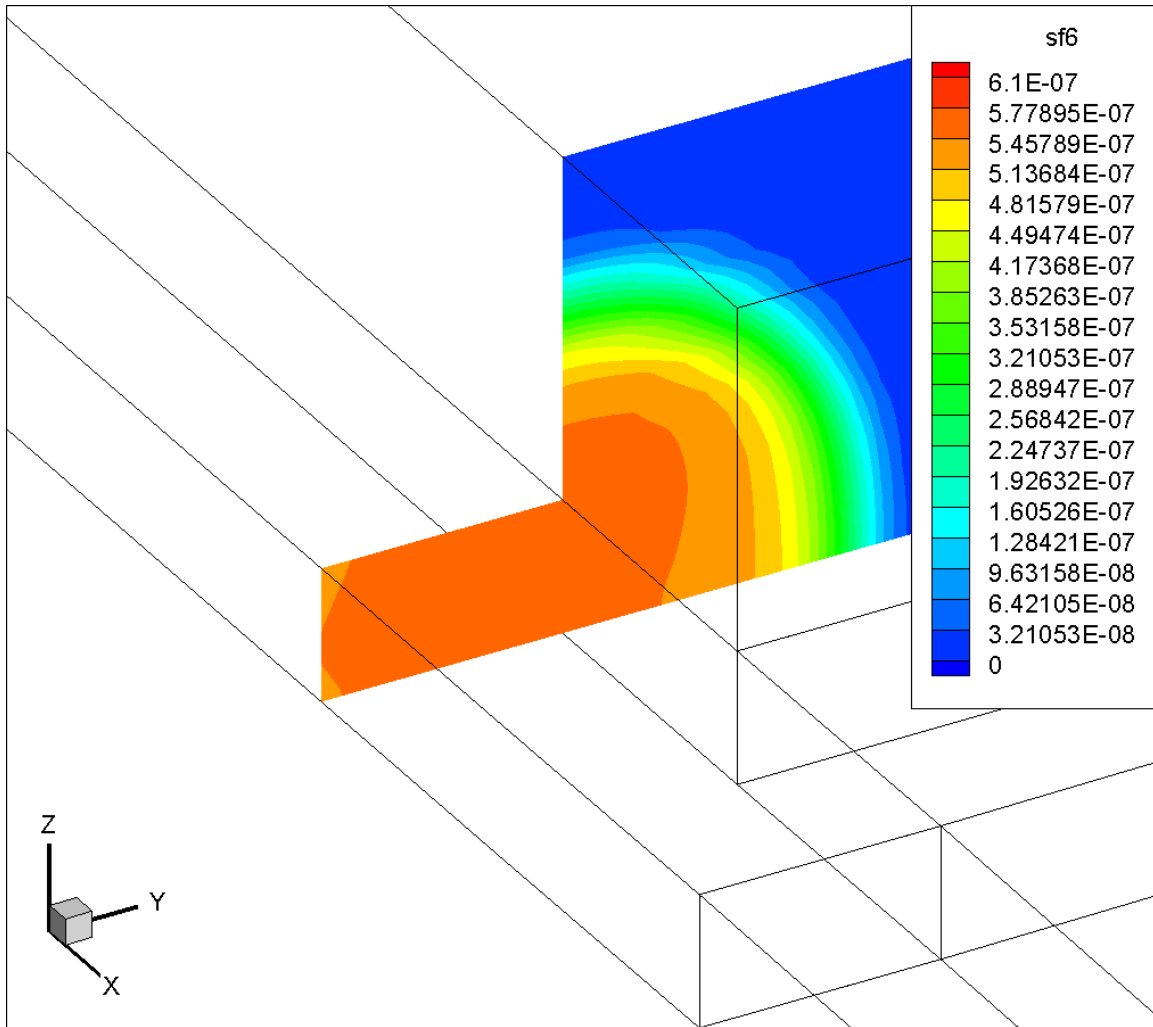
Figure 97. Visualization (in YZ plane) of SF$_6$ mass concentration distribution at SP3 in the six-hour simulation in the species transport model.

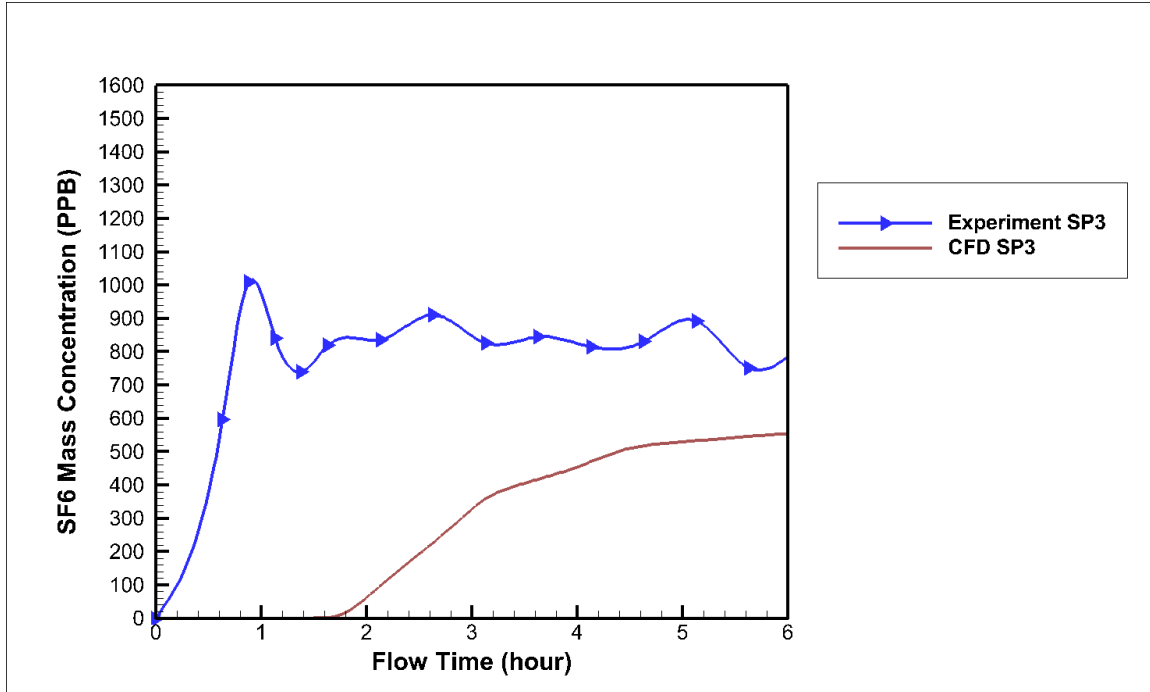**4.5.8.2.5   Comparisons on SF₆ Mass Concentration at SP9**
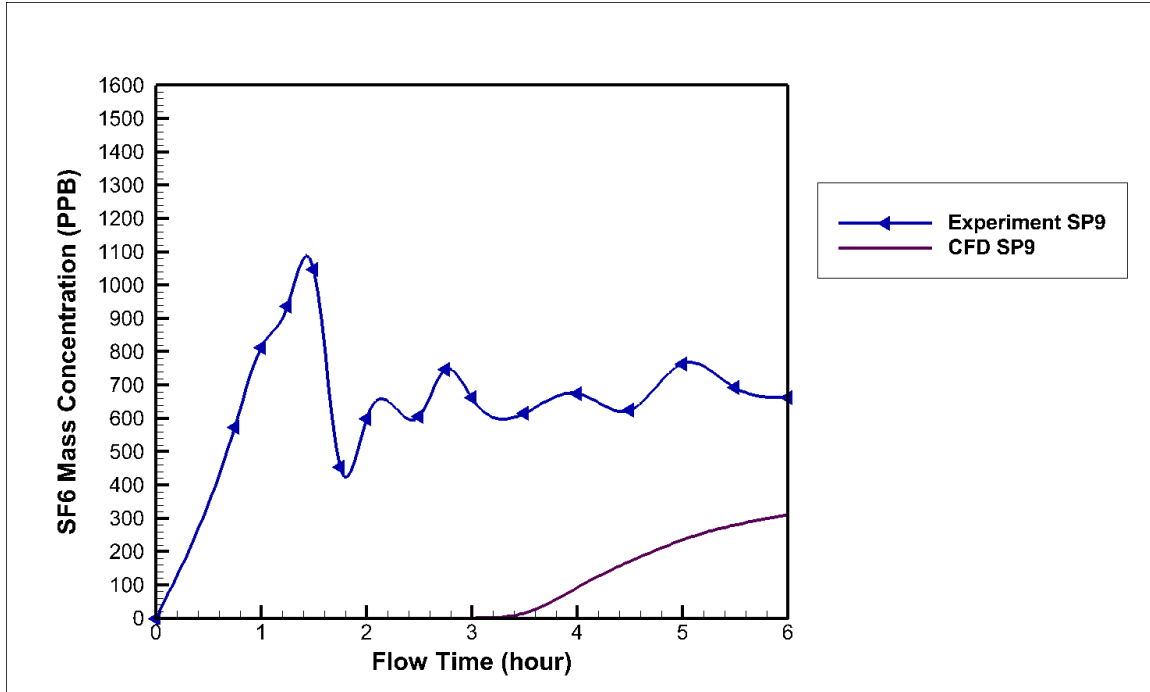
Figure 98. Comparison for the six-hour transient simulation results at SP9.

According to Figure 98, it is clear that the SF$_6$ mass concentration at SP9 simulated in the CFD model is lower than that measured in the experiment. The range for the SF$_6$ mass concentration in the CFD model is from 600 PPB to 800 PPB after it reaches a relatively stable level. It still increases in the CFD model after the six-hour simulation. However, it reaches a stable level in the ten-hour simulation and the final SF$_6$ mass concentration is about 360 PPB as shown in Figure 99.
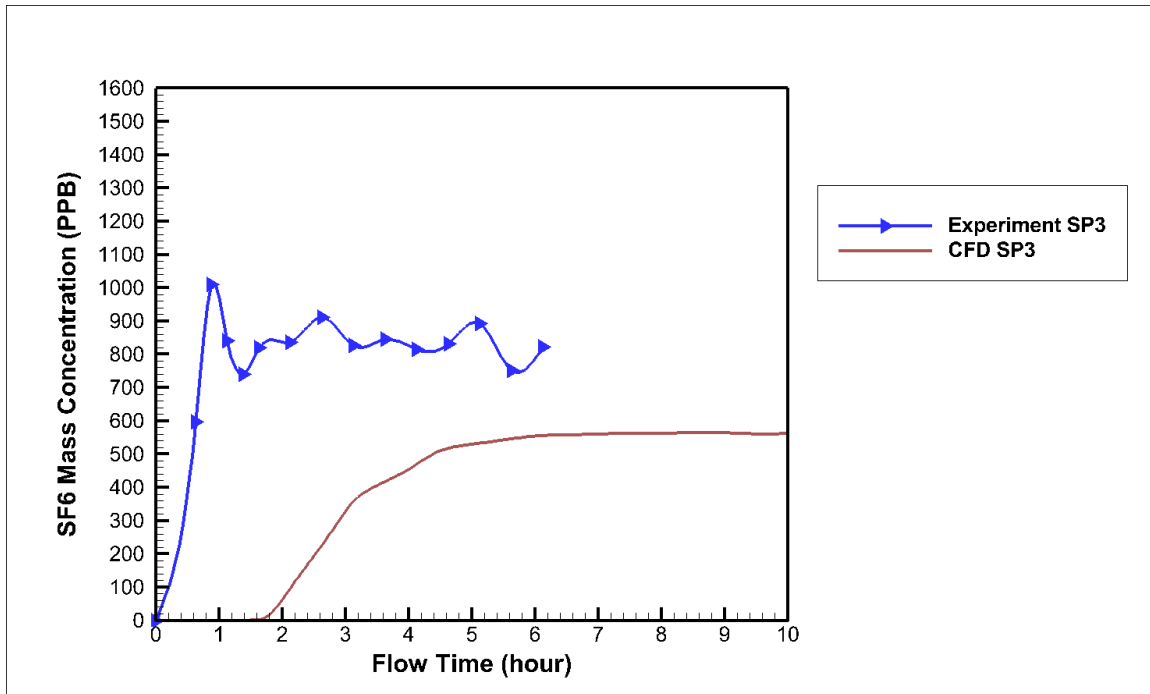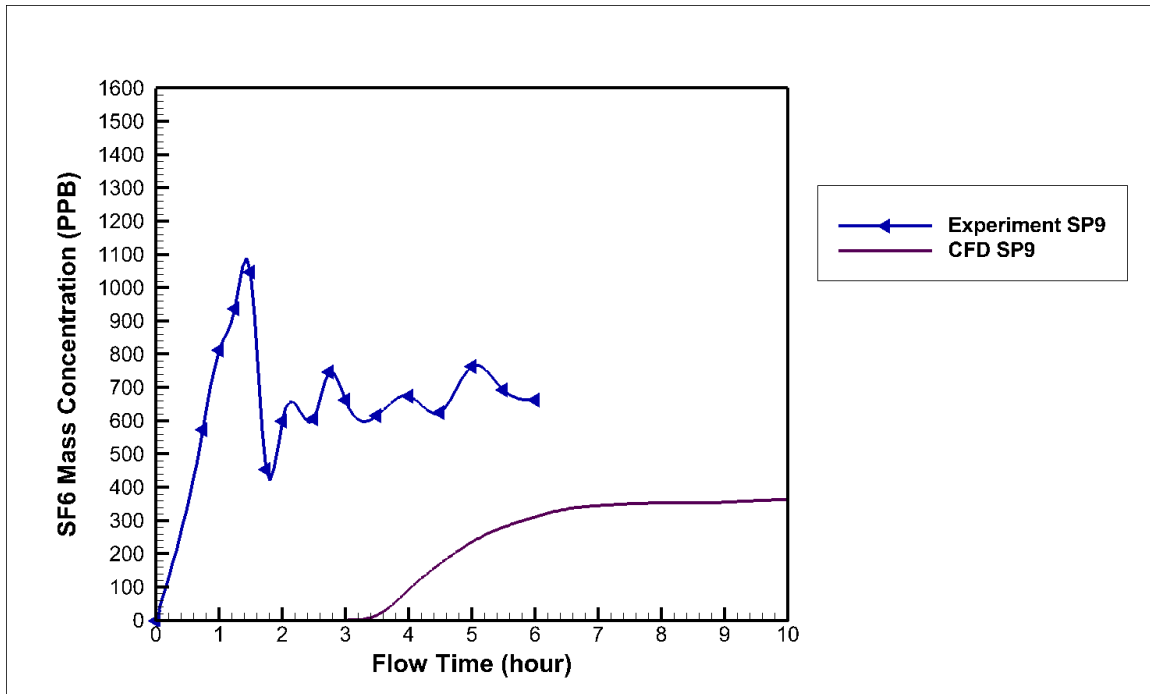
Figure 99. Comparison for the ten-hour transient simulation results at SP9.

A SF_6 mass concentration contour at the plane, where SP9 was located, was created and shown in Figure 100 to visualize the concentration distribution in the plane after the six-hour simulation. According to Figure 100, the approximate SF_6 mass concentration in the center of the contour is 320 PPB, which matches the CFD results shown in Figure 98. It is a little smaller than the final SF_6 mass concentration in the ten-hour simulation because it still increases at the six-hour simulation.
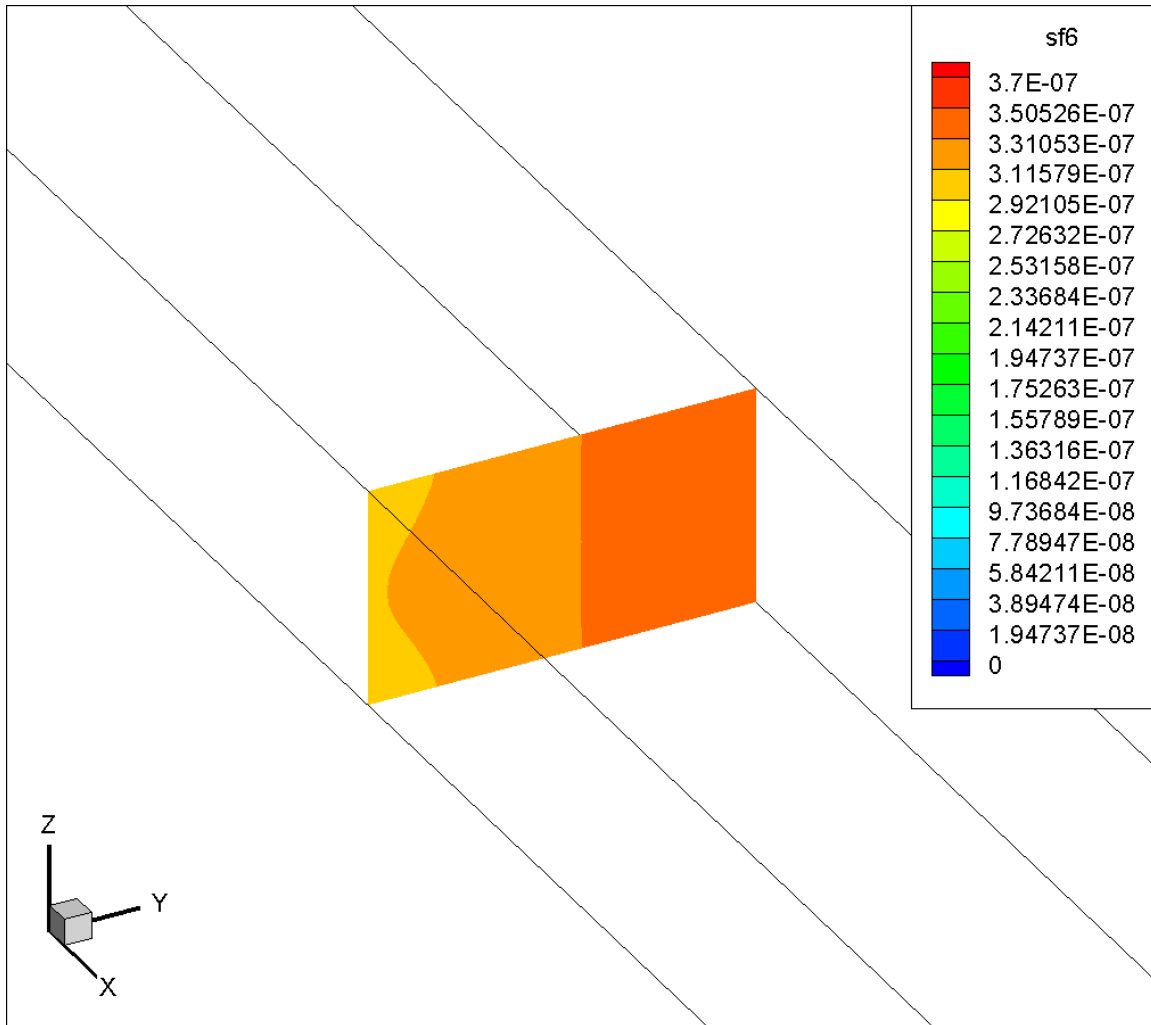
Figure 100. Visualization (in YZ plane) of SF$_6$ mass concentration distribution at SP9 in the six-hour simulation in the species transport model.

4.6 Flownex Model

4.6.1 Model Setup

Since the 3D CFD model with tracer gas was time consuming, the Flownex model was built up to get a quicker solution and it was used as a reference for the user to define the locations where the airflow needs to be carefully analyzed by using the CFD model. An overview for the Flownex model was shown in Figure 101. The results from the model were provided in Table 20. As a network modeling software, Flownex has the same setup process as VnetPC. All the inputs, except the trace element, in this Flownex model, came

directly from the VnetPC model used in the preliminary study (Zhang et al. 2014) for this study. Trace element (PADT, 2014) (in this case, SF_6) was created in the Flownex model to simulate the distribution of the SF_6 concentration in the model mine.
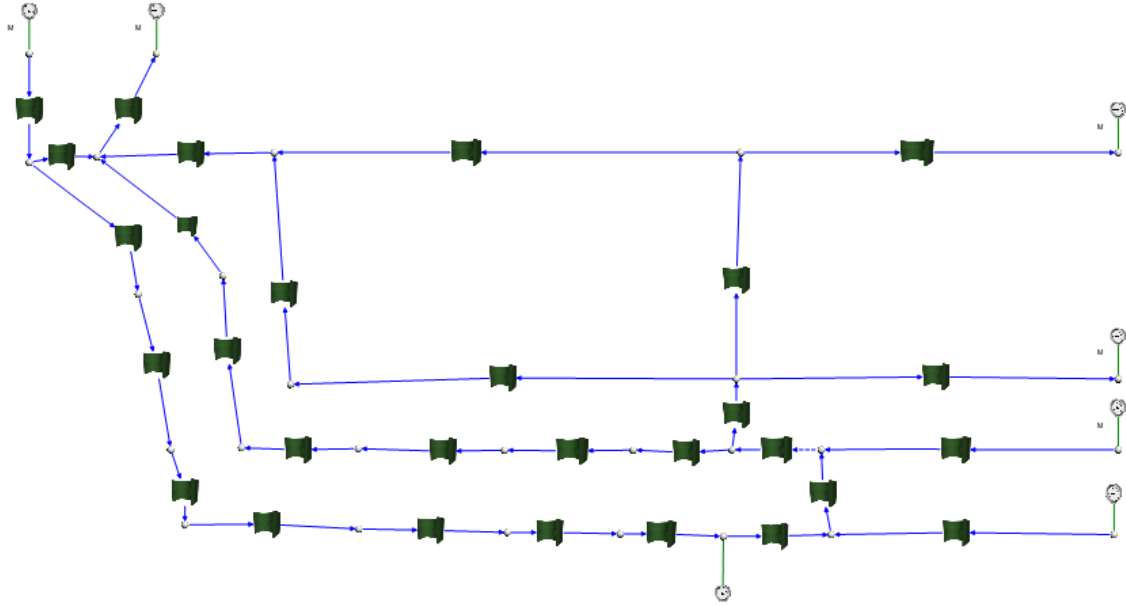
Figure 101. Plan view of the Flownex model.

4.6.2 Results

Table 20. Results from the Flownex model with tracer gas.

Sample points	Air quantity (kcfm)	SF_6 (cfm)	SF_6 (kcfm)	Flownex Results Air (kcfm)	Flownex Results SF_6 (kcfm)	Air Error (%)	SF_6 Error (%)
1	81.00	0.0129	1.29×10^{-5}	86.36	8.73×10^{-6}	6.62	32.36
2	19.60	0.0033	3.30×10^{-6}	19.59	1.98×10^{-6}	0.05	40.02
3	17.00	0.0028	2.80×10^{-6}	0.51	5.19×10^{-8}	96.98	98.15
7	53.74			53.70		0.07	
9	63.00	0.0089	8.90×10^{-6}	63.07	6.37×10^{-6}	0.10	28.41
RP1	53.60	0.0088	8.80×10^{-6}	52.38	8.72×10^{-6}	2.28	0.85

From Table 20, sample point 3 has the largest error for both airflow quantity and SF_6 concentration. Airflow quantity at sample point 3 is only 17 kcfm (1000 cubic feet per minute). It is reasonable because network modeling is not significantly sensitive to the areas with low airflow velocity. In addition, the gob was represented by four pathways with high resistance values in the Flownex model. There was no accurate gob model in

the Flownex model, which made the model less accurate compared with the 3D CFD model. Since sample point 3 is located next to the gob, both the airflow quantity and the SF_6 concentration are certainly affected due to the lack of an accurate gob model in the Flownex model.

4.7 Hybrid Model

After taking the computing time into account, a hybrid model of Fluent and Flownex become the idea to simulate both the airflow quantity and SF_6 concentration for the model mine. Working face area in the model mine was determined to be the CFD component in this case. However, according to the results from the Flownex model, sample point 3 should be taken into account in the hybrid account since the airflow near sample point 3 was complex and had the largest error compared to the experimental results. The reason for not having the area close to sample point 3 as the CFD component in this specific geometry was that the gob would be added to the CFD component together with the area around sample point 3. It would increase both the complexity and difficulty of the hybrid model, which was not the purpose of the study. The rest of the model mine was simulated in Flownex. An overview of the link was shown in Figure 102. The working face CFD component and an enlarged view for part of the mesh in the CFD model were presented in Figure 103.
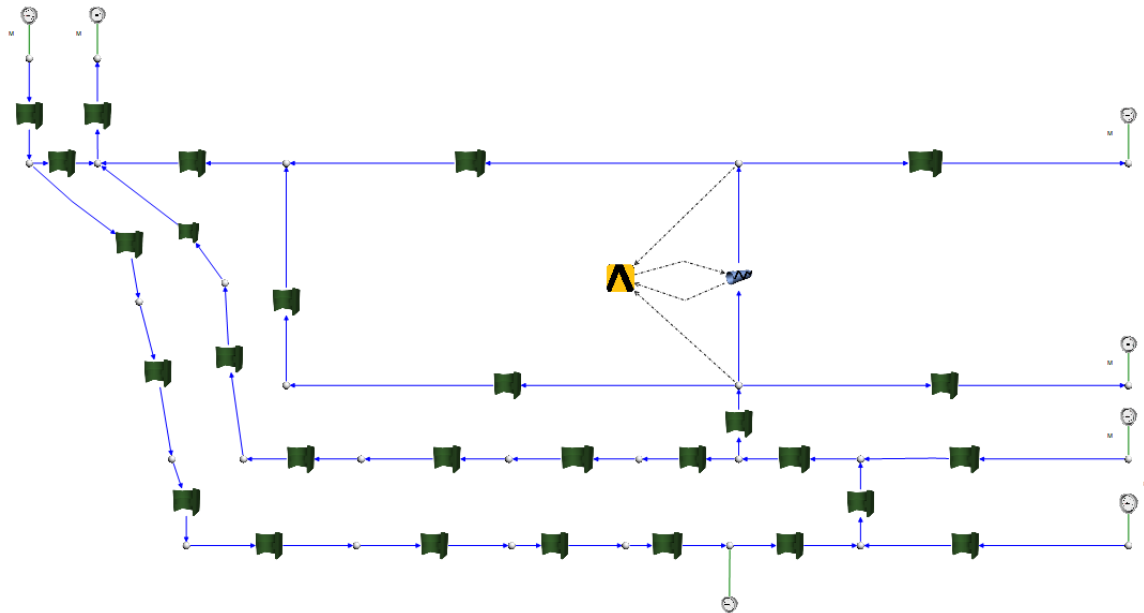
Figure 102. Plan view of the hybrid model.
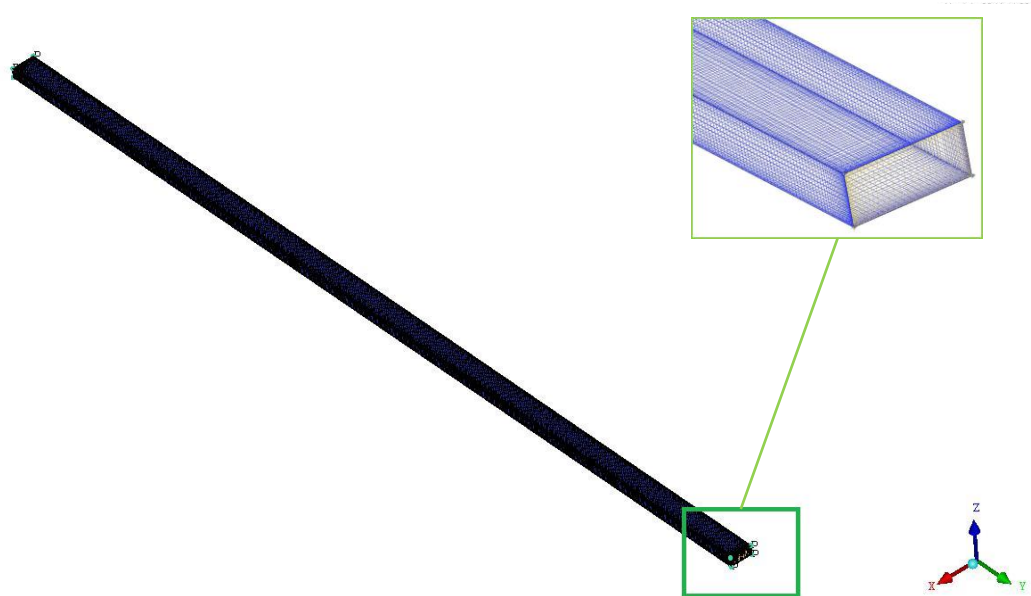
Figure 103. Overview of the CFD component and an enlarged isometric view for part of its mesh in the hybrid model.

The motivation for building up the hybrid model is to improve the accuracy of Flownex model by using a 3D CFD component model. The 3D CFD model only focuses on a component of interest, like working face and gob areas. With the help of this hybrid model, accuracy of the 3D CFD component model is also improved due to constantly updating boundary conditions obtained from Flownex system (PADT 2013). The procedure of how the hybrid model works is shown in Figure 105 (PADT 2013).

4.7.1 Hybrid Model Setup
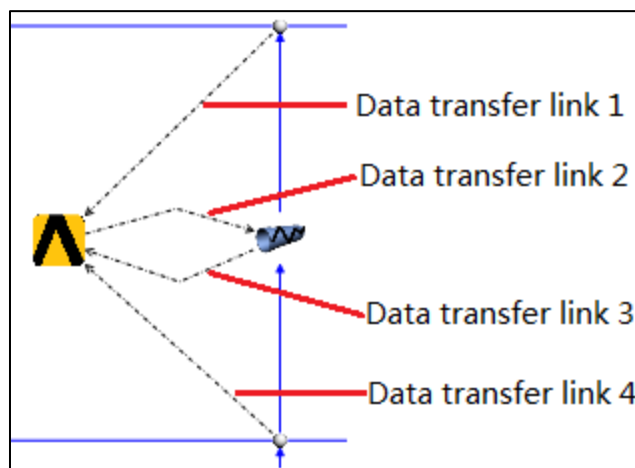
Figure 104. Data transfer links.

In Figure 102, there were four data transfer links established between Flownex and Ansys Fluent. An enlarged view of the data transfer links was shown in Figure 104. The data transfer link 3 was used to check the error of mass flow rate between Fluent and Flownex. The big yellow Ansys icon in this link acted as a Fluent controller. It passed the updated boundary conditions and mass flow rate data between Fluent and Flownex back and force. Behind the Ansys icon were large amounts of code that making this hybrid model works.

Due to the requirements of Flownex, inlet and outlet boundary conditions in the CFD model should be set as pressure-inlet and pressure-outlet separately. The inputs for inlet and outlet in the CFD component were not important because Flownex would transfer the two inputs to Fluent through data transfer link 1 and 4 (Figure 104) no matter what the inputs were at the beginning. To get more stabilized results from the CFD model, the standard k-omega model was used in this hybrid model after several tries with other turbulent models.

Average total pressure values were used for both inlet and outlet boundary conditions. The reason was that this hybrid model was made by a 1D Flownex model and a 3D CFD model. Since the pressure distribution in the 3D model was not constant, average values were taken to be filled in the 1D model.

Fluent was run 50 iterations per coupling iteration. The coupling simulation did not stop until the error of mass flow rate values reached an acceptable convergence. Here, mass flow rate values came from both Fluent and Flownex. To stabilize the coupling results, Fluent was set to not stop running even if it reaches its convergence criteria. Fluent ran much longer than it need to until the coupling converged. Flownex was converging very well in this hybrid model.
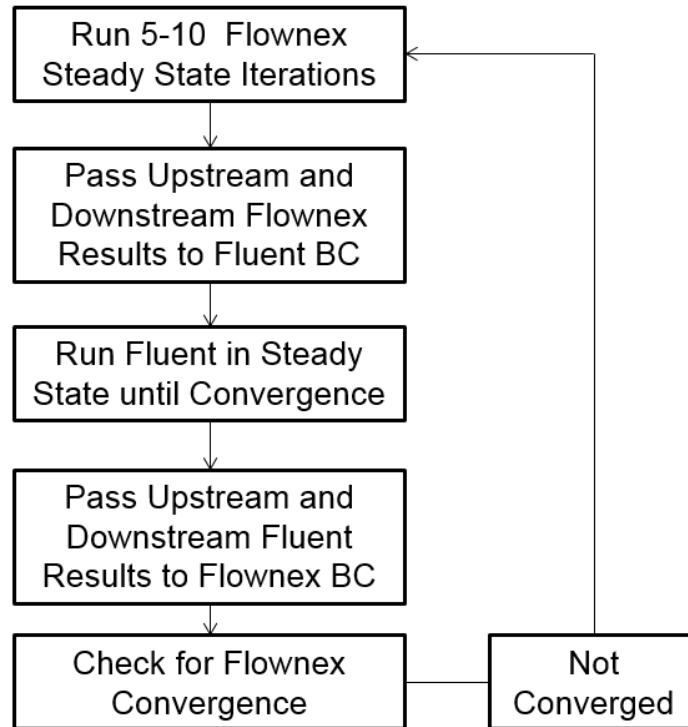
Figure 105. Flownex-Fluent flow chart.

4.7.2 Results

After about 6500 iterations in the CFD model, results converged in Fluent. Convergence history for several parameters in the CFD model was shown in Figure 106. Results from Flownex got converged only after 137 iterations. Final results from the hybrid model were shown in Table 21.
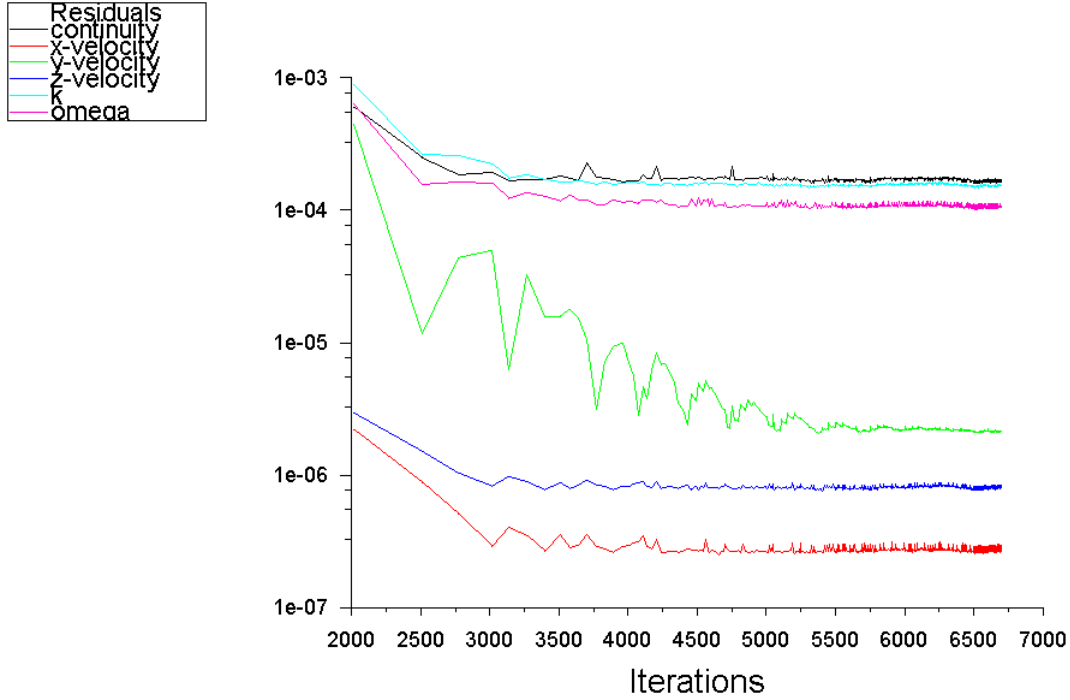
Figure 106. Convergence history for some parameters in the CFD model.

Table 21. Hybrid Model Results.

Sample points	Air quantity (kcfm)	SF$_6$ (cfm)	SF$_6$ (kcfm)	Hybrid Results Air (kcfm)	Hybrid Results SF$_6$ (kcfm)	Air Error (%)	SF$_6$ Error (%)
1	81.00	0.0129	1.29×10^{-5}	86.59	8.76×10^{-6}	6.90	32.08
2	19.60	0.0033	3.30×10^{-6}	19.59	1.98×10^{-6}	0.05	39.92
3	17.00	0.0028	2.80×10^{-6}	0.41	4.12×10^{-8}	97.60	98.53
7	53.74			53.70		0.07	
9	63.00	0.0089	8.90×10^{-6}	63.01	6.37×10^{-6}	0.02	28.47
RP1	53.60	0.0088	8.80×10^{-6}	52.60	8.76×10^{-6}	1.87	0.43

From Table 21, airflow quantity at SP3 in the hybrid model is still inconsistent with the experimental results. The reason is that gob area is not simulated in this hybrid model. SP3 is right next to the gob and airflow at SP3 is affected by the gob. The ideal solution for this case is to establish a hybrid model with gob taken into account. It means that the CFD component in the hybrid model will contain the gob and several entries connected with the gob. Then Flownex will be able to update the boundary conditions for the CFD component. However, it will be too complex if including the gob in the hybrid model in this study. The purpose of establishing this hybrid model in the study is to show that CFD can be linked with other software to get an accurate solution.

128

4.8 Results Comparisons among 3D Species Transport Model, Flownex Model, and Hybrid Model

All the results from the three important models established in this paper were compared and shown from Figure 107 to Figure 110. Because the contours of SF_6 mass concentration in the CFD models (by interpreting UDF) with and without turbulent diffusivity did not make sense, results from the two models were not compared with that from experiment and other models.
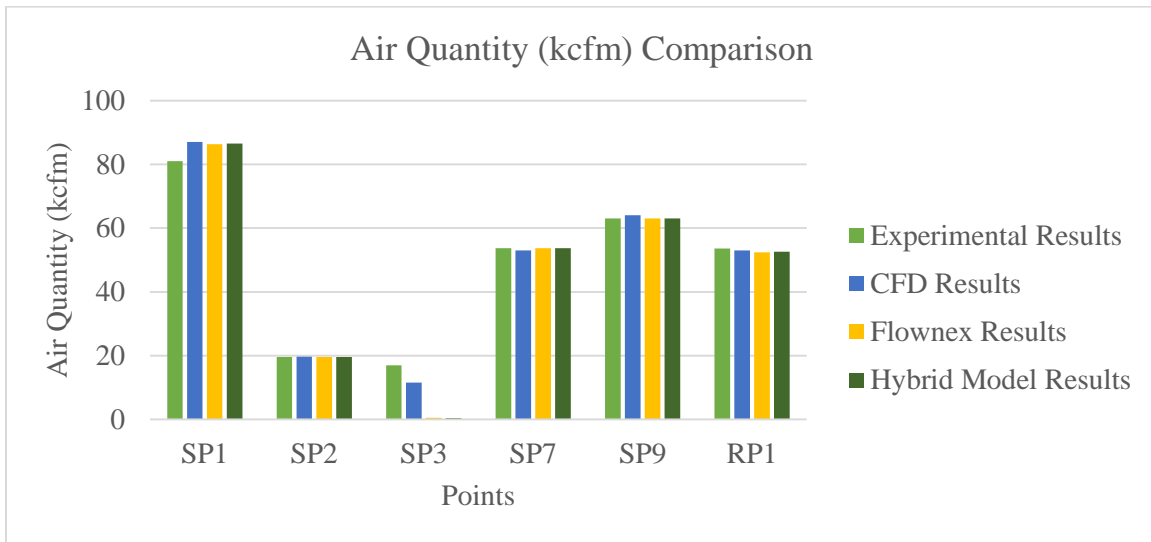
Figure 107. Airflow quantity (kcfm) comparison.
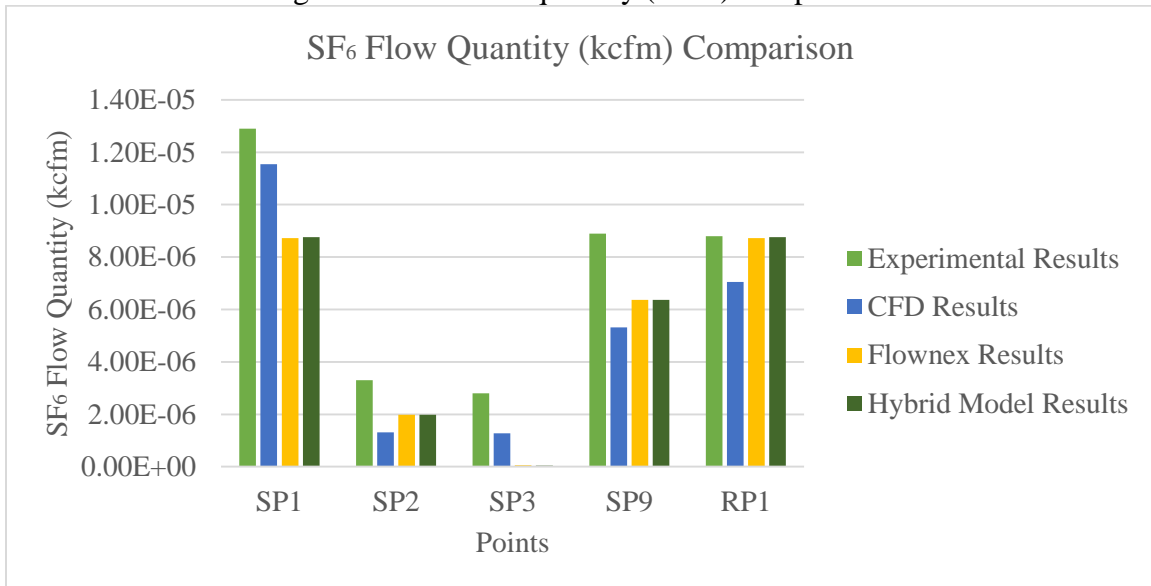
Figure 108. SF_6 flow quantity (kcfm) comparison.
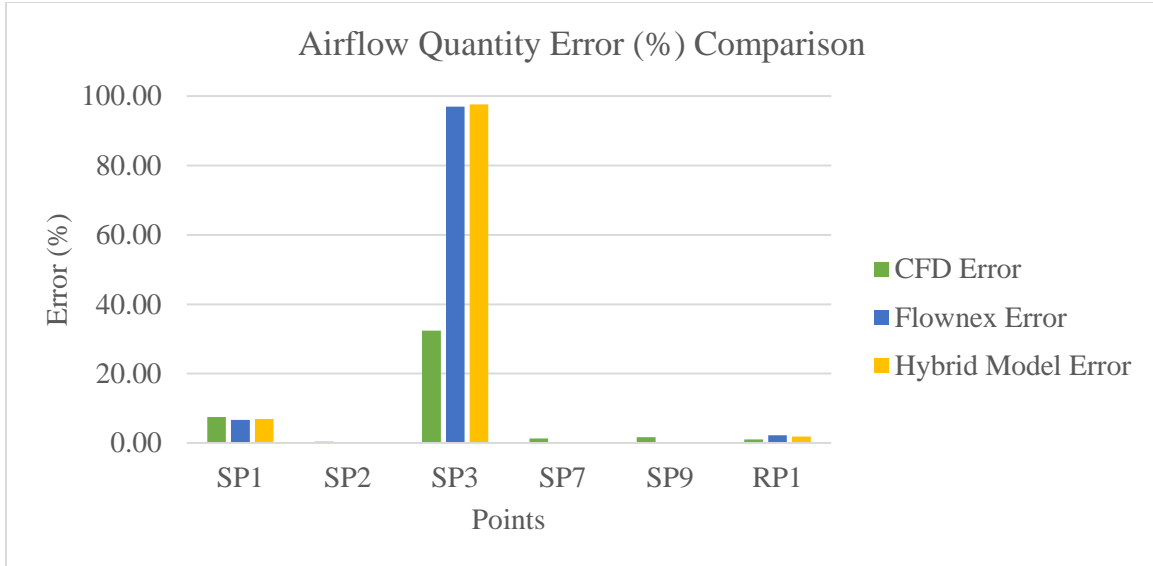
Figure 109. Airflow quantity error (%) comparison.
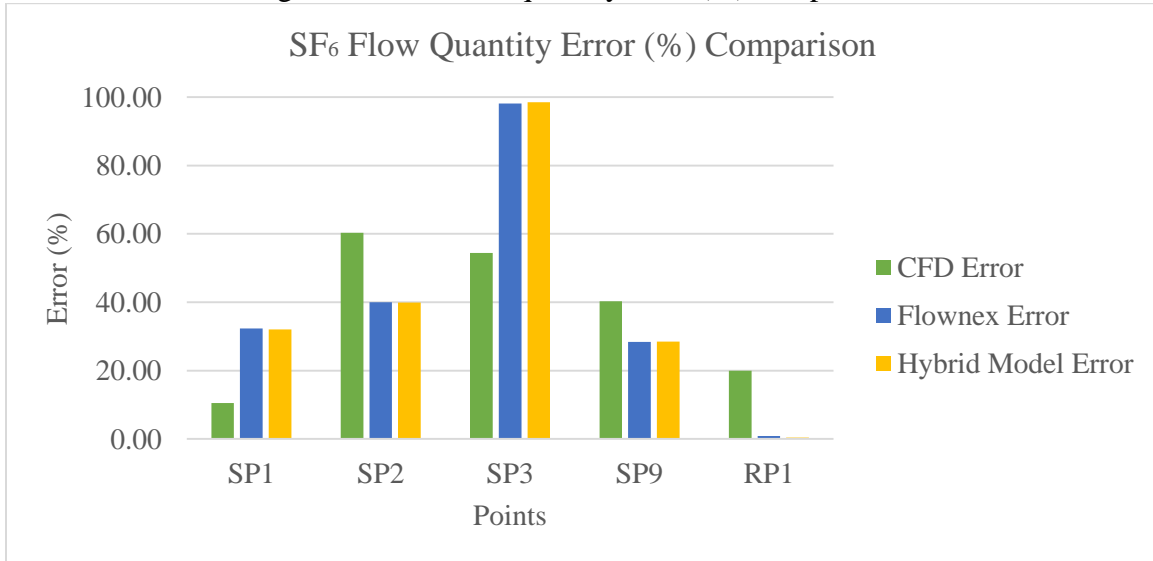
Figure 110. SF_6 flow quantity error (%) comparison.

4.9 Conclusions and Discussion

In summary, this paper mainly discusses three models, the 3D CFD model, Flownex model, and hybrid model. Based on Figure 107 to Figure 110, both airflow and SF_6 flow results at sample point 3 are inconsistent with the experimental data in both the Flownex model and the hybrid model. However, results from the 3D CFD model at SP3 matches the experimental results much better than the Flownex model and the hybrid model. In Figure 108, it looks like the experimental results are much higher than the other three

modeling results. However, the y axis in the figure represents the SF_6 flow quantity and the largest SF_6 flow quantity value is still less than 0.000014 kcfm. The comparison was made in Figure 108 to show the fact that SF_6 flow quantity from the experiment is higher than that from the three models. One reason is that SF_6 concentration was affected by the airflow recirculation at the sample points. The other reason is that experimental data is not recorded accurately due to human error and moving equipment.

Overall, the 3D CFD model are the most accurate model among the three models. However, the long computing time make the CFD model time-consuming. In terms of the results, the Flownex and hybrid model are almost the same for this mine geometry. On one hand, the CFD component in the hybrid model does not affect the results very much because the gob area was not simulated accurately. On the other hand, the hybrid model works correctly in this paper, and it verifies the coupling capability of Flownex. Moreover, the CFD component in the hybrid model will make a big difference for other cases, such as a mine gob area, and areas with low airflow velocity. The reason is that network modeling is not sensitive to the areas with low airflow velocity. If the CFD component can be applied in this areas, network modeling will be as good as the CFD model. Then the hybrid model will save both the time for building up and solving the CFD model.

5 Conclusions and Future Work

The purpose for this research was to figure out the best approach to simulate the flow behaviors in an underground mine. Both the experiment and the models with different software packages have been conducted in this research.

The field study was done in the underground mine for a six-hour period with the help of releasing-sampling SF_6 in different locations. The models created for the model mine basically consisted of network modeling and CFD modeling. Network modeling was built at first. For the network modeling, a VetPC model and a Flownex model were made. In terms of the CFD modeling, several 2D CFD models and 3D CFD models with various settings were made. Finally, a hybrid model was made.

From Chapter 3, two models were created based on the mine geometry. One was the VnetPC model provided by the mine. The other one was a 2D CFD model without the mine gob. In examining the results from these two models, the 2D CFD model appeared to be the better choice to simulate the underground mine. However, it did not take the gob into account. Besides, distribution of the SF_6 concentration was not simulated in both the VnetPC model and the 2D CFD model. Airflow quantity results from the two models were compared with the results from experiment and then the results from the two models were compared with each other. Several conclusions are made for Chapter 3. The network modeling is not sensitive to the low airflow quantity areas. Besides, an underground mine can be simulated with both a CFD model and a network model to achieve a high accuracy on the results. The network model should be created at first and the CFD model will be applied to the areas where there are large errors appearing in the network model.

To improve these models, 3D CFD models with the gob included and a Flownex model were built in Chapter 4. Since Flownex has the capability to model a trace element, Flownex was used to represent network modeling instead of VnetPC. Several 2D CFD models were created in Chapter 4 to verify the fact that the gob area had no need to be divided into five zones for this specific model mine. All the 3D CFD models were then

built up with the one-zone gob. At the same time, SF_6 concentration was simulated in the 3D CFD models. A mesh independence study and a sensitivity study on the porosity and permeability values were generated for the 3D CFD model with and without turbulent viscosity to make sure that mesh size, porosity and permeability values did not affect the results from the 3D CFD model. Another mesh independence study was performed for the 3D CFD model with species transport model. As a result. the fine mesh and the porosity and permeability values from Lolon's dissertation (Lolon 2008) were determined to be applied in both the steady-state simulation and transient simulation in the two 3D CFD models. In terms of the 3D CFD model using UDF approach, two cases (with and without turbulent diffusivity) were created for the steady-state simulation to see the effects of interpreting the turbulent diffusivity. Surprisingly, the turbulent diffusivity did not affect the 3D CFD results for this mine geometry. Then a transient simulation was established without turbulent diffusivity interpreted. Results from both the steady-state simulation and the transient simulation were carefully analyzed in Chapter 4. Because the SF_6 mass concentration contours obtained from the 3D CFD model using UDF approach cannot be explained, the 3D CFD model with species transport model was created to explore the correct results. Similar to the 3D CFD model using UDF approach, both steady-state and transient simulation were conducted in the species transport model. Results were analyzed in detail in Chapter 4.

The hybrid model was the last model built up in Chapter 4 and the purpose was to make full use of the coupling capability of Flownex. It was much easier to establish the hybrid model than the 3D CFD model for the model mine because both the Flownex part and the CFD component part were not complex. Although the results from the hybrid model was almost the same to that from the Flownex model without the CFD component, it still proved the success of the hybrid model. Since working face in the 3D CFD model was taken out and used as the CFD component in the hybrid model, it was correct to have no difference between the Flownex model and the hybrid model. If the gob area was used as the CFD component in the hybrid model, results from the hybrid model should be the same as that from the 3D CFD model. However, it will increase the complexity for building up the hybrid model, which is not the purpose of this research.

To sum up, the goal of this research is to find an optimal method to simulate an underground mine with an easy-setup and high-accuracy model. Obviously, the ideal approach will be the 3D CFD model with species transport model. But it is impractical and time consuming to simulate an entire underground mine only with the 3D CFD model. Practically, the hybrid model is the best approach to achieve the goal. The hybrid model represents a combination of network modeling and CFD model. It takes advantages of both the two models. According to the findings in this research, there are several suggestions on using this hybrid model for an underground mine.

The hybrid model is unique only when it is applied appropriately. For a large scale underground longwall mine where a 3D CFD model is impractical to use, the hybrid model will be a good fit. Areas with low airflow velocity should be simulated in the CFD component. Gob area is also required to be modeled in the CFD component.

Computing time should be considered when using the hybrid model. The hybrid model is time-saving but it also depends on how you assign the CFD component. It is not a good idea to simulate the airways without any obstacles or areas where airflow is not complex in the CFD component. The reason is that Flownex can also simulate these areas with less time on establishing and solving the model. The CFD component should be used to simulate the areas with complicated airflow, which cannot be simulated in the Flownex model. It is always good to build up a model for the entire underground longwall mine with only Flownex. Then the low airflow velocity areas can be determined.

There are also some limitations for the hybrid model. Like other modeling software, both Ansys Fluent and Flownex have numerical errors. Then the hybrid model also has some numerical errors. The hybrid model cannot simulate exactly what happens in the underground, such as equipment moves in the underground while samples are taken. Besides, turbulent models used in the CFD component in the hybrid model does not perfectly represent turbulent flow when the model mine geometry is considerably complex.

Additionally, there are some future work can be done for this research. A sensitivity study on the effects of different turbulent models on both the 3D CFD model and the CFD component in the hybrid model will be interesting to investigate. Moreover, the gob area instead of the working face can be used as the CFD component in the hybrid model.

References

Ansys. 2006. *Fluent 6.3 User's Guide*.

Ansys. 2009a. *Ansys Fluent 12.0 Theory Guide*.

Ansys. 2009b. *Ansys Fluent 12.0 UDF Manual*.

Edwards, J C, and C C Hwang. 2006. "CFD Modeling of Fire Spread Along
    Combustibles in A Mine Entry." In *SME Annual Meeting*, St. Louis, Missouri, 1–5.

Esterhuizen, G, and C Karacan. 2007. "A Methodology for Determining Gob
    Permeability Distributions and Its Application to Reservoir Modeling of Coal Mine
    Longwalls." In *SME Annual Meeting*, Denver, CO, 1–6.

Gerwin, H., W. Scherer, and E. Teuchert. 1989. "The TINTE Modular Code System for
    Computational Simulation of Transient Processes in the Primary Circuit of a Pebble-
    Bed High-Temperature Gas-Cooled Reactor." *Nuclear Science and Engineering* 103:
    302–12.

Heerden, Johan Van, and Peter Sullivan. 1993. "The Application of CFD for Evaluation
    of Dust Suppression and Auxiliary." In *The 6th US Mine Ventilation Symposium*,
    Salt Lake City, Utah.

Huang, T H. 2008. "Integrated System CFD Modelling of the Flow Distribution." In
    Proceedings of the 16th International Conference on Nuclear Engineering, Orlando,
    Florida, USA, 1–7.

Janse Van Rensburg, J. J., and M. Kleingeld. 2010. "A CFD Method to Evaluate the
    Integrated Influence of Leakage and Bypass Flows on the PBMR Reactor Unit."
    Nuclear Engineering and Design 240(11): 3841–50.
    http://dx.doi.org/10.1016/j.nucengdes.2010.08.011.

Jong, E. 2013. "Development and Evaluation of a Permeation Plug Release Vessel
    (PPRV) for the Release of Perfluoromethylcyclohexane (PMCH) in Underground
    Mine Tracer Gas Studies." Virginia Polytechnic and State University.

Karacan, C Ö, T Ren, and R. Balusu. 2008. "Advances in Grid-Based Numerical
    Modeling Techniques for Improving Gas Management in Coal Mines." In *12th
    U.S./North American Mine Ventilation Symposium*, Pittsburgh, Pennsylvania, USA,
    313–20.

Kelsey, Adrian et al. 2003. "CFD Modelling of Methane Movement in Mines Ian S
    Lowndes David Whittles." In Johannesburg, South Africa, 475–86.

Lazzara, C.P., and F.J. Perzak. 1987. "Effect of Ventilation on Conveyor Belt Fires." In *Symposium on Safety in Coal Mining*, Pretoria, South Africa.

Lolon, S.A. 2008. "Computational Fluid Dynamics Simulation Study on Hot Spot Location in a Longwall Mine Gob." The University of Utah.

Marais, D. 2007. "Validation of the Point Kinetic Neutronic Model of the PBMR." Potchefstroom Campus of the North-West University Supervisor:

Olivier, Jacobus C. 2005. "Network Modelling of Transient Heat Exchanger Performance." Potchefstroom University for Christian Higher Education.

PADT. 2013. *Flownex–Fluent Link*.

PADT. 2014. *Flownex General User Manual*.

Ren, T, and R Balusu. 2005. "CFD Modelling of Goaf Gas Migration to Improve the Control of Spontaneous Combustion in Longwalls." In Brisbane, QLD, 26–28.

Ren, T, R Balusu, and C Claassen. 2011. "Computational Fluid Dynamics Modelling of Gas Flow Dynamics in Large Longwall Goaf Areas." In Wollongong, NSW, 24–30.

Ren, T, R Balusu, and P Humphries. 2005. "Development of Innovative Goaf Inertisation Practices to Improve Coal Mine Safety." In *COAL OPERATORS' CONFERENCE*, Brisbane, QLD, 26–28.

Scheidegger, A.E. 1957. *The Physics of Flow through Porous Media*. New York: The Macmillan Co.

Slabbert, Rohan. 2011. "Thermal-Hydraulics Simulation of a Benchmark Case for a Typical Materials Test Reactor Using FLOWNEX." North-West University.

Smith, A C, and L Yuan. 2008. "Simulation of Spontaneous Heating in Longwall Gob Area with a Bleederless Ventilation System." *Mining Engineering* (August): 61–66.

Walter, Ayelet, Alexander Schulz, and Günter Lohnert. 2004. "Comparison of Two Models for a Pebble Bed Modular Reactor Core Coupled to a Brayton Cycle." In *2nd International Topical Meeting on HIGH TEMPERATURE REACTOR TECHNOLOGY*, Beijing, China.

Xu, Guang. 2013. "Remote Characterization of Underground Ventilation Systems Using Tracer Gas and CFD." Virginia Polytechnic Institute & State University.

Yuan, L, and A C Smith. 2008a. *Computational Fluid Dynamics Modeling of Spontaneous Heating in Longwall Gob Areas*.

Yuan, L, Smith, A. 2008b. "Effects of Ventilation and Gob Characteristics on Spontaneous Heating in Longwall Gob Areas." In *12th U.S./North American Mine Ventilation Symposium*, Pittsburgh, Pennsylvania, USA.

Yuan, L, Alex C Smith, and Jürgen F Brune. 2006. "Computational Fluid Dynamics Study on the Ventilation Flow Paths in Longwall Gobs." In *11th US/North American Mine Ventilation Symposium*, Pennsylvania, USA.

Zhang, H et al. 2014. "The Feasibility of Hybrid Network and CFD Modeling for Mine Ventilation Applications." In Salt Lake City, UT, 1–4.

Appendix
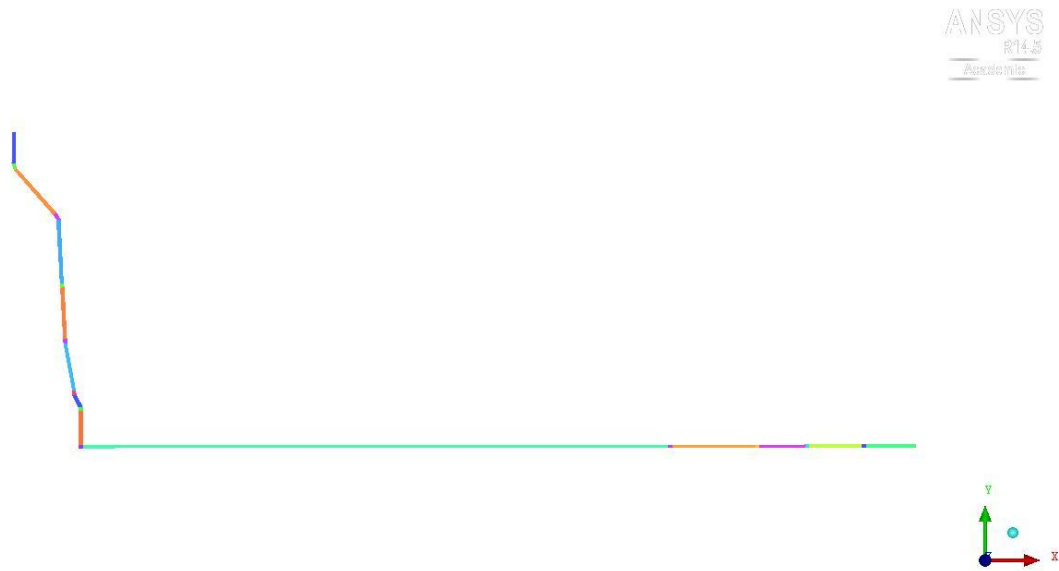
Figure 111. Plan view of part1 in the 3D CFD model with tracer gas.
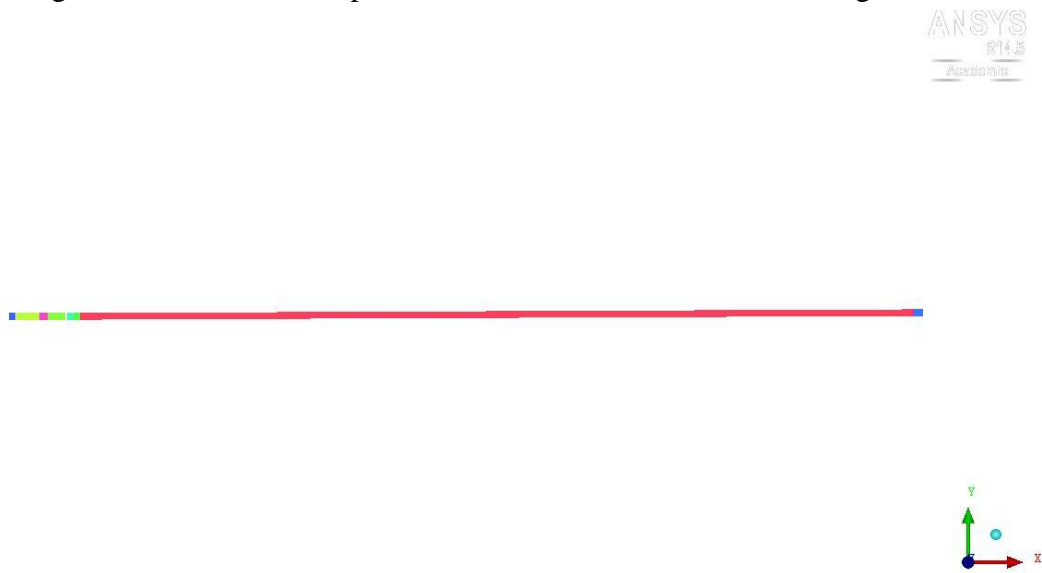
Figure 112. Plan view of part2 in the 3D CFD model with tracer gas.
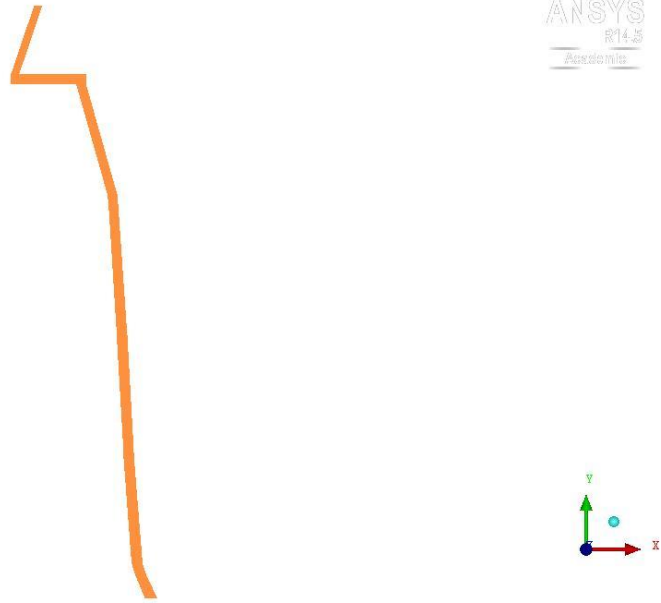
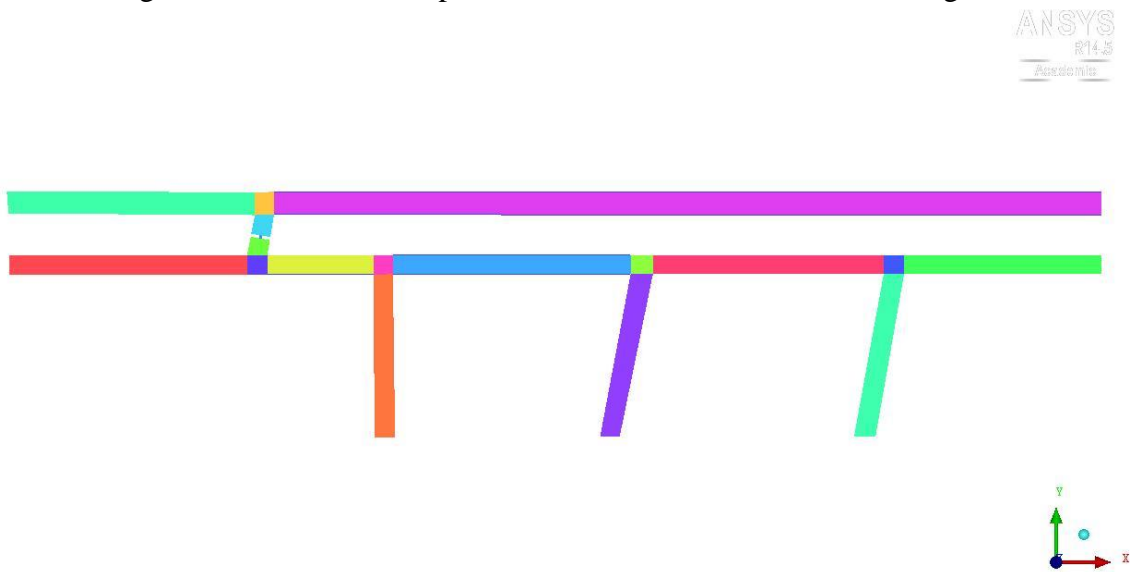Figure 113. Plan view of part3 in the 3D CFD model with tracer gas.

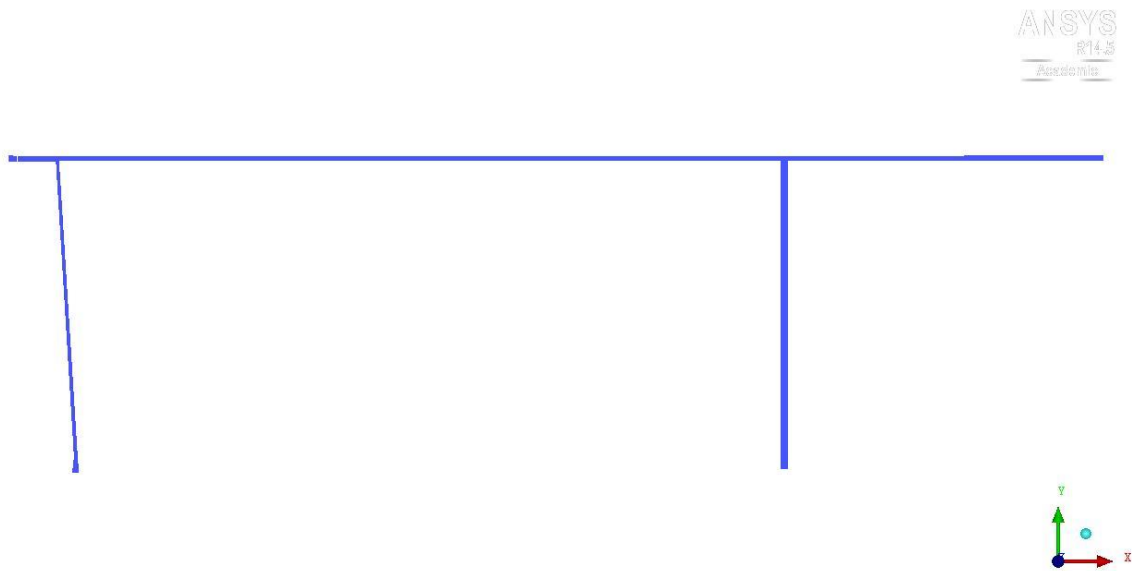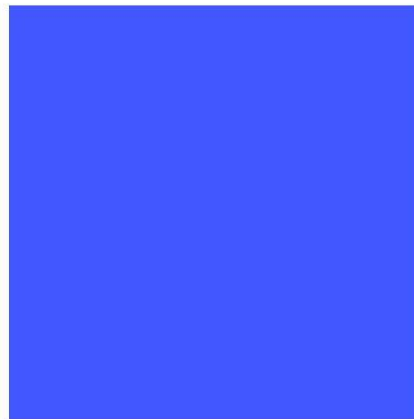Figure 114. Plan view of part4 in the 3D CFD model with tracer gas.

Figure 115. Plan view of part5 in the 3D CFD model with tracer gas.

Figure 116. Plan view of part6 in the 3D CFD model with tracer gas.

Figure 117. Plan view of part7 in the 3D CFD model with tracer gas.

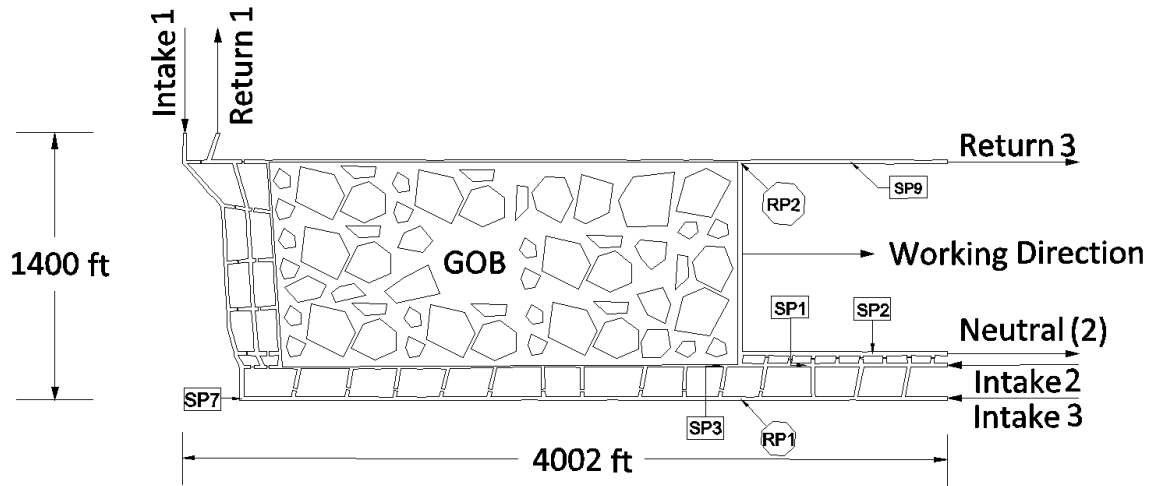Figure 118. Plan view of part8 in the 3D CFD model with tracer gas.

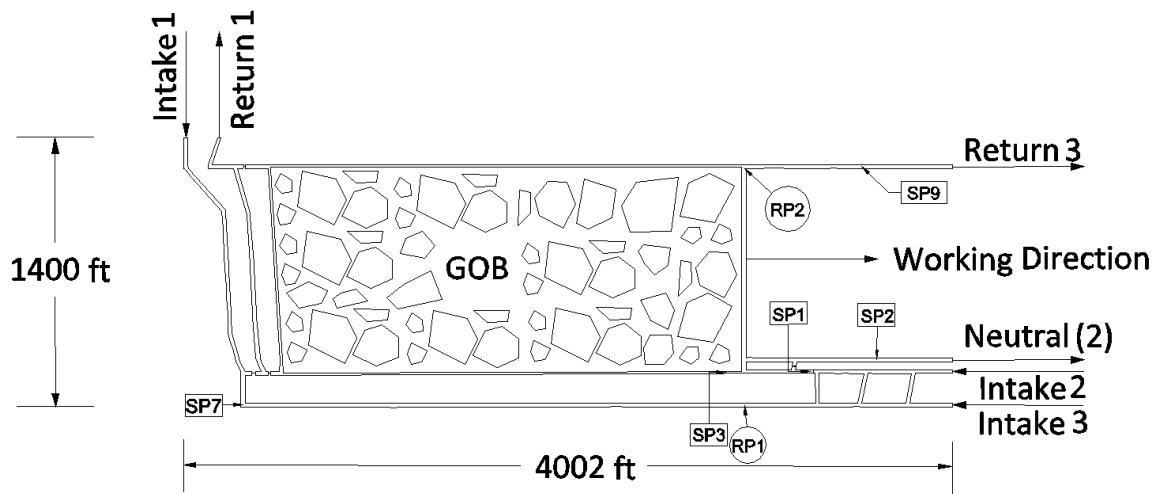Figure 119. Original geometry of the mine (plan view).

Figure 120. Simplified geometry of the mine (plan view).

Table 22. Results from the case when porosity is 0.15 for the porosity and permeability sensitivity study.

Sample points	Air quantity (kcfm)	SF$_6$ (cfm)	SF$_6$ (kcfm)	Fluent Results Air (kcfm)	Fluent Results SF$_6$ (kcfm)	Air Error (%)	SF$_6$ Error (%)
1	81.00	0.0129	1.29×10^{-5}	86.59	8.98×10^{-6}	6.90	30.38
2	19.60	0.0033	3.30×10^{-6}	19.60	1.99×10^{-6}	0.00	39.61
3	17.00	0.0028	2.80×10^{-6}	16.60	1.69×10^{-6}	2.34	39.70
7	53.74			53.74		0.00	
9	63.00	0.0089	8.90×10^{-6}	62.99	6.39×10^{-6}	0.01	28.22
RP1	53.60	0.0088	8.80×10^{-6}	52.58	8.83×10^{-6}	1.90	0.37

Table 23 Results from the case when porosity is 0.2 for the porosity and permeability sensitivity study.

Sample points	Air quantity (kcfm)	SF$_6$ (cfm)	SF$_6$ (kcfm)	Fluent Results Air (kcfm)	Fluent Results SF$_6$ (kcfm)	Air Error (%)	SF$_6$ Error (%)
1	81.00	0.0129	1.29×10^{-5}	86.79	8.98×10^{-6}	7.14	30.37
2	19.60	0.0033	3.30×10^{-6}	19.60	1.99×10^{-6}	0.01	39.76
3	17.00	0.0028	2.80×10^{-6}	16.63	1.69×10^{-6}	2.20	39.76
7	53.74			53.74		0.00	
9	63.00	0.0089	8.90×10^{-6}	62.99	6.38×10^{-6}	0.01	28.33
RP1	53.60	0.0088	8.80×10^{-6}	52.79	8.83×10^{-6}	1.51	0.37

Table 24. Results from the case when porosity is 0.24 for the porosity and permeability sensitivity study.

Sample points	Air quantity (kcfm)	SF$_6$ (cfm)	SF$_6$ (kcfm)	Fluent Results Air (kcfm)	Fluent Results SF$_6$ (kcfm)	Air Error (%)	SF$_6$ Error (%)
1	81.00	0.0129	1.29×10^{-5}	86.88	8.98×10^{-6}	7.26	30.37
2	19.60	0.0033	3.30×10^{-6}	19.60	1.99×10^{-6}	0.00	39.82
3	17.00	0.0028	2.80×10^{-6}	15.47	1.57×10^{-6}	9.02	44.02
7	53.74			53.74		0.00	
9	63.00	0.0089	8.90×10^{-6}	62.99	6.36×10^{-6}	0.01	28.56
RP1	53.60	0.0088	8.80×10^{-6}	52.87	8.82×10^{-6}	1.37	0.28

Table 25. Results from the case when porosity is 0.26 for the porosity and permeability sensitivity study.

Sample points	Air quantity (kcfm)	SF$_6$ (cfm)	SF$_6$ (kcfm)	Fluent Results Air (kcfm)	Fluent Results SF$_6$ (kcfm)	Air Error (%)	SF$_6$ Error (%)
1	81.00	0.0129	1.29×10^{-5}	86.85	8.99×10^{-6}	7.22	30.34
2	19.60	0.0033	3.30×10^{-6}	19.60	1.99×10^{-6}	0.00	39.79
3	17.00	0.0028	2.80×10^{-6}	15.37	1.56×10^{-6}	9.57	44.33
7	53.74			53.74		0.00	
9	63.00	0.0089	8.90×10^{-6}	62.99	6.36×10^{-6}	0.01	28.55
RP1	53.60	0.0088	8.80×10^{-6}	52.83	8.82×10^{-6}	1.44	0.25

Table 26. Results from the case when porosity is 0.3 for the porosity and permeability sensitivity study.

Sample points	Air quantity (kcfm)	SF$_6$ (cfm)	SF$_6$ (kcfm)	Fluent Results Air (kcfm)	Fluent Results SF$_6$ (kcfm)	Air Error (%)	SF$_6$ Error (%)
1	81.00	0.0129	1.29×10^{-5}	86.77	8.98×10^{-6}	7.12	30.39
2	19.60	0.0033	3.30×10^{-6}	19.60	1.99×10^{-6}	0.01	39.75
3	17.00	0.0028	2.80×10^{-6}	17.36	1.76×10^{-6}	2.13	37.09
7	53.74			53.74		0.00	
9	63.00	0.0089	8.90×10^{-6}	62.99	6.39×10^{-6}	0.01	28.25
RP1	53.60	0.0088	8.80×10^{-6}	52.78	8.83×10^{-6}	1.54	0.37

Table 27. Results from the case when porosity is 0.35 for the porosity and permeability sensitivity study.

Sample points	Air quantity (kcfm)	SF$_6$ (cfm)	SF$_6$ (kcfm)	Fluent Results Air (kcfm)	Fluent Results SF$_6$ (kcfm)	Air Error (%)	SF$_6$ Error (%)
1	81.00	0.0129	1.29×10^{-5}	86.79	8.99×10^{-6}	7.15	30.34
2	19.60	0.0033	3.30×10^{-6}	19.60	1.99×10^{-6}	0.01	39.75
3	17.00	0.0028	2.80×10^{-6}	16.28	1.65×10^{-6}	4.25	41.02
7	53.74			53.74		0.00	
9	63.00	0.0089	8.90×10^{-6}	62.99	6.37×10^{-6}	0.01	28.47
RP1	53.60	0.0088	8.80×10^{-6}	52.78	8.82×10^{-6}	1.53	0.26

Table 28. Results from the case when porosity is 0.4 for the porosity and permeability sensitivity study.

Sample points	Air quantity (kcfm)	SF$_6$ (cfm)	SF$_6$ (kcfm)	Fluent Results Air (kcfm)	Fluent Results SF$_6$ (kcfm)	Air Error (%)	SF$_6$ Error (%)
1	81.00	0.0129	1.29×10^{-5}	86.81	8.98×10^{-6}	7.17	30.39
2	19.60	0.0033	3.30×10^{-6}	19.60	1.99×10^{-6}	0.00	39.78
3	17.00	0.0028	2.80×10^{-6}	18.16	1.84×10^{-6}	6.81	34.23
7	53.74			53.74		0.00	
9	63.00	0.0089	8.90×10^{-6}	62.99	6.37×10^{-6}	0.01	28.45
RP1	53.60	0.0088	8.80×10^{-6}	52.81	8.83×10^{-6}	1.48	0.37
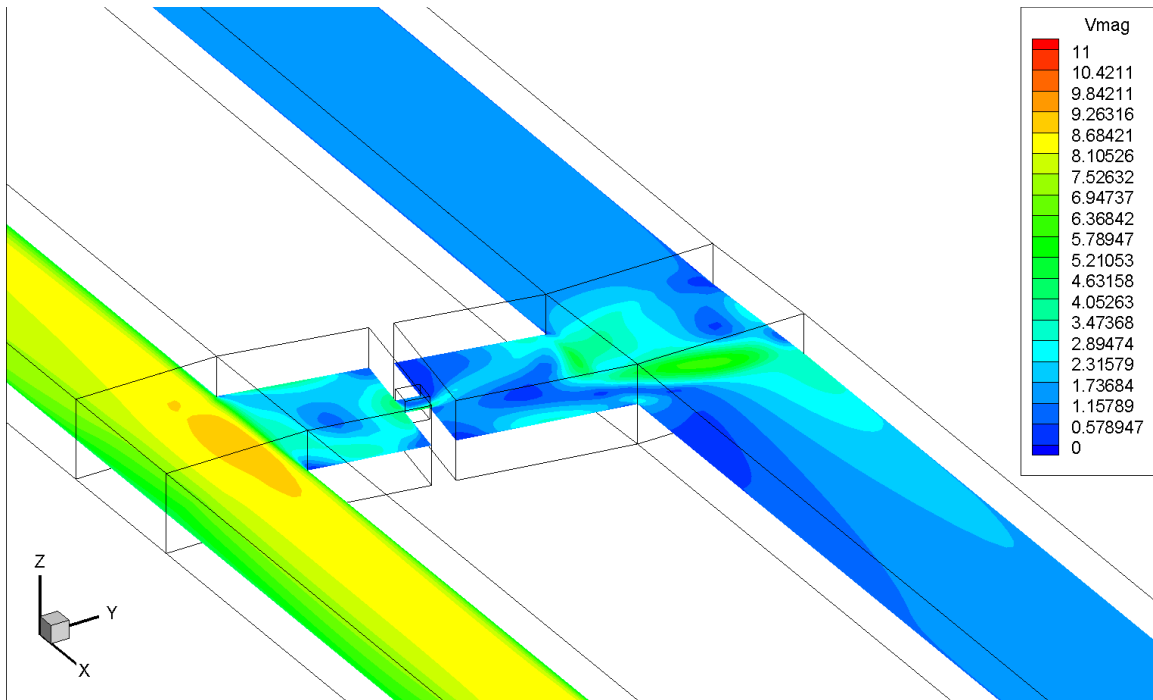
Figure 121. Contour (XY plane) of velocity magnitude (ft/s) around the mandoor in the CFD model without turbulent diffusivity.
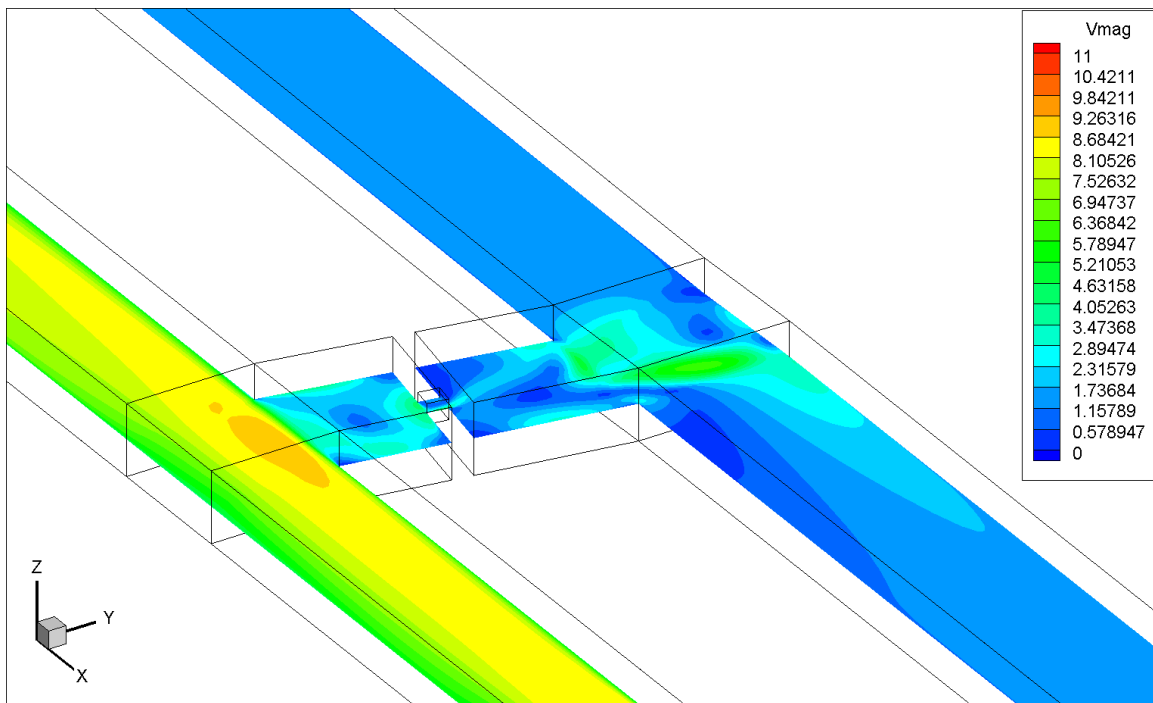

Figure 122. Contour (XY plane) of velocity magnitude (ft/s) around the mandoor in the CFD model with turbulent diffusivity.
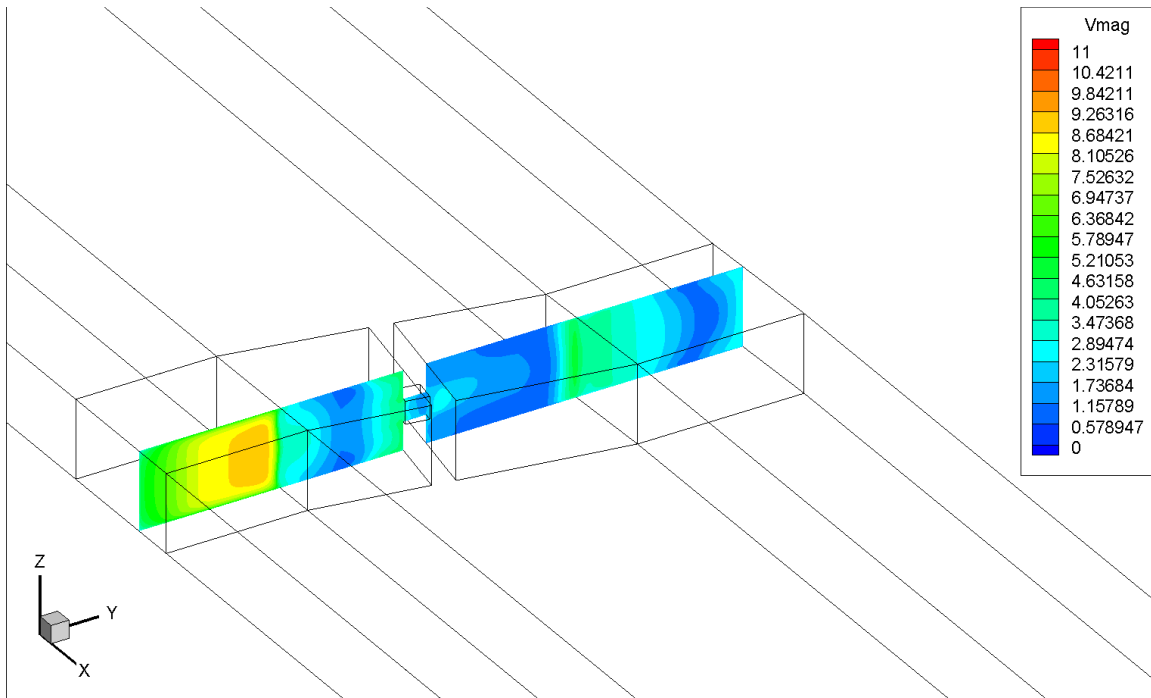
Figure 123. Contour (YZ plane) of velocity magnitude (ft/s) around the mandoor in the CFD model without turbulent diffusivity.
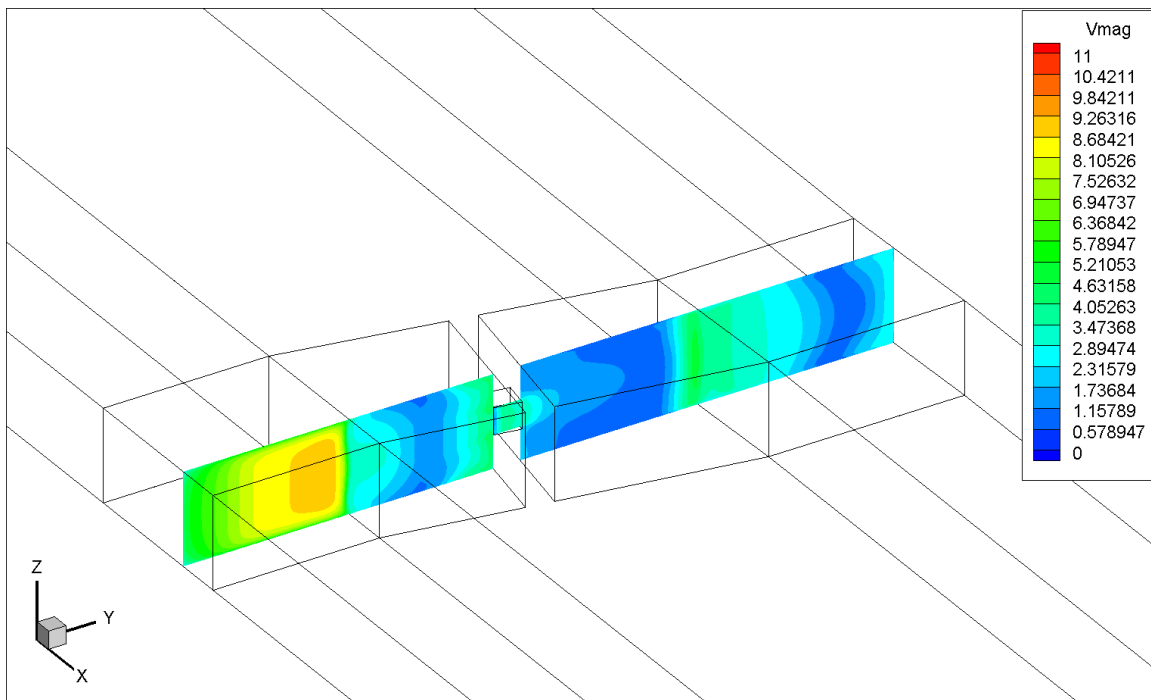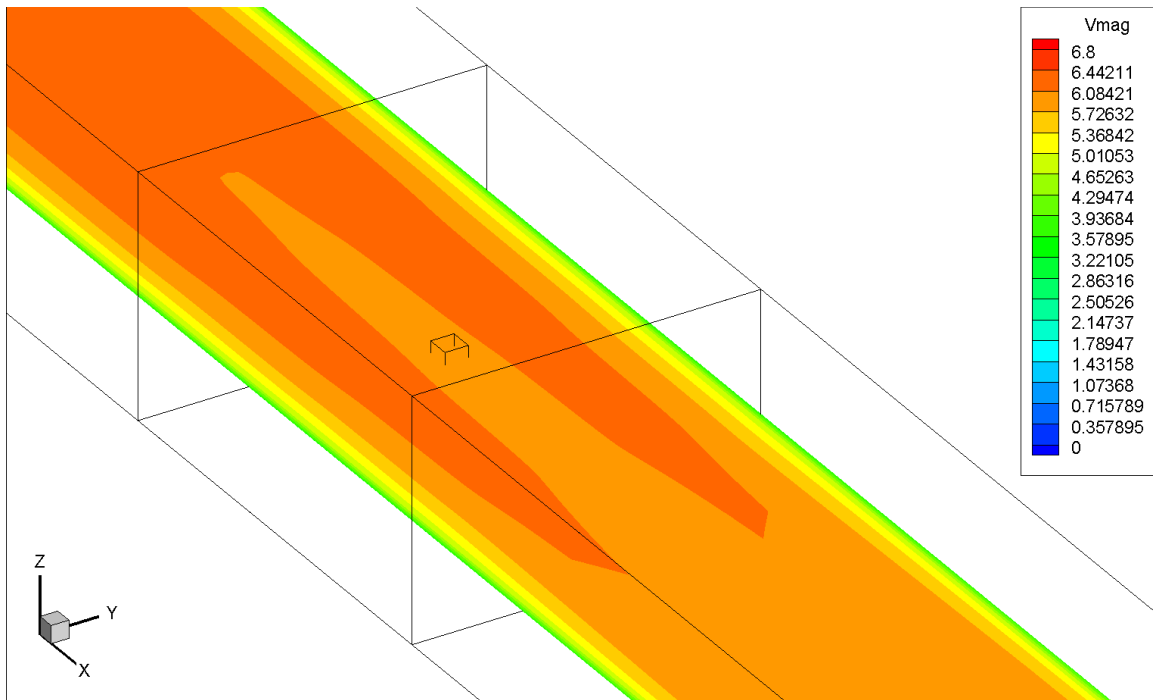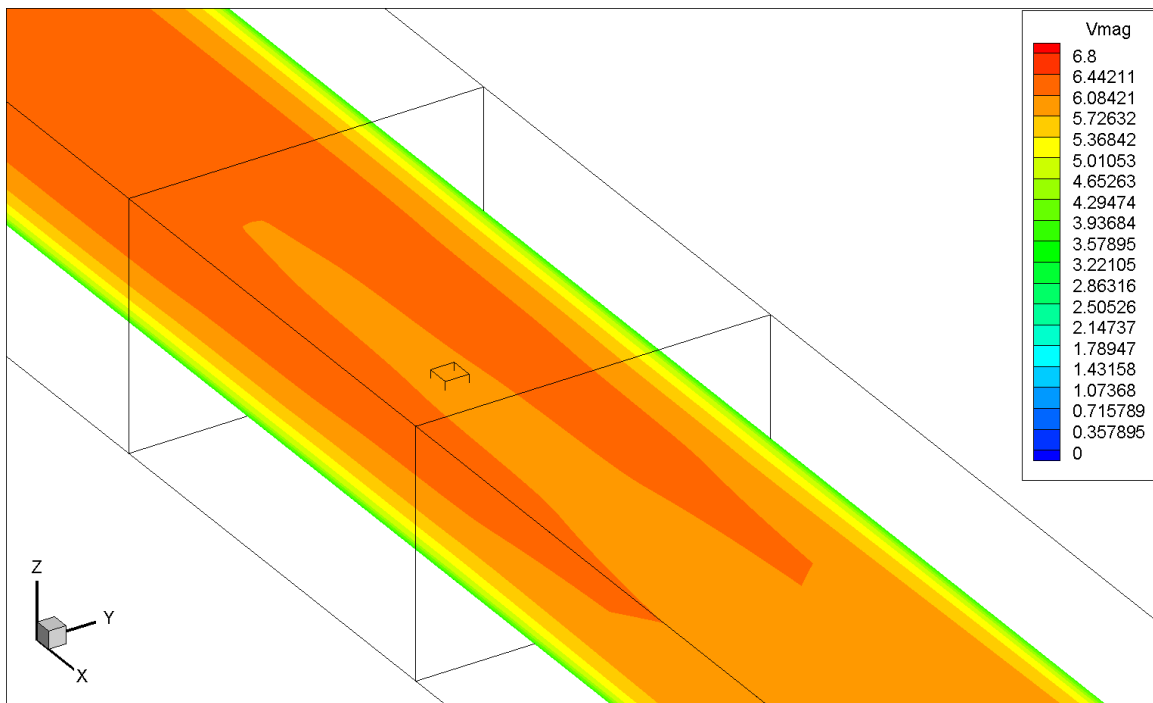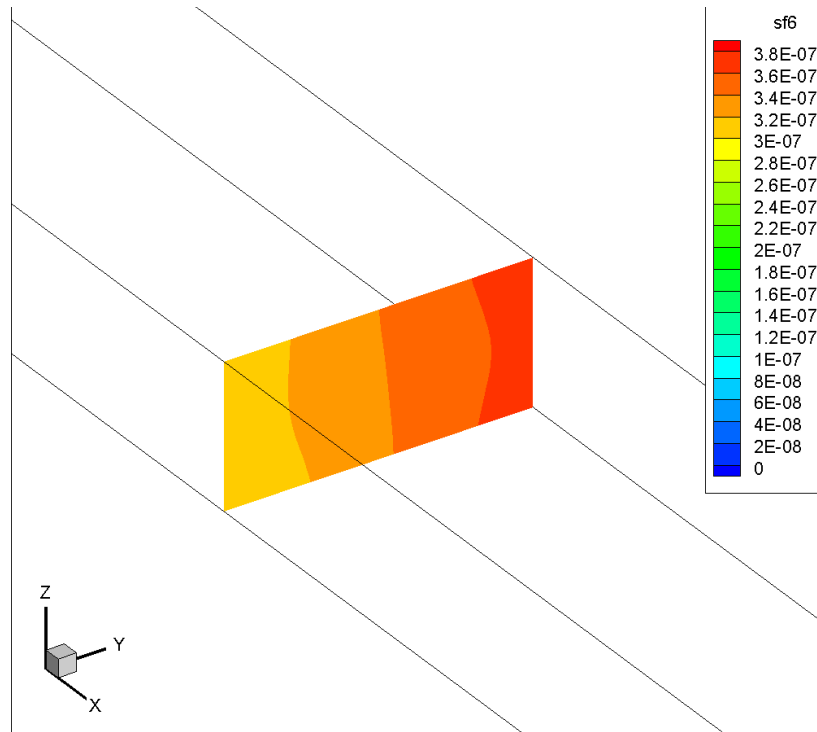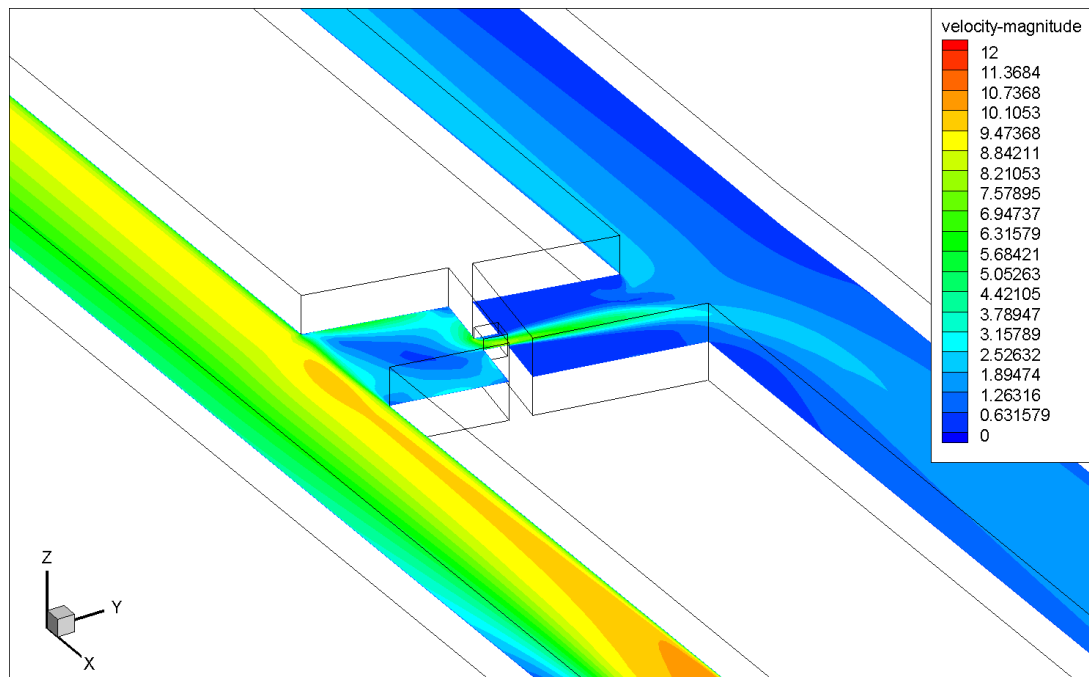

Figure 124. Contour (YZ plane) of velocity magnitude (ft/s) around the mandoor in the CFD model with turbulent diffusivity.

Figure 125. Contour (XY plane) of velocity magnitude (ft/s) around the release point in the CFD model without turbulent diffusivity.

Figure 126. Contour (XY plane) of velocity magnitude (ft/s) around the release point in the CFD model with turbulent diffusivity.
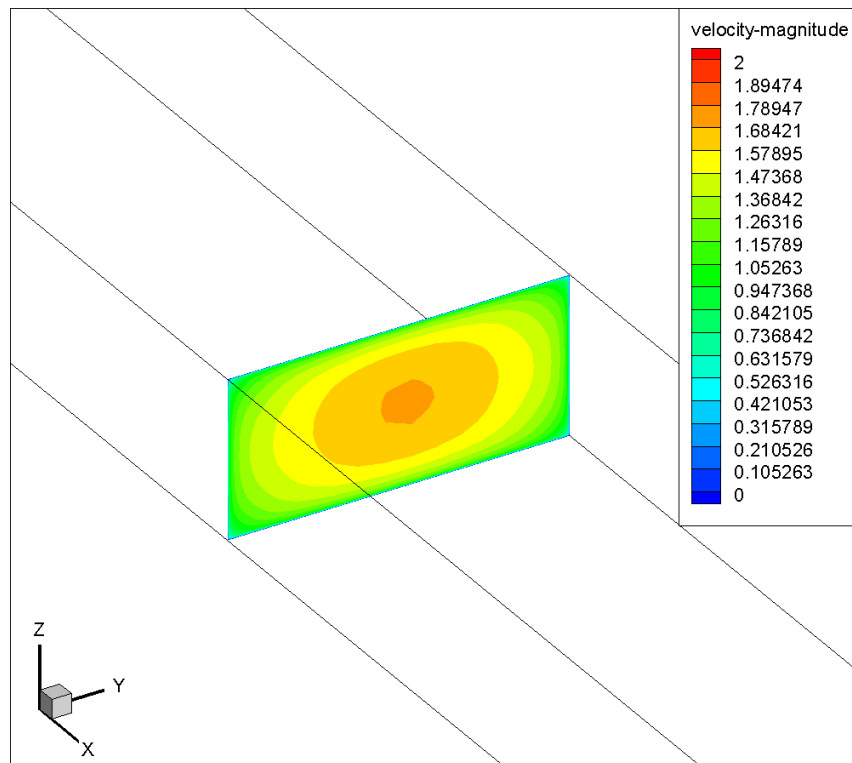
Figure 127. Contour (YZ plane) of SF6 mass concentration at SP2 in the species transport model (steady-state simulation).
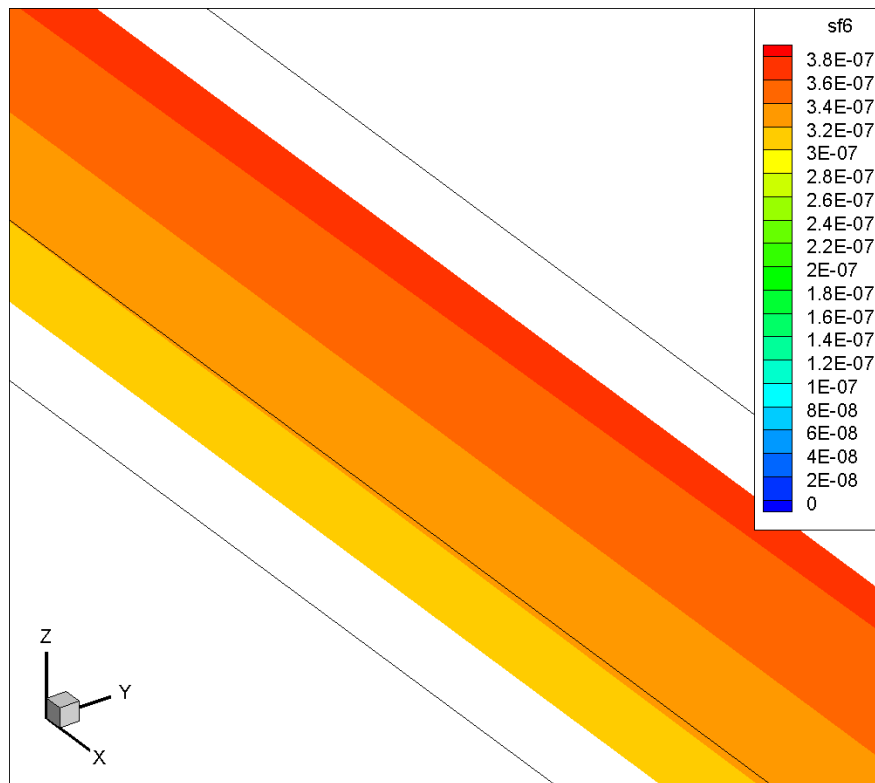
Figure 128. Contour (XY plane) of SF6 mass concentration at SP2 in the species transport model (steady-state simulation).
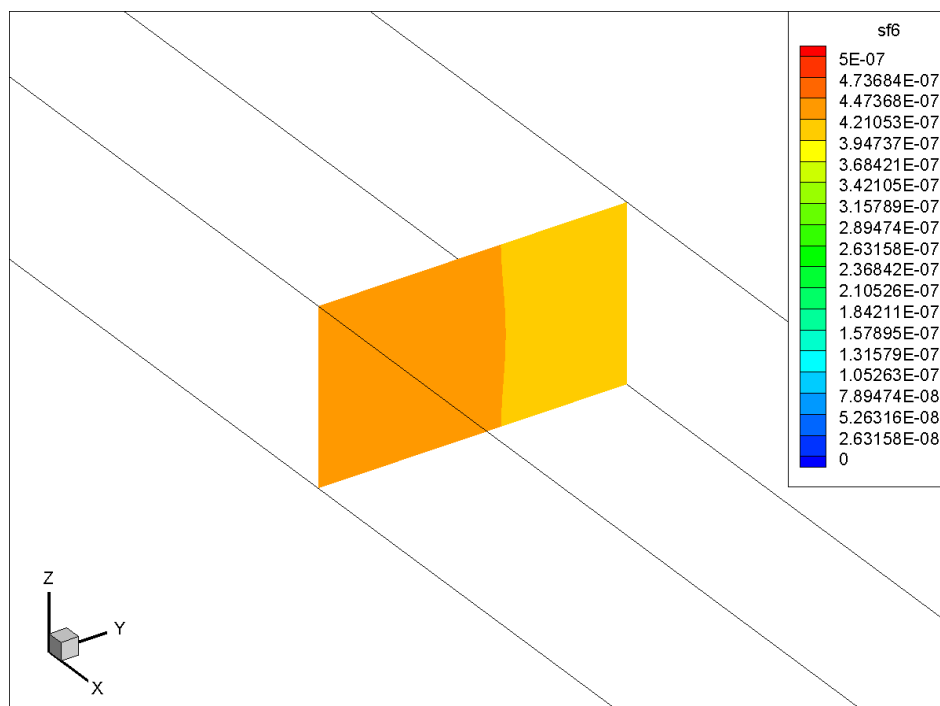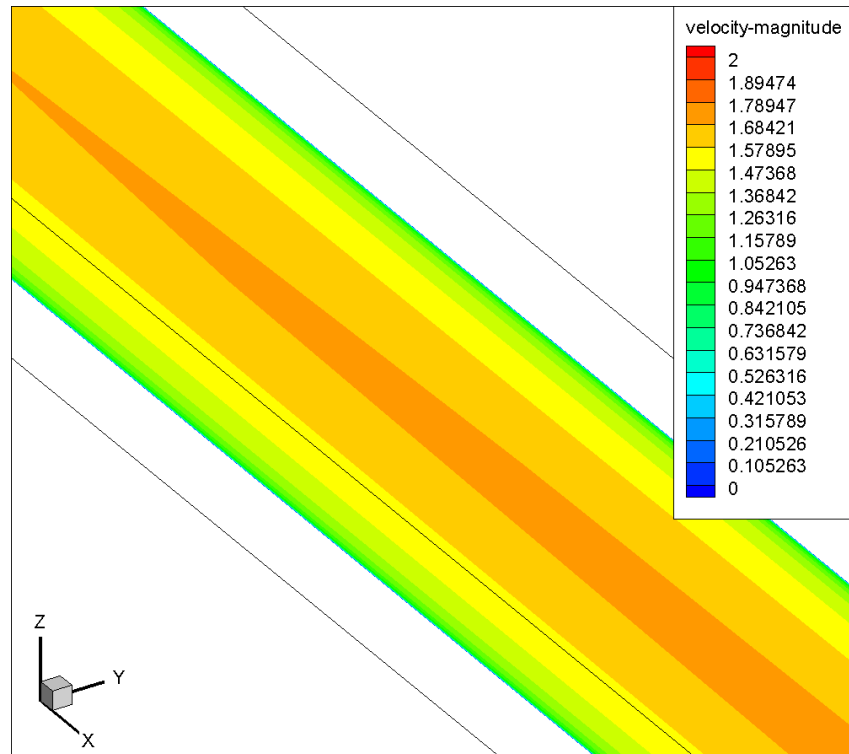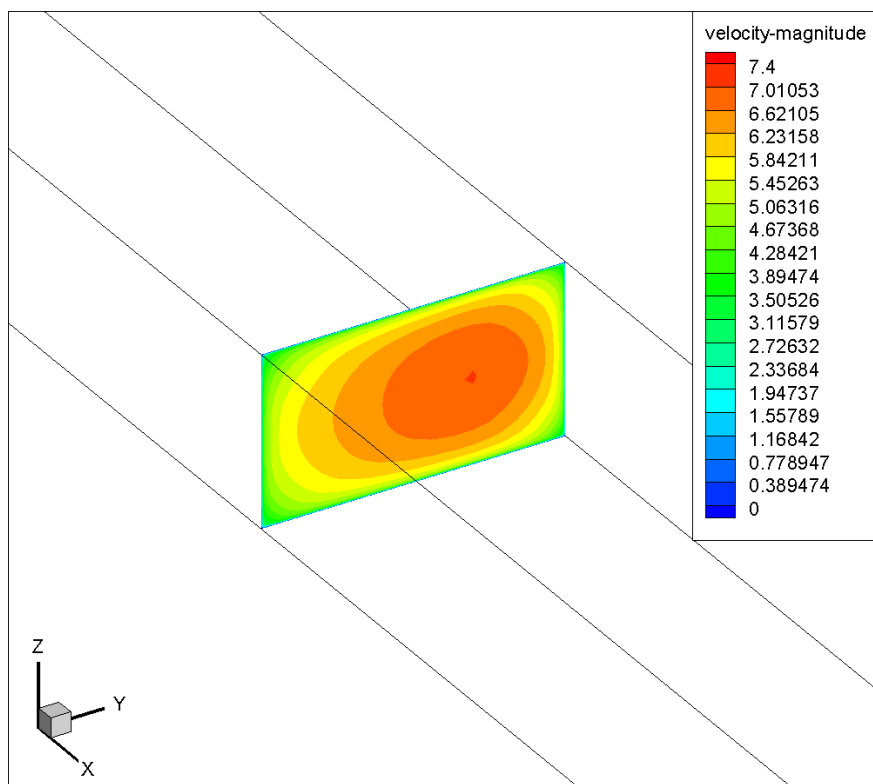
Figure 129. Contour (YZ plane) of SF6 mass concentration at SP9 in the species transport model (steady-state simulation).
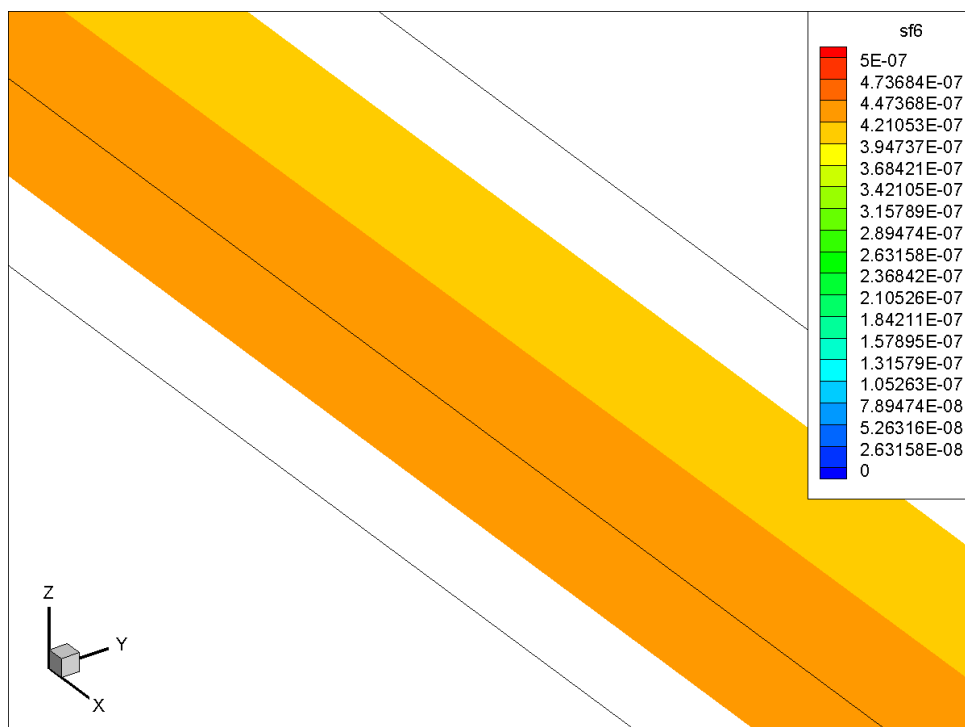
Figure 130. Contour (XY plane) of SF6 mass concentration at SP9 in the species transport model (steady-state simulation).
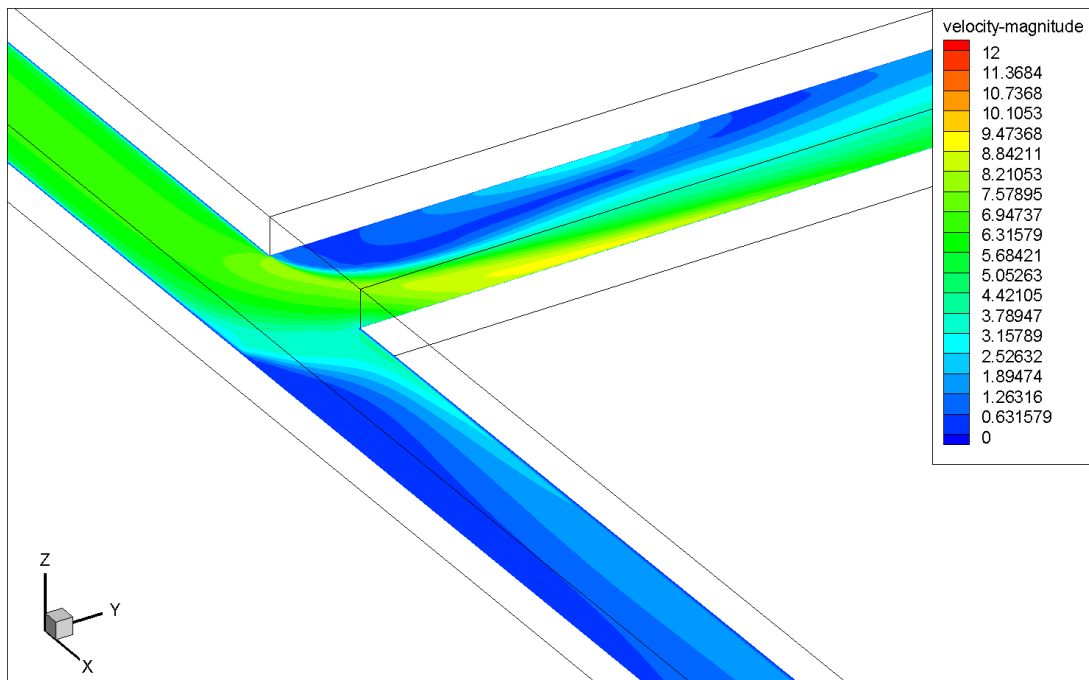
Figure 131. Contour (XY plane) of velocity magnitude (ft/s) at first turn after RP1 in the CFD model (steady-state simulation).

Figure 132. Contour (XY plane) of velocity magnitude (ft/s) around the mandoor in the CFD model (steady-state simulation).

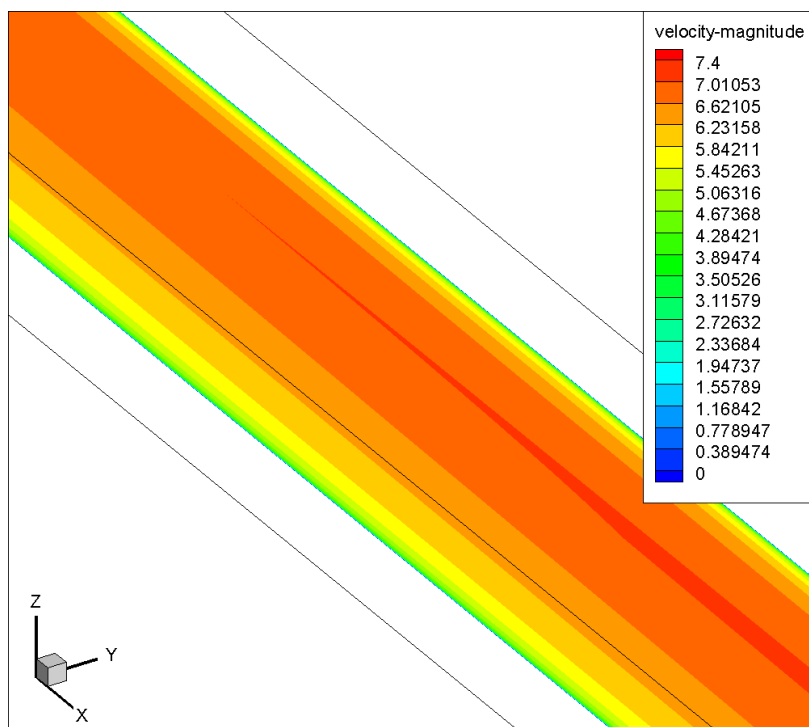Figure 133. Contour (YZ plane) of velocity magnitude at SP2 in the species transport model (steady-state simulation).

Figure 134. Contour (XY plane) of velocity magnitude at SP2 in the species transport model (steady-state simulation).
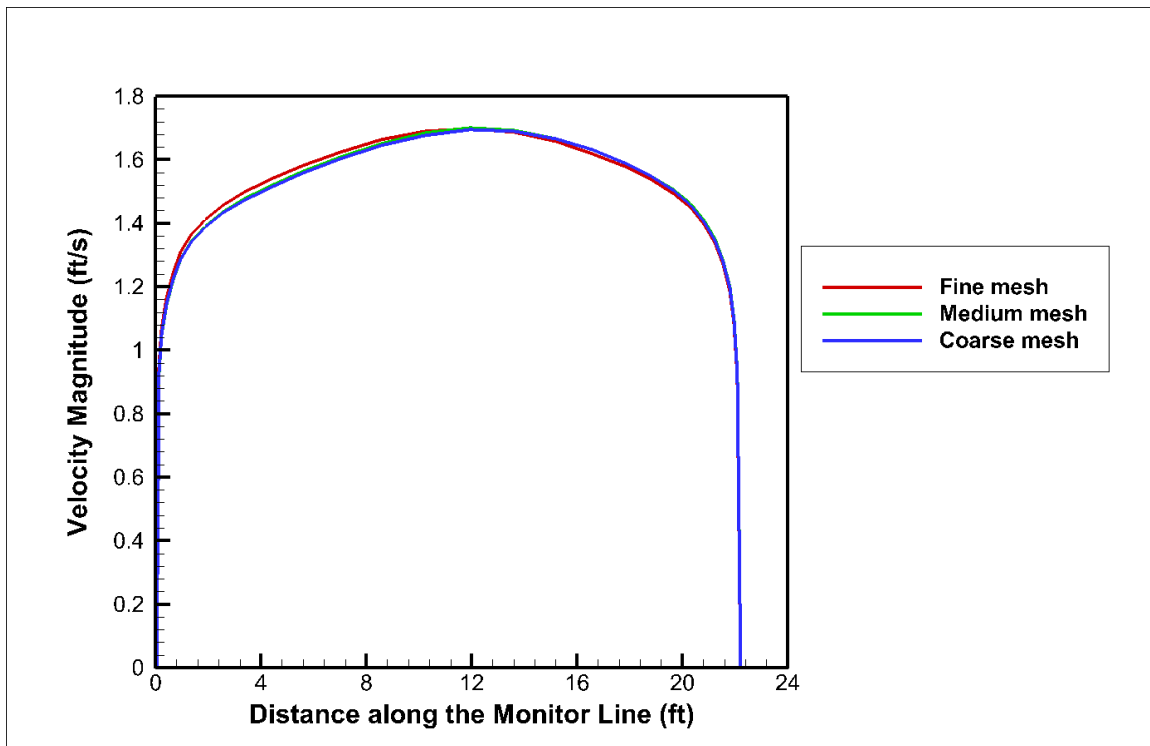
Figure 135. Contour (YZ plane) of velocity magnitude at SP9 in the species transport model (steady-state simulation).

Figure 136. Contour (XY plane) of velocity magnitude at SP9 in the species transport model (steady-state simulation).

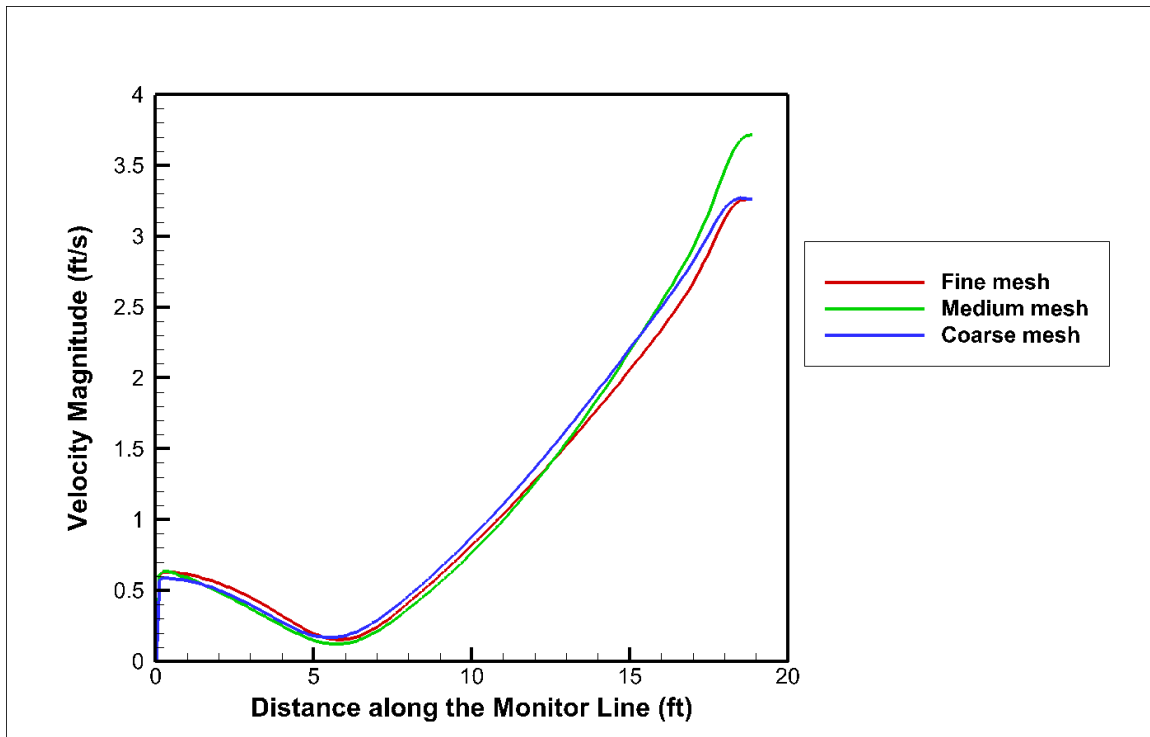Figure 137. Velocity profile at the monitor line where SP2 is located.

Figure 138. Velocity profile at the monitor line where SP3 is located.
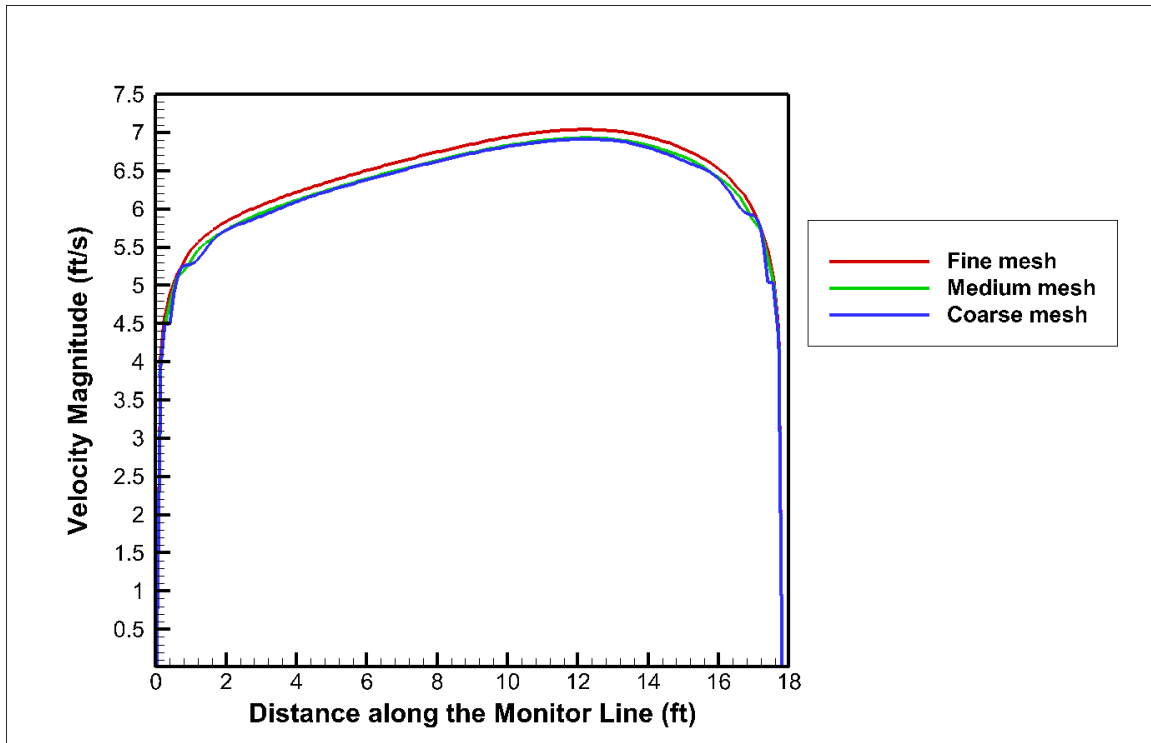
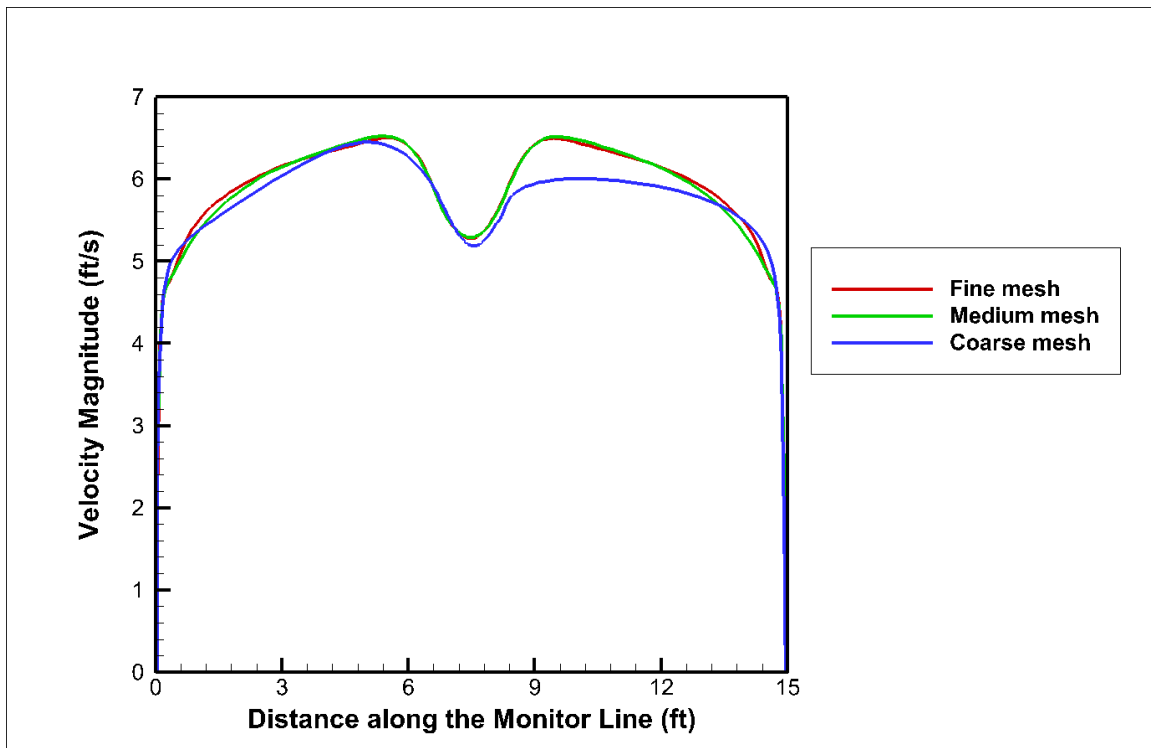Figure 139. Velocity profile at the monitor line where SP9 is located.

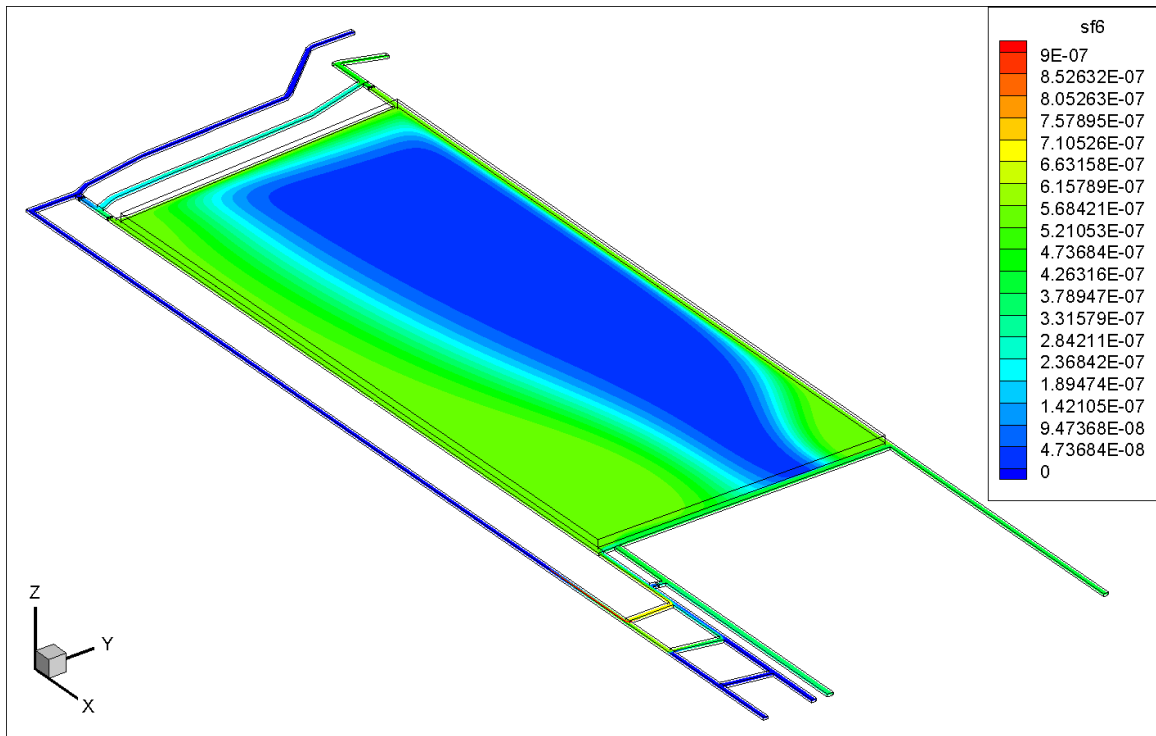Figure 140. Velocity profile at the monitor line where monitor plane A is located.

Figure 141. Visualization (in XY plane) of overall SF6 concentration distribution (created when the steady-state simulation reached 36560 iterations) in the CFD model.